

CHEMIA

2/2017
Tom II

**STUDIA
UNIVERSITATIS BABEȘ-BOLYAI
CHEMIA**

**2/2017
Tom II**

EDITORIAL BOARD OF STUDIA UNIVERSITATIS BABEȘ-BOLYAI CHEMIA

ONORARY EDITOR:

IONEL HAIDUC - Member of the Romanian Academy

EDITOR-IN-CHIEF:

LUMINIȚA SILAGHI-DUMITRESCU

EXECUTIVE EDITOR:

CASTELIA CRISTEA

EDITORIAL BOARD:

PAUL ȘERBAN AGACHI, Babeș-Bolyai University, Cluj-Napoca, Romania

LIVAIN BREAU, UQAM University of Quebec, Montreal, Canada

HANS JOACHIM BREUNIG, Institute of Inorganic and Physical Chemistry,
University of Bremen, Bremen, Germany

MIRCEA DIUDEA, Babeș-Bolyai University, Cluj-Napoca, Romania

JEAN ESCUDIE, HFA, Paul Sabatier University, Toulouse, France

ION GROSU, Babeș-Bolyai University, Cluj-Napoca, Romania

EVAMARIE HEY-HAWKINS, University of Leipzig, Leipzig, Germany

FLORIN DAN IRIMIE, Babeș-Bolyai University, Cluj-Napoca, Romania

FERENC KILAR, University of Pecs, Pecs, Hungary

BRUCE KING, University of Georgia, Athens, Georgia, USA

ANTONIO LAGUNA, Department of Inorganic Chemistry, ICMA, University of
Zaragoza, Zaragoza, Spain

JURGEN LIEBSCHER, Humboldt University, Berlin, Germany

KIERAN MOLLOY, University of Bath, Bath, UK

IONEL CĂȚĂLIN POPESCU, Babeș-Bolyai University, Cluj-Napoca, Romania

CRISTIAN SILVESTRU, Babeș-Bolyai University, Cluj-Napoca, Romania

<http://chem.ubbcluj.ro/~studiachemia/>; studiachemia@chem.ubbcluj.ro

http://www.studia.ubbcluj.ro/serii/chemia/index_en.html

YEAR
MONTH
ISSUE
TOM

Volume 62 (LXII) 2017
JUNE
2
II

S T U D I A
UNIVERSITATIS BABEȘ-BOLYAI
CHEMIA

2

Tom II

ISSUE DOI:10.24193/subbchem.2017.2

STUDIA UBB EDITORIAL OFFICE: B.P. Hasdeu no. 51, 400371 Cluj-Napoca, Romania,
Phone + 40 264 405352

CUPRINS – CONTENT – SOMMAIRE – INHALT

- ANA-MARIA GHELDIU, ALEXANDRA CSAVDARI, MARCELA ACHIM,
LAURIAN VLASE, IOAN TOMUȚĂ, DANA MARIA MUNTEAN,
Kinetics of Zolpidem and Its Metabolite After Single Dose Oral
Administration 179
- ȘTEFANA STĂCESCU, GABRIEL HANCU, LASZLO GAGYI, RUXANDRA
MARIA SOARE, HAJNAL KELEMEN, Simultaneous Determination
of Hydrochlorothiazide and Telmisartan from Pharmaceutical
Preparations Using Capillary Electrophoresis 189
- ZVEZDELINA YANEVA, NEDYALKA GEORGIEVA, A Sensitive Analytical
(RP-HPLC-PDA, UV/VIS) Method for the Determination of Newly
Synthesized N-ISONICOTINOYL-N'-(3-Fluorobenzal) Hydrazone
(SH2) in Aqueous Phase 199

PETRA HERMAN, SÁNDOR HARANGI, MILÁN FEHÉR, ISTVÁN FÁBIÁN, EDINA BARANYAI, The Development of Analytical Methods for the Elemental Determination of Biotic Indicators Present in Aquatic Ecosystems.....	213
TIMEA-ANITA DULL-SZABÓ, MELINDA-EMESE FÜSTÖS, MARIA SUCIU, GABRIEL KATONA, Synthesis and Characterization of Derivatized Carbon Nanostructures.....	223
HAMIDREZA SADEGH, GOMAA A.M. ALI, ZEYNAB ABBASI, MALLIKARJUNA N. NADAGOUDA, Adsorption of Ammonium Ions Onto Multi-Walled Carbon Nanotubes.....	233
PÉTER GERGÓ, ANDRÁS HOLLÓ, ANDRÁS GEIGER, Rheological Investigation of Rubber Bitumen Containing Various Waxes as Warm Mix Additive.....	247
GÁBOR VERÉB, LILLA NAGY, SZABOLCS KERTÉSZ, ILDIKÓ KOVÁCS, CECILIA HODÚR, ZSUZSANNA LÁSZLÓ, Highly Efficient Purification of Finely Dispersed Oil Contaminated Waters by Coagulation/ Flocculation Method and Effects on Membrane Filtration.....	259
JULIETA DANIELA CHELARU, FIRUTA GOGA, MARIA GOREA, Corrosion and Mechanical Properties and Microstructure of Cement Mortar Containing Calcium Sulphate Waste	271
FATEMEH SHEKHOLIA LAVASANI, ABOLGHASEM SHAMELI, EBRAHIM BALALI, DFT Study of the Tubular Size Effects on the Properties of Zigzag Boron Nitride Nanotubes	287
HOSSEIN HOSSEINI, FATEMEH SHAFIEI, Entropy Prediction of Benzene Derivatives Using Topological Indices.....	297
BIANCA MOLDOVAN, LUMINIȚA DAVID, SORIN CLAUDIU MAN, Impact of Thermal Treatment on the Antioxidant Activity of Cornelian Cherries Extract	311
ADYANI AZIZAH ABD HALIM, HABSAH ABDUL KADIR, SAAD TAYYAB, Increased Chemical Stability of <i>Bacillus Licheniformis</i> α -Amylase Upon Acetylation.....	319
PÁL SALAMON, ILDIKÓ MIKLÓSSY, BEÁTA ALBERT, MÓNIKA KORODI, KATALIN NAGY, ILDIKÓ BAKOS, SZABOLCS LÁNYI, CSONGOR ORBÁN, Heterologous Expression and Purification of Recombinant Proapoptotic Human Protein Smac/Diablo with EGFP as Fusion Partner.....	333

ADRIAN PATRUT, STEPHAN WOODBORNE, ROXANA T. PATRUT, LASZLO RAKOSY, GRANT HALL, ILEANA-ANDREEA RATIU, KARL F. VON REDEN, Final Radiocarbon Investigation of Platland Tree, the Biggest African Baobab.....	347
ADRIAN PATRUT, ROXANA T. PATRUT, ROBERT VAN PELT, DANIEL A. LOWY, EDIT FORIZS, JENÖ BODIS, DRAGOS MARGINEANU, KARL F. VON REDEN, Radiocarbon Dating of a Very Large African Baobab from Limpopo, South Africa: Investigation of the Sagole Big Tree	355
ADRIANA GROZAV, BOGDAN STANCU, COSMINA BOARI, FLORE CHIRILA, NICODIM FIT, CASTELIA CRISTEA, <i>N'</i> -benzylidene- <i>N</i> -(thiazolyl)acetohydrazide Derivatives: Synthesis and Antimicrobial Activity Evaluation	365
RAMONA BLEIZIFFER, CORNELIA MESAROS, SONIA SUVAR, PAULA PODEA, ANDREEA IORDACHE, FLORENTINA-DIANA YUDIN, MONICA CULEA, Comparative Characterization of Basil, Mint and Sage Extracts	373
NIKOLAOS GOUGOULIAS, LIVIU GIURGIULESCU, IOANNIS VAGELAS, ELENI WOGIATZI, MARIA-NEKTARIA NTALLA, Changes in Total Phenol Content and Antioxidant Activity of Greek Table Olive Cultivar <i>Amfissis</i> During Maturation.....	387

Studia Universitatis Babes-Bolyai Chemia has been selected for coverage in Thomson Reuters products and custom information services. Beginning with V. 53 (1) 2008, this publication is indexed and abstracted in the following:

- Science Citation Index Expanded (also known as SciSearch®)
- Chemistry Citation Index®
- Journal Citation Reports/Science Edition

KINETICS OF ZOLPIDEM AND ITS METABOLITE AFTER SINGLE DOSE ORAL ADMINISTRATION

ANA-MARIA GHELDIU^a, ALEXANDRA CSAVDARI^b, MARCELA ACHIM^a,
LAURIAN VLASE^{a*}, IOAN TOMUȚĂ^a, DANA MARIA MUNTEAN^a

ABSTRACT. The present study aimed to describe the basic pharmacokinetics of zolpidem and its metabolite zolpidem phenyl-4-carboxylic acid after a single oral dose of 5 mg zolpidem. Six competing kinetic models were created in order to analyze the experimental data obtained from the 20 healthy volunteers enrolled in a clinical study. Based on rational model discrimination criteria (Akaike index value), the best one was chosen and further used for a better understanding of the kinetics of zolpidem and its metabolite in the body after administration. The kinetic model considers that zolpidem absorption process follows a first-order kinetics and during this stage it is partially metabolized (pre-systemic metabolism) to its main metabolite. The kinetics of both zolpidem and its metabolite is characterized by bicompartmental distribution and first order kinetics of both elimination and systemic metabolism.

Keywords: *zolpidem, zolpidem phenyl-4-carboxylic acid, compartmental pharmacokinetic analysis*

INTRODUCTION

Zolpidem is an imidazopyridine which acts at the benzodiazepine ω 1-receptor subtype [1,2] exhibiting hypnotic-sedative action exclusively due to agonist binding on the α ₁- gamma-aminobutyric acid type A (GABA_A)

^a *University of Medicine and Pharmacy "Iuliu Hatieganu", Faculty of Pharmacy, Department of Pharmaceutical Technology and Biopharmaceutics, 8 Victor Babes str., RO-400012, Cluj-Napoca, Romania*

^b *Babeş-Bolyai University, Faculty of Chemistry and Chemical Engineering, 11 Arany Janos str., RO-400028, Cluj-Napoca, Romania*

* *Corresponding author: laurian.vlase@yahoo.com*

receptors. Zolpidem is recommended for the reduction of sleep onset time, increase total duration of sleep and sleep efficiency, given in doses of 5 up to 7.5 mg [1,6] for the short-term treatment of insomnia [7].

Zolpidem displays rapid absorption after oral administration and has an absolute bioavailability of about 70% [5,8]. Is characterized by linear kinetics in the 5-20 mg dose range [5], is highly bound to plasma proteins (around 92%) [6] and it is subjected to extensive hepatic metabolism [7,8]. Zolpidem is a substrate to several distinct CYP 450 isoenzymes, among which the major metabolism pathway occurs through CYP3A4 (61%) [9,10,11]. It is converted to three pharmacologically inactive metabolites in the liver via oxidation and hydroxylation, of which the 4-carboxy-derivative is the predominant one (zolpidem phenyl-4-carboxylic acid – Z4CA), representing 72 up to 86% of the administered dose [12,13,14]. The time to reach the maximum plasma concentration is around 0.5-3 hr and the half-life time of zolpidem is about 2-3 hours [3,4].

Pharmacokinetics, by the quantitative study of the processes that take place depending on time, offers a better understanding of the relationship between the given/administered dose and the pharmacological effect [15]. The compartmental modeling approach of pharmacokinetics consists in describing the processes that the administered drug is subjected to in the body, depicted as an entity divided into distinct compartments with different properties and specific affinities for the drug or drug metabolites [16]. The drug leaves the site of administration by the process of absorption in order to reach the central compartment from which is it further exchanged both-ways with the peripheral compartments (distribution process) and it is later irreversibly eliminated from the body (by metabolism and/or excretion). All the kinetic processes that the drug undergoes in the body can be characterized by transfer rate constants, which in linear kinetics (1st order kinetics) are assumed to be directly proportional to the mass of transfer available drug [1,8]. By performing compartmental and non-compartmental analysis, the corresponding pharmacokinetic parameters of the drug can be obtained, and they can be further used in drug formulation development [17], bioequivalence assays or in therapeutic drug monitoring for patient-specific dose adjustment [18].

The aim of this study was to create and to use a pharmacokinetic model that can accurately describe the kinetic processes involved in absorption, distribution, metabolism and elimination of zolpidem and zolpidem phenyl-4-carboxylic acid (Z4CA) after oral administration of a single dose of zolpidem in healthy volunteers, by comparing predicted values with actual experimental data.

RESULTS AND DISCUSSION

A number of six distinct mathematical models were created with the purpose of assessing the pharmacokinetics of zolpidem and its main metabolite, Z4CA. The characteristics of each individual kinetic model are summarized in Table 1.

Table 1. Pharmacokinetic models of zolpidem and its metabolite used in compartmental analysis

Model	Pre-systemic metabolism kinetics	Systemic metabolism kinetics	Zolpidem, number of compartments	Zolpidem phenyl-4-carboxylic acid, number of compartments
M1	No process	1 st order	1	1
M2	No process	1 st order	2	1
M3	No process	1 st order	2	2
M4	1 st order	1 st order	1	1
M5	1 st order	1 st order	2	1
M6	1 st order	1 st order	2	2

The differences between the evaluated mathematical models consisted in suppositions about the existence of pre-systemic metabolism of zolpidem and about the number of compartments for both zolpidem and Z4CA. For instance, the first pharmacokinetic model (M1) assumes no pre-systemic metabolism of zolpidem and monocompartmental distribution for both zolpidem and its metabolite. The model M6 employs existence of pre-systemic metabolism and bicompartamental distribution for both zolpidem and Z4CA. For each tested model, the process of compounds elimination along with the systemic metabolism of zolpidem to zolpidem phenyl-4-carboxylic acid were regarded as 1st order kinetic processes.

The schematic representation of the kinetic processes from model M6 are shown in Figure 1.

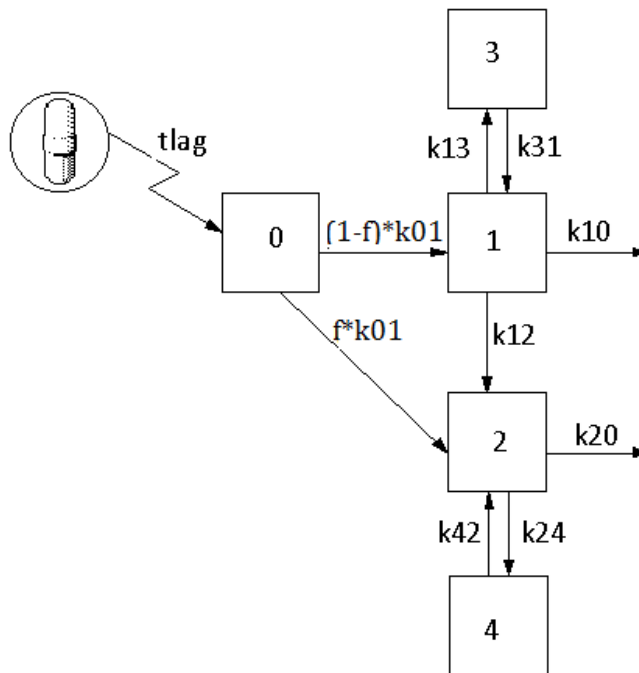


Figure 1. Schematic representation of kinetic processes from model M6, where “0” is absorption compartment of zolpidem; “1” and “2” are central compartments of zolpidem and zolpidem phenyl-4-carboxylic acid; “3” and “4” are their corresponding peripheral distribution compartments; t_{lag} is the latency time for absorption; k_{01} is the absorption rate constant of zolpidem, f is the fraction of zolpidem converted into metabolite during absorption (pre-systemic metabolism); k_{13} , k_{31} , k_{24} , k_{42} are the distribution rate constants; k_{12} is the systemic metabolization rate constant of zolpidem to metabolite; k_{10} and k_{20} are the elimination rate constants for zolpidem (non-metabolic) and zolpidem phenyl-4-carboxylic acid. The kinetic processes are represented by straight arrows.

For each analyzed kinetic model, the corresponding mathematical differential equations were written and run by using Phoenix 6.1 software package (Certara, SUA). The equations of model M6 are illustrated in Figure 2.

$$\begin{cases}
 \frac{\partial QZ_{abz}}{\partial t} = -k_{01} * QZ_{abz} \\
 \frac{\partial QZ_c}{\partial t} = (1-f) * k_{01} * QZ_{abz} - k_{10} * QZ_c - k_{13} * QZ_c + k_{31} * QZ_p - k_{12} * QZ_c \\
 \frac{\partial QZ_p}{\partial t} = k_{13} * QZ_c - k_{31} * QZ_p \\
 \frac{\partial QM_c}{\partial t} = f * k_{01} * QZ_{abz} + k_{12} * QZ_c - k_{20} * QM_c - k_{24} * QM_c + k_{42} * QM_p \\
 \frac{\partial QM_p}{\partial t} = k_{24} * QM_c - k_{42} * QM_p \\
 ConcZ_c = \frac{QZ_c}{V_F} \\
 ConcM_c = \frac{QM_c}{V_F}
 \end{cases}$$

Figure 2. The mathematical equations of the kinetic model M6, where QZ_c and QZ_p are the amount of zolpidem in central and peripheral compartment respectively; QM_c and QM_p are the quantities of metabolite in central and peripheral compartments; $ConcZ$ and $ConcM$ are the plasma concentrations of zolpidem and zolpidem phenyl-4-carboxylic acid, V_F is the apparent volume of distribution of the central compartment. All the other parameters used were previously presented

The mean plasma concentrations of zolpidem and zolpidem phenyl-4-carboxylic acid were evaluated using the six kinetic models previously described, after their implementation in Phoenix software. It was used the same settings of the software minimisation engine for all models analysis: weighting scheme 1/y (1/observed concentration), minimisation method: Gauss-Newton (Levenberg and Hartley variant), convergence criterion: 0.0001.

The Akaike index (automatically calculated and provided by the analysis software) was used for model discrimination [22,23]. The model that proved a better fitting to the experimental data was characterised by a smaller Akaike index. The Akaike values for the six analysed models are presented in Figure 3.

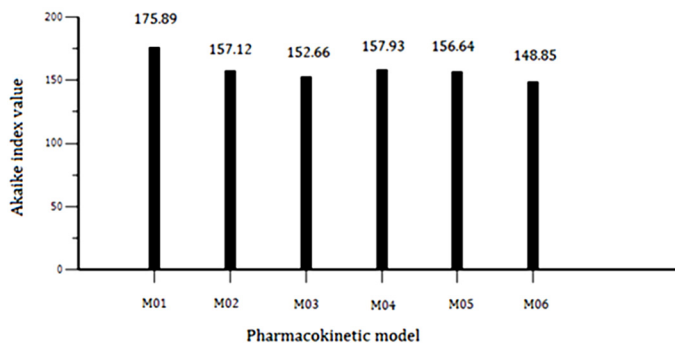


Figure 3. Akaike index values for mathematical models used for characterisation of zolpidem and zolpidem phenyl-4-carboxylic acid pharmacokinetics

By visually inspecting the Akaike values presented in Figure 3, it can easily be observed that model M6 fits the experimental data better than its concurrent models, displaying the smallest Akaike value, therefore it was elected as representative for describing the kinetics of zolpidem and Z4CA after oral administration of a single dose of zolpidem.

Figure 4 presents a typical fitting of a subject dataset to representative model M6 in comparison with M1. Zolpidem and Z4CA plasma concentrations displayed a better correlation between the experimental (observed) and the fitted (predicted) values in case of model M6 than in case of model M1.

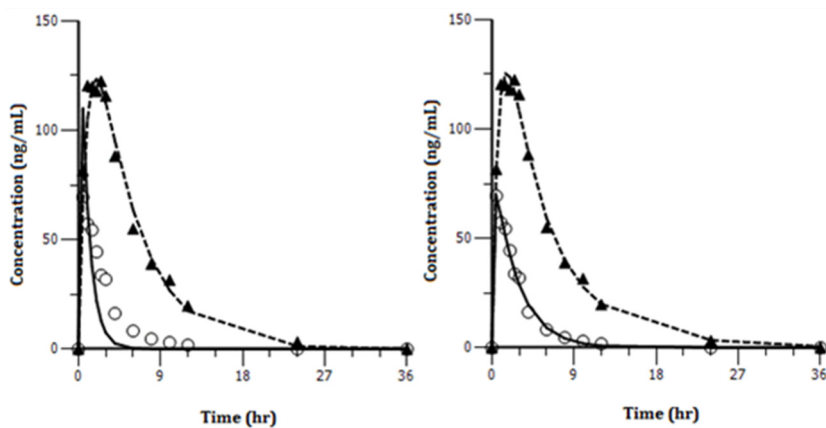


Figure 4. Typical fitting of model M1 (left) and model M6 (right) to a subject dataset (○ and ▲ denote the experimental determined concentrations of zolpidem and its metabolite, respectively; the continues and dotted lines are the fitted/computed concentrations predicted by the kinetic model)

According to kinetic model M6, the pharmacokinetics of zolpidem is characterised by a first order absorption kinetics with pre-systemic metabolism to zolpidem phenyl-4-carboxylic acid. Once inside the body, both zolpidem and Z4CA are characterised by bicompartamental distribution. After absorption, zolpidem is subject to systemic metabolism leading to the formation of the main metabolite, zolpidem phenyl-4-carboxylic acid, following a first-order kinetic process. Both compounds are further eliminated from the body by first order kinetic processes. By using this representative pharmacokinetic model for zolpidem and Z4CA, their characteristic pharmacokinetic parameters were calculated (Table 2).

Table 2. The kinetic parameters of zolpidem and zolpidem phenyl-4-carboxylic acid calculated with model M6

Variable	Mean	SD	% CV	Median	Geometric mean
T _{lag} (hr)	0.281	0.251	89.2	0.327	0.0248
k ₀₁ (hr ⁻¹)	0.644	0.603	93.7	0.367	0.47
f	0.311	0.177	57	0.251	0.226
k ₁₀ (hr ⁻¹)	0.135	0.164	121	0.0733	0.026
k ₁₂ (hr ⁻¹)	3.54	2.98	84.3	2.82	1.37
k ₁₃ (hr ⁻¹)	4.66	3.92	84.2	3.48	2.44
k ₃₁ (hr ⁻¹)	2.21	3.09	140	0.255	0.358
k ₂₀ (hr ⁻¹)	2.37	2.37	100	2.04	1.5
k ₂₄ (hr ⁻¹)	2.08	2.36	113	1.12	0.451
k ₄₂ (hr ⁻¹)	1.69	2.08	123	0.826	0.608
V _F (L)	5660	4330	76.5	3690	4030

A considerable variability of calculated kinetic parameters of zolpidem and its metabolite can be observed between the 20 subjects enrolled in the study (Table 2). However, this is currently observed in clinical studies, involving human subjects participation, due to natural biological and physiological differences between subjects (inter-subject variability) [24,25].

The absorption of zolpidem is delayed for about 0.28 ± 0.25 hours after oral administration, the time needed for the biopharmaceutical processes to take place (disintegration, release, dissolution of the drug molecules in the liquid interior body medium) and for the drug molecules to reach into duodenum. The absorption rate constant is 0.644 ± 0.603 hr⁻¹, which means an absorption half-life time of about 1.076 hr. During the stage of absorption, about 30% of the bioavailable amount of zolpidem is converted to inactive metabolite which appears in plasma, meaning that the oral bioavailability of zolpidem (pharmacologically active molecule) is approximately 70%.

The apparent volume of distribution for central compartment of both zolpidem and metabolite is about 5660 ± 4330 L, this high value being expected as both compounds are lipophilic and highly bounded on tissue proteins (approximately 92% protein binding). The kinetic model M6 considers two possible elimination pathways for zolpidem: by systemic metabolism to zolpidem phenyl-4-carboxylic acid (characterised by a rate constant k₁₂) and by other processes, primarily by renal excretion (characterised by an overall rate constant k₁₀). As it can be observed from Table 2, the value of k₁₂ (3.54 ± 2.98 hr⁻¹) is much higher than k₁₀ (0.135 ± 0.164 hr⁻¹). This means that the majority of zolpidem (99.6%) is eliminated from the body by metabolism to Z4CA, the rest being eliminated by metabolization to other metabolites or by direct renal excretion. Both zolpidem and its metabolite are distributed between central and peripheral compartments, the latter exhibiting a higher affinity for each compound ($k_{13} > k_{31}$ and $k_{24} > k_{42}$).

The observed plasma concentrations of zolpidem phenyl-4-carboxylic acid are due to both pre-systemic and systemic biotransformation of zolpidem. The metabolite is eliminated following a first-order kinetic process, characterised by a rate constant of $2.37 \pm 2.37 \text{ hr}^{-1}$.

CONCLUSIONS

Six different mathematical models were tested in order to describe the kinetics of zolpidem and its metabolite Z4CA after oral administration of a single oral dose of 5 mg zolpidem. These models involved differences regarding the pre-systemic metabolism of zolpidem to its metabolite and the mono- or bicompartamental distribution of the compounds in the body.

After experimental data analysis, the representative model for the pharmacokinetics of zolpidem and its metabolite was found and described. The model considers that zolpidem is absorbed following a first-order kinetic process and is partially converted during absorption to its main metabolite, Z4CA. The kinetics of zolpidem is characterized by bicompartamental distribution and first order kinetic elimination processes (99.6% by biotransformation to metabolite, the rest by other paths). The metabolite zolpidem phenyl-4-carboxylic acid displays also a bicompartamental distribution and a first order elimination kinetics.

The knowledge of drug kinetics in the body through compartmental modeling is the starting point for other important analysis such as pharmacokinetic population modelling, prediction of drug plasma levels at other doses or when multiple doses are administered or further mathematical correlations between drug kinetics and pharmacological effect intensity. It also allows a better calculation of dosage regimen of a drug in a particular situation, considering the influence of altered physiology or disease state on drug absorption, distribution, metabolism and elimination as well as giving a better understanding of drug interactions, if the case.

EXPERIMENTAL SECTION

Subjects: In this study were enrolled 20 healthy volunteers and all gave their written informed consent prior to study inclusion. The study was conducted according to the principles of Declaration of Helsinki (1964) and its amendments (Tokyo 1975, Venice 1983, Hong Kong 1989). The clinical protocol was reviewed and approved by the Ethics Committee of the University of Medicine and Pharmacy "Iuliu Hatieganu", Cluj-Napoca, Romania.

Study protocol: After an overnight fast, the volunteers received a single 5 mg zolpidem dose at 8:00 a.m. with 150 ml of water. The pharmaceutical product used was Stilnox (10 mg film-coated tablets, Sanofi-Aventis – Romania). Venous blood samples (5 ml) were taken according to the following time schedule: before drug administration (0 h), and at 0.5, 1, 1.5, 2, 2.5, 3, 4, 6, 8, 10, 12, 24, 36 and 48 hours after drug administration. Within 10 minutes of collection, blood samples were centrifuged at 5000 rpm for 10 minutes and plasma samples were frozen stored at -20°C until further analysis.

Drug analysis from plasma: Zolpidem and Z4CA plasma concentrations were determined using a validated high-throughput liquid chromatography tandem mass spectrometry method. The HPLC system was an Agilent 1100 series (binary pump, autosampler, thermostat) (Agilent Technologies, USA) and was coupled with a Bruker Ion Trap SL (Bruker Daltonics GmbH, Germany). A Zorbax SB-C18 chromatographic column (100 mm x 3.0 mm i.d., 3.5 µm) (Agilent Technologies) was used.

The mobile phase was a mixture of 2 mM ammonium formate solution and acetonitrile, elution in gradient: 11 % acetonitrile at start, 41% at 2 minutes. The flow rate was 1 ml/min and the thermostat temperature was set at 48°C. The mass spectrometry detection was in multiple reaction monitoring mode, positive ions, using an electrospray ionization source. The ion transitions monitored were for zolpidem were m/z (235.5; 263.2) from 308 and for its metabolite m/z (265.1; 266.1; 293.1) from 338, respectively [19,20,21]. The calibration curves for both zolpidem and its metabolite were linear between 2-400 ng/ml.

Pharmacokinetic analysis: The compartmental pharmacokinetic analysis was performed in order to analyze the plasma versus time levels of zolpidem and its metabolite for each individual dataset obtained from volunteers (20 datasets).

Six distinct mathematical models were created in order to assess the pharmacokinetics of zolpidem and its metabolite (see Table 1).

REFERENCES

1. Langtry H.D., Benfield P., *Drugs*, **1990**, *40*(2), 291.
2. Hoehns J.D., Perry P.J., *Clinical Pharmacy*, **1993**, *12*(11), 814.
3. Vlase L., Popa A., Neag M., Muntean D., Leucuta S.E., *European Journal of Drug Metabolism and Pharmacokinetics*, **2011**, *35*(3), 83.
4. Vlase L., Popa A., Neag M., Muntean D., Baldea I., Leucuta S.E., *Journal of Clinical Pharmacology*, **2011**, *51*(8), 1233.
5. Swainston Harrison T, Keating GM., *CNS Drugs*, **2005**, *19*(1), 65.
6. Holm K.J., Goa K.L., *Drugs*, **2000**, *59*(4), 865.

7. Darcourt G, Pringuey D, Sallière D, Lavoisy J., *Journal of Psychopharmacology*, **1999**, 13(1), 81.
8. Drover DR., *Clinical Pharmacokinetics*. **2004**, 43(4), 227.
9. Barkin R.L., *American Journal of Therapeutics*, **2007**, 14(3), 299.
10. Greenblatt DJ, Roth T., *Expert Opinion on Pharmacotherapy*, **2012**, 13(6), 879.
11. Von Moltke LL, Greenblatt DJ, Granda BW, Su XD, Grassi JM, Venkatakrishnan K, et al., *British Journal of Clinical Pharmacology*, **1999**, 48, 89.
12. Krylova EA, Kataev SS, Khomov Y, *Journal of Analytical Chemistry*, **2013**, 68(8), 722.
13. Zhou SF, Zhou ZW, Yang LP, Cai JP, *Current Medicinal Chemistry*, **2009**, 16(27), 3480.
14. Pichard L, Gillet G, Bonfils C, Domergue J, Thenot JP, Maurel P, *Drug Metabolism and Disposition*, **1995**, 23(11), 1253.
15. Benet L.Z., Zia-Amirhosseini P., *Toxicologic Pathology*, **1995**, 23(2), 115.
16. Himmelstein K.J., Lutz R.J., *Journal of Pharmacokinetics and Biopharmaceutics*, **1979**, 7(2), 127.
17. Peck C.C., Barr W.H., Benet L.Z., Collins J., Desjardins R.E., Furst D.E., et al, *Journal of Pharmaceutical Sciences*, **1992**, 81(6), 605.
18. Mangoni A.A., Jackson S.H.D., *British Journal of Clinical Pharmacology*, **2003**, 57(1), 6.
19. Gheldiu A.M., Popa A., Neag M., Muntean D., Bocsan C., Buzoianu A., Vlase L., Achim M., Todor I., Briciu C., *Farmacia*, **2015**, 63(3), 453.
20. Vlase L., Popa A., Neag M., Muntean D., Baldea I., Leucuta S.E., *Journal of Clinical Pharmacology*, **2011**, 51, 1233.
21. Vlase L., Popa A., Neag M., Muntean D., Leucuta S.E., *European Journal of Drug Metabolism and Pharmacokinetics*, **2011**, 35, 83.
22. Akaike H., *IEEE Transactions on Automatic Control*, **1974**, 19, 716.
23. Ben-Akiva M, Swait J., *Transportation Science*, **1986**, 20(2), 133.
24. Lin J. H., *Current Drug Metabolism*, **2007**, 8(2), 109.
25. Leucuta S. E., Vlase L., *Current Clinical Pharmacology*, **2006**, 1(1), 5.

SIMULTANEOUS DETERMINATION OF HYDROCHLOROTHIAZIDE AND TELMISARTAN FROM PHARMACEUTICAL PREPARATIONS USING CAPILLARY ELECTROPHORESIS

ȘTEFANA STĂCESCU^a, GABRIEL HANCU^{a*}, LASZLO GAGYI^b,
RUXANDRA MARIA SOARE^a, HAJNAL KELEMEN^a

ABSTRACT. Fixed-dose combinations of an angiotensin II receptor antagonist (telmisartan) and a thiazide diuretic (hydrochlorothiazide) provide an effective antihypertensive therapy while promoting patient compliance with the convenience of once-daily single dose administration. The current study investigated two capillary electrophoretic methods: a capillary zone electrophoresis (CZE) and micellar electrokinetic capillary chromatography one (MEKC) for the simultaneous determination of hydrochlorothiazide and telmisartan. In order to optimize the analytical conditions, efforts were focused on establishing the influence of several experimental parameters on the separation: buffer composition, concentration and pH, applied voltage, temperature, injection pressure and time. The separation of the two analytes can be achieved by CZE using a 25 mM phosphate buffer at pH 2.50 and by MEKC using a 50 mM borate buffer at pH 9.50 containing 25 mM sodium dodecyl sulfate as surfactant. The analytical performance of the two methods was verified in terms of their linearity, precision, accuracy and robustness, and the methods were applied for the determination of the analytes from fixed-dose combinations.

Keywords: *hydrochlorothiazide, telmisartan, fixed dose combinations, capillary electrophoresis, pharmaceutical preparations*

^a University of Medicine and Pharmacy Tîrgu Mureș, Faculty of Pharmacy, Department of Pharmaceutical Chemistry, 38 Gh. Marinescu str., RO-540139, Tîrgu Mureș, Romania.

^b SC Vim Spectrum SRL Tîrgu Mureș, 409 Corunca, RO-547367, Corunca, Romania.

* Corresponding author: gabriel.hancu@umftgm.ro

Taking into consideration the great prevalence and importance of this type of fixed dose combination in modern therapy, the elaboration of new methods of analysis for the simultaneous determination of combined substances can be considered a necessity and also a challenge for the analysts.

Capillary electrophoresis (CE) is a modern separation technique, considered to be an alternative and also a complementary method in drug analysis to the more frequently used high performance liquid chromatography (HPLC) techniques. In CE, separation is based on the differences in the electrophoretic mobilities of the charged molecules due their charge, size, shape or nature of the background electrolyte (BGE). BGE may contain additives, which can interact with the analytes and modify their electrophoretic mobilities. CE encompasses several capillary electro migration techniques, but among them capillary zone electrophoresis (CZE) and micellar electrokinetic chromatography (MEKC) are the most frequently used in drug analysis [6].

Simultaneous determination of the TEL – HCT combination can be obtained using first-derivative and ratio derivative spectrophotometry [7], UV-spectrophotometry using simultaneous equation method [8,9], TLC-densitometry [7], spectrofluorimetry [7], HPLC [10] and RP-HPLC [11,12,13].

Only one CE method has been published so far for the simultaneous estimation of TEL among other five ARA derivates and HCT from combined pharmaceutical forms [14].

Our aim was the development of simple, efficient and rapid CE protocols for the simultaneous determination of TEL and HCT, the optimization of the analytical conditions and to verify the applicability of the newly developed methods for the determination of the two analytes from fixed dose combination product.

RESULTS AND DISCUSSION

Preliminary analysis

The separation in CE is highly dependent on the pH of the BGE which influences the dissociation of the acidic groups or the protonation of basic functional groups on the analyte. The pH of the BGE will determine the charge of the compounds and also the magnitude of the electroosmotic flow (EOF).

Several preliminary experiments were made using phosphate BGEs with different compositions at different pH levels, over a pH ranging from 2.00 to 11.00.

TEL is a weak acid has with pKa values of 3.50, 4.10 and 6.00, being ionized can be determined over the entire studied pH range [15,16]. HCT is a basic compound with pKa values of 7.90 and 9.20, and subsequently, will be ionized only in an acidic environment [16].

Both substances can be determined simultaneously by ECZ, over a pH range between 2.50 and 4.50, but the best results were obtained using a pH of 2.50; at this pH, the best peak shapes and the shortest analysis time were obtained.

In MEKC, an anionic surfactant, sodium dodecyl sulfate (SDS) was added in a borate buffer in order to modify the electrophoretic behavior of the analytes; both analytes can be determined by MEKC over a pH range between 9.00 and 11.00, the best results were obtained at a pH of 9.50.

Optimization of the analytical conditions

The concentration of the BGEs was varied from 25 to 100 mM; when the concentration of the BGE increased the selectivity of the separation improved; but also migration times increased and higher currents were generated.

In the MEKC method the effects of SDS concentrations (25-50 mM) were investigated; an increase in the SDS concentration may result in a more efficient separation but at the same time, raises the current in the capillary and increases migration times.

In order to determine the optimal voltage to be applied, the influence of voltage (15 – 30 kV) on the migration times was investigated in the optimized BGE conditions; higher voltages reduced migration times but also increased the current intensity.

The influence of capillary temperature (15 – 25 °C) was evaluated under the optimized BGE conditions; when temperature increased, migration time decreased.

To determine the optimal injection parameters, the influence of injection time (1 – 5 seconds) and injection pressure (30 – 50 mbar) were studied in order to attain low detection limits without affecting the quality of peak shape, reproducibility and resolution.

From the above experiments, the optimal separation conditions for the simultaneous analysis of TEL and HCT by ECZ were: 50 mM phosphate buffer, pH 2.50, applied voltage + 25 kV, capillary temperature 25 °C, injection parameters 50 mbar/1 sec., UV detection wavelength 230 nm. Using optimized conditions, we obtained the separation of the two analytes, in approximately 3 minutes, the order of migration being: TEL followed by HCT (**Figure 2**).

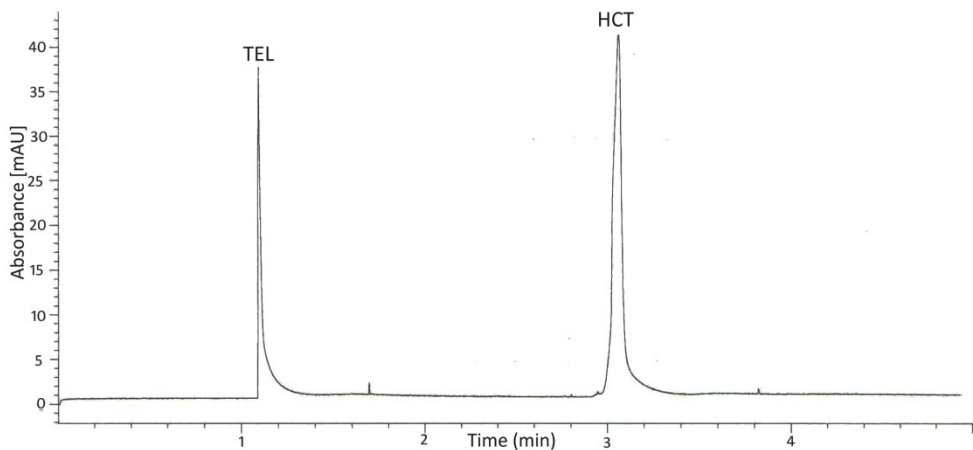


Figure 2. Simultaneous separation of TEL and HCT by ECZ (analytical conditions: 25 mM phosphate, pH 2.50, + 25 kV, 25 °C, 50 mbar/1s, UV 230 nm)

In the case of MEKC method, the optimal analytical conditions were: 25 mM borate buffer, 25 mM SDS, pH 9.50, applied voltage + 25 kV, capillary temperature 25 °C, injection parameters 50 mbar/1 sec., UV detection wavelength 230 nm. Using optimized condition, we obtained the separation of the two analytes, also in approximately 3 minutes, but the order of migration changed as HCT was followed by TEL (**Figure 3**).

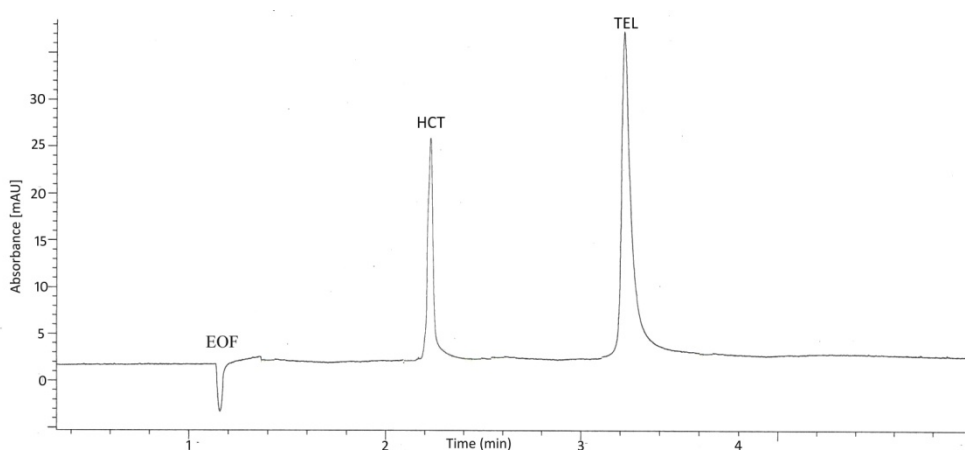


Figure 3. Simultaneous separation of TEL and HCT by MEKC (analytical conditions: 25 mM borate, 25 mM SDS, pH 9.50, + 25 kV, 25 °C, 50 mbar/1s, UV 230 nm)

Analytical performances

The analytical parameters of both CE methods were verified regarding precision, linearity, accuracy and robustness.

In order to evaluate intra-day and inter-day precision three concentration levels (0.025, 0.050, 0.100 mg mL⁻¹) of standard solutions were used; the results were evaluated taking in consideration the peak areas. The intra-day determination was performed by analysing six replicates on the same day; while the inter-day determination was conducted over three consecutive days. The results are presented in **Table 1**.

Table 1. Intra- and inter-day precision for the simultaneous determination of TEL and HCT

Analyte (µg/mL)	RSD (%)			
	CZE		MEKC	
	TEL	HCT	TEL	HCT
Intra-day precision				
(n = 6)				
0.025	0.14	0.67	0.10	0.12
0.050	0.18	0.83	0.18	0.21
0.100	0.36	0.98	0.24	0.25
Inter-day precision				
(n = 18)				
0.025	0.52	0.77	0.28	0.33
0.050	0.50	0.88	0.57	0.59
0.100	0.95	1.12	0.80	0.82

In order to evaluate linearity, stock solution at six concentration levels and three replicates per concentration were measured. The calibration curves were linear in the studied range (0.010-0.500mg mL⁻¹ for both TEL and HCT) with correlation coefficients above 0.99 (**Table 2**). Regression analysis data for the calibration curves were calculated using the peak areas.

Table 2. Linearity parameters for the simultaneous determination of TEL and HCT

Analytes	CZE		MEKC	
	Regression equation	Correlation coefficient	Regression equation	Correlation coefficient
TEL	$y = 167.5x - 1,483$	0.996	$y = 218.4x + 1.039$	0.991
HCT	$y = 234.4x + 4.191$	0.991	$y = 166.4x + 4.714$	0.991

The approach based on the standard deviation of the response and the slope of the calibration plots was used to determine detection (LOD) and quantification limits (LOQ). LOD and LOQ values were estimated as [(standard deviation of the response)/ (slope of the regression equation)] by multiplying with 3.3 and 10 respectively. The values obtained are presented in **Table 3**.

Table 3. Sensitivity data for the simultaneous determination of INH and RIF

Analytes	CZE		MEKC	
	LOD (mg/mL)	LOQ (mg/mL)	LOD (mg/mL)	LOQ (mg/mL)
TEL	0.017	0.051	0.036	0.108
HCT	0.008	0.024	0.062	0.185

To demonstrate the robustness of the method, minor changes in the experimental conditions have been made; as pH of the buffer was varied in the range ± 0.25 pH units, separation temperature in the range ± 2 °C while applied voltage in the range ± 2 kV. None of the modifications caused significant changes in the resolution between the substances with RSD (%) for migration times and peak areas under 2%.

The accuracy study was performed by weighing an appropriate amount of Micardis Plus 80/25 mg tablet powder and spiking it with known amount of standard compounds (0.050, 0.100, 0.150mg mL⁻¹); the resulting mixtures were analysed in triplicates and the results obtained were compared with the expected results. Accuracy values ranged from 98.32% to 101.75% for TEL and 96.26 and 100.42% for HCT in the ECZ method and from 99.12% to 102.11% for TEL and 99.04% to 102.36% for HCT in the MEKC method.

Analysis of pharmaceutical formulations

The optimized method was successfully applied for the simultaneous determination of TEL and HCT in the co-formulated original tablet, Micardis Plus 80/25 mg. Satisfactory results were obtained for each compound as the found amounts were in good agreement with label claims (**Table 4**).

Table 4. Assay results of TEL and HCT determination in pharmaceutical formulations

Method	Declared amount (mg)		Found amount (mg)		RSD (%)	
	TEL	HCT	TEL	HCT	TEL	HCT
CZE	80	25	79.2	23.9	0.45	0.67
MEKC	80	25	79.4	24.2	0.75	0.82

CONCLUSIONS

The usefulness of CZE and MEKC for the quantitative determination of these compounds in their pharmaceutical formulations was investigated, and the most important parameters for quantitative analysis were validated. The results presented above demonstrate that CE represents a good alternative for the simultaneous determination of TEL and HCT.

In CZE, at an acidic pH both analytes are positively charged, and the migration order can be explained by the differences between the own electrophoretic mobilities of the analytes

In MEKC, both TEL and HCT are negatively charged and migrates after the EOF; the order of migration will depend on the individual partitioning equilibrium of the two analytes between the micellar and the aqueous phase. The greater percentage of analyte is distributed into the micelle, the slower it will migrate.

High separation efficiency and minimization of use of solvents and analytes are the inherent advantages features of both CE methods.

Both the CZE and the MEKC methods can be applied successfully to the qualitative and the quantitative determination of the studied compounds in fixed-dose pharmaceutical formulations.

EXPERIMENTAL SECTION

Chemicals and Reagents

Telmisartan and hydrochlorothiazide of pharmaceutical grade were obtained from RA Chem Pharma Limited (Hyderabad, India). Phosphoric acid was purchased from Chimopar (București, Romania), methanol and sodium hydroxide from Lach-Ner (Neratovice, Czech Republic), dihydrogen sodium phosphate, disodium hydrogen phosphate, sodium tetraborate and sodium dodecyl sulfate from Merck (Darmstadt, Germany). All reagents were of analytical grade. Deionised water was purified by a Milli-Q purification system (Millipore, Bedford, USA). The pharmaceutical dosage forms used in this study was Micardis Plus (Boehringer Ingelheim, Germany) containing a TEL/HCT ratio of 80/25 mg.

Instrumentation

Separations were conducted on a Agilent 1600 CE system (Agilent Technologies, Waldbronn, Germany) equipped with a DAD detector. Uncoated fused-silica capillary of 38 cm length (30 cm effective length) x 50 μm ID (Agilent Technologies, Waldbronn, Germany) was used. Data acquisition was performed using ChemStation software (Agilent Technologies, Waldbronn, Germany).

Electrophoretic conditions

The new capillary was conditioned by flushing with 0.1 N NaOH and water each for 30 minutes. Between injections the capillary was preconditioned for 1 minute with 0.1 N NaOH, water and 2 minutes with the BGE. Samples and standards were injected hydrodynamically at the anodic end of the capillary. Detection was performed at 210, 230 and 270 nm, and full spectra of the analytes were also stored to facilitate peak identification.

BGE solutions were prepared dissolving the appropriate amount of buffer constituents in ultrapure water and adjusting the pH if necessary with 1 M H₃PO₄ or 1 M NaOH solutions. Both BGE and sample solutions were filtered through a 0.45 µm pore size membrane filter and sonicated in an ultrasonic bath for 5 minutes prior to use.

The stock solution of HCT was prepared in methanol in a concentration of 1 mg/mL. The stock solution was prepared by dissolving 10 mg TEL in in 1 mL 0.1 N HCl and then diluting it to 10 mL with methanol.

Preparation of pharmaceutical samples

Twenty Micardis Plus 80/25 mg tablets from the same batch were weighed accurately, average weight was calculated, the tablets were finely powdered in a mortar into a homogenous powder; an amount of powder equivalent to the weight of one tablet was dissolved in 100 mL methanol by sonication for 5 minutes with intermittent shaking. The solution was filtered through a 0.45 µm syringe, centrifuged at 3500 rpm for 10 minutes and diluted with methanol to the appropriate concentration. The same procedure was applied as in the separation from standard solutions.

ACKNOWLEDGMENTS

This research did not receive any specific grant from funding agencies in the public, commercial, or not-for-profit sectors.

REFERENCES

1. A. Salahuddin, M. Mustaq, B.J. Materson, *Journal of American Society of Hypertension*, **2013**, 7, 401.
2. A.H. Gradman, J.N. Basile, B.L. Carter, G.L. Bakris, *Journal of American Society of Hypertension*, **2010**, 4, 42.

3. X. Wan, P. Ma, X. Zhang, *Asian Journal of Pharmaceutical Sciences*, **2014**, 9, 1.
4. S.E. Kjeldsen, I. Os, A. Hojegggen, K. Beckey, G.W. Gleim, S. Oparil, *American Journal of Cardiovascular Drugs*, **2005**, 5, 17.
5. M. Maillard, M. Burnier, *Expert Review of Cardiovascular Therapy*, **2005**, 3, 375.
6. S. El Deeb, H. Watzig, D. Abd El-Hady, C. Sanger-van der Griend, G.K. Scriba, *Electrophoresis*, **2016**, 37, 1591.
7. L.I. Bebawy, S.S. Abbas, L.A. Fattah, H.H. Refaat, *Il Farmaco*, **2005**, 60, 859.
8. R. Gangola, S. Kaushik, P. Sharma, *Journal of Applied Pharmaceutical Sciences*, **2011**, 1, 46.
9. R.S. Bathe, A.M. Tamboli, M.J. Jamadar, N.I. Khan, J.Y. Manure, *International Journal of Advances in Pharmaceutical Analysis*, **2014**, 4, 18.
10. I. Samala, *Bulletin of Faculty of Pharmacy, Cairo University*, **2011**, 49, 19.
11. L.R. Bhat, R.K. Godge, A.T. Vora, M.C. Damle, *Journal of Liquid Chromatography & Related Technologies*, **2007**, 30, 3059.
12. S.B. Wankhede, M.R. Tajne, K.R. Gupta, S.G. Wadodkar, *Indian Journal of Pharmaceutical Sciences*, **2007**, 69, 298-300.
13. H.M. Hafez, A.A. Elshanaawane, L.M. Abdelaziz, M. M. Kamal, *Iranian Journal of Pharmaceutical Research*, **2013**, 12, 635.
14. S. Hillaert, W. van de Bossche, *Journal of Pharmaceutical and Biomedical Analysis*, **2003**, 31, 329.
15. W. Wienen, M. Entzeroth, J.C.A. van Meel, J. Stangier, U. Busch, T. Ebner, J. Schmid, H. Lehmann, K. Matzek, J. Kempthorne-Rawson, V. Gladigau, N.H. Huel, *Cardiovascular Drug Reviews*, **2000**, 18, 127.
16. G.L. Plosker, W. B. White, *Drugs*, **2008**, 68, 1877.

A SENSITIVE ANALYTICAL (RP-HPLC-PDA, UV/VIS) METHOD FOR THE DETERMINATION OF NEWLY SYNTHESIZED N-ISONICOTINOYL-N'-(3-FLUOROBENZAL)HYDRAZONE (SH2) IN AQUEOUS PHASE

ZVEZDELINA YANEVA^{a*}, NEDYALKA GEORGIEVA^a

ABSTRACT. The purpose of the present study was to develop a simple, rapid and reproducible analytical method for the determination of N-isonicotinoyl-N'-(3-fluorobenzal)hydrazone (SH2) - a synthesized by us halogenated isoniazid derivative with high tuberculostatic activity, in aqueous phase, on the basis of RP-HPLC-PDA and UV/VIS spectrophotometric investigations. Despite of the high linearity (R^2 0.9984) of the UV/VIS spectrophotometric method applied, the significantly higher LOQ and LOD values indicated its unsuitability for detection and quantification of low N-isonicotinoyl-N'-(3-fluorobenzal)hydrazone concentrations ($< 10 \mu\text{g/mL}$). The proposed RP-HPLC-PDA method with mobile phase ACN/phosphate buffer (60:40, v/v) offered short retention time (3.1 min), high precision (RSD 3.50 %) and linearity (R^2 0.9898). It characterized with satisfactory LOD (0.346 $\mu\text{g/mL}$) and LOQ (1.05 $\mu\text{g/mL}$) values and allowed the qualitative detection of SH2 E/Z-isomer.

Keywords: *N-isonicotinoyl-N'-(3-fluorobenzal)hydrazone, RP-HPLC-PDA, UV/VIS, aqueous phase*

INTRODUCTION

The rise in drug-resistant strains of *Mycobacterium tuberculosis* is a major threat to human health and highlights the need for new therapeutic strategies [1].

Despite its strong antibacterial effect, sometimes isoniazid (rimifon, INH), a widely used medication (xenobiotic) with a confirmed tuberculostatic activity, is proved to be ineffective due to the rapid appearance of drug resistance of

^a *Chemistry Unit, Department of Pharmacology, Animal Physiology and Physiological Chemistry, Faculty of Veterinary Medicine, Trakia University, Students Campus, 6000 Stara Zagora, Bulgaria.*

* *Corresponding author: z.yaneva@abv.bg*

tuberculosis bacteria [2]. These two problems – the toxicity and the resistance, motivate the necessity of synthesis of new tuberculostatics: more active, overcoming the resistance and with a lower toxicity. Particularly good results in the study of antituberculosis activity and toxicity are obtained for the family of isonicotinoyl hydrazones – structural analogues of isoniazid [1,3,4]. The blockade of the active hydrazide group ($-HNNH_2$) results in a significant decrease in the toxicity of isonicotinoyl hydrazones vs that of INH [5-7].

In experiments of ours, we synthesized and evaluated the tuberculostatic activity of new xenobiotics, not described in the literature – structural analogues of INH [8] against a standard *Mycobacterium tuberculosis* H37Rv-London strain, that is highly virulent, causes a generalized tuberculosis and is used in international studies. The results of the screening showed that all newly synthesized xenobiotics had a highly inhibiting activity against tuberculosis bacteria [9].

The study of Potuckova et al. (2014) highlighted important structure-activity relationships and provides insights into the further development of arylhydrazone iron chelators with more potent and selective anti-neoplastic effects [10]. Analysis of new chelators were performed using an Ascentis C18 chromatographic column (1063 mm, 3 mm) protected with a guard column with the same sorbent (Sigma-Aldrich). The mobile phase was composed of 1 mM EDTA in 5 mM phosphate buffer and methanol in different ratios. The column oven was set at 25°C and the autosampler at 5°C. A flow rate of 0.3 mL/min and injection volume of 20 µL were used. The linearity, precision and accuracy of the methods were examined by the analysis of plasma samples spiked with different amounts of the chelators. Selectivity was confirmed by an analysis of blank plasma samples. All evaluated parameters reached acceptable values [10].

It is accepted by some scientists that UV/VIS spectrophotometric methods are less time-consuming in terms of preparation and analysis of samples and are more cost effective than chromatographic methods. A new analytical method for the quantification of isonicotinoyl lactosyl hydrazone (INH-Lac) in oral solid dosage forms by UV-spectrophotometry was developed and validated by Cordoba-Diaz et al. (2009) [11]. The influence of several direct compression excipients on the specificity of the proposed analytical method were evaluated. The applied methodology showed a good repeatability as well as good accuracy. The results obtained from the assay of isoniazid tablets demonstrated that the proposed method constitutes a clear alternative to chromatographic methods and to the official titration method. It would be of interest for the routine quality control of oral dosage forms containing isoniazid and lactose and for stability studies [11]. In the study of Georgieva and Yaneva (2015) subjected to encapsulation of rimifon on natural and acid-modified zeolites, rimifon concentrations before and after encapsulation were determined by a UV/VIS spectrophotometric method. The standard curve was linear over the range of the tested concentrations [12]. A RP-HPLC-PDA analytical

methodology for the determination of the veterinary antibiotic tylosine in aqueous phase, which characterized with short analysis time, high precision, high linearity and satisfactory LOD and LOQ values, was developed [13].

Previous investigations of the scientific team proved the superoxide scavenging, radical scavenging and tuberculostatic activities of substituted isonicotynoylhydrazones [9,14]. However, no analytical methods for the determination of halogenated isonicotynoylhydrazones in aqueous medium have been reported so far, which provoked the present research.

The aim of this study was to develop a simple, rapid and reproducible analytical method for the determination of N-isonicotynoyl-N'-(3-fluorobenzal)hydrazone – a synthesized by the authors halogenated isoniazid derivative with high tuberculostatic activity, in aqueous phase, on the basis of RP-HPLC-PDA and UV/VIS spectrophotometric investigations.

RESULTS AND DISCUSSION

UV/VIS spectrophotometric analyses

The UV/VIS spectra of SH2 in acidic aqueous solutions (pH 2.4) (Fig. 1) displayed maximum absorbance peaks in the UV region at λ 250 nm for the entire concentration range 10 – 100 $\mu\text{g/mL}$. The pH of all solutions was adjusted to pH 2.4.

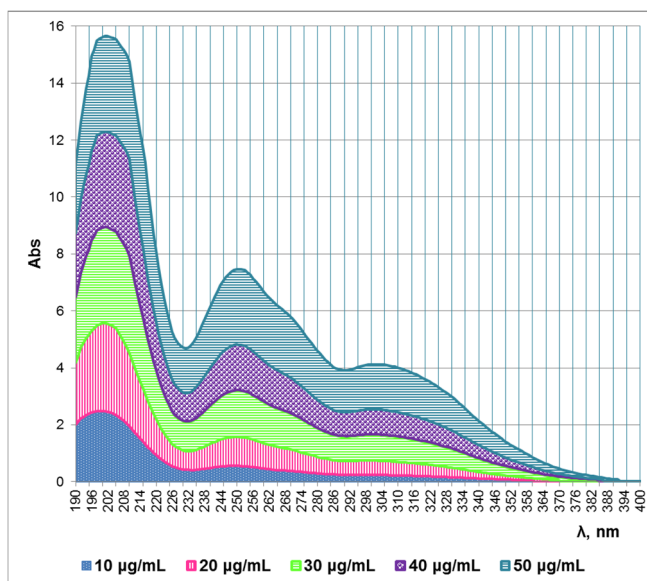


Figure 1. UV/VIS spectra of SH2.

The obtained standard curve for SH2 (Fig. 2) was linear over the tested range of initial concentrations C_0 10 - 100 $\mu\text{g/mL}$.

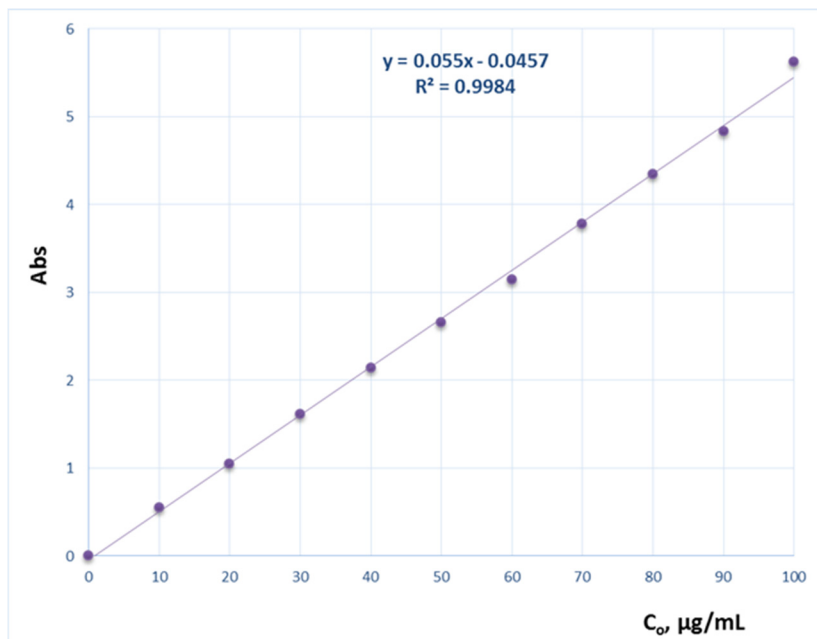


Figure 2. UV/VIS calibration curve of SH2 at λ 250 nm.

The obtained linear equation (Eq. 1) characterized with a slope $a = 0.055$ and an intercept $b = -0.0457$.

$$y = 0.055 \cdot x - 0.0457 \quad (1)$$

The high value of the calculated correlation coefficient - R^2 0.9984, and the well resolved UV absorption peaks of the heterocyclic compound proved the applicability of this method for determination of SH2 concentrations in aqueous medium in the range C_0 10 - 100 $\mu\text{g/mL}$.

HPLC method development

The development and optimization of a sensitive and rapid HPLC method for SH2 determination in aqueous phase included the performance of several preliminary experiments testing different HPLC conditions: mobile phases, temperatures and wavelengths.

HPLC Method I

The first experimental series were conducted with ten SH2 standard solutions with concentrations 10, 20, 30, 40, 50, 60, 70, 80, 90 and 100 $\mu\text{g/mL}$. The used mobile phase consisted of phosphate buffer (pH 5.0) and methanol (90:10, v/v). Optimal performance was obtained at a flowrate 0.8 mL/min. The effect of temperature on the separation process was studied in the range 18 - 30°C. Satisfactory peak resolution and optimum analyses time were established at 30°C, at wavelength λ 254 nm. SH2 was successfully detected within 3.35 min in the solution with C_0 10 $\mu\text{g/mL}$ (Fig. 3). However a mode of reduction of the detection time from 3.35 min to 3.1 min with an increase in the initial SH2 concentration within the range C_0 10-100 $\mu\text{g/mL}$ was observed (Fig. 3). The base lines of the chromatograms characterized with signal noise in the time range 1.9-2.5 min and unstable base line, especially in the lower concentration range. Besides, the characteristic peak for C_0 100 $\mu\text{g/mL}$ contained a curvature, which could affect the accuracy of the quantitative determination.

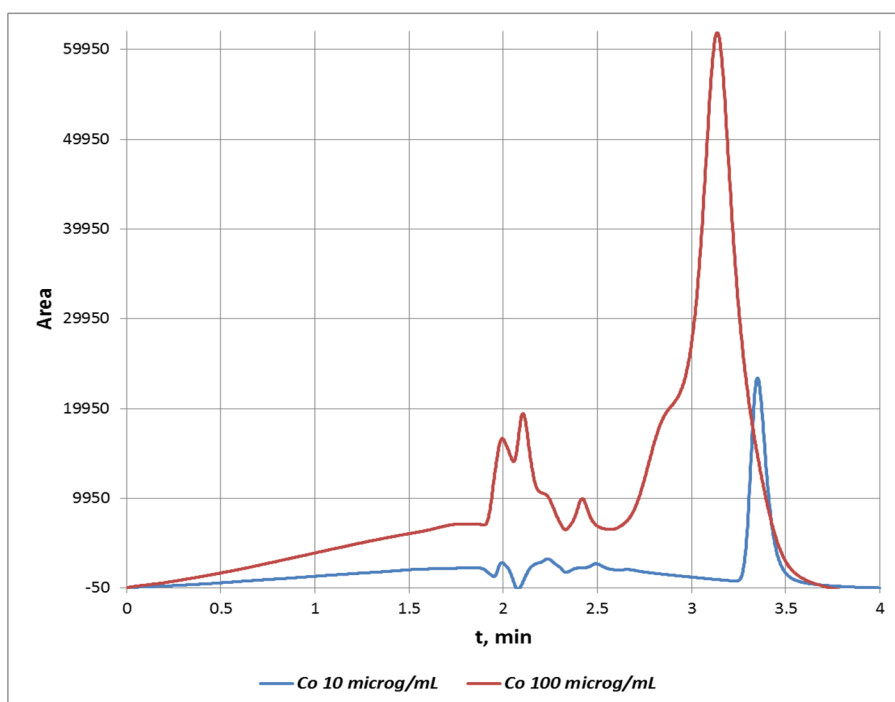


Figure 3. HPLC spectra of N-isonicotinoyl-N'-(3-fluorobenzal)hydrazone at λ 254 nm, mobile phase: phosphate buffer (pH 5.0)/methanol (90:10, v/v).

The standard calibration curve based on the spectral peak areas is presented in Fig. 4.

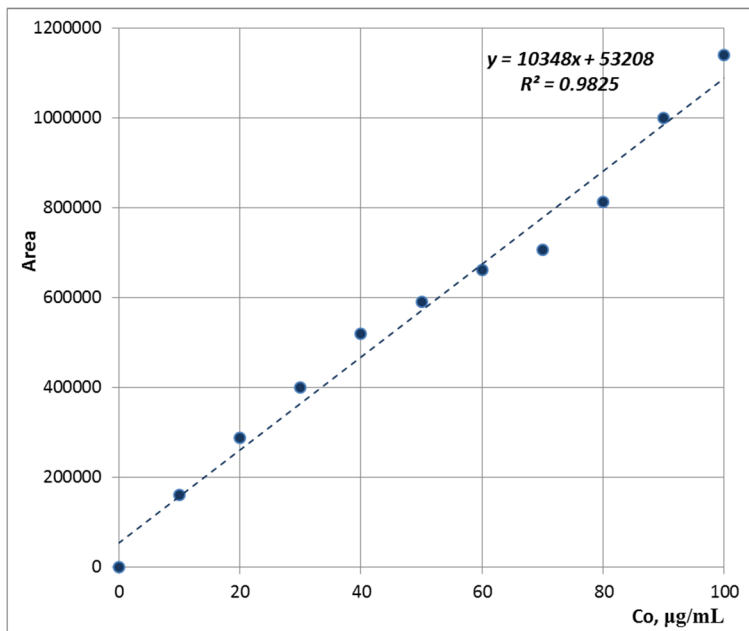


Figure 4. HPLC calibration curve of N-isonicotinoyl-N'-(3-fluorobenzal)hydrazone at λ 254 nm (mobile phase: phosphate buffer (pH 5.0)/methanol (90:10, v/v).

It characterized with a reasonable correlation coefficient R^2 0.9825 and the following linear equation (2):

$$y = 10348 \cdot x + 53208 \quad (2)$$

HPLC Method II

The second experimental series were conducted with the same ten SH2 standard solutions in the concentration range C_0 10 – 100 $\mu\text{g/mL}$. The used mobile phase consisted of ACN and H_3PO_4 (0.1M) (60:40, v/v). Optimal performance was obtained at a flowrate 0.8 mL/min. The effect of temperature on the separation process was studied in the range 18 - 30°C. Satisfactory peak resolution and optimum analyses time were established at 30°C, at wavelength λ 300 nm. SH2 was successfully detected within 3.1 min (Fig. 5).

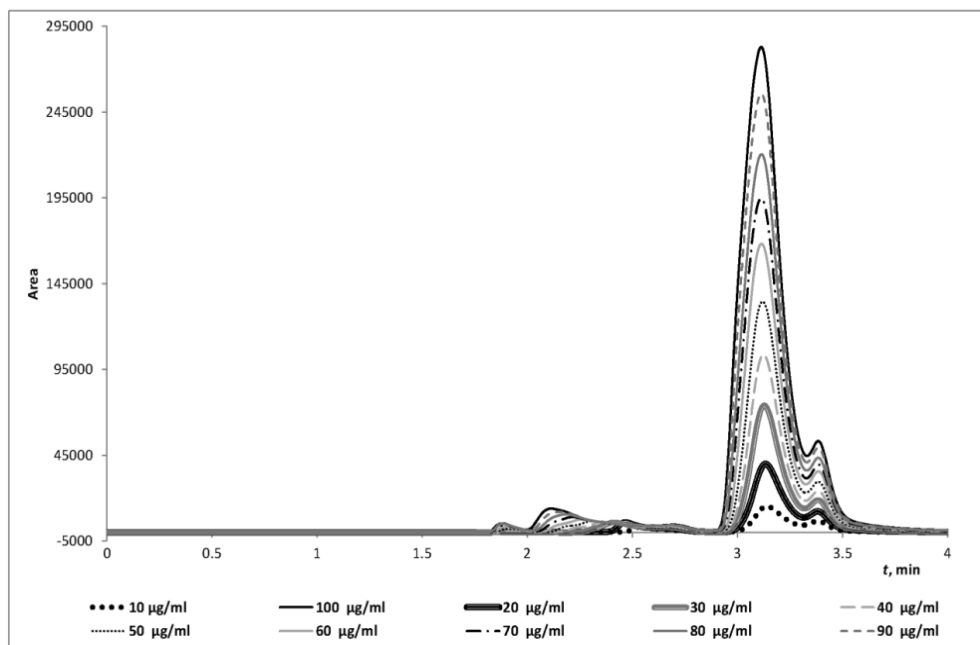


Figure 5. HPLC of *N*-isonicotinoyl-*N'*-(3-fluorobenzal)hydrazone detection at λ 300 nm, mobile phase: ACN/phosphate buffer (60:40, v/v), pH 2.4.

The obtained HPLC chromatograms did not contain any interference peaks, which could influence the quantitative results. However, the peaks obtained by this method were split, which could be due to the presence of *E/Z*-isomer of SH2 (Fig. 6), and consequently a sign for better separation of the main product. Besides, the base line is straight and stable with lower signal noise.

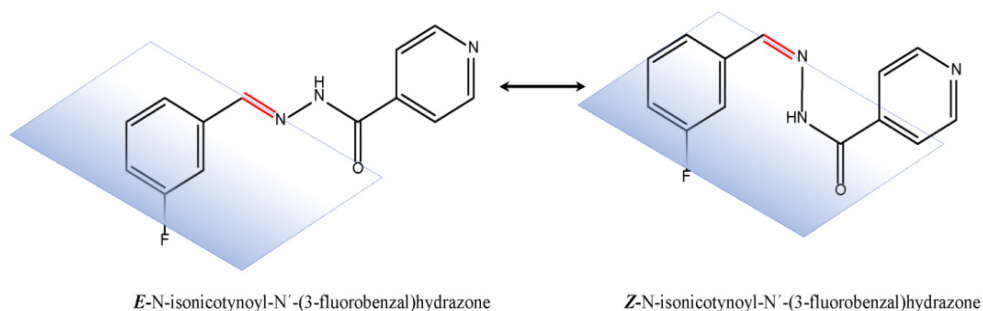


Figure 6. Structural formulas of *E/Z*-isomers of SH2.

The obtained standard calibration curve at these HPLC conditions is presented in Fig. 7.

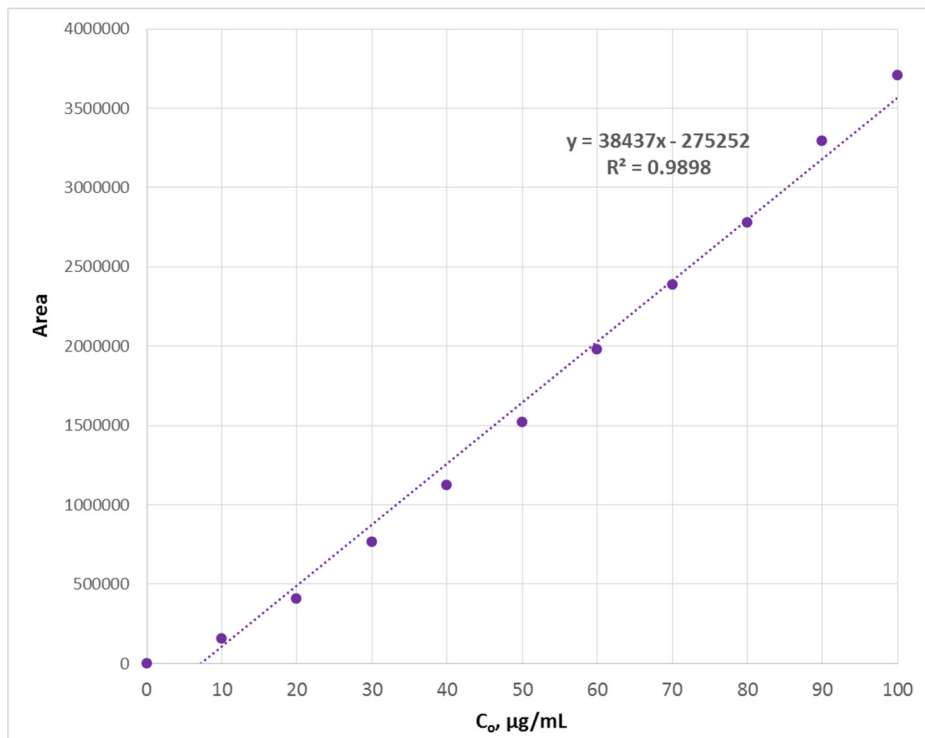


Figure 7. HPLC calibration curve of N-isonicotinoyl-N'-(3-fluorobenzal)hydrazone at λ 290 nm (mobile phase: ACN/H₃PO₄ (60:40, v/v)).

The correlation regression coefficient in this case was higher (R^2 0.9898) when compared to that obtained by HPLC Method I and lower than the value of the UV/VIS method. The linear equation (Eq. 3) characterized with a greater slope $a = 38437$ and with a negative intercept $b = -275252$.

$$y = 38437 \cdot x - 275252 \quad (3)$$

Accuracy and effectiveness of the applied analytical methods

To assess the applicability of the three methods investigated, the RSD, LOD and LOQ were determined based on the obtained in the recent study experimental data.

The values of LOD and LOQ were estimated according to the guidelines of the International Conference on Harmonization of Technical Requirements for Registration of Pharmaceuticals for Human Use (ICH) based on the standard deviation of the response and the slope of the calibration curve of the analyte [15]. The values of these parameters are presented in Table 1.

Table 1. Values of *RSD* %, *LOD* ($\mu\text{g/mL}$) and *LOQ* ($\mu\text{g/mL}$) for the UV/VIS and HPLC methods

Method	<i>RSD</i> , %	<i>LOD</i> , $\mu\text{g/mL}$	<i>LOQ</i> , $\mu\text{g/mL}$
UV/VIS Method	2.12	3.31	10.04
HPLC Method I	3.77	0.682	2.54
HPLC Method II	3.50	0.346	1.05

The comparative analyses of the obtained experimental results revealed that the developed and applied UV/VIS spectrophotometric method characterized with the highest correlation coefficient and lowest *RSD* value. However, the determined *LOD* and *LOQ* values were the highest. Thus, it could be suitable for analyses of aqueous samples with higher heterocyclic compound concentrations. According to the spectra presented in Fig. 1 solutions with SH2 concentrations lower than 10 $\mu\text{g/mL}$ characterized with not well-resolved spectral peaks, i.e. the accuracy of the method below this limit would be unsatisfactory. However, the main advantage of this method is its cost-effectiveness and rapidity.

Regarding the developed HPLC methodologies, and based on the data from Table 1, it could be concluded that undoubtedly HPLC Method II displayed the highest accuracy and efficiency as the determined *RSD*, *LOD* and *LOQ* values were the lowest. The comparative estimation of the HPLC spectral data of SH2 obtained by both liquid-chromatographic methods (Fig. 2, 3) revealed that the spectral peaks of Method II characterized with approximately 3 times greater area. Besides, they were significantly more pronounced in the entire tested concentration range. The presence of a secondary small peak at the bottom of the main one could be attributed to the detection of an isomer molecule, which is a sign for better separation of the biologically active compound(s), as well as for the higher accuracy of the method. The proportional increase of the secondary peak area could be used for the quantitative analyses of the detected isomer by a proper modification of the current analytical method in future investigations of the present scientific team. The latter observations are supported by the significantly lower *LOD* and *LOQ* values. Another main advantage of Method II is the registered short retention time.

CONCLUSIONS

A RP-HPLC-PDA analytical methodology appropriate for the quantitative determination of the novel drug candidate N-isonicotinoyl-N'-(3-fluorobenzal)hydrazone in aqueous phase, and the qualitative analyses of its isomer was developed in the present study. Desirable chromatographic separation was achieved on a C₁₈ column employing a mixture of ACN and 0.1M H₃PO₄ (60:40; v/v) as the mobile phase. The obtained HPLC chromatograms were well pronounced and did not contain any interference peaks, which could influence the quantitative results. The applied method offered short analysis time (3.1 min), high precision (*RSD* 3.5%) and high linearity (*R*² 0.9898). It characterized with satisfactory *LOD* and *LOQ* values. The simple and rapid method developed enhances the capabilities for the accurate and selective determination of SH2 in concentrations even below 10 µg/mL in aqueous phase, as well as detection of its E/Z isomer.

EXPERIMENTAL SECTION

Chemicals

Isonicotinoylhydrazide (Bristol-Myers Squibb Co.), 3-fluorobenzaldehyde, acetonitrile (ACN, ≥99.8%), orthophosphoric acid (H₃PO₄ 85%), methanol (≥ 99.9%), ethanol (p.a. ≥ 99.8%), and Na₂HPO₄·2H₂O (HPLC, ≥98.5%) HPLC grade, were obtained from Sigma-Aldrich.

Synthesis of N-isonicotinoyl-N'-(3-fluorobenzal)hydrazone SH2

N-isonicotinoyl-N'-(3-fluorobenzal)hydrazone was synthesized according to our previously reported procedure [8,9]. In brief: isonicotinoylhydrazide 2.74 g (0.02 mol) was mixed with 3-fluorobenzaldehyde in 50 mL absolute ethanol. The reaction mixture was heated to reflux for 4 hours. After cooling of the filtrate, white crystals crystallized, which after recrystallization from absolute ethanol had a melting temperature of 201.5-203°C. The yield was 86%.

Standard stock solutions (100 µg/mL) were prepared by dissolving the appropriate amount of N-isonicotinoyl-N'-(3-fluorobenzal)hydrazone in *Milli-Q* water acidified with H₃PO₄ at *pH* 2.4. Working standard solutions (10 – 100 µg/mL) were prepared daily.

Physicochemical characteristics of N-isonicotinoyl-N'-(3-fluorobenzal)hydrazone

The software package CS Chem 3D ultra was used to calculate the basic molecular characteristic of N-isonicotinoyl-N'-(3-fluorobenzal)hydrazone. Elemental analysis and testing of the organic compound were conducted for identification and quantification of elements. The molecular formula of the compound is presented in Fig. 8.

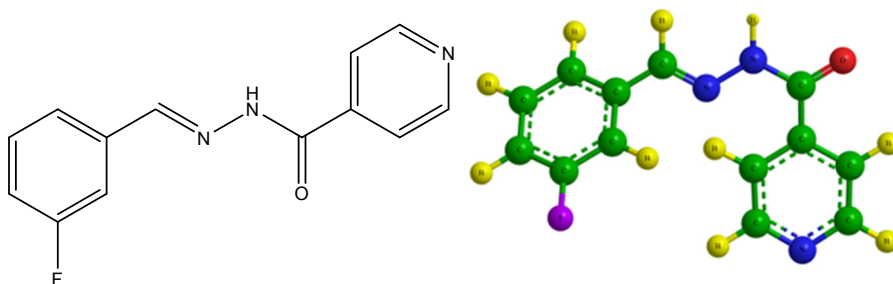


Figure 8. Molecular formula of SH2.

The physicochemical, molecular properties and elemental analyses data of SH2 are displayed in Table 2.

UV/VIS spectrophotometric analyses

N-isonicotinoyl-N'-(3-fluorobenzal)hydrazone concentrations were measured with UV-VIS spectrophotometer DR 5000 Hach Lange (Germany), supplied with 10 mm quartz cells. All spectra were recorded in the UV region at λ 250 nm with 2 nm slit width, 900 nm min⁻¹ scan speed and very high smoothing.

Table 2. Physicochemical characteristics of N-isonicotinoyl-N'-(3-fluorobenzal)hydrazone

Molecular formula	C ₁₃ H ₁₀ FN ₃ O
UIPAC name	3-fluorobenzaldehyde isonicotinoylhydrazone
Molecular mass, g/mol	243.236
Molecular ovality	1.42697
Connolly Accessible Area, Å ²	440.753

Connolly Molecular Area, Å ²	219.941
Connolly Solvent Excluded Volume, Å ²	179.932
Mass-to-charge ratio, <i>m/z</i>	243.08 (100.0%), 244.08 (15.2%), 245.09 (1.1%)
Elemental analyses:	
calculated (%):	C 64.19 H 4.14 N 17.28
determined (%):	C 64.03 H 4.01 N 17.57

HPLC system and conditions

RP-HPLC system comprising of a Hypersil BDS C₁₈ (5 μM, 4.6 x 150 mm) column, Surveyor LC Pump Plus, PDA detector, and Surveyor Autosampler Plus (Thermo Fisher Scientific) was used. The tested mobile phases consisted of a mixture of ACN/0.1M H₃PO₄ (60:40, v/v) and phosphate buffer (pH 5)/methanol (90:10, v/v). The samples were monitored at 290 nm and 254 nm, respectively. The buffer pH was adjusted to 2.4 with H₃PO₄. The volume injected into the HPLC column was 20 μl.

All UV/VIS spectrophotometric and HPLC analyses were made in triplicate.

The experimental data was analyzed by regression analyses and determination of the corresponding correlation coefficients (*R*²) and relative standard deviation (*RSD*, %).

The efficiency and accuracy of the developed UV/VIS and HPLC methods was estimated based on the calculated limit of detection (*LOD*) and limit of quantification (*LOQ*).

ACKNOWLEDGMENTS

The study was supported financially by Scientific Project No. 14-15 VMF, Faculty of Veterinary Medicine, Trakia University, Stara Zagora, Bulgaria.

REFERENCES

1. S. Ellis, D.S. Kalinowski, L. Leotta, M.L.H. Huang, P. Jelfs, V. Sintchenko, D.R. Richardson, J.A. Triccas, *Mol. Pharmacol.*, **2014**, *85*, 269.
2. C.E. Cade, A.C. Dlouhy, K.F. Medzihradzsky, S.P. Salas-Castillo, R.A. Ghiladi, *Protein Sci.*, **2010**, *19* (3), 458.
3. D. Sriram, P. Yogeewari, K. Madhu, *Bioorganic & Medicinal Chemistry Letters*, **2005**, *15*, 4502.
4. B. Moksharagni, K.D. Kumar, S. Chandrasekhar, K.H. Reddy, *Int. J. Pharm. Bio. Sci.*, **2015**, *6* (3), 11.
5. S. Rollas, S.G. Küçükgülzel, *Molecules*, **2007**, *12*, 1910.
6. M. Hermes-Lima, M. S. Gonçaves, R. G. Andrade Jr., *Molec. Cell. Biochem.*, **2001**, *228*, 73.
7. A.Q. Mauricioa, G.K.B. Lopes, C.S. Gomes, R.G. Oliveira, A. Alonso, M. Hermes-Lima, *Biochimica et Biophysica Acta*, **2003**, *1620*, 15.
8. S. Varbanova, N. Georgieva, *Veterinary Science*, **1993**, *27*, 81.
9. N. Georgieva, V. Gadjeva, *Biochemistry (Moscow)*, **2002**, *67*, 588.
10. E. Potuckova, K. Hruskova, J. Bures, P. Kovarikova, I.A. Spirkova, *PLoS ONE*, **2014**, *9* (11), 112059.
11. A. Córdoba-Díaz, M. Córdoba-Díaz, M., B. Elorza, *Spectroscopy*, **2009**, *23*, 201.
12. N. Georgieva, Z. Yaneva, *Cogent Chemistry* (2015), *1*, 1-16.
13. Z. Yaneva, N. Georgieva, V. Koinarski, D. Petrova, *Trakia Journal of Sciences*, *13*, Suppl. 2, 309-314, 2015.
14. N. Georgieva, Z. Yaneva, G. Nikolova, S. Simova, *Advances in Bioscience and Biotechnology*, **2012**, *3*(7A), 1.
15. International Conference on Harmonization of Technical Requirements for Registration of Pharmaceuticals for Human Use, ICH Harmonized Tripartite Guideline, *Validation of Analytical Procedures: Text and methodology*, Q2 (R1), p. 1-13 (2005).

THE DEVELOPMENT OF ANALYTICAL METHODS FOR THE ELEMENTAL DETERMINATION OF BIOTIC INDICATORS PRESENT IN AQUATIC ECOSYSTEMS

PETRA HERMAN^{a*}, SÁNDOR HARANGI^a, MILÁN FEHÉR^b,
ISTVÁN FÁBIÁN^a, EDINA BARANYAI^a

ABSTRACT. In our research we investigate the accumulation extent of the inorganic contaminants accessing the aquatic food chain, including zooplankton and fish species through model experiments. In this paper we discuss the preliminary experiments considering the measurement of iron and manganese accumulated in *Artemia sp.* after hatched and reared in metal contaminated model media. The goal is to develop the sample preparation and analytical methods required for the determination of metals adsorbed in the studied organisms. We proved that rinsing the zooplankton organisms three times with 2 mL per grams (wet weight *Artemia*) of rinsing solution prior to the sample preparation process decreased the possibility of analytical error. European Reference Material of fish tissue (ERM[®]-BB422) was used to validate the applied sample preparation and atomic spectrometric methods. The average recovery value for the measured elements by open system digestion with conventional heating was 96% and 92% with microwave digestion. With MP-AES 99% and 92% were gained, respectively. According to our results no significant difference occurred between the digestion in open system with conventional heating and microwave assisted digestion as well as the cost effective microwave plasma atomic emission spectrometry (MP-AES) proved to be appropriate for the routine quantitative analysis of adsorbed elements in zooplankton organisms and fish tissues.

Keywords: zooplankton, fish tissue, sample preparation, elemental analysis, atomic emission spectrometry

^a Department of Inorganic and Analytical Chemistry, Agilent Atomic Spectroscopy Partner Laboratory, University of Debrecen, Debrecen H-4010, Hungary

^b Faculty of the Agricultural and Food Sciences and Environmental Management, University of Debrecen, Debrecen H-4032, Hungary.

* Corresponding author: hpetra327@gmail.com

INTRODUCTION

Considering their shape and their expansion, ecosystems can be quite diverse. All the trophic levels setting up the system have their own functions: animals are the consumers, plants are the producers, while microorganisms play an important role in decomposing organic matter. In case of aquatic ecosystems, zooplankton are the base of the food chain, serving resource for consumers on higher trophic levels (including fish). These organisms are able to effectively accumulate several inorganic nutrients and pollutants in their body without suffering significant damage. However, more advanced and more complex organisms consuming them can create much higher concentrations in their cells and tissues through bioaccumulation than it was in the initial environmental media [1-2].

In the aquatic systems elements occur in the form of organic and inorganic compounds. They can be grouped according to multiple criteria: based on their effect on living organisms there are essential and toxic elements, while considering their quantity we talk about macro or micro elements [3]. The elemental contaminants may enter surface water in different ways. Nowadays more and more attention is given to anthropogenic activities (industrial production, agricultural production, traffic) as well as communal waste, which all play significant role in increasing the elemental concentrations above the environmental threshold limits [4-5]. However, there are heavy metals that occur in a naturally high concentration (background value) in the earth's crust, thus contributing to their presence in the surface waters.

For the aquatic organisms, the right elemental dose of the surrounding medium is indispensable. The elements have important biological role in the body, so both their absence and presence above the permitted levels can lead to adverse health problems. Thus animals maintain a delicate balance in their body, properly coordinating the different parameters of ingestion, storage and excretion. The availability of the various elements is affected by many factors, including their different chemical form and concentration, and also their interaction with other elements [6].

Toxicity tests are used to investigate the effect of several chemicals and pollutants on organisms, comparing the sensitivity of the individual species. In aquatic toxicity studies bacteria, zooplankton and fish are examined most commonly [7-9]. These organisms represent different trophic levels in the food chain and indicate the quality of the surrounding water.

In our research group we investigate the accumulation of inorganic contaminants accessing the aquatic ecosystems. Zooplankton and fish species are used in these experiments as bio indicator organisms which are reared in contaminated model media. The accumulated concentrations of elements are measured from their tissues providing information about the

extent of pollution. In present study we discuss the results of preliminary experiments considering the techniques applied for the sample preparation and elemental determination. The widely applied instrumental techniques for elemental analysis require the samples to be in solution. In case of environmental studies the correctly chosen sample preparation has a particular importance, since over 90% of the measurement errors arise from this step of the analytical process.

Emission methods of atomic spectroscopy uses different plasma based induction sources to produce the excited atoms required for the qualitative and quantitative analytical information. Inductively coupled plasma optical emission spectrometers (ICP-OES) use argon as plasma gas, which provides a high temperature emission source (~10000 K). This can be an advantage in case of elements which require higher excitation energy, yet the continuous gas supply can increase the operating and measuring costs. The newly launched microwave plasma atomic emission spectrometer (MP-AES) works on a similar principle but the plasma requires nitrogen gas which is produced continuously by a generator. The microwave induced excitation source has a lower temperature (~5000 K) compared to that of the ICP, thus while the method itself is quite cost effective, its sensitivity is overall lower.

The first aim of our study is to determine the need of rinsing the zooplankton organisms with ultrapure water after the enrichment period. The second aim is to find the analytical method suitable for the sample preparation and elemental analysis. In order to verify the required analytical steps fish tissue ERM[®]-BB422 was applied that contains elements in certified values and has a matrix similar to that of the samples. In the method development process two different sample preparation techniques - digestion in open system with conventional heating and in a microwave assisted system – were compared. The more expensive microwave assisted digestion utilizes microwave energy which enables the efficient and rapid heating of the samples, while the cost effective digestion in open system with conventional heating is a more time consuming technique [10]. In the elemental analytical step we further compared the performance of the well-known and widely applied ICP-OES method with MP-AES, regarding the digested ERM[®]-BB422 samples.

RESULTS AND DISCUSSION

Rinsing of enriched zooplankton organisms

After harvesting *Artemia* samples we rinsed them in ultrapure water prior to the further analysis to remove the remaining surface contamination. The three rounds of rinsing solutions were collected and analyzed for Fe and Mn.

Literature data is quite controversial: some suggest washing the organisms with distilled water [11] although it can cause the remove of the elements from the cells due to osmosis. Other papers mention seawater or tap water depending on the rearing media [12-14], however it can contaminate the samples; while not rinsing the zooplankton organisms at all can result in a positive measurement error. According to our results in the first round of rinsing the collected solutions enriched Fe and Mn in a relatively large concentration. Thus we concluded that this could not be a result of releasing the elements from *Artemia* due to osmosis rather from the Fe and Mn contaminated model water remained on the surface of the zooplankton organisms.

As we expected, the concentration of the elements used for the enrichment was gradually decreased in the rinsing liquids, as indicated in figure 1 and 2. The higher the original concentration was in the treatments the higher percentage decrease was observed in the rinsing solutions. The Fe and Mn concentration was reduced by an average of $45 \pm 6\%$ in CC, $75 \pm 6\%$ in MC, $82 \pm 2\%$ in CM and $80 \pm 1\%$ in MM treatment in the last round of rinsing compared to the first.

According to our results, rinsing the organisms three times definitely proved to be necessary, since it causes smaller systematic measurement error. It is important to mention, that the rinsing should happen with a very small amount of water (2 ml per g of wet weight *Artemia*) and short contact time.

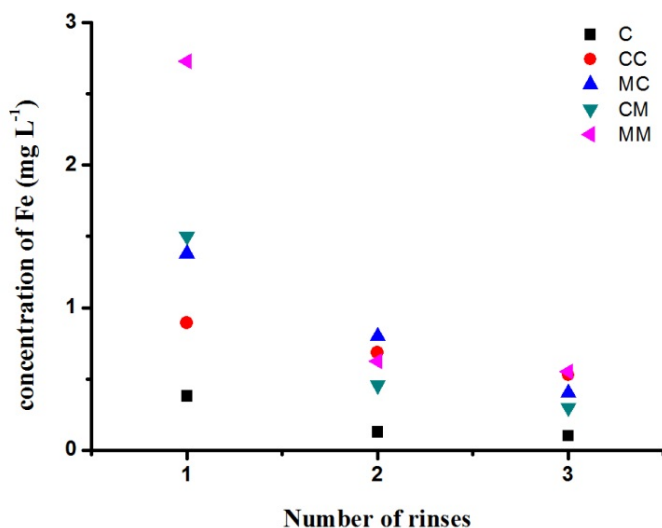


Figure 1. Decreasing of Fe concentration in the rinsing liquids
 Notations: C - no supplementation; CC - 5.70 mg L^{-1} Fe, 2.90 mg L^{-1} Mn;
 CM - 5.70 mg L^{-1} Fe, 6.25 mg L^{-1} Mn; MC - 15 mg L^{-1} Fe, 2.90 mg L^{-1} Mn;
 MM - 15 mg L^{-1} Fe, 6.25 mg L^{-1} Mn.

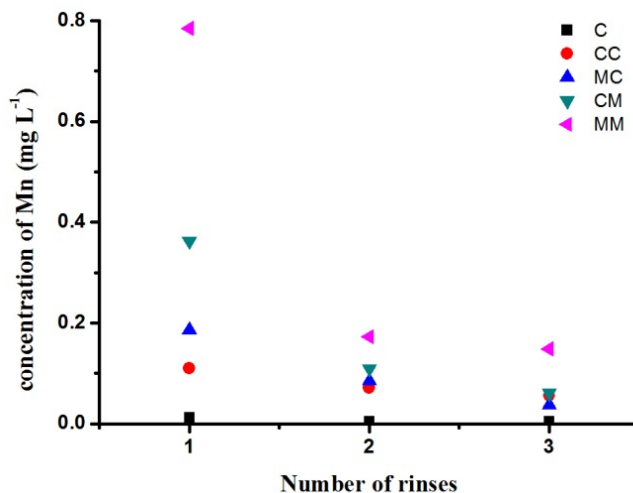


Figure 2. Decreasing of Mn concentration in the rinsing liquids

Notations: C - no supplementation; CC - 5.70 mg L⁻¹ Fe, 2.90 mg L⁻¹ Mn; CM - 5.70 mg L⁻¹ Fe, 6.25 mg L⁻¹ Mn; MC - 15 mg L⁻¹ Fe, 2.90 mg L⁻¹ Mn; MM - 15 mg L⁻¹ Fe, 6.25 mg L⁻¹ Mn.

Development of sample preparation methods

The applied method should carry the samples into solution by oxidizing the organic compounds without sample loss and contamination. In order to find the most suitable digestion two sample preparation methods (digestion in open system with conventional heating and in microwave assisted system) were compared for the ERM[®]-BB422 sample. Elemental analytical results and recoveries are indicated in table 1.

No significant difference occurred between the two sample pre-treatment methods ($p > 0.05$) neither for ICP-OES nor for MP-AES measurements, according to the statistical analysis. For the macro elements our results suggest that the more cost effective digestion in open system with conventional heating is suitable to eliminate the organic compounds and mobilize the measured elements present in the ERM[®]-BB422 sample. The concentration values of Zn show a higher standard deviation in case of the MP-AES analysis, which may arise from the chosen wavelength (213.857 nm). The optical system of the MP-AES instrument was not purged since the generator produces nitrogen gas enough only for the sample introduction (nebulizing), plasma supply and rinsing the pre-optics. In the UV range, further nitrogen supply is required from an additional gas cylinder to avoid the absorption of photons in air before reaching the detector, which would increase the sensitivity and decrease the standard

deviation of parallel measurements in the lower range of emission lines, such as for Zn. For the micro elements, further optimization of the digestion is necessary to improve the recovery results and decrease the standard deviation.

Table 1. The ICP-OES and MP-AES results of ERM[®]-BB422 (fish tissue) prepared by digestion in open system with conventional heating and in a microwave assisted system (N=3)

Elements		Found result±U				Recovery±U (%)			
		ICP-OES		MP-AES		ICP-OES		MP-AES	
(g kg ⁻¹)	Certified value±U	Open syst. dig.	Microwave dig.						
Ca	0.342 [*]	0.327±0.026	0.329±0.015	0.335±0.033	0.320±0.002	96±8	96±4	98±9	94±1
Mg	1.37 [*]	1.45±0.05	1.42±0.04	1.37±0.01	1.37±0.02	106±4	104±3	100±1	100±1
Na	2.80 [*]	2.75±0.1	2.79±0.15	2.58±0.04	2.59±0.01	98±4	99±5	92±2	93±1
K	21.4 [*]	20.4±1	21.3±1.3	18.2±0.2	18.6±0.2	95±5	99±6	85±1	87±1
(mg kg ⁻¹)									
Cu	1.67±0.16	1.65±0.04	1.45±0.06	1.75±0.15	1.46±0.11	99±3	87±3	105±9	88±4
Fe	9.4±1.4	8.1±0.4	8.2±0.4	10.3±0.3	7.7±0.5	87±4	88±9	109±3	83±5
Mn	0.368±0.028	0.361±0.029	0.306±0.011	0.427±0.012	0.344±0.023	98±8	83±3	116±3	94±6
Zn	16.0±1.1	13.9±0.5	12.0±0.4	14.1±1.6	15.0±1.2	87±3	76±2	88±10	94±8

*Concentration values for macro elements are given without uncertainty in the certification document of ERM[®]-BB422

The measurement results gained by MP-AES and ICP-OES were both compared to the expected data provided in the certificate document of the ERM[®]-BB422 sample. Although the applied statistical analysis proved no significant difference, the results of micro elements show higher percentage difference in case of Fe and Zn for the ICP-OES analysis. For these elements the measuring parameters of the ICP-OES method should be further optimize, yet it is clearly seen, that the MP-AES technique is appropriate for the elemental analysis of biotic indicators of aquatic ecosystems, such as fish tissue.

Since MP-AES instrument has recently appeared commercially and only a few literature data is available discussing its applications so far [15-16], the method must be verified prior to the planned model experiments. According to our results a good agreement was found between the two techniques: with ICP-OES the digestion in open system with conventional heating gave a recovery of 96% as the average of the measured elements and 92% with microwave digestion. The same values are 99% and 92% with MP-AES, respectively. These results indicate that despite the lower temperature of the nitrogen supplied microwave plasma, fish tissue samples can be analyzed

with a similar precision to that of the ICP-OES. It suggests that with the applied initial sample masses, the more cost-effective MP-AES can be used for the elemental determination of biotic indicator organisms after the appropriate sample pre-treatment. The standard deviation is higher for the Zn values than for the other elements - additional nitrogen supply from a gas cylinder by an external gas box would decrease it significantly.

CONCLUSIONS

In this paper the development of analytical methods are described for the elemental analysis of biotic indicators applied in model experiments of toxicity studies. It was found that rinsing the zooplankton organisms after rearing in contaminated media is important prior to the sample preparation process to decrease the error of the elemental analytical results. The rinsing should occur three times with 2 ml per grams (wet weight *Artemia*) of solution. It is further concluded that the digestion in open system with conventional heating is suitable for the sample pre-treatment of indicator organisms as well as the more cost-effective microwave plasma atomic emission spectrometer can be applied successfully for the quantitative determination of macro and micro elements. With ICP-OES the digestion in open system with conventional heating gave a recovery of 96% of ERM[®]-BB422 (fish tissue) as the average of the measured elements and 92% with microwave digestion. With MP-AES 99% and 92% were gained, respectively. The sensitivity of the MP-AES method can be increased for elements that have lines in the lower wavelengths of the emission spectra with additional nitrogen purge.

EXPERIMENTAL SECTION

Enrichment and preparation of zooplankton organisms

The examined zooplankton organisms (*Artemia sp.*, Sera, Germany) were reared and enriched under laboratory conditions. During the experiment we have developed a model system, which ensures the optimal conditions to raise and breed the organisms. The brine shrimps were hatched in 1.5 L plastic containers, with the density of 4 grams egg per L. The vessels were filled up with tap water aerated for 24 h and 20 g L⁻¹ salt concentration was set. The temperature of the water was 27 °C and 2000 lux illumination was adjusted by table lamps. After 24 h the newly hatched nauplii were separated from the shells and then collected by plankton net (mesh size of 150 µm).

A series of preliminary experiments were set to choose the right concentrations of the applied elements (Fe and Mn) used for the enrichment period. In a previous study in a joint research we found oxbows of the second largest Hungarian river (Tisza) to be contaminated with Fe and Mn [17-19]. Ten times of these levels were taken in our experiments since the originally found concentrations proved to be too low for the zooplankton to accumulate.

The applied concentrations were the followings:

- CC (Fe: 5.70 mg L⁻¹, Mn: 2.90 mg L⁻¹),
- CM (Fe: 5.70 mg L⁻¹, Mn: 6.25 mg L⁻¹),
- MC (Fe: 15 mg L⁻¹, Mn: 2.90 mg L⁻¹),
- MM (Fe: 15 mg L⁻¹, Mn: 6.25 mg L⁻¹),
- C (control, no supplementation).

The solutions of FeCl₃ and MnCl₂ (SPEKTRUM 3D) were used to adjust the above mentioned concentrations in the model media. Separated newly hatched *Artemia* were placed and reared in the model solutions for 24 hours with continuous light and aeration. Each treatment was set in five replicates. After the enrichment period brine shrimps were filtered and rinsed with ultrapure water in three rounds to investigate the effect of rinsing on the level of enriched elements. Rinsing solutions were collected in polypropylene centrifuge tubes.

Development of sample preparation methods

European reference material (ERM[®]-BB422, Fish Muscle) was used to test the sample preparation and elemental analytical methods. The ERM[®]-BB422 is certified for both micro and macro elements. The exact amount of two different initial masses (0.2 g and 0.5 g) were measured of the reference material on analytical balance (Precisa 40SM-200A), as well as two different sample preparation methods were compared. During the digestion in open system with conventional heating, samples were weighted into glass beakers and digested on an electric hot plate with 6.0 ml 65% (m/m) nitric acid (reagent grade, Merck) and 1.0 ml 30% (m/m) hydrogen peroxide (reagent grade, Merck) at 80 °C for 4 hours [20]. After digestion, samples were diluted with 1% (v/v) nitric acid (reagent grade, Merck and Milli-Q water) to a final volume of 10 ml. During the microwave assisted sample preparation method the samples were measured into closed Teflon containers and were digested with 4.0 ml 65% (m/m) nitric acid (reagent grade, Merck) and 1.0 ml 30%

(m/m) hydrogen peroxide (reagent grade, Merck). After digestion, samples were diluted with 1% (v/v) nitric acid (reagent grade, Merck and Milli-Q water) to a final volume of 10 ml (Milestone, EthosUp).

Elemental analysis

Elemental concentration was determined from both rinsing solution applied for *Artemia* (Fe and Mn) and ERM[®]-BB422 samples (Ca, Mg, Na, K, Cu, Fe, Mn, and Zn) by microwave plasma atomic emission spectrometer (Agilent MP-AES 4200) as well as inductively coupled plasma optical emission spectrometer (Agilent Technologies ICP-OES SVDV 5100). Auto sampler (Agilent SPS3), Meinhard[®] type nebulizer and double pass spray chamber were used. We applied a five-point calibration procedure prepared from multi-element standard solution (Merck ICP IV). For the method development each element was measured on at least 3 of the most intensive wavelengths; the shape of the gained spectra, the fitting of the calibration curve and the signal/background ratio was carefully investigated to choose the most appropriate wavelengths for further measurements. These were: Ca (315.887 nm), Mg (279.552 nm), Na (589.592 nm), K (766.491 nm), Cu (324.754 nm), Fe (234.350 nm), Mn (257.610 nm), Zn (202.548 nm) for the ICP-OES measurements, and Ca (445.478 nm), Mg (383.829 nm), Na (589.592 nm), K (769.897 nm), Cu (324.754 nm), Fe (371.993 nm), Mn (403.076 nm) and Zn (213.857 nm) for the MP-AES measurements.

Statistical analysis

The two digestion methods (digestion in open system with conventional heating and in microwave assisted system) as well as the two techniques applied for the elemental analysis (MP-AES and ICP-OES) for the ERM[®]-BB422 samples were compared by two way ANOVA (multivariate). The homogeneity was tested by Levene's test, while the significant differences were evaluated by Tukey's multiple comparison test. The calculations were conducted in SPSS software package (SPSS Statistics IBM 22) [11].

ACKNOWLEDGMENTS

We acknowledge the Agilent Technologies, the Milestone Srl. and the Novo-Lab Ltd. (Hungary) for providing the MP-AES 4200, the ICP-OES 5100 and the EthosUp. The research was supported by the EU and co-financed by the European Regional Development Fund under the project GINOP-2.3.2-15-2016-00008. Petra Herman was supported through the ÚNKP-16-2-I New National Excellence Program of the Ministry of Human Capacities.

REFERENCES

1. S.N. Gajbhiye, R. Hirota, *Journal of the Indian Fisheries Association*, **1990**, *20*, 43.
2. A. Gupta, D.K. Rai, R.S. Pandey, B. Sharma, *Environmental Monitoring and Assessment*, **2009**, *157*, 449.
3. D.G. Sfakianakis, E. Renieri, M. Kentouri, A.M. Tsatsakis, *Environmental Research*, **2014**, *137*, 246.
4. S. Islam, K. Ahmed, M. Raknuzzaman, H. Al-Mamun, M.K. Islam, *Ecological Indicators*, **2014**, *48*, 282.
5. H. Lin, T. Sun, S. Xue, X. Jiang, *Science of The Total Environment*, **2016**, *541*, 435.
6. T. Watanabe, V. Kiron, S. Satoh, *Aquaculture*, **1997**, *151*, 185.
7. R.-J. Qu, X.H. Wang, M.B. Feng, Y. Li, H. X. Liu, L.-S. Wang, Z.Y. Wang, *Ecotoxicology and Environmental Safety*, **2013**, *95*, 83.
8. R. Sarabia, A. Torreblanca, J.J. Del Ramo, J. Díaz-Mayans, *Comparative Biochemistry and Physiology Part A: Molecular & Integrative Physiology*, **1997**, *120*, 93.
9. C. Claus, F. Benijts, G. Vandeputte, W. Gardner, *Journal of experimental Marine Biology and Ecology*, **1979**, *36*, 171.
10. K. S. Subramanian, *Spectrochimica acta*, **1995**, *B51*, 291-319.
11. M. Fehér, E. Baranyai, E. Simon, P. Bársony, I. Szűcs, J. Posta, L. Stündl, *Aquaculture*, **2013**, *414–415*, 92.
12. P. Lo Nostro, B.W. Ninham, E. Carretti, L. Dei, P. Baglioni, *Chemosphere*, **2015**, *135*, 335.
13. V.T. Nguyen, S. Satoh, Y. Haga, H. Fushimi, T. Kotani, *Aquaculture*, **2008**, *285*, 184.
14. S. Matsumoto, S. Satoh, T. Kotani, H. Fushimi, *Aquaculture*, **2009**, *286*, 113.
15. C.T. Kamala, V. Balaram, V. Dharmendra, M. Satyanarayanan, K.S.V. Subramanyam, A. Krishnaiah, *Environmental Monitoring and Assessment*, **2014**, *186*, 7097.
16. W. Li., P. Simmons, D. Shrader, T.J. Herrman, S.Y. Dai, *Talanta*, **2013**, *112*, 43.
17. Z. Balogh, S. Harangi, J.T. Kunderát, I. Gyulai, B. Tóthmérész, E. Simon, *Water, Air, & Soil Pollution*, **2016**, *227*.
18. J.T. Kunderát, I. Gyulai, E. Baranyai, K. Hubay, S. Harangi, Zs. Balogh, M. Braun, E. Simon, *Hidrológiai Közlöny*, **2014**, *5-6*, 53.
19. G. Lakatos, *Toxicology Letters*, **2003**, *140-141*, 333.
20. S. Harangi, E. Baranyai, M. Fehér, Cs.N. Tóth, P. Herman, L. Stündl, I. Fábíán, B. Tóthmérész, E. Simon, *Biological Trace Element Research*, **2016**.

SYNTHESIS AND CHARACTERIZATION OF DERIVATIZED CARBON NANOSTRUCTURES

TIMEA-ANITA DULL-SZABÓ^a, MELINDA-EMESE FÜSTÖS^a,
MARIA SUCIU^b, GABRIEL KATONA^{a,*}

ABSTRACT. Carbon nanotube-triethanolamine and carbon nanotube-dendrimer structures were obtained from carboxyl functionalized nanotubes (SW-, DW-, MW-COOH). The synthesized compounds were characterized by elemental analysis, scanning transmission electron microscopy coupled with energy-dispersive X-ray spectroscopy (STEM-EDX). The toxicity of the obtained derivatized carbon nanostructures was tested on human immortalized keratinocyte cell line (HaCaT). The viability of the cells was determined using the 3-[4,5-dimethylthiazol-2-yl]-2,5-diphenyl-tetrazolium-bromide (MTT) cell proliferation assay.

Keywords: carbon nanotube, dendrimer, biological activity, MTT assay, HaCaT

INTRODUCTION

Carbon nanotubes (CNTs) are hollow cylinders derived from rolled sheets of graphene. These nanostructures belong to the fullerene family, the third allotropic form of carbon; have unique electrical, mechanical and optical properties [1].

Three types of carbon nanotubes are distinguished based on the number of graphene sheets rolled upon itself: single-walled carbon nanotubes (SWCNTs), double-walled (DWCNTs) and multi-walled CNTs (MWCNTs). Different methods are used for the derivatization of nanotubes: covalent and non-covalent functionalization. Due to functionalization, problems such as

^a Babeş-Bolyai University, Faculty of Chemistry and Chemical Engineering, Arany János street no 11, 400028 Cluj-Napoca, Romania

^b Babeş-Bolyai University, Faculty of Biology and Geology, Gh. Bîlaşcu street no 44, Cluj-Napoca, Romania

* Corresponding author: gabik@chem.ubbcluj.ro

agglomeration and bundle formation can be avoided, which enhances their dispersion in organic solvents. A good dispersion of nanotubes can be also induced by the use of surfactants [2].

Carbon nanotubes found application in many fields, being suitable for biomedical application thanks to their low toxicity. Different type of nanotubes can be used in drug delivery, gene delivery or anticancer therapy [3].

Dendrimers are hyperbranched, monodisperse macromolecules with nanometer-scale dimension [4]. The solubility and reactivity of dendrimers depend on the nature and number of functional groups on their periphery. Biomedical application is the most important utilization of dendrimers. They can be used as contrast agents in magnetic resonance imaging (MRI), as carriers in drug delivery and gene therapy and also as catalysts in industrial processes [5].

Combination of carbon nanotubes and dendrimers via covalent linkage leads to structures with unique properties and low toxicity. Polyamidoamine dendrimers (PAMAM) covalently attached to the surface of MWCNTs were described by B. Zhanga *et al.* [6]. According to their results, the MWCNT-PAMAM hybrids showed good dispersibility and activity in aqueous solution. Synthesis of PAMAM G4.0 dendrimer-functionalized carbon nanotubes was reported by Yang *et al.* [7]. They investigated the cellular toxicity of the obtained structures on HeLa cells and found that MWCNT-PAMAM-G1 is the least toxic and the functionalized nanotubes can be used as vectors to deliver pEGFP-N1 into HeLa cells.

Herein we present the cytotoxicity investigation of some derivatized carbon nanostructures obtained upon covalent functionalization of different types of carbon nanotubes with the commercially available triethanolamine and also with the zero-generation dendrimer synthesized according to the procedure described previously [8]. The cytotoxicity of these species was studied on HaCaT cell line using the MTT cell proliferation assay. The derivatized nanostructures can be used in catalysis or in medicine as supports for drug delivery.

RESULTS AND DISCUSSION

The synthesized structures were characterized by elemental analysis and STEM-EDX technique, respectively.

It is noticeable, that the N content of the functionalized carbon nanotubes is significantly higher compared to the nitrogen content of the substrates (SW-, DW-, MW-COOH) which originates from the air while sample preparation, confirming the covalent linkage of the dialkylamino-linker molecules and the N-atom containing compounds (triethanolamine, dendrimer).

The functionalized double-wall carbon nanotubes were further characterized by STEM-EDX technique. This technique allows the determination of the elemental composition at a well-defined position of the transmission electron microscopy pictogram. In **Figure 1** is presented the TEM-EDX analysis of the DW-COOH. The spectra indicate the presence of carboxyl groups on the surface of the nanotubes, but no nitrogen content is detected. The copper signs originate from the sample holder (copper grid) in each case.

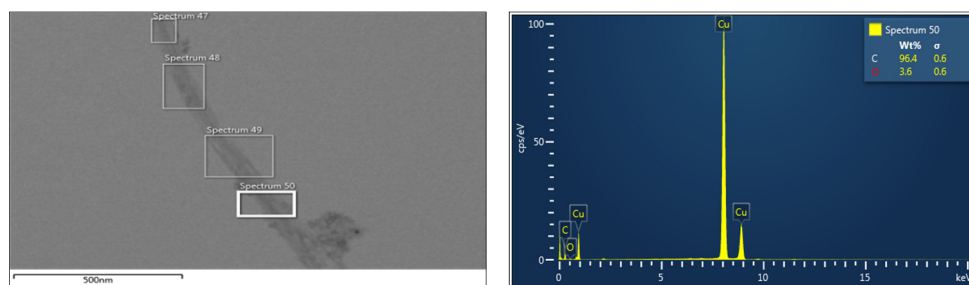


Figure 1. TEM-EDX spectra of DW-COOH

In **Figure 2** is depicted the TEM image and the corresponding EDX spectra of the dendrimer functionalized double-wall carbon nanotubes (DW-TMB). The presence of N atom in the structure proves the covalent attachment of the dendrimer to the surface of the nanotubes.

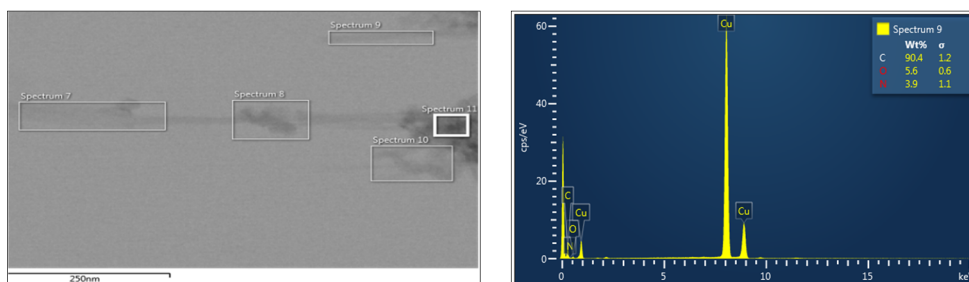


Figure 2. TEM-EDX spectra of DW-TMB

The TEM-EDX spectra of DW-TEA structure is presented in **Figure 3**. The EDX analysis results prove the functionalization of the carbon nanotubes with triethanolamine by the detection of the N atom.

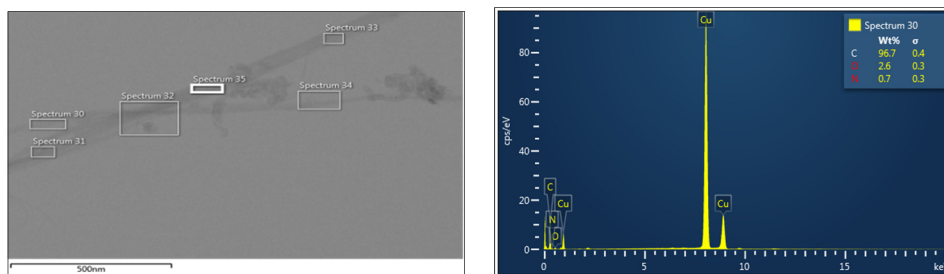


Figure 3. TEM-EDX spectra of DW-TEA

The toxicity of the obtained derivatized carbon nanostructures was investigated on HaCaT cell line. In **Figure 4** and **Figure 5** is represented the viability of the cells in the presence of different derivatized nanostructures. In each graphic CA symbolizes the so-called positive control (the cells are in their media without surfactant or carbon nanostructures) and 0 stands for the negative control (a 0.05% solution of Triton X-100 added to the cell media without carbon nanostructures).

In case of the two nanotube-linker species (**Figure 4**), the DAO-functionalized nanotubes (**5d-f**) presented lower toxicity on the studied cell line than the CNT-DAPr.

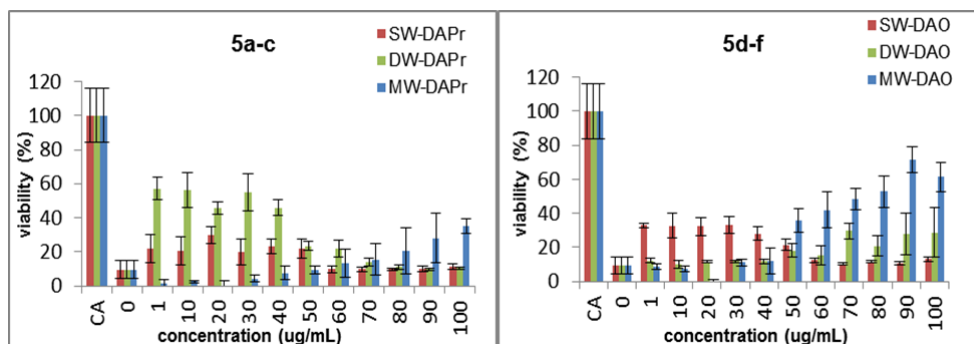


Figure 4. Cytotoxicity of 5a-c and 5d-f nanostructures

The TEA functionalized nanotubes (**8d-f**) seemed to be the most toxic nanostructures. In the case of dendrimer modified nanotubes the double-wall carbon nanotube species (**11e**) presented the lowest cytotoxicity (**Figure 5**).

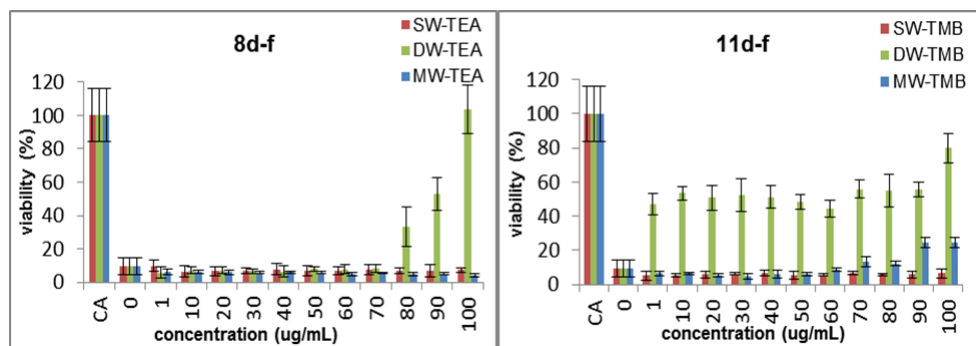


Figure 5. Cytotoxicity of 8d-f and 11d-f nanostructures

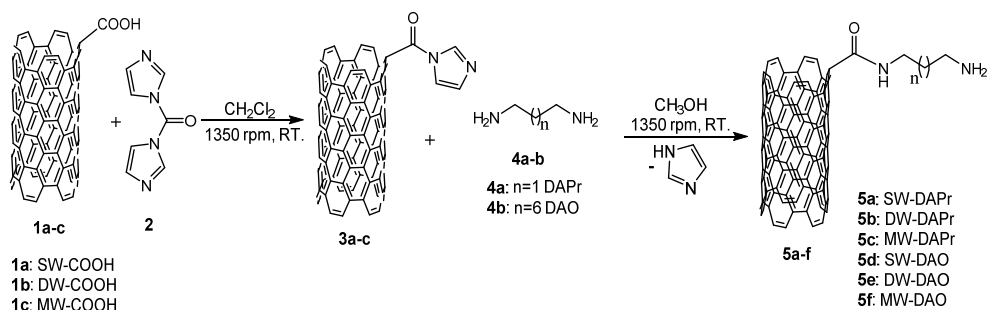
CONCLUSIONS

The covalent functionalization of the carbon nanotubes with N atom containing compounds: 1,3-diaminopropane, 1,8-diaminooctane, triethanolamine and the zero generation dendrimer, was confirmed by elemental and TEM-EDX analysis.

The cytotoxicity test results on the investigated HaCaT cell line indicated that in the presence of the surfactant the cell viability decreased up to 20%. By adding the derivatized carbon nanostructures in different concentrations this toxicity was overcome and cell viability increased almost in each case. The best results were obtained in case of the dendrimer functionalized double walled carbon nanotubes added to the cell media in high concentration.

EXPERIMENTAL SECTION

In order to synthesize the desired nanotube-dendrimer and the nanotube-triethanolamine structures, respectively, in the first step two diaminoalkyl linker-like molecules were attached covalently to the carbon nanotubes scaffold using N,N'-carbonyldiimidazole (CDI) as an activating agent for the carboxyl functional groups. *Scheme 1* illustrates the synthesis steps for obtaining the CNT-DAPr and CNT-DAO species.



Scheme 1. Functionalization of CNTs with diaminoalkyl-linkers

Synthesis of nanotube-linker (5a-f) structures

In a 50 mL Falcon tube 200 mg carboxyl derivatized carbon nanotubes (single-, double- and multi-walled) were suspended in 30 mL dry dichloromethane and sonicated for 15 minutes. 500 mg CDI dissolved in dry dichloromethane (5 mL) was added to the suspension. The mixture was left overnight on shaker at 1350 rpm with occasional sonication to avoid bundling.

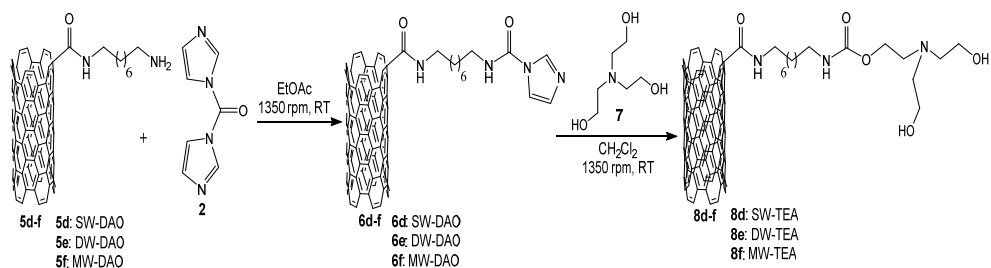
The **3a-c** nanotube derivatives were filtered on PTFE membrane (pore size 0.22 μm) and washed with dichloromethane repeatedly until the complete removal of the unreacted CDI and the produced imidazole. The procedure was monitored by thin layer chromatography (TLC) using dichloromethane: methanol 9:1 eluent mixture ($R_f = 0.54$). The product was dried at room temperature and used further being suspended in 10 mL methanol and sonicated for 20 minutes. 200 mg diaminoalkyl derivative (DAPr, DAO) was dissolved in methanol and added to the suspension. The mixture was left overnight on shaker at 1350 rpm at room temperature.

The derivatized nanotubes were separated from the suspension by vacuum filtration, washed with methanol repeatedly in order to remove the unreacted diaminoalkyl derivatives and dried in vacuo.

Synthesis of carbon nanotube-triethanolamine (8d-f) structures

The synthesis steps are depicted in *Scheme 2*. Triethanolamine was covalently bonded to the linker-type carbon nanotube species while imidazole was formed as by-product.

SYNTHESIS AND CHARACTERIZATION OF DERIVATIZED CARBON NANOSTRUCTURES



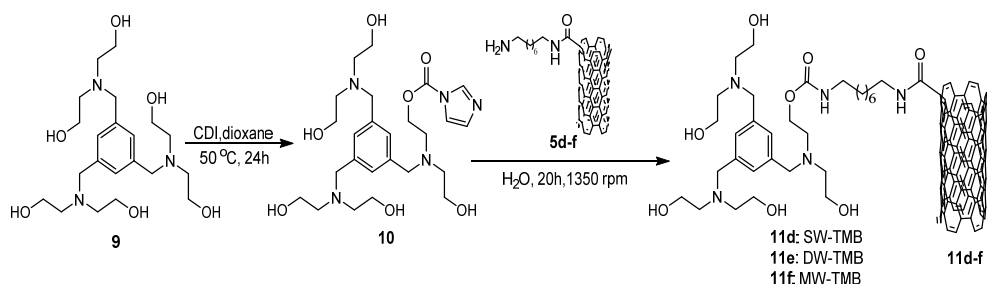
Scheme 2. Synthesis of the **8d-f** derivatized structures

The **8d-f** conjugates were synthesized according to the following procedure. 50 mg diamino-octane-functionalized carbon nanotubes (SW-DAO, DW-DAO, MW-DAO) were suspended in 10 mL ethyl acetate and sonicated for 20 minutes. 100 mg CDI dissolved in ethyl acetate was added to the suspension. The mixture was left overnight on shaker at 1350 rpm with occasional sonication. The **6d-f** compounds were separated from the suspension by vacuum filtration and washed with ethyl acetate repeatedly until no CDI was detectable in the filtrate on the TLC plate.

Further the dried carbon nanotubes were suspended in 10 mL dichloromethane and 150 mg TEA was added. The suspension was left overnight on shaker (1350 rpm). The functionalized carbon nanotubes were filtered off and washed with dichloromethane to eliminate the excess of the triethanolamine. The removal of the triethanolamine adsorbed on the surface of the carbon nanotubes was monitored by TLC in CH₂Cl₂:CH₃OH 8:2 eluent mixture ($R_f = 0.48$).

Synthesis of CNTs-TMB-DEA 0G (11d-f) conjugates

In *Scheme 3* is illustrated the functionalization of CNTs-DAO species with an aromatic core G0 dendrimer (TMB).



Scheme 3. Synthesis of the CNTs-dendrimer nanostructures

318 mg dendrimer was dissolved in 30 mL dry dioxane. The mixture was heated at 50 °C and 100 mg CDI was added. The reaction mixture was stirred for 24 hours at 50 °C. The solvent was evaporated on rotary evaporator and the remained viscous substance was used in the next step without further purification. Compound **10** dissolved in water was added to an aqueous suspension of 100 mg diaminoctane functionalized nanotubes. After sonication for 30 minutes, the suspension was left on shaker at 1350 rpm overnight. The functionalized nanotubes **11d-f** were removed from the suspension by vacuum filtration and washed with water and acetone, respectively. The obtained nanotube-dendrimer species were dried at room temperature.

In **Table 1** are presented the results of the elemental analysis.

Table 1. Results of the elemental analysis

Sample	N%	C%	H%
<i>SW-COOH</i>	0,23	91,72	1,20
SW-DAPr	1,03	90,31	1,21
SW-DAO	1,04	92,94	1,54
<i>DW-COOH</i>	0,18	89,29	0,96
DW-DAPr	1,24	91,73	1,33
DW-DAO	0,99	94,01	1,49
DW-TEA	1,23	89,39	1,98
<i>MW-COOH</i>	0,19	86,49	1,25
MW-DAPr	1,11	90,45	1,38
MW-DAO	1,12	90,50	1,57
MW-TMB	1,36	89,50	1,89

Sample preparation for biological testing

10 mg derivatized carbon nanostructure (**5a-f**, **8d-f**, **11d-f**) was suspended in 10 mL 0.05% Triton X-100 aqueous solution. Each sample was sonicated for 30 minutes and stored in the fridge until testing.

The HaCaT cells were cultivated in a freshly made media consisting of 88% DMEM (Dulbecco's Modified Eagle Medium), 10% fetal calf serum (FCS), 1% penicillin/streptomycin and 1% L-glutamine.

Determination of cell viability

The viability of the cells was determined using the colorimetric MTT cell proliferation assay. The cells were incubated in plates of 96 wells for 24 hours and the prepared nanostructures were added in different concentrations

(range 1-100 µg/mL). After the repeated incubation, MTT solution was added to each well (10 µL, 5 mg/mL in phosphate buffer) and the samples were incubated at 37 °C for 90 minutes (humidity ~90%, CO₂ content ~5%). The formed insoluble purple formazan crystals were dissolved by adding an acidified isopropanol solution (40 mM HCl, 0.1% Triton X-100). The absorbance of samples was measured at 550 nm. The reference wavelength used was at 630 nm. Each sample absorbance was measured consecutive 5 times and the average value was used for the determination of the number of viable cells, which can be expressed with the following formula:

$$\text{Viability (\%)} = (A_S * 100) / A_{CA},$$

where **A_S** is the absorbance of the sample; **A_{CA}** is the absorbance of the positive control.

Instruments used

The thin layer chromatography analysis was accomplished on Silica Merck TLC 60 F₂₅₄ aluminum plates. The elemental analysis measurements were performed on vario MICRO cube CHN elemental analyzer. The transmission electron microscopy images were recorded on STEM HD 2700 Hitachi microscope with EDX system. The cytotoxicity was measured with a BioTek Synergy HT plate reader using Gen5 Plate Reader software.

ACKNOWLEDGMENTS

This research was possible with the financial support of the PN-II-ID-PCE-2011-3-0346 project.

REFERENCES

1. S. Vardharajula, Sk. Z. Ali, P. M. Tiwari, E. Erođlu, K. Vig, V.A. Dennis, S.R. Singh, *Int J Nanomedicine*, **2012**, 7, 5361–5374.
2. K. S. Ibrahim, *Carbon Letters*, **2013**, 14(3), 131-144.
3. H. Sadegh, R. Shahryari-ghoshekandi, *Nanomed. J.*, **2015**, 2(4), 231-248.
4. U. Gupta, O. Perumal, "Dendrimers and Its Biomedical Applications", *Natural and Synthetic Biomedical Polymers*, **2014**, chapter 15.
5. B. Klajnert, M. Bryszewska, *Acta Biochimica Polonica*, **2001**, 48, 199-208.

7. B. Zhanga, Q. Chena, H. Tanga, Q. Xiea, M. Maa, L. Tana, Y. Zhanga, S. Yaoa, *Colloids and Surfaces B: Biointerfaces*, **2010**, *80*, 18-25.
8. K. Yang, W. Qin, H. Tang, L. Tan, Q. Xie, M. Ma, Y. Zhang, S. Yao, *J Biomed Mater Res Part A*, **2011**, *99A*, 231-239.
9. M. E. Füstös, T. A. Sipos, M. V. Diudea, G. Katona, *Croat. Chem. Acta*, **2015**, *88* (2), 129-132.

ADSORPTION OF AMMONIUM IONS ONTO MULTI-WALLED CARBON NANOTUBES

HAMIDREZA SADEGH^{a,*}, GOMAA A. M. ALI^{b,c}, ZEYNAB ABBASI^d,
MALLIKARJUNA N. NADAGOUDA^e

ABSTRACT. Multi-walled carbon nanotubes (MWCNTs) surfaces have been characterized by FTIR and SEM techniques. The adsorption performance of MWCNTs was investigated for the removal of ammonium ions from wastewater. The effect of contact time, temperature and initial ions concentration on the adsorption of ammonium ions by MWCNTs were studied and optimized. The results showed a high adsorption capacity of 129 mg/g according to Langmuir isotherm model and removal efficiency of 95%. In addition, the adsorption kinetic and equilibrium data were fitted to the pseudo-second-order model. The potential application of MWCNTs for adsorption of ammonium ions from wastewater was successfully accomplished using a batch adsorption technique.

Keywords: Carbon nanotubes; Removal; Adsorption; Kinetics; Isotherm; Ammonium ions; Langmuir

INTRODUCTION

The scientific community has a growing interest in environmental protection against aquatic pollution from various industrial activities for the reduction and/or the valorization of solid wastes. In this context, many studies were performed using nanoadsorbents. These adsorbents are used for removal and adsorption of ammonium ions from wastewater [1, 2]. The use of these

^a West Pomeranian University of Technology, Szczecin; Faculty of Chemical Technology and Engineering; Institute of Inorganic Chemical Technology and Environment Engineering; ul. Pułaskiego 10, 70 - 322 Szczecin, Poland

^b Chemistry Department, Faculty of Science, Al-Azhar University, Assiut, 71524, Egypt

^c Faculty of Industrial Sciences and Technology, Universiti Malaysia Pahang, Gambang, 26300, Kuantan, Malaysia

^d Department of Chemistry, Science and Research Branch, Islamic Azad University, Tehran, Iran

^e Department of Mechanical and Materials Engineering, Wright State University, Dayton, USA

* Corresponding author: hamidreza.sadegh@srbiau.ac.ir, h.sadegh@chemist.com

nanomaterials has shown many advantages, such as large specific surface area, effective and economical removal, high adsorption capacity, and surface reactivity [3-7].

Carbon nanotubes (CNTs), which were discovered by Iijima in 1991 [8], are one of the most widely studied carbon nanomaterials and can serve as excellent adsorbents [9-11] because of their hollow and layered structure and large specific surface area, which make CNTs the most commonly used nanomaterials for adsorbing toxic material [12]. CNTs can be classified into three types: single-walled (SWCNTs), multi-walled (MWCNTs), and functionalized (f-CNTs) [12-15]. Such materials have already played a key role in the effective removal of several organic contaminants from water [16]. For example, MWCNTs are much more effective in the removal of organic chemicals from wastewater than activated carbon [17, 18].

The aim of the present work is to evaluate the potential and effectiveness of MWCNTs for the removal of ammonium ions from wastewater. The effect of various parameters such as contact time (t), temperature (T), and initial ions concentration (C) on the adsorption process were studied and optimized. The objects of this work are as follows: (i) to study the feasibility of using MWCNTs as adsorbents for the removal of ammonium ions, (ii) to determine the applicability of various isotherm models (i.e., Langmuir and Freundlich) to find the best-fit isotherm equation, and (iii) to evaluate kinetic parameters and explain the nature of adsorption.

RESULTS AND DISCUSSION

FTIR was used to characterize the functional groups present on the surface of the adsorbent. Figure 1 (a) showed a weak band at 3785 cm^{-1} which indicates the presence of unbound or free hydroxyl group ($-\text{OH}$) [19]. The strong band at 3445 cm^{-1} might be due to the presence of intermolecular hydrogen bonding or $\text{O}-\text{H}$ stretching vibrations of the carboxylic acid groups [19, 20]. The band at 1720 cm^{-1} can be assigned to the $\text{C}=\text{O}$ stretching mode of the $-\text{COOH}$ groups [21]. The band at 1570 cm^{-1} can be assigned to the $\text{C}=\text{C}$ stretching, which indicates the graphite structure of MWCNTs [20]. The bands at 1120 and 900 cm^{-1} can be assigned to the $\text{C}-\text{O}$ and $\text{C}-\text{C}$ stretching modes, respectively [19, 22].

In addition, the surface textural and morphological properties of the developed adsorbent were carried out using SEM imaging, as shown in Figure 1 (b). MWCNTs were entangled and some were in the form of agglomerates with various bunches of rope-like structures with smooth surfaces. The tube lengths were several micrometers while the diameters were lower than 50 nm .

ADSORPTION OF AMMONIUM IONS ONTO MULTI-WALLED CARBON NANOTUBES

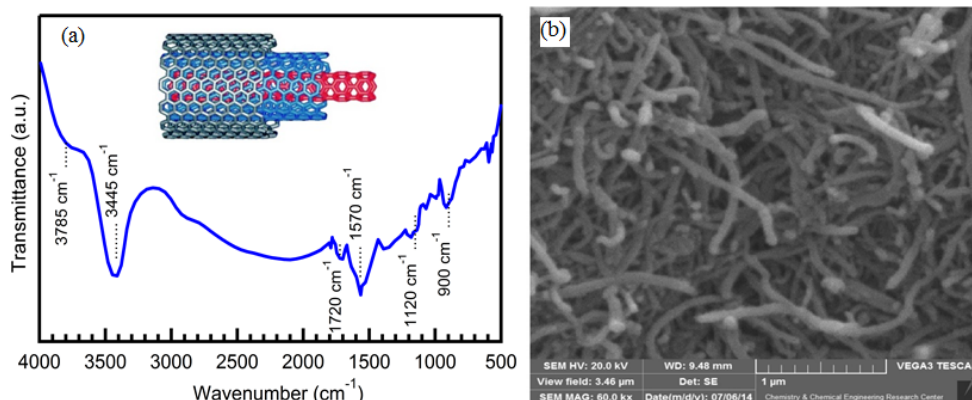


Figure 1. FTIR spectrum through graphical representation (a) and SEM image (b) of MWCNTs.

In this work, the adsorption capacity of ammonium ions on MWCNTs surface was studied. Effect of contact time at adsorption experiments occurred at various time between 10 and 100 min. As shown in Figure 2, removal of ammonium ions by MWCNTs adsorbent was very slow after 55 min; therefore, 60 min was selected as the optimum time for the adsorption process of ammonium ions on MWCNTs surface at pH = 6 and T = 298 K.

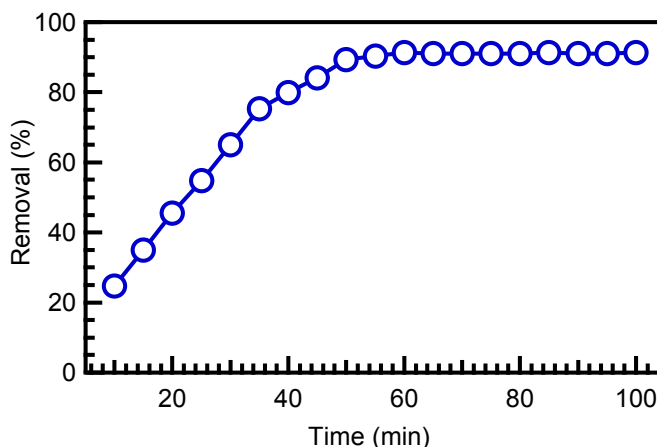


Figure 2. Effect of contact time on the removal of ammonium ions by MWCNTs (at pH = 6, T = 298 K, C₀ = 140 mg/L, dosage = 0.05 g and 10 mL solution).

To study the effect of temperature on ammonium ions removal on MWCNTs surface, adsorption experiments were carried out at several temperatures ranging from 298 to 338 K. All adsorption experiments were performed at 60 min and at a pH of 6. Figure 3 displays the effect of temperature on the removal of ammonium ions by MWCNTs adsorbents. The removal of ammonium ions on MWCNTs surface increased with increasing the temperature; removal was 75 % at 298 K and reached 93% at 338 K.

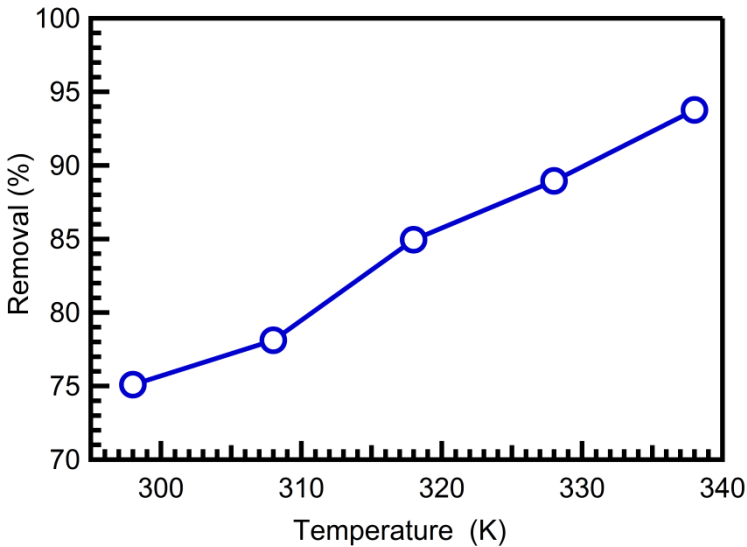


Figure 3. Effect of temperature on the removal of ammonium ions by MWCNTs (at pH = 6, time = 60 min, $C_0 = 140$ mg/L, dosage = 0.05 g and 10 mL solution).

The effect of initial ammonium ion concentrations on the adsorption by MWCNTs surface is shown in Figure 4. The percentage of adsorbed ions increased with the increase in initial ion concentration. Around 60% of ammonium ions were removed using 80 mg/L MWCNTs, while at 140 mg/L more than 93% of the ions were been removed. This is because at higher concentrations, the ratio of the initial number of ammonium ions to the available surface area is high and, subsequently, the fractional adsorption becomes independent on the initial concentration. However, at high concentrations, the available sites for adsorption become wider and the adsorption of ions depends upon the concentration [23].

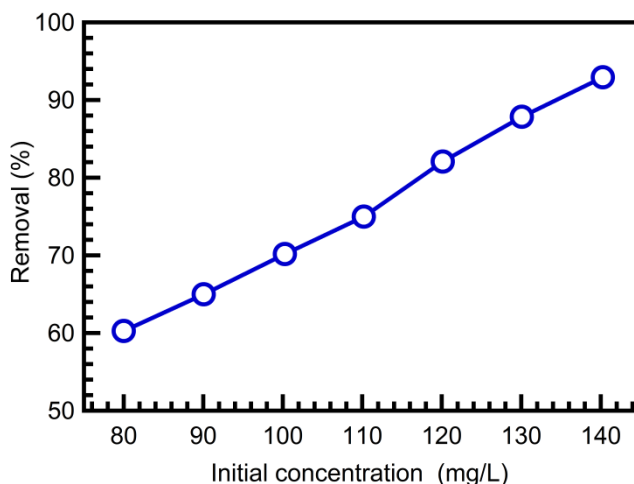


Figure 4. Effect of initial ions concentration on the removal of ammonium ions by MWCNTs (at pH = 6, time = 60 min, T = 298 K, dosage = 0.05 g, and 10 mL solution).

Adsorption is a physicochemical process that involves mass transfer of a solute from liquid phases to the adsorbent surface. Four of the most widely used kinetic models, pseudo-first-order, pseudo-second-order, intra-particle diffusion, and Elovich models, were used to study the adsorption kinetic behavior of ammonium ions onto MWCNTs. The best-fit model was selected based on the linear regression correlation coefficient values (R^2) and the average relative error (ARE). The differential form of the pseudo-first-order kinetic equation [24, 25] can be expressed as:

$$\frac{dq_t}{dt} = k_f (q_e - q_t) \quad (1)$$

where q_e and q_t are the amounts of dye per unit of adsorbent (mg/g) at time t , respectively; k_f is the pseudo-first rate constant (min^{-1}); t is the contact time between the adsorbent and adsorbate (min). Integrating equation (1) and using boundary condition, $t = 0$ to $t = t$ and $q_t = 0$ to $q_t = q_t$, the next linear form will be obtained, known as a first order Lagergren's rate equation [23]:

$$\log(q_e - q_t) = \log q_e - \frac{k_f}{2.303} t \quad (2)$$

A linear fit of $\log(q_e - q_t)$ versus t showed the applicability of this kinetic model. The pseudo-first-order rate constant (k_f) and q_e values can be determined from the slope and intercept of the plotted line.

The pseudo-second-order model [25] is expressed as:

$$\frac{dq_t}{dt} = k_s (q_e - q_t)^2 \quad (3)$$

where k_s (g/(mg.min)) is the rate constant of the pseudo-second-order sorption. The linear forms of equation (3) may be presented as follow [26, 27]:

$$\frac{t}{q_t} = \frac{1}{k_s q_e^2} + \frac{1}{q_e} t \quad (4)$$

According to equation (4), plotting t/q_t versus t gives a straight line with a slope of $1/(k_s q_e^2)$ and an intercept of $1/q_e$.

Weber and Morris developed a widely accepted kinetic-based model that represents the time dependent intra-particle diffusion of components. Their model showed that the sorption process is diffusion-controlled if the rate is dependent upon the rate at which adsorbate and adsorbent diffuse toward one another [28]. The adsorbate uptake varies almost proportionally with $t^{1/2}$ rather than with the contact time, t . According to the following Weber–Morris’s equation:

$$q_t = k_i t^{1/2} + C \quad (5)$$

where C (mg/g) is the intercept, and k_i is the intra-particle diffusion rate constant (mg/g.min^{1/2}), which can be calculated from the slope of the linear plots of q_t versus $t^{1/2}$. A kinetic equation of chemisorption was established by Zeldowitsch [29] and was used to describe the rate of adsorption of carbon monoxide on manganese dioxide that decreases exponentially with an increase in the amount of gas adsorbed [27], which is the so-called Elovich equation as follows [30]:

$$dq_t/dt = \alpha_{exp} (-\beta q^2) \quad (6)$$

where α is the initial adsorption rate (mg/g.min), and β is the adsorption constant (g/mg) during any experiment. With the assumption of $\alpha \beta \gg 1$, equation (6) was integrated by using the boundary conditions of $q = 0$ at $t = 0$ and $q = q$ at $t = t$ to yield:

$$q_t = 1/\beta \ln(\alpha\beta) + 1/\beta \ln(t) \quad (7)$$

If ammonium ion adsorption fits the Elovich model, a plot of q_t versus $\log t$ should yield a linear relationship with a slope of $1/\beta$ and an intercept of $1/\beta \log (\alpha\beta)$. Kinetic parameters of ammonium ion adsorption onto MWCNTs initial ion concentrations are shown in Table 1. The results obtained indicate that only the pseudo-second order model fit the kinetic data for MWCNTs on ammonium ions in the whole data range. Furthermore, the values of R^2 and ARE for the pseudo-second-order model are much higher than other kinetic models. There was good agreement between the model fit and experimentally observed equilibrium adsorption capacities in addition to the large correlation coefficients. This suggests that ammonium ion adsorption onto MWCNTs followed the pseudo-second-order kinetic model.

Table 1. Comparison of kinetic models for adsorption of ammonium ion.

Model	Parameters	Value
Pseudo-first-order	q_e exp (mg/g)	95.74
	q_e cal (mg/g)	41.21
	K_f (min^{-1})	0.121
	R^2	0.875
	ARE	3.90
Pseudo-second-order	q_e exp (mg/g)	97.92
	q_e cal (mg/g)	98.1
	K_s (g/mg.min)	0.0071
	R^2	0.999
	ARE	1.1
Intra-particle diffusion	k_i (mg/g/min ^{1/2})	0.1352
	C (mg/g)	0.0181
	R^2	0.988
	ARE	3.2
	Elovich	α
	β	10.1351
	R^2	0.895
	ARE	0.7

Adsorption isotherms are essential for the description of the interactive behaviour between adsorbate and adsorbent, and they are critical in optimizing the application of an adsorbent. To estimate adsorption capacities, the equilibrium data was fitted to the well-known Langmuir and Freundlich isotherm models [31]. The mathematical representations of these models are given in the equations below ((8) and (9), respectively):

$$\frac{1}{Q_e} = \frac{1}{Q_o} + \left(\frac{1}{Q_o K_L} \right) \frac{1}{C_e} \tag{8}$$

$$\log Q_e = \log K_f + \frac{1}{2.303 n} \log C_e \tag{9}$$

where, Q_e is the adsorbate equilibrium amount in solid phases (mg/g), Q_o is the maximum adsorption capacity according to Langmuir monolayer adsorption (mg/g), and K_L is constant according to the Langmuir isotherm (L/mg). K_F (mg/g)(L/mg) and n are Freundlich constants related to adsorption capacity and adsorption intensity of the adsorbent, respectively. The values of K_F and $1/n$ can be obtained from the intercept and slope, respectively, of the linear plot of experimental data of $\log Q_e$ versus $\log C_e$. $1/n$ values indicate the type of isotherm to be irreversible ($1/n = 0$), favorable ($0 < 1/n < 1$) and unfavorable ($1/n > 1$) [20]. Langmuir isotherm values of Q_o and K_L can be calculated from the slope and intercept of the linear plot of $1/Q_e$ versus $1/C_e$. The adsorption isotherm for ammonium ions by MWCNTs surface is listed in Table 2.

Table 2. Fitting parameters of the ammonium ions adsorption experimental results to the Langmuir and Freundlich isotherm models.

Model	Parameter	Value
Langmuir	Q_o (mg/g)	129
	K_L (L/mg)	3.08
	R^2	0.999
Freundlich	$1/n$	0.802
	K_F (mg/g)(L/mg)	41.3
	R^2	0.852

Based on the correlation coefficient as shown in Table 2, isotherm Langmuir represents a better fit of experimental data than Freundlich isotherm in all cases. It indicates that the surfaces of adsorbents are mainly made up of heterogeneous adsorption patches [24] in addition to less homogeneous patches [32]. The Freundlich constant (n) is a measure of adsorption intensity. As seen from Table 2, the values of $1/n$ for adsorbent were below 1, which indicate high adsorption intensity [25]. K_F , which is related to the adsorption capacity, also shows that the adsorption capacity increased with temperature increase, indicating that the adsorption processes are exothermic in nature. But the increase of the values of $1/n$ with the temperature decrease suggests the

increasing trend of the adsorption intensity. As temperature increased, the more ammonium ions were adsorbed, the keener the competitions for the limited adsorption sites and the stronger the attraction among the molecules, which resulted in an increase of adsorption intensity. From the results, MWCNTs surface has advantages for adsorption of ammonium ions. The favorability of the ammonium ion adsorption process onto adsorbent surfaces evaluated using a dimensionless parameter (R_L) derived from the Langmuir expression is defined as follows [33]:

$$R_L = \frac{1}{1 + K_L C_0} \quad (10)$$

The adsorption process can be defined as irreversible ($R_L = 0$), favorable ($0 < R_L < 1$), linear ($R_L = 1$) or unfavorable ($R_L > 1$) in terms of R_L [30]. The calculated values of R_L for adsorption of ammonium ions by MWCNTs surface fall between 0 and 1; thus, the adsorption of ammonium onto adsorbent is favorable. The adsorption capacity of the MWCNTs, calculated by the Langmuir equation, was about 129 mg/g. In addition, the removal efficiency for adsorbate was found to be 95%.

CONCLUSIONS

In this study, multi-walled carbon nanotubes (MWCNTs) were tested as adsorbent for the removal of ammonium ions. The effect of contact time, temperature and initial ions concentration on the removal of ammonium ions was investigated through batch experiments. The optimum contact time, temperature and initial concentration for adsorption were obtained to be 60 min, 338 K and 140 mg/L, respectively. The kinetics of adsorbent was experimentally studied and the obtained rate data were analysed using the pseudo-first-order, pseudo-second-order, intra-particle diffusion, and Elovich models. Based on the values of the correlation coefficient (R^2) and average relative error (ARE) obtained for all tested models, pseudo-second-order was found to best correlate the rate kinetic data of MWCNTs. In addition, adsorption parameters for the Langmuir and Freundlich isotherms were determined and the equilibrium data were found to be best described by the Langmuir isotherm model with maximum adsorption capacity of 129 mg/g. Moreover, the removal efficiency for adsorbate respectively was found to be 95%. Therefore, MWCNTs could be considered as a promising adsorbent for water treatment or environmental management in terms of high efficiency and feasibility.

EXPERIMENTAL SECTION

MWCNTs were purchased from Nano Amor Nanostructured & Amorphous Materials, Inc., USA (Purity, > 95%; outer > 50 nm; length, 500-115 2000 nm; surface area, ~ 40 m²/g; and the manufacturing method, catalytic chemical vapour deposition (CVD)). Ammonium chloride salt (NH₄Cl) (molecular weight, 53.16 g/mol) was supplied by Merck (Germany) (maximum purity available). Doubly distilled deionized water (HPLC grade 99.99% purity) was obtained from Sigma Aldrich Co. (Germany). All supplementary chemicals were of analytical grades and were purchased from Merck Inc., USA.

The functional groups of the prepared materials were identified by Fourier transform infrared spectroscopy (FTIR) using a Tensor 27, Bruker, Germany. Small portions (about 5 mg) of powder samples were homogenized with KBr (about 100 mg) using an agate mortar and pelletized prior to measurement. Moreover, the surface morphology of MWCNTs was investigated with a JEOL JSM-5900LV scanning electron microscope (SEM) (Japan) with an acceleration voltage of 20 KV.

For the purpose of studying the adsorption process, a 1000 mg/L stock solution of ammonium was prepared by dissolving 3.819 g of ammonium chloride (NH₄Cl) in deionized water. The solutions to be used were prepared by diluting the stock solution with deionized water when necessary.

Adsorption experiments were conducted by using 100 mL glass flask containing 0.05 g of the adsorbent and 10 mL of the ammonium ions solution with the initial concentration of 140 mg/L. The glass flask was sealed with a glass stopper. The samples were then mounted on an ultrasonic bath for 60 min at various temperatures (298 - 328 K). The ultrasonic bath (71020-DTH-E; Model 1510 DTH, 220V; EMS Company) was used to prevent particles aggregation and bulk formation. Then, the samples were centrifuged at 4500 rpm and the supernatant was filtered by 0.2 μm filter paper for subsequent ammonium concentration analysis. The initial and final ammonium concentrations remaining in solutions were analysed by a UV spectrophotometer (Varian-Cary100 Bio), monitoring the absorbance changes at a wavelength of maximum absorbance ($\lambda = 400$ nm). The difference between the initial and equilibrium ion concentrations could determine the amount of ions adsorbed onto the MWCNTs surface. The amount of ammonium adsorbed was determined by the difference between the initial and residual concentration of ammonium ion solution. The removal capacity of ammonium ions by MWCNTs was calculated using the equations (11) and (12), respectively [34, 36]:

$$q_e = \frac{(C_o - C_e)V}{m} \quad (11)$$

$$Removal (\%) = 100 \times \frac{(C_o - C_e)}{C_o} \quad (12)$$

where q_e was the amount of ammonium ions taken up by the MWCNTs (mg/g), C_o was the initial ammonium ions concentration put in contact with the MWCNTs (mg/L), C_e is the ammonium ions concentration (mg/L) after the adsorption procedure, m is MWCNTs mass (g) and V is the volume of the ammonium ions solution (L). To evaluate the fitness of kinetic and isotherm equations to the experimental data, ARE was calculated using equation (13) and used to measure the kinetic and isotherm constants [37]. ARE can be expressed as:

$$ARE(\%) = \frac{100}{n} \sum_i^n \left| \frac{q_{i,cal} - q_{i,exp}}{q_{i,exp}} \right| \quad (13)$$

where n is the number of data points. Each experiment was conducted in triplicate under in the same conditions to confirm the results, and was found reproducible. Also, all the experiments were performed in triplicate, and only the mean values have been reported. Ammonium ions concentration was measured by Nesslerization Method [38].

ACKNOWLEDGMENTS

The authors would like to thank Islamic Azad University Science and Research Branch for all supports.

REFERENCES

1. K. Zare, H. Sadegh, R. Shahryari-Ghoshekandi, M. Asif, I. Tyagi, S. Agarwal, V.K. Gupta, *Journal of Molecular Liquids*, **2016**, 213, 345.
2. V. K. Gupta, H. Sadegh, M. Yari, R. Shahryari Ghoshekandi, B. Maazinejad, M. Chahardori, *Global Journal of Environmental Science and Management*, **2015**, 1, 149.
3. H. Sadegh, R. Shahryari-Ghoshekandi, A. Masjedi, Z. Mahmoodi, M. Kazemi, *International Journal of Nano Dimension*, **2016**, 7, 109.

4. V.K. Thakur, M.K. Thakur, *Chemical Functionalization of Carbon Nanomaterials: Chemistry and Applications*, CRC Press, USA, **2015**, chapter 30.
5. V.K. Gupta, I. Tyagi, H. Sadegh, R. Shahryari-Ghoshekandi, A.S.H. Makhlof, B. Maazinejad, *Science, Technology and Development*, **2015**, *34*, 195.
6. H. Sadegh, G.A.M. Ali, V.K. Gupta, A.S.H. Makhlof, R. Shahryari-Ghoshekandi, M.N. Nadagouda, M. Sillanpää, E. Megiel, *Journal of Nanostructure in Chemistry*, **2017**, *7(1)*, 1.
7. H.H. Abdel Ghafar, G.A.M. Ali, O.A. Fouad, S.A. Makhlof, *Desalination and Water Treatment*, **2015**, *53(11)*, 2980.
8. S. Iijima, *Nature*, **1991**, *354*, 56.
9. H. Sadegh, R. Shahryari-Ghoshekandi, M. Kazemi, *International Nano Letters*, **2014**, *4*, 129.
10. K. Zare, F. Najafi, H. Sadegh, *Journal of Nanostructure in Chemistry*, **2013**, *3*, 1.
11. K. Zare, H. Sadegh, R. Shahryari-Ghoshekandi, B. Maazinejad, V. Ali, I. Tyagi, S. Agarwal, V.K. Gupta, *Journal of Molecular Liquids*, **2015**, *212*, 266.
12. H. Sadegh, K. Zare, B. Maazinejad, R. Shahryari-Ghoshekandi, I. Tyagi, S. Agarwal, V.K. Gupta, *Journal of Molecular Liquids*, **2016**, *215*, 221.
13. H. Sadegh, R. Shahryari-Ghoshekandi, *Nanomedicine Journal*, **2015**, *2*, 231.
14. V.K. Gupta, O. Moradi, I. Tyagi, S. Agarwal, H. Sadegh, R. Shahryari-Ghoshekandi, A.S.H. Makhlof, M. Goodarzi, A. Garshasbi, *Critical Reviews in Environmental Science and Technology*, **2016**, *46*, 93.
15. S. Soni, A. Salhotra, M. Suar, *Handbook of Research on Diverse Applications of Nanotechnology in Biomedicine, Chemistry, and Engineering*, IGI-Global, Hershey PA, **2015**, chapter 6.
16. M. Rajabi, B. Mirza, K. Mahanpoor, M. Mirjalili, F. Najafi, O. Moradi, H. Sadegh, R. Shahryari-Ghoshekandi, M. Asif, I. Tyagi, S. Agarwal, V.K. Gupta, *Journal of Industrial and Engineering Chemistry*, **2016**, *34*, 130.
17. B. Pan, B. Xing, *Environmental Science & Technology*, **2008**, *42*, 9005.
18. K. Zare, V.K. Gupta, O. Moradi, A.S.H. Makhlof, M. Sillanpää, M.N. Nadagouda, H. Sadegh, R. Shahryari-Ghoshekandi, A. Pal, Z. Wang, I. Tyagi, M. Kazemi, *Journal of Nanostructure in Chemistry*, **2015**, *5*, 227.
19. N.B.A. Mansor, J.-P. Tessonier, A. Rinaldi, S. Reiche, M.G. Kutty, *Sains Malaysiana*, **2012**, *41(5)*, 603.
20. H. Sadegh, R. Shahryari-Ghoshekandia, I. Tyagib, S. Agarwalb, V.K. Gupta, *Journal of Molecular Liquids*, **2015**, *207*, 21.
21. X. Cheng, J. Zhong, J. Meng, M. Yang, F. Jia, Z. Xu, H. Kong, H. Xu, *Journal of Nanomaterials*, **2011**, *2011*, doi.org/10.1155/2011/938491.
22. R. Wahab, S.T. Khan, J. Ahmad, S.G. Ansaric, J. Musarrat, A.A. Al-Khedhairy, *Vacuum*, **2017**, <http://dx.doi.org/10.1016/j.vacuum.2017.01.022>.
23. S. Agarwal, H. Sadegh, M. Monajjemi, A.S. Hamdy, G.A.M. Ali, A.O.H. Memar, R. Shahryari-Ghoshekandi, I. Tyagi, V.K. Gupta, *Journal of Molecular Liquids*, **2016**, *218*, 191.
24. N. Gupta, A.K. Kushwaha, M.C. Chattopadhyaya, *Journal of the Taiwan Institute of Chemical Engineers*, **2012**, *43(1)*, 125.

25. V. Mishra, C. Balomajumder, V.K. Agarwal, *CLEAN–Soil, Air, Water*, **2012**, *40*, 718.
26. Y.-S. Ho, *Journal of Hazardous Materials*, **2006**, *136*, 681.
27. Y.-S. Ho, G. McKay, *Process Biochemistry*, **1999**, *34*, 451.
28. H. Fan, J. Yang, T. Gao, H. Yuan, *Journal of the Taiwan Institute of Chemical Engineers*, **2012**, *43*, 386.
29. J. Zeldowitsch, *Acta Physicochim URSS*, **1934**, *1*, 364.
30. M.J.D. Low, *Chemical Reviews*, **1960**, *60*, 267.
31. O. Moradi, H. Sadegh, R. Shahryari-Ghoshekandi, Adsorption and desorption in carbon nanotubes, discovery and evolution, LAP LAMBERT Academic Publishing, **2014**.
32. H. Sadegh, R. Shahryari-Ghoshekandi, S. Agarwal, I. Tyagi, M. Asif, V.K. Gupta, *Journal of Molecular Liquids*, **2015**, *206*, 151.
33. O.A. Habeeb, K. Ramesh, G.A.M. Ali, R.M. Yunus, T.K. Thanusha, O.A. Olalere, *Australian Journal of Basic and Applied Sciences*, **2016**, *10(17)* 136.
34. R. Sivaraj, C. Namasivayam, K. Kadirvelu, *Waste Management*, **2001**, *21*, 105.
35. V.K. Gupta, I. Tyagi, S. Agarwal, H. Sadegh, R. Shahryari-Ghoshekandi, M. Yari, O. Yousefi-Nejat, *Journal of Molecular Liquids*, **2015**, *206*, 129.
36. O. Moradi, V.K. Gupta, S. Agarwal, I. Tyagi, M. Asif, A.S.H. Makhlof, H. Sadegh, R. Shahryari-Ghoshekandi, *Journal of Industrial and Engineering Chemistry*, **2015**, *28*, 294.
37. R. Shahryari-Ghoshekandi, H. Sadegh, *Jordan Journal of Chemistry*, **2014**, *9*, 267.
38. APHA, AWWA, and WEF (American Public Health Association, American Water Works Association, and Water Environment Federation), *Standard Methods for the Examination of Water and Wastewater*, 20th ed. APHA, Washington, DC, **1998**.

RHEOLOGICAL INVESTIGATION OF RUBBER BITUMEN CONTAINING VARIOUS WAXES AS WARM MIX ADDITIVE

PÉTER GERGÓ^{a*}, ANDRÁS HOLLÓ^a, ANDRÁS GEIGER^b

ABSTRACT. The aim of this study is to investigate the effect of various wax type warm mix additives on the rheological properties of Chemically Stabilized Rubber Bitumen (CSRB). The rubber bitumen samples were prepared by the modified wet process (HU 226481) and the bitumen tests were carried out according to the relevant standards. Two types of warm mix additives (polypropylene wax - produced by thermal cracking of polypropylene and Fischer-Tropsch wax) with different concentrations (1.0%, 3.0%, 5.0%, 7.0% by weight) were used in our research. The influence of these warm mix additives on the rheological properties was evaluated by Dynamic Shear Rheometer (DSR) test. Multiple-stress creep and recovery (MSCR) test was also used for the determination of percent recovery and non-recoverable creep compliance of wax-modified and neat asphalt rubber samples. According to the results of DSR tests the addition of the Fischer-Tropsch wax resulted a higher complex modulus (thereby stiffness) and favourable higher recovery values based on MSCR tests unlike the addition of polypropylene wax.

Keywords: *warm mix additive, asphalt rubber, rheological properties, MSCR*

INTRODUCTION

The major source of pollution in asphalt application originates from its production and lay down. Moreover, the energy consumption of the high-temperature Hot Mix Asphalt (HMA) technologies is also large. The lower energy consumption of road construction and thus lower greenhouse gas emission can be achieved with the production of so-called warm mix asphalt [1]. The most

^a *University of Pannonia, Faculty of Engineering, MOL Department of Hydrocarbon and Coal Processing, 10 Egyetem street, HU-8200, Veszprém, Hungary*

^b *MOL Hungarian Oil and Gas Plc., 2 Olajmunkás street, HU-2440, Százhalombatta, Hungary*

* *Corresponding author: gergop@almos.uni-pannon.hu*

common manufacturing technologies of Warm Mix Asphalt (WMA) can be classified into three groups based on the technology used. In the first group, there are water-based, foaming technologies. The second group contains organic additives applying technologies. In the third group there are chemical additives applying technologies. The most commonly used chemical additives include waxes produced by Fischer-Tropsch (FT) synthesis, fatty acid amides, and Montan wax [2-3].

Applying the latter additives during the temperature rise the wax will melt and remains above the melting point and because of the lower viscosity it decreases the viscosity of the whole mixture. During cooling the asphalt mixture, the applied additive solidifies – distributed uniformly in the mixture, in microscopic form. These crystalline particles increase the rigidity of the mixture similarly to the fiber reinforced materials.

An important requirement of this process is the selection of the right additive type, which avoids problems that can occur with the temperature [4]. One such problem may arise if the wax has a melting point lower than the temperature of application and therefore care must be taken in selecting the wax having the strength and toughness on the application temperature. In addition, the selection of the wax having appropriate properties reduces the low temperature embrittlement problems [5].

Waxes used in these technologies have generally high molecular weight, paraffins having high carbon numbers (C_{45}) and a melting point between 80 and 120°C are applied [6]. Depending on the technology a small amount of these waxes, about 2-4% are applied concerning the total weight of the bitumen binder. The available mixing and processing temperature decrease is approximately 20-30°C.

In addition to the three main wax types experiments are conducted with waxes originating from waste polypropylene pyrolysis or cracking in order to decrease the application temperature of hot asphalt technologies [7].

Rubber bitumen is a special type of modified bitumen. Thanks to the crumb rubber in the composition, it has better characteristics than the base bitumen, similarly to the conventional Polymer modified Bitumen (PmB). In addition to this because of the partly diluted rubber particles the traffic noise is lower, the pavement is more flexible, it has better resistance to fatigue and load, in the meantime it has outstanding cold weather resistance. The stability of the rubber bitumen produced according to the modified wet process is better compared to the conventional rubber bitumen, namely it has low separation tendency [8-9].

The viscosity of CSRb is lower compared to conventional rubber bitumen and similar to the well-known PmB's and higher than base bitumen, thus it requires higher mixing temperature. Because of this in case of CSRb the mixing

temperature and the decrease of the viscosity are important R&D target. Because of the above reasons the application of WMA additives are also recommended.

Different WMA additives were recently studied by other researchers in rubber bitumen. E.g. 2-4% Fischer-Tropsch wax addition could result 10-30°C lower mixing temperature in similar asphalt rubber binder [10].

RESULTS AND DISCUSSION

In order to determine the base properties of the samples the softening point, penetration, Fraass breaking point and storage stability were measured.

Based on the changes in the softening point, the admixing of polypropylene wax reduced this value of samples. Increasing the concentration, the effect has increased slightly (figure 1).

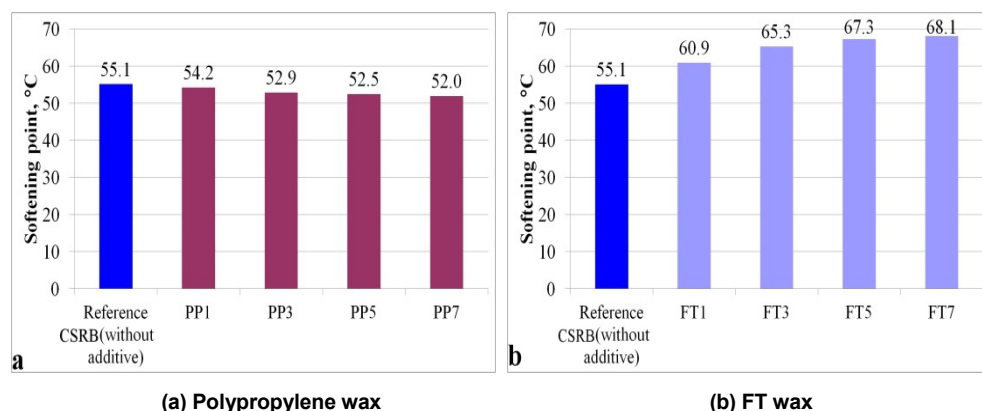


Figure 1. Influence of polypropylene wax and FT wax on softening point of the samples

The mixing of polypropylene wax had an impact also on the penetration of the samples (figure 2.). This value increased for higher doping concentration (5.0 to 7.0%); the effect was more significant. In contrast the FT wax highly hardened the samples, thus reduced the penetration value, but due to this effect the samples were also brittle (figure 3).

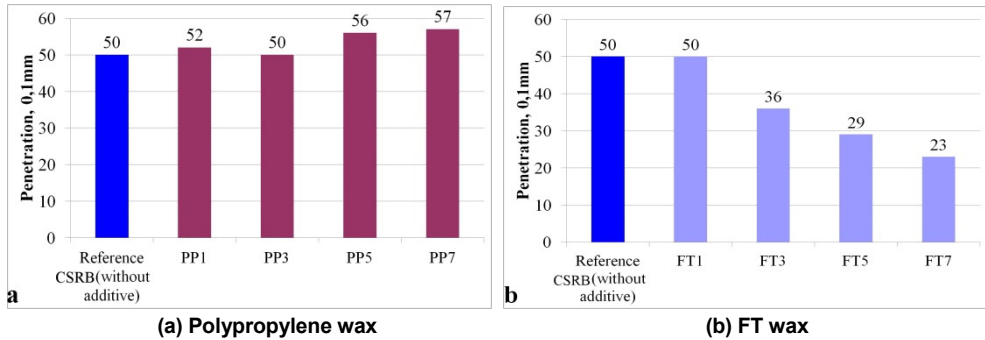


Figure 2. The influence of PP heavy residue and FT wax on the penetration of the samples

Based on the Fraass breaking point of the samples which characterizes the cold side properties; the mixing of polypropylene wax was more favourable compared to the FT wax, because in this case, to a lesser extent increased the breaking point with the additive concentration. This effect may have caused by the olefin content of polypropylene wax and the resulting higher pour point compared to the pure paraffin type FT wax (figure 3).

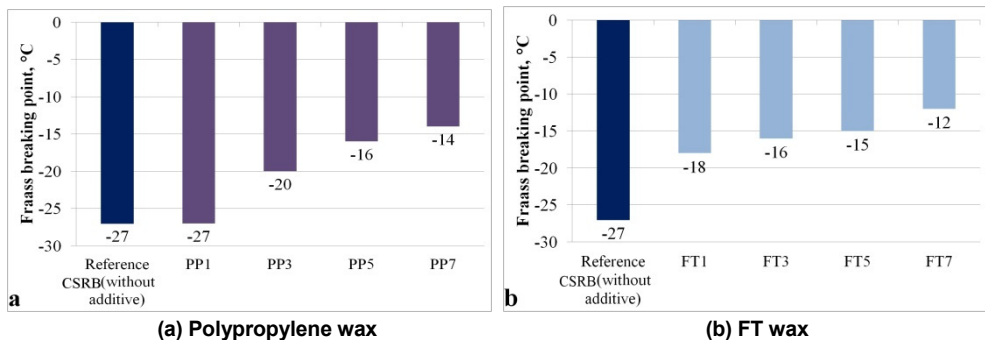


Figure 3. The influence of polypropylene wax and FT wax on Fraas breaking point of the samples

To characterize the storage stability of bitumen, the softening point difference between the upper and lower section of bitumen are measured after storage. However, this basic test method is not always characterising correctly the application properties of the samples. This is especially true for the multi-component systems such as modified bitumen containing different modifying agent with different functions, composition and thus different characteristics.

Both the studied additives slightly deteriorated the stability. Based on the measured values significant differences were not experienced between the two additives used. The stability of the samples reduced (softening point difference increased) slightly by increasing the concentration of the waxes (figure 4).

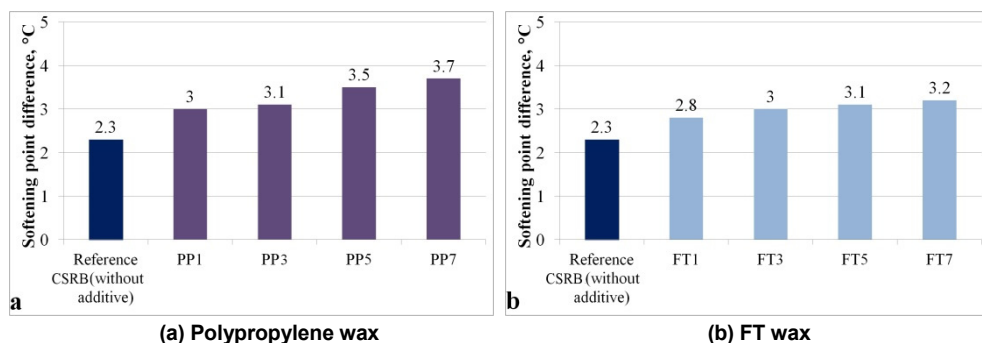


Figure 4. The influence of polypropylene wax and FT wax on the storage stability (softening point difference) of the samples

We also investigated the high temperature viscosity of the lower and upper part of the stored samples. Due to the increased sedimentation, great differences of the viscosity were measured between the lower and upper part of the samples containing the polypropylene wax on both investigated temperatures. This difference is increased by increasing the additive concentration. In case of measuring FT wax containing patterns, we have also seen separation, however, the trend was different (figure 5).

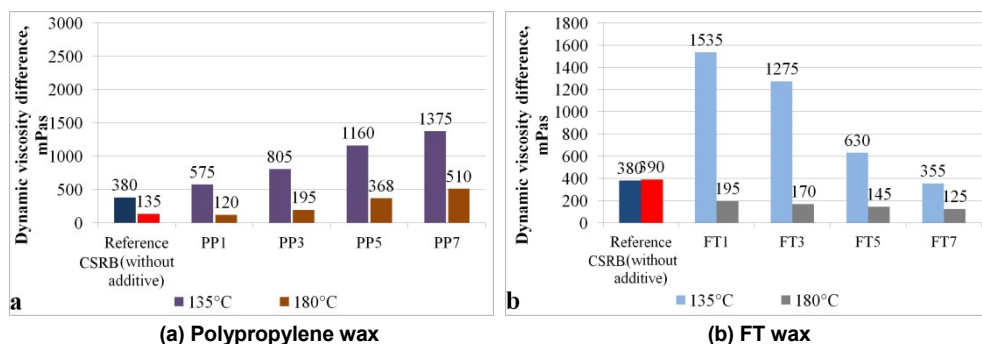


Figure 5. The influence of polypropylene wax and FT wax on the storage stability (dynamic viscosity difference) of the samples

The viscosity reducing effect of the flow modifiers was tested on the compaction (135° C) and the mixing (180° C) temperatures of the asphalt mixture as well. Based on the results both additives have favourable viscosity decreasing effect; the result of polypropylene wax admixing was slightly lower than the FT wax admixing (figure 6).

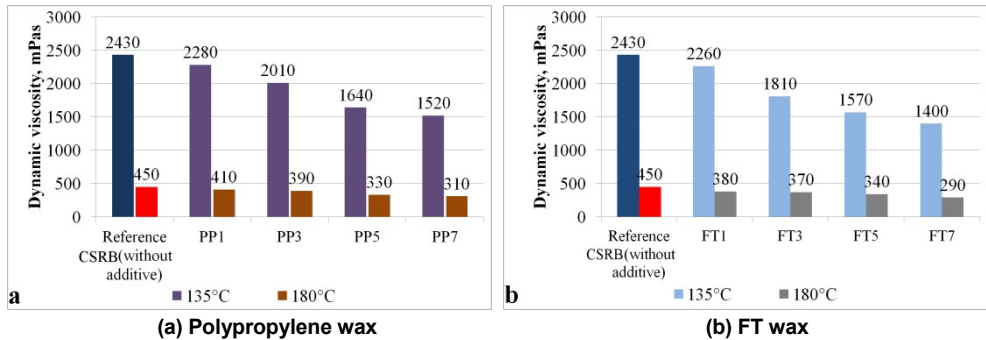


Figure 6. The influence of polypropylene wax and FT wax on the dynamic viscosity of the samples

We determined the changes of complex modulus (stiffness) for polypropylene wax containing samples varying the temperature. We found that this value decreased in the whole temperature range. In the lower temperature range (below 35°C) with increasing the doping concentration, the stiffness value approached the value of the reference sample. In contrast, with the application of the FT wax, the stiffness increased greater extent below 70°C because its plastomer type (figure 7).

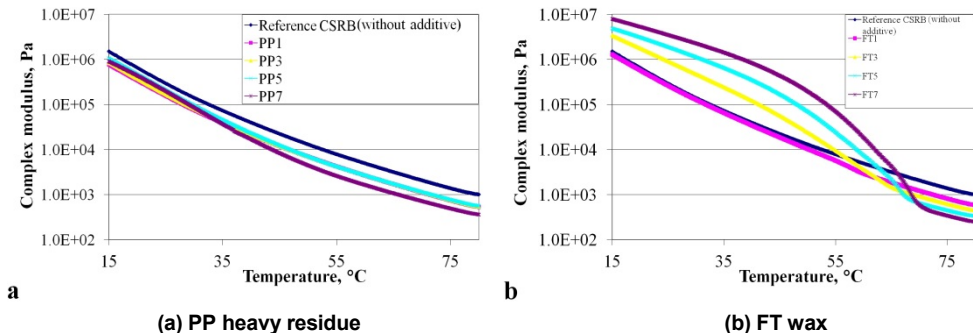


Figure 7. The influence of polypropylenewax and FT wax on the complex modulus of the samples

The multiple creep relaxation test provides information on elastic, resilient properties of the samples. During this test, the sample is first loaded with a force of 100 N for 1 second, followed by a 9 seconds-long relaxation phase. This cycle was performed 10 times, and then the force increased to 3200N and a further 10 cycles were performed as previously mentioned monitoring the changes of deformation, according to the MSZ EN 16659 standard [11]. The samples which contained polypropylene wax additive were more susceptible to deformation. The 100N cycles resulted less deformation, while the samples were being greatly deformed during the 3200N cycles. In case of addition of the FT wax opposite effect was observed. When the additive concentration increased, susceptibility to deformation reduced compared to the reference sample due to the intake of hard parts (figure 8-9).

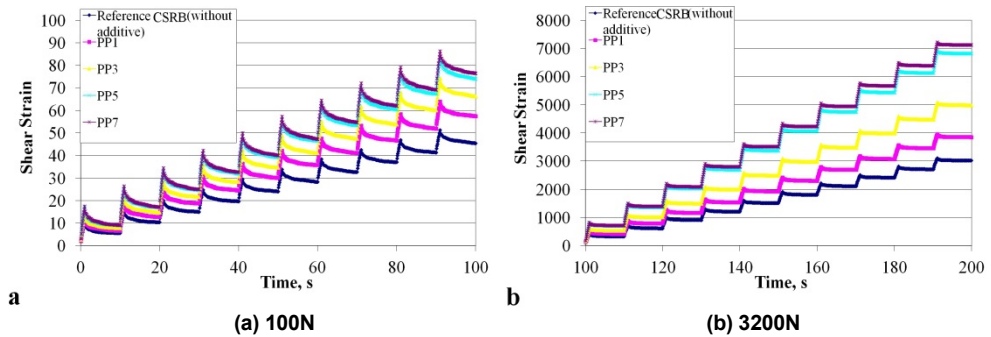


Figure 8. The results of multiple creep relaxation tests of polypropylene waxe modified samples

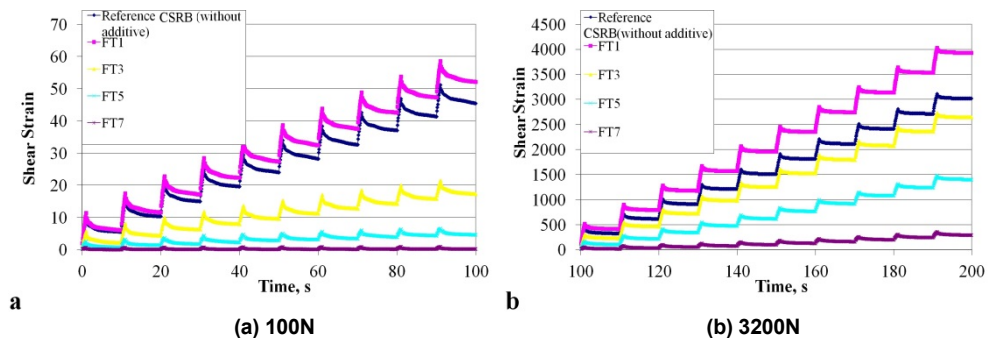


Figure 9. The results of multiple creep relaxation tests of FT wax modified samples

The amount of recovery was also calculated. The elasticity of polypropylene containing samples were about the same during the 100N load, however, the value fell short of the reference sample of over 3200N loads. In case of FT wax containing samples, when the concentration increased; the maximum deformation is reduced, however, based on the favourable relaxation characteristics of the matrix the residual deformation was less, so the samples showed better reversion (figure 10-11).

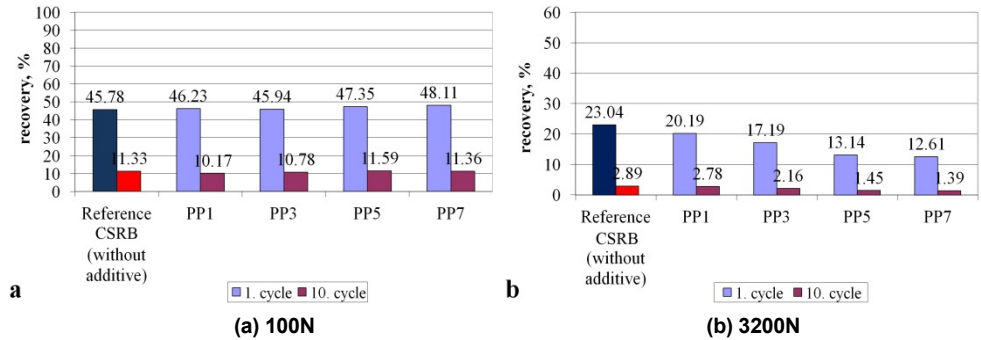


Figure 10. The recovery of polypropylene wax modified samples

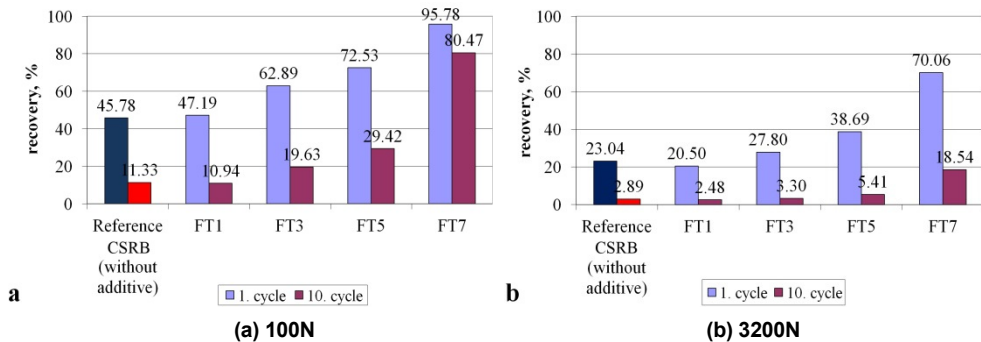


Figure 11. The recovery of FT wax modified samples

The application of polypropylene wax at 1 and 3% concentration increased the modulus (stiffness) at 15°C and 10Hz load, but the further increase in additive concentration largely reduced this value due to the weak stiffness of the additive. The FT wax increased this value at all concentrations, but due to the increasing effect, the samples become rigid (figure 12).

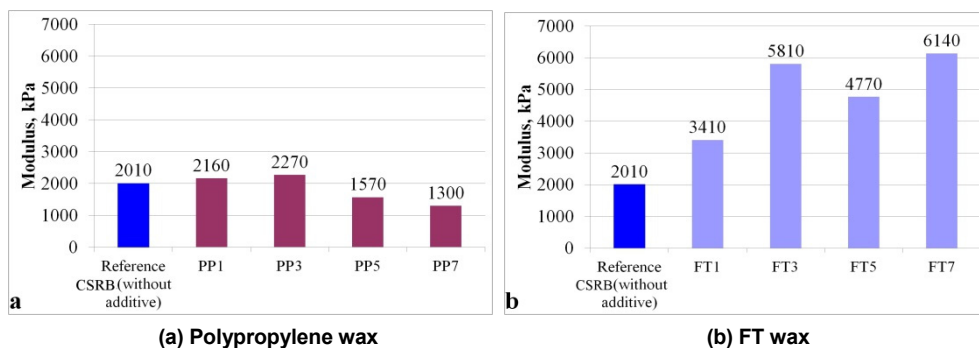


Figure 12. The influence of polypropylene wax and FT wax on the modulus of the samples

CONCLUSIONS

As a result, it can be concluded that both polypropylene wax and Fischer-Tropsch wax favourably reduced the viscosity of chemically stabilized rubber bitumen at high temperature (135-180°C). With the application of these wax type additives, the breaking point of the samples significantly deteriorated.

In the rheological measurements we found greater changes in properties and different behaviour of the samples.

The resistance to deformation improved with the use of Fischer-Tropsch wax in medium asphalt temperature (15°C), the modulus also increased, which resulted the improvement of resistance to loads, nevertheless the rigidity of the samples increased. In contrast, the polypropylene wax modified samples were sensitive to deformation and their elastic recovery values also reduced.

Regarding the industrial application further studies are needed to determine the optimal concentration of the additives for these binders meeting the standard properties of the rubber bitumen. These tests are ongoing.

EXPERIMENTAL SECTION

The following materials were used in the study to carry out the experiments: Sasolwax C80 hard wax (congealing point: 80-85°C, drop point: 88°C) from Novochem Ltd. (Overlack Group) and polypropylene wax made by thermal cracking of polypropylene (drop point: 58°C). The base material was a commercial, Chemically Stabilized Rubber Bitumen (CSRB) produced

according to the modified wet process (HU 226481) [12], by MOL Plc., meeting the requirements of the Hungarian MSZ 930:2015 standard [13].

Different concentrations of the warm mix additives (1.0%, 3.0%, 5.0%, 7.0% by weight) were used in our research program. The influence of the warm mix additives on the rheological properties was evaluated by Dynamic Shear Rheometer (DSR) tests with an Anton Paar MCR301 Dynamic Shear Rheometer. Complex modulus (G^*) changes of each bitumen samples at 15°C in various frequency load were measured compared to the asphalt stiffness and fatigue tests. The measured properties are shown in Table 1.

Table 1. Investigated parameters of the bitumen samples

Standard tests	
Properties	Standard
Softening point, °C	MSZ EN 1427
Penetration, 0,1mm	MSZ EN 1426
Fraass breaking point, °C	MSZ EN 12593
Dynamic viscosity, mPas	MSZ EN 13302
Storage stability, °C	MSZ EN 13399 MSZ EN 1427
Multiple Stress Creep Recovery (at 60°C)	MSZ EN 16659
Non-standard rheological tests	
Temperature sweep (80-15°C temperature range, 10Hz frequency, 1°C cooling rate)	
Frequency sweep (at 15°C, 0,1-100 Hz frequency range)	

ACKNOWLEDGMENTS

This work was supported by the University of Pannonia and MOL Hungarian Oil and Gas Co. The authors appreciate the technical and financial support.

REFERENCES

1. A. Almeida-Costa, A. Benta, *Journal of Cleaner Production*, **2016**, 112, 2308-2317.
2. M.C. Rubio, G. Martínez, L. Baena, F. Moreno, *Journal of Cleaner Production*, **2012**, 24, 76-84.
3. J. D'Angelo, E. Harm, J. Bartoszek, G. Baumgardner, M. Corrigan, J. Cowser, T. Harman, M. Jamshidi, W. Jones, D. Newcomb, B. Prowell, R. Sines, B. Yeaton, "Warm-Mix Asphalt: European Practice. Report No.FHWA-PL-08-007." American Trade Initiatives, Alexandria, USA, **2008**.
4. H.M.R.D. Silva, J.R.M. Oliveira, J. Peralta, S.E. Zoorob, *Construction and Building Materials*, **2010**, 24, 1621-1631.
5. L. Shang, S. Wang, Y. Zhang, Y. Zhang, *Construction and Building Materials* **2011**, 25, 886-891.
6. N. Bueche, "Warm Asphalt Bituminous Mixtures with Regards to Energy, Emissions and Performance" Young Researchers Seminar (YRS) LAVOC-CONF-2010-002, Torino, Italy, **2009**.
7. G.C. Hurley, B.D. Browell, "Evaluation of Sasobit for Use In Warm Mix Asphalt. NationalCenter for Asphalt Technology. Report 05-06.", Auburn University, Auburn, USA., **2005**.
8. A. Geiger, A. Holló, G. Szalmásné Pécsvári, P. Fehér, *MOL Group Scientific Magazine*, **2012**, 2, 54-61.
9. A. Geiger, L. Gáspár, A. Holló, M. Péter, R. Durgó, Cs. Csóke, S. Czibor, *MOL Group Scientific Magazine*, **2014**, 2, 74-83.
10. A.M. Rodrigez-Alloza, J. Gallego, I. Perez, A. Bonati, F. Giuliani, *Construction and Building Materials*, **2014**, 53, 460-466.
11. MSZ EN 16659:2016, "Bitumen and Bituminous Binders. Multiple Stress Creep and Recovery Test (MSCRT)", **2016**.
12. HU 226481, Sz. Bíró, L. Bartha, Gy. Deák, A. Geiger, "Chemically stabilized asphalt rubber compositions and a mechanochemical method for preparing the same", **2009**.
13. MSZ 930:2015 standard, "Bitumen and bituminous binders. Rubber modified bitumen. Requirements", **2015**.

HIGHLY EFFICIENT PURIFICATION OF FINELY DISPERSED OIL CONTAMINATED WATERS BY COAGULATION/FLOCCULATION METHOD AND EFFECTS ON MEMBRANE FILTRATION

GÁBOR VERÉB^{a*}, LILLA NAGY^a, SZABOLCS KERTÉSZ^a,
ILDIKÓ KOVÁCS^a, CECILIA HODÚR^a, ZSUZSANNA LÁSZLÓ^a

ABSTRACT. In the present study the purification of finely dispersed oil contaminated water (100 ppm crude oil; $d_{oil\ droplets} < 2\ \mu m$) was investigated by using coagulation/flocculation process, membrane separation and combined methods. As coagulant, polyaluminum chloride (*Bopac*) iron(III) chloride and aluminum(III) chloride, while as flocculant anionic polyelectrolyte were applied. For the membrane separation, hydrophilic polyethersulfone (PES) microfilter ($d=0.2\ \mu m$) was used, while for the determination of the purification efficiencies turbidity, chemical oxygen demand and extractable oil content were measured. The utilization of *Bopac* polyaluminum chloride coagulant (by setting Al^{3+} content to 20 ppm) resulted in high purification efficiency (96.7%). The extra addition of 1 ppm anionic polyelectrolyte lead to the increase in efficiency up to 98.8%. Due to the effective destabilization of oil in water emulsion the flux highly increased during the microfiltration of the emulsion, since both irreversible and reversible membrane resistances were greatly reduced.

Keywords: *oil contaminated waters, coagulation, flocculation, Bopac, membrane filtration*

INTRODUCTION

Large amount of oil contaminated waters are produced by many industrial processes, including food processing, petrochemical industries, metal industry and oily contaminants can appear in ground waters as well [1-6].

^a *Department of Process Engineering, Faculty of Engineering, University of Szeged, H-6725 Szeged, Moszkvai krt. 9., Hungary*

* *Corresponding author: verebg@mk.u-szeged.hu*

For the elimination of oily pollutants of waters, the most common processes are gravity separation, centrifugation [7], skimming [8], flotation [9], thermal process [10], adsorption [6] and chemical destabilization [2, 5, 7, 10-12]. These traditional methods are sufficiently effective in case of free (or floating) oil ($d_{\text{oil droplets}} > 150 \mu\text{m}$) and in case of coarse dispersions. However, oil in water emulsions (which is characterized in the literature by droplets smaller than $20 \mu\text{m}$) and “dissolved oils” (when droplets are smaller than $5 \mu\text{m}$) require to develop more effective destabilization methods and/or more effective water treatment processes [3, 13-17].

Membrane separation (micro- [15, 17-25] and ultrafiltration [13, 18, 23, 26-29]) can also be efficient for the treatment of these kind of water pollutants, however membrane fouling [10, 30] is a general problem (not only in case of oily contaminants), which inhibit the economic utilization in many cases. Microfilters have relatively higher fluxes compared to ultrafiltration, but the latter results in higher purification efficiency. To reduce fouling, highly hydrophilic membranes [25, 31, 32] can be used (in case oil in water emulsions), or membrane separation can be combined with other methods such as gas injection [33], ozonation [34, 35] or destabilization [5, 36]. In the recent study of M. Matos et al. [5] destabilization/centrifugation/ultrafiltration hybrid process was applied with high efficiency (97.4%) to purify oil in water emulsion, using calcium chloride coagulant and ZrO_2 ceramic ultrafilter (300 kDa) membrane. Their results are very promising, however the utilization of microfilter membranes (in order to achieve relatively higher fluxes) can be more preferable if the destabilization method is effective enough to allow its utilization with similarly high purification efficiency.

In the present study finely dispersed oil ($d_{\text{oil droplets}} < 2 \mu\text{m}$) contaminated water was purified with destabilization, and the effect of pretreatment on membrane microfiltration was investigated.

For the destabilization of the emulsion polyaluminum chloride was used as coagulant. Polyaluminum chlorides are extensively used in water and waste water treatments, which have several beneficial properties in comparison with conventional aluminum chloride such as higher removal efficiency, lower pH sensitivity and lower residual Al^{3+} content [11, 12]. Polyaluminum chlorides contain $\text{Al}_2(\text{OH})_2^{4+}$, $\text{Al}_8(\text{OH})_{20}^{4+}$, $\text{AlO}_4\text{Al}_{12}(\text{OH})_{24}(\text{H}_2\text{O})_{12}^{7+}$ and other species [11, 37]. $\text{AlO}_4\text{Al}_{12}(\text{OH})_{24}(\text{H}_2\text{O})_{12}^{7+}$ (generally referred as Al_{13}) has been reported as the most effective species of polyaluminum chlorides, which has a pre-hydrolyzed structure with high positive charge (Al_{13}^{7+}) making it less sensitive to pH changes [11, 38-40]. Al_{13} can be described by the Keggin structure: The central tetrahedral AlO_4 unit is surrounded by octahedral AlO_6 units. This structure allows the molecule to hydrate and dehydrate without significant structural changes. These Al_{13} units can connect at the peaks and edges of octahedrals creating long chains which contain hydroxyl functional groups and cause high adsorption efficiency resulting in high elimination performance of colloid pollutants.

Since polyethersulfone is one of the most extensively used material to produce nano-, ultra-, and microfilter membranes [4, 23, 24, 41], because of its chemical- and thermal stability, easy processing and environmental endurance [4, 42], therefore in the present study polyethersulfone microfilter was used to eliminate the oily contaminants with and without the destabilization pretreatment. Permeate fluxes, resistances, fouling models and purification efficiencies were investigated in both cases.

RESULTS AND DISCUSSION

Destabilization of finely dispersed oil in water emulsion

In the first step *Bopac* was added into the emulsion in 6 different amounts which resulted in 2, 5, 10, 15, 20 and 40 ppm Al^{3+} content in the total volume. After 30 min sedimentation, the turbidity of the supernatants was measured and the purification efficiencies (**Figure 1**) were calculated from the initial turbidities (155 ± 5).

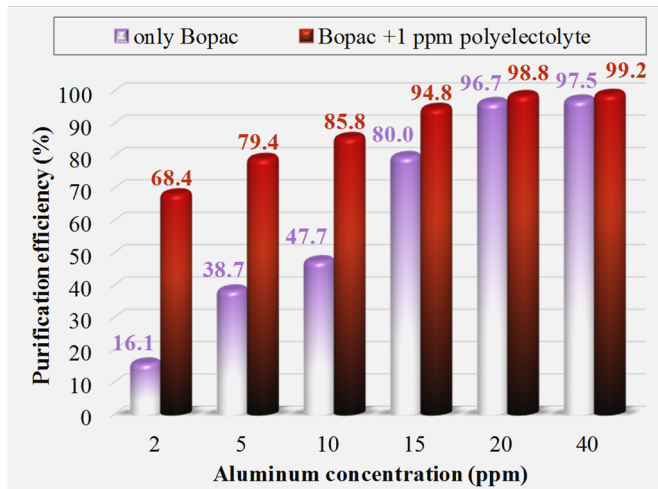


Figure 1. Purification efficiencies (calculated from turbidity values) in case of different *Bopac* coagulant dose (resulted 2, 5, 10, 15, 20 and 40 ppm aluminum content) with and without the addition of 1 ppm anionic polyelectrolyte flocculant.

As it can be seen in **Figure 1** higher coagulant dose resulted in increased purification efficiencies. It should be noted that in case of lower aluminum doses (2, 5 and 10 ppm Al^{3+} content) the created flakes were floating in the treated emulsions because of the very similar density of the flakes to water due to the low

density of original oil droplets (~ 0.73 g/mL). At higher aluminum doses (15, 20, 40 ppm), the flakes were easily sedimented. 20 ppm aluminum concentration resulted in 96.7% purification efficiency, while double dose increased this value up to 97.5%, but this high concentration is not recommended because of the double amount of sediment.

Experiments were also carried out by the further addition of 1 ppm anionic polyelectrolyte to the emulsion as flocculant. In this series similar tendency was observed, however purification efficiencies were higher in all cases compared to the results in the absence of anionic polyelectrolyte (see **Figure 1**). By the utilization of flocculant the produced flakes were much bigger than in the absence of the polyelectrolyte, therefore the flakes sedimented much faster in case of 15, 20 and 40 ppm aluminum doses. At lower aluminum content (2,5 and 10 ppm) the flakes were floating in this case as well. 20 ppm aluminum concentration with the simultaneous utilization of 1 ppm anionic polyelectrolyte resulted in 98.8 % purification efficiency. However, doubled dose of aluminum (40 ppm) resulted in a marginally higher purification efficiency (99.2%) again, but the sediment volume was much higher in this case as well. Based on the achievable purification efficiencies and the sedimentation tendencies (see **Figure 2**), 20 ppm aluminum concentration and the extra addition of 1 ppm anionic polyelectrolyte can be beneficial.

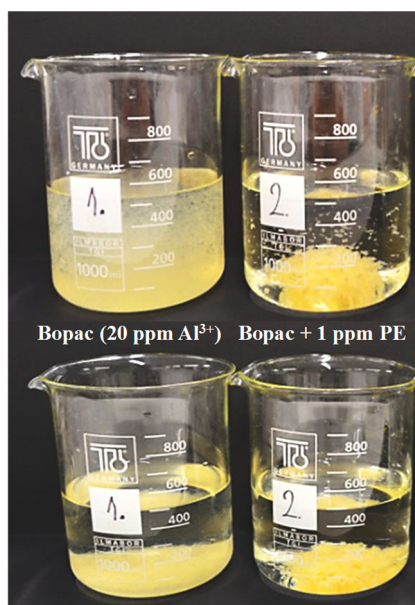


Figure 2. Sedimentation of the destabilized oil in water emulsion by *Bopac* coagulant (20 ppm aluminum content) and by the further addition of 1 ppm anionic polyelectrolyte. Top row: after 30 sec sedimentation; bottom row: after 30 min sedimentation.

Purification efficiencies were determined by measuring COD and extractable oil content as well (over the turbidity) when 20 ppm aluminum was applied with or without the utilization of 1ppm anionic polyelectrolyte. Results are shown in **Figure 3**.

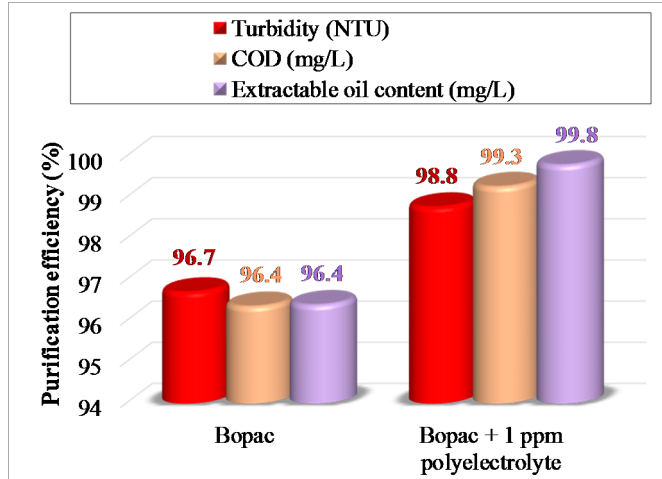


Figure 3. Purification efficiencies - calculated from turbidity, COD value and extractable oil content - in case of 20 ppm aluminum content with and without the addition of 1 ppm anionic polyelectrolyte flocculant.

Without the utilization of polyelectrolyte, the COD and extractable oil content eliminations are slightly smaller (96.4%) than colloid elimination (96.7% - determined by turbidity measurements) because of the small amount of water-soluble organic compounds. When the polyelectrolyte was also used, the determined COD and extractable oil content eliminations were higher (99.3 and 99.8%), which presumably due to the more effective adsorption of water-soluble organic compounds onto the flakes formed by the polyelectrolyte. These results also confirmed the beneficial utilization of 1 ppm anionic polyelectrolyte flocculant.

Additionally, conventional iron(III) chloride and aluminum(III) chloride were also applied as reference coagulants in calculated amounts, to set the Fe^{3+} or Al^{3+} concentration similarly to 20 ppm. Based on turbidity measurements iron(III) chloride resulted in a very low purification efficiency (33%) while aluminum(III) chloride was more efficient (72%), although to a substantially lower degree compared to the efficiency of polyaluminum chloride (96.7%) The outstanding purification efficiency of *Bopac* polyaluminum chloride can be explained

by its pre-hydrolyzed form, the high basicity, and by the Keggin structure, which can result in higher adsorption ability compared to conventional aluminum coagulants.

Membrane microfiltration of finely dispersed oil in water emulsion

Finely dispersed oil in water emulsion was filtered by a polyethersulfone membrane microfilter ($d_{\text{pore}}=0.2 \mu\text{m}$), with and without the destabilization of the emulsion. In case of destabilization pretreatment, *Bopac* (20 ppm aluminum content) and anionic polyelectrolyte (1 ppm) were also used. The measured flux declines are presented in **Figure 4**. It can be seen, that in case of not pretreated oil in water emulsion the flux was rapidly and immensely declining, while in case of pretreated (destabilized) emulsion much higher flux was measured. Therefore, the total filtration time (until the VRR=5 filtration ratio) was only 406 s in case of the destabilized emulsion, while 5493 s in case of not-pretreated emulsion.

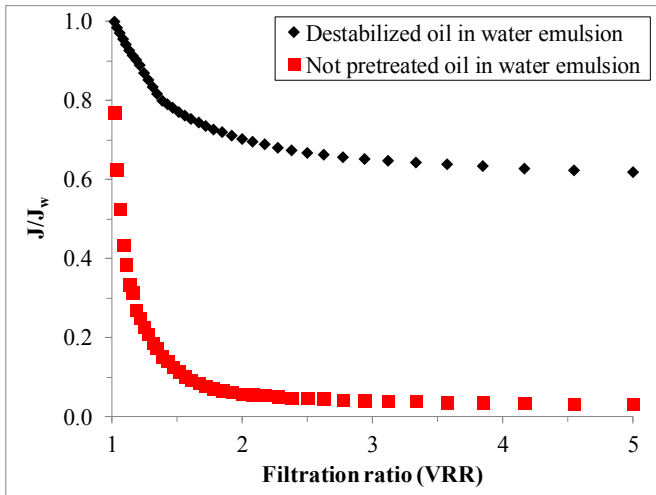


Figure 4. Measured fluxes during membrane microfiltration (PES – $d_{\text{pore}}=0.2 \mu\text{m}$) of oil in water emulsion with and without destabilization pretreatment (destabilization was carried out with *Bopac* – resulting 20 ppm aluminum content – and 1 ppm anionic polyelectrolyte).

Based on the calculations which are described in the “Experimental” section, in the “Resistance-in-series model” chapter, the different resistances were determined in both cases of filtrations. Results are presented in **Figure 5**,

which demonstrates that the total resistance was ~96% lower in case of destabilized oil in water emulsion compared to the flux of not pretreated emulsion. Both irreversible- and reversible membrane resistances were also significantly reduced by the used destabilization pretreatment.

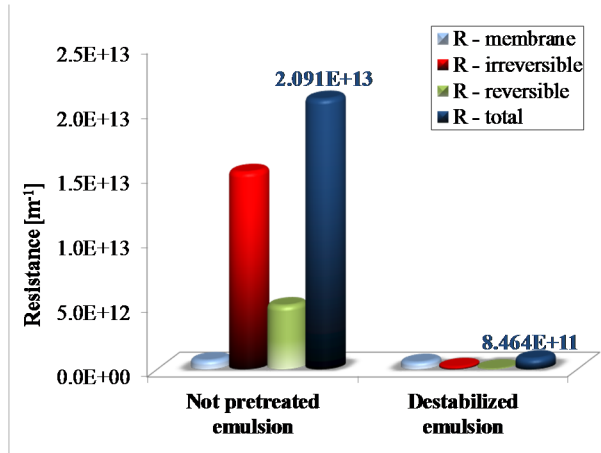


Figure 5. Different resistances in case of not pretreated and destabilized emulsion during the microfiltration.

Purification efficiency was 98% in case of not pretreated emulsion and 99% in case of destabilized emulsion (based on measured COD values), which means that the investigated oil in water emulsion can be effectively purified by membrane microfiltration without any pretreatment, but filtration resistances can be significantly reduced with the described destabilization method.

Additionally, widely used fouling models such as complete pore blocking-, gradual pore blocking-, intermediate filtration- and cake filtration models [38] were fitted onto the measured flux curves and it was found that both with or without the destabilization pretreatment the filtrations can be described mostly by the cake filtration model.

Comparing our results with the recent results of M. Matos et al. [5] (they applied destabilization/ultrafiltration (300 kDa) hybrid process with a 97.4% purification efficiency using calcium chloride coagulant and ZrO₂ ceramic ultrafilter) it can be concluded, that using polyaluminum chloride and anionic polyelectrolyte similarly very high purification efficiency can be achieved. Destabilized emulsion can be filtered with high flux and with high elimination efficiency by a microfilter, therefore the utilization of ultrafiltration is not necessary.

CONCLUSIONS

Bopac polyaluminum chloride successfully destabilized finely dispersed oil in water emulsions ($d_{\text{oil droplets}} < 2 \mu\text{m}$) with high efficiency, without any additional flocculant, due to the high basicity, the pre-hydrolyzed form and the Keggin structure. The efficient doses are not lower than 15 ppm aluminum concentration (in case of 100 ppm oil content) since below this concentration the flakes were floating because of their low density. 20 ppm aluminum concentration resulted in 96.7% purification efficiency, while with the further addition of 1 ppm anionic polyelectrolyte the efficiency increased up to 98.8%, and the sedimentation ability was also significantly increased by the added flocculant.

The investigated finely dispersed oil in water emulsion can be effectively purified by membrane microfiltration without any pretreatment, but both irreversible- and reversible filtration resistances can be significantly reduced with the described destabilization method.

EXPERIMENTAL SECTION

Preparation of finely dispersed oil in water emulsion

Finely dispersed oil in water emulsion ($c_{\text{oil}}=100 \text{ ppm}$; $d_{\text{oil droplets}}=100\text{-}2000 \text{ nm}$) was prepared in two steps using crude oil (from *Algyő, Hungary*, supported by *MOL Zrt.*). Firstly 1 wt.% emulsion was prepared by intensive stirring (35000 rpm), then 5 mL of this emulsion was inoculated into 495 mL of model ground water directly below the transducer of an ultrasonic homogenizer (*Hielscher UP200S*). The duration of homogenization was 10 minutes, maximal amplitude and cycle was applied and the emulsion was thermostated to 25°C.

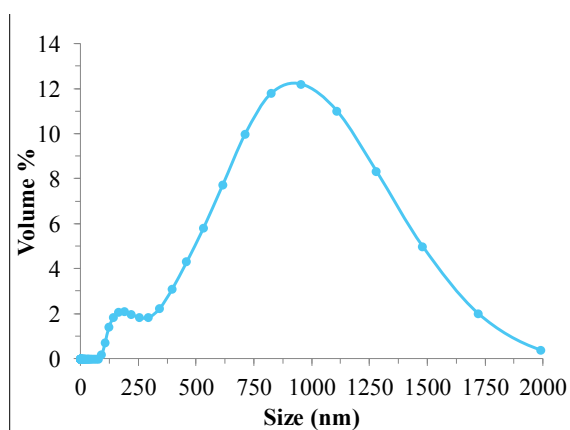


Figure 6. Size distribution of the investigated finely dispersed oil in water emulsion.

The investigated water was a model of real groundwater located in south Hungary, which contained the following salts: 2.26 g/L NaHCO₃; 53.4 mg/L NH₄Cl; 19.1 mg/L CaCl₂; 20.9 mg/L KCl; 93.5 mg/L NaCl; 4.5 mg/L FeCl₃ and 35.1 mg/L MgSO₄ (*Sigma Aldrich*; analytical grade). The size distribution of the oil droplets in the produced emulsion was described by dynamic light scattering using a *Malvern ZetaSizer4* type equipment (**Figure 6**).

Destabilization experiments

Coagulation/flocculation experiments were carried out in a four-backer Jar Test flocculator (*VELP Scientifica*) at room temperature. Coagulants and flocculant were added during intensive stirring (200 rpm); after 30 s homogenization 2 min slow stirring (20 rpm) was applied, then the formed flakes were left to settle for 30 min. As highly efficient coagulant a polyaluminum chloride (named as “*Bopac*”, produced by *Unichem Kft.*- Hungary) was used, while as reference coagulants iron(III) chloride, and aluminum(III) chloride (named as “*Unifloc-C*” and “*Unipac*” respectively; produced by *Unichem Kft.*- Hungary) were used. *Bopac* is an ACH type pre-hydrolyzed polyaluminum chloride which allowed in drinking water production with high basicity (82.0±2%) and with an n_{Al}:n_{Cl}=2.0±0.2 ratio. Enhanced flocculation was carried out by further addition of an anionic polyelectrolyte flocculant (named as “*Unifloc LT 27*”; produced by *Unichem Kft.*- Hungary).

Membrane filtration

Membrane filtration experiments were carried out in a batch-stirred membrane reactor (*Millipore XFUF07601*; produced by *New Logic Research Inc.*) equipped with a hydrophilic polyethersulfone (PES) microfilter membrane (d_{pore}=0.2 μm; filtration area was 0.00332 m²). The applied transmembrane pressure was 0.1 MPa (provided by nitrogen gas). The volume of the treated emulsion was 250 mL and filtration was carried out until 200 mL of permeate was produced (VRR=5).

Determination of purification efficiency

Purification efficiencies were determined by measuring turbidity (*Hach 2100N*) and in some cases chemical oxygen demand (COD) and extractable oil content (TOG/TPH). COD values were measured by the standard potassium dichromate oxidation method using standard test tubes (*Hanna Instruments*) and applying digestions for 120 min at 150°C in a *Lovibond ET 108* type COD digester. The COD values were measured with a *Lovibond COD Vario* type COD photometer. Extractable oil content was measured by a *Wilks InfraCal TOG/TPH* type analyzer, using hexane as extracting solvent.

The purification efficiency (R) was determined as:

$$R = \left(1 - \frac{a}{a_0}\right) \cdot 100\% \quad (1)$$

where a_0 is the turbidity, COD, or TOG/TPH values of the feed while a indicates the values of the permeate.

Resistance-in-series model

The membrane resistance (R_M) was calculated as [43]:

$$R_M = \frac{\Delta p}{J_w \eta_w} \quad [\text{m}^{-1}] \quad (2)$$

where Δp is the transmembrane pressure (Pa), J_w is the water flux of the clean membrane and η_w is the viscosity of the water (Pas).

The irreversible resistance (R_{Irrev}) was determined by re-measuring the water flux on the used membrane after the filtration, followed by a purification step (intensive rinsing with distilled water):

$$R_{Irrev} = \frac{\Delta p}{J_{WA} \eta_w} - R_M \quad [\text{m}^{-1}] \quad (3)$$

where J_{WA} is the water flux after the cleaning procedure.

The reversible resistance (R_{Rev}), caused by not adhered contaminants and concentration polarisation layer can be calculated as:

$$R_{Rev} = \frac{\Delta p}{J_c \eta_{ww}} - R_{Irrev} - R_M \quad [\text{m}^{-1}] \quad (4)$$

where J_c is the flux at the end of the filtration and η_{ww} is the viscosity of wastewater. The total resistance (R_T) can be evaluated from the steady-state flux by using the resistance-in-series model:

$$R_T = R_M + R_{Irrev} + R_{Rev} \quad [\text{m}^{-1}] \quad (5)$$

Fouling mechanisms were described with widely used filtration laws (complete pore blocking, gradual pore blocking, intermediate filtration and cake filtration) [44] to characterize membrane fouling.

ACKNOWLEDGEMENTS

This project was supported by the János Bolyai Research Scholarship of the Hungarian Academy of Sciences. The authors are grateful for the financial support provided by the project Hungarian Science and Research Foundation (NKFI contract number K112096). The authors are also grateful to Unichem Kft. for supporting our work by supplying the coagulant/flocculant materials for this study.

REFERENCES

1. M. Padaki, R. Surya Murali, M.S. Abdullah, N. Misdan, A. Moslehyani, M.A. Kassim, N. Hilal, A.F. Ismail, *Desalination*, **2015**, 357, 197.
2. P. Cañizares, F. Martínez, C. Jiménez, C. Sáez, M.A. Rodrigo, *Journal of Hazardous Materials*, **2008**, 151, 44.
3. M. Gryta, K. Karakulski, A.W. Morawski, *Water Research*, **2001**, 35, 3665.
4. J. Yin, J. Zhou, *Desalination*, **2015**, 365, 46.
5. M. Matos, C.F. García, M.A. Suárez, C. Pazos, J. M. Benito, *Journal of the Taiwan Institute of Chemical Engineers*, **2016**, 59, 295.
6. Y. Hu, Y. Zhu, H. Wang, C. Wang, H. Li, X. Zhang, R. Yuan, Y. Zhao, *Chemical Engineering Journal*, **2017**, 322, 157.
7. J. Benito, G. Ríos, E. Ortea, E. Fernández, A. Cambiella, C. Pazos, J. Coca, *Desalination*, **2002**, 147, 5.
8. A.B. Nordvik, J.L. Simmons, K. R. Bitting, A. Lewis, T. Strøm-Kristiansen, *Spill Science & Technology Bulletin*, **1996**, 3, 107.
9. A.A. Al-Shamrani, A. James, H. Xiao, *Water Research*, **2002**, 36, 1503.
10. R. Zolfaghari, A. Fakhru'l-Razi, L.C. Abdullah, S.S.E.H. Elnashaie, A. Pendashteh, *Separation and Purification Technology*, **2016**, 170, 377.
11. C. Wang, A. Alpatova, K.N. McPhedran, M. Gamal El-Din, *Journal of Environmental Management*, **2015**, 160, 254.
12. E. Bazrafshan, F.K. Mostafapoor, M.M. Soor, A.H. Mahvi, *Fresenius Environmental Bulletin*, **2012**, 21, 2694.
13. B. Chakrabarty, A.K. Ghoshal, M.K. Purkait, *Journal of Membrane Science*, **2008**, 325, 427.
14. R.S. Souza, P.S.S. Porto, A.M.A. Pintor, G. Ruphuy, M.F. Costa, R.A.R. Boaventura, V.J.P. Vilar, *Chemical Engineering Journal*, **2016**, 285, 709.
15. M. Abbasi, A. Salahi, M. Mirfendereski, T. Mohammadi, A. Pak, *Desalination*, **2010**, 252, 113.
16. M. Cheryan, N. Rajagopalan, *Journal of Membrane Science*, **1998**, 151, 1328.
17. C. Song, T. Wang, Y. Pan, J. Qiu, *Separation and Purification Technology*, **2006**, 51, 80.
18. A. Salahi, A. Gheshlaghi, T. Mohammadi, S.S. Madaeni, *Desalination*, **2010**, 262, 235.
19. H. Shokrkar, A. Salahi, N. Kasiri, T. Mohammadi, *Chemical Engineering Research and Design*, **2012**, 90, 846.
20. F.L. Hua, Y.F. Tsang, Y.J. Wang, S.Y. Chan, H. Chua, S.N. Sin, *Chemical Engineering Journal*, **2007**, 128, 169.
21. H. Ohya, J.J. Kim, A. Chinen, M. Aihara, S.I. Semenova, Y. Negishi, O. Mori, M. Yasuda, *Journal of Membrane Science*, **1998**, 145, 1.
22. S.R.H. Abadi, M.R. Sebzari, M. Hemati, F. Rekabdar, T. Mohammadi, *Desalination*, **2011**, 265, 222.

23. K. Masoudnia, A. Raisi, A. Aroujalian, M. Fathizadeh, *Desalination and Water Treatment*, **2014**, 55, 901.
24. Z.L. Kiss, L. Kocsis, G. Keszthelyi-Szabó, C. Hodúr, Z. László, *Desalination and Water Treatment*, **2014**, 55, 3662.
25. X. Hu, Y. Yu, J. Zhou, Y. Wang, J. Liang, X. Zhang, Q. Chang, L. Song, *Journal of Membrane Science*, **2015**, 476, 200.
26. J. Lindau, A.S. Jijnsson, *Journal of Membrane Science*, **1994.**, 87, 71.
27. B. Chakrabarty, A.K. Ghoshal, M.K. Purkait, *Chemical Engineering Journal*, **2010**, 165, 447.
28. N. Moulai-Mostefa, O. Akoum, M. Nedjihoui, L. Ding, M.Y. Jaffrin, *Desalination*, **2007**, 206, 494.
29. X.S. Yi, S.L. Yu, W. X. Shi, N. Sun, L.M. Jin, S. Wang, B. Zhang, C. Ma, L.P. Sun, *Desalination*, **2011**, 281, 179.
30. L.Y. Susan, S. Ismail, B.S. Ooi, H. Mustapa, *Journal of Water Process Engineering*, **2017**, 15, 55.
31. J. Zhang, Q. Xue, X. Pan, Y. Jin, W. Lu, D. Ding, Q. Guo, *Chemical Engineering Journal*, **2017**, 307, 643.
32. Y.Z. Song, X. Kong, X. Yin, Y. Zhang, C.C. Sun, J.J. Yuan, B. Zhu, L.P. Zhu, *Colloids and Surfaces A: Physicochemical and Engineering Aspects*, **2017**, 522, 585.
33. M.J. Um, S.H. Yoon, C.H. Lee, K.Y. Chung, J.J. Kim, *Water Research*, **2001**, 35, 4095.
34. Y.G. Park, *Desalination*, **2002**, 147, 43.
35. S.G. Lehman, L. Liu, *Water Research*, **2009**, 43, 2020.
36. D. Metcalfe, P. Jarvis, C. Rockey, S. Judd, *Separation and Purification Technology*, **2016**, 163, 173.
37. Z. Yang, B. Gao, B. Cao, W. Xu, Q. Yue, *Separation and Purification Technology*, **2011**, 80, 59.
38. B.Y. Gao, Y.B. Chu, Q.Y. Yue, B.J. Wang, S.G. Wang, *Journal of Environmental Management*, **2005**, 76, 143.
39. C. Hu, H. Liu, J. Qu, *Colloids and Surfaces A: Physicochemical and Engineering Aspects*, **2005**, 260, 109.
40. C. Hu, H. Liu, J. Qu, D. Wang, J. Ru, *Environmental Science and Technology*, **2006**, 40, 325.
41. W. Chen, J. Peng, Y. Su, L. Zheng, L. Wang, Z. Jiang, *Separation and Purification Technology*, **2009**, 66, 591.
42. B. Van der Bruggen, *Journal of Applied Polymer Science*, **2009**, 114, 630.
43. S. Kertész, Z. László, E. Forgács, G. Szabó, C. Hodúr, *Desalination and Water Treatment*, **2012**, 35, 195.
44. B. Hu, K. Scott, *Chemical Engineering Journal*, **2008**, 136, 210.

CORROSION AND MECHANICAL PROPERTIES AND MICROSTRUCTURE OF CEMENT MORTAR CONTAINING CALCIUM SULPHATE WASTE

JULIETA DANIELA CHELARU^a, FIRUTA GOGA^{ax}, MARIA GOREA^a

ABSTRACT. The study presents the preliminary research on possibility to use the calcium sulphate waste (CSW) as replacing of sand in the cement mortar. The waste was chemically and mineralogical characterized. Four compositions of mortar without and with 7.5 %, 18.78 % and 37.50 % waste were prepared. The X-ray powder diffraction evidenced the main mineral compounds in mortar as hydration products of calcium silicates (CSH) with a low index of crystallinity and different oxide ratio $\text{CaO}:\text{SiO}_2:\text{H}_2\text{O}$, quartz, calcite, anhydrite and gypsum. Optical microscopy reveals that the samples contains aggregates as quartz, muscovite and rocks, especially of metamorphic origin (quartzite, micaschists, and quartzitic schists) embedded in a fine matrix resulted by hydration reactions of cement compounds or reactions of waste components with other compounds from system. The corrosion properties of mortar, at different **CSW** concentrations, on rebar, were investigated by polarization measurements and electrochemical impedance spectroscopy. The results revealed that at 7.5 % addition of waste anticorrosion properties are improved. As expected, the mechanical resistances (compressive and flexural strenght) decrease with increasing of waste in mortar composition.

Keywords: *waste materials, corrosion, reinforced mortar steel, electrochemical techniques, mechanical properties*

INTRODUCTION

In last years, the increasing quantities of waste materials has required finding of practical solutions for their recycling. There are many studies focused on using different wastes in oxide materials compositions,

^a Department of Chemical Engineering, "Babes-Bolyai" University, 11 Arany Janos St., 400028 Cluj-Napoca, Romania

* Corresponding author: firutagoga@yahoo.com

especially in cement concrete. In these cases, the wastes can replace the sand or aggregates in different proportions. This fact involves the reducing of energy and natural resources and obtaining of low cost final products.

In this way, there are studies on the mechanical properties or the corrosion properties of the concrete made with steel slag furnace [1], fly-ash [2, 3], plastics, crushed seashells [4], lime rich sludge, fine kaolinite sand [5], waste glass [3, 6], glass and polypropylene fibers [7]. Many studies conducted in order to examine the possibility of using plastic and glass powders in civil engineering and construction were reported [8]. The use of glass waste in road construction, asphalt and others building materials was experimented [9]. A lot of researches are focused on using agriculture wastes in concrete compositions. For examples in [10] the durability properties of sustainable concrete incorporating high volume of palm oil waste were investigated.

On the other hand a major importance is accorded to the corrosion process in reinforced concrete, especially because its early identification is difficult. Many researches are focused on techniques for evaluation of the corrosion process in reinforced concrete mostly electrochemical techniques [11 - 13].

In this context, this paper reports the corrosion and mechanical properties correlated with chemical and mineralogical composition of waste and cement mortar which contain different percentage of calcium sulphate waste (**CSW**). The corrosion properties were studied in normal atmospheric conditions on steel embedded in mortar mixtures using electrochemical techniques (potentiodynamic polarization measurements and electrochemical impedance spectroscopy).

RESULTS AND DISCUSSION

Characterization of raw materials

In the experiments for obtaining the mortar cement mixtures the usual EN 197-1- CEM II/A-LL 42,5 R Portland cement was used. The usual sand and the calcium sulphate waste were incorporated as mortar aggregates. The calcium sulphate waste is resulted by thermal treatment at 600 °C of a mixture of 50 % sand, 25 % fired clay and 25 % gypsum during the casting process of the art statues.

Chemical composition of aggregates

The chemical composition of sand and waste obtained by traditional wet chemistry analyses are presented in Table 1.

Table 1. Chemical composition of sand and calcium sulphate waste

Oxide / sample [%]	SiO ₂	TiO ₂	Al ₂ O ₃	Fe ₂ O ₃	CaO	MgO	Na ₂ O	K ₂ O	LOI	Total
Sand	93.39	0.20	4.15	0.29	0.43	0.51	0.16	0.32	0.55	100
Waste	61.04	0.71	11.16	0.56	23.41	0.20	0.20	0.60	2.12	100

The usually sand for mortar contains a high amount of silicon oxides besides of small quantities of aluminum oxide respectively earth and alkaline oxides.

The calcium sulphate waste is mainly composed of silicon dioxide and aluminum oxide from sand and fired clay and calcium oxide from gypsum. The minor oxides are originating from impurities presented in clay.

Mineralogical composition of calcium sulphate waste

The mineral compounds of waste influence the hydration reactions of the cement components and/or react with other oxides from mixture forming new reaction products. The resulting compounds can be an inert/reactive material, a material with/without hydraulic properties and can alter the final characteristics of cement mortar. The mineralogical composition of the waste used in experiments was investigated by X-ray powder diffraction and the pattern is illustrated in Figure 1.

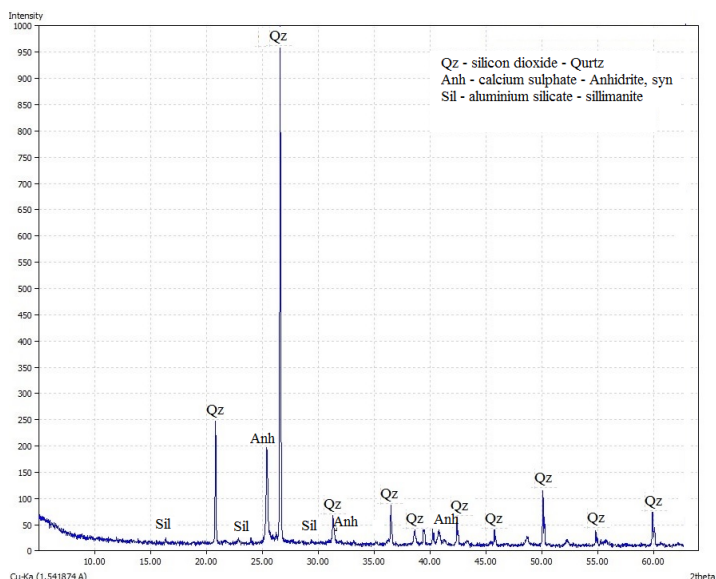


Figure 1. X-ray powder diffraction pattern of calcium sulphate waste. Qz – quartz, Anh – anhydrite, Sil – sillimanite.

The X-ray powder diffraction evidence the main mineral compounds in calcium sulphate waste as quartz, calcium sulphate anhydrous, and silimanite.

Characterization of mortar samples

Investigation of the corrosion process in reinforced mortar

Potentiodynamic polarization measurements

Before the corrosion tests, the samples were cured for 30 days in humidity conditions. In order to evaluate behaviour of rebar in mortar with different **CSW** concentrations, the experiments were started with the open circuit potential (OCP) measurements for a period of 1 hour.

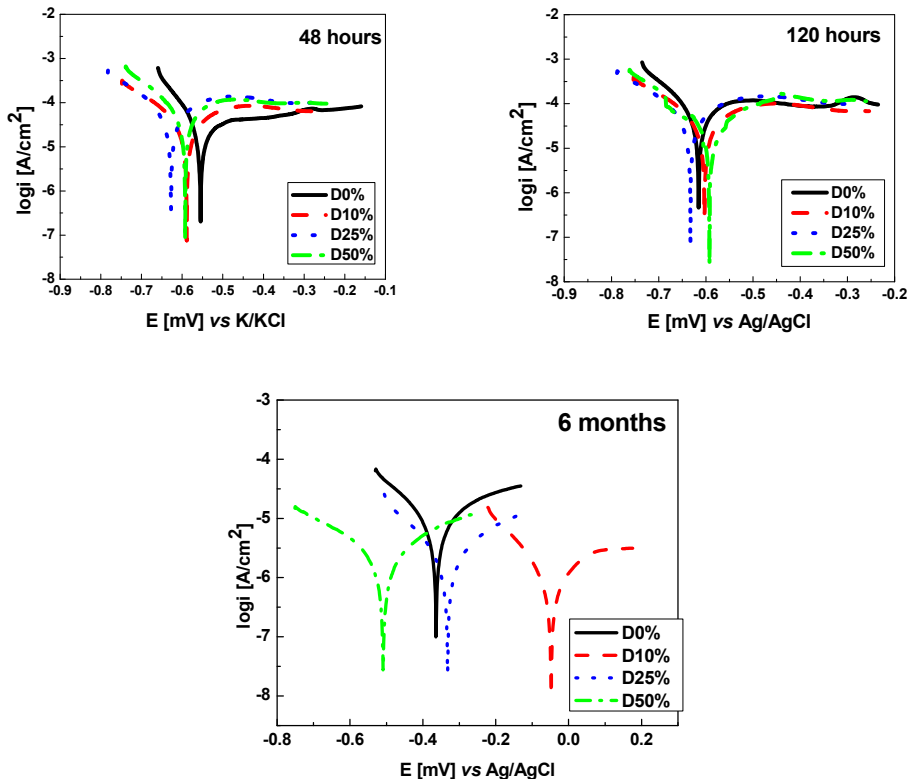


Figure 2. Polarization curves (± 200 mV vs. ocp) for the studied samples at different concentrations of **CSW**, potential scan rate, 10 mV / min.

In order to determine the corrosion process parameters (i_{corr} - corrosion current density, E_{corr} – potential corrosion) polarization curves in the potential range of ± 200 mV vs. OCP were realised (Figure 2).

To determine the polarization resistance values, the linear polarization curves were recorded, in the potential domain of ± 20 mV vs. OCP. The results obtained by Tafel interpretation and the polarization resistance values (R_p), calculated as the inverse of the slope of each curve in case of all **CSW** concentrations, are shown in Table 2.

Table 2. Corrosion process parameters for the experimented samples

	Time	i_{corr} [$\mu\text{A}/\text{cm}^2$]	E_{corr} [mV vs K/KCl]	R_p [$\text{k}\Omega\text{cm}^2$]
D₀	48 [h]	0.288	-554	0.79
	120 [h]	0.526	-615	0.50
	6 months	7.924	-364	3.23
D₁₀	48 [h]	0,309	-589	1.56
	120 [h]	0,371	-605	0.87
	6 months	1.315	-43	33.64
D₂₅	48 [h]	0,479	627	0.52
	120 [h]	0,304	-633	0.48
	6 months	2.082	-502	12.53
D₅₀	48 [h]	0,493	-595	0.52
	120 [h]	0,275	-585	0.51
	6 months	1.891	-508	15.83

Analyzing the Table 2 data, it can observe that in the first two cases there are no visible differences between samples without and with different percentage of **CSW**. In case of corrosions tests after 6 months, it can see an increase of the corrosion current density values for all investigated samples. Though, it can observe that the best result was noticed at 7.5 % **CSW**. This fact is suggested by the high value of the polarization resistance ($R_p=33.64$ [$\text{k}\Omega\text{cm}^2$]) and the low value of the corrosion current density ($i_{corr}= 1.315$ [$\mu\text{A}/\text{cm}^2$]). Probably a small amount of **CSW** (7.5 %) in the mortar composition leads to the formation of a protective layer on the rebar.

Electrochemical impedance spectroscopy

The Nyquist diagrams obtained for the all samples, after 6 months (the samples were maintained in this time in humidity conditions) are presented in Figure 3b.

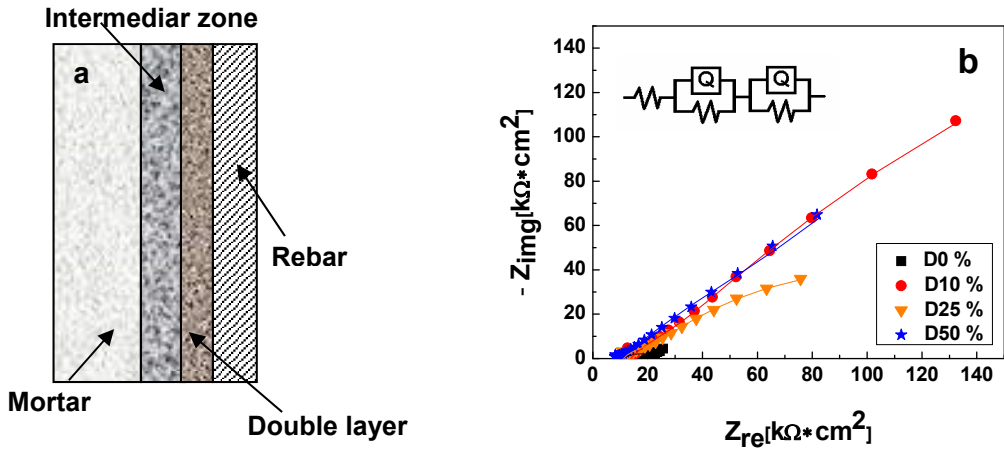


Figure 3. a) Schematic representation of the mortar / rebar interface; b) Nyquist impedance diagrams of samples with 0 %, 7.5 %, 18.78 %, respectively 37.50 % **CSW**; the lines represent fitted data.

Table 3. Electrochemical parameters for studied samples

<i>C</i> [mM]	<i>R_m</i> [kΩcm ²]	<i>n_f</i>	<i>R_f</i> [kΩcm ²]	<i>C_f</i> [μF/cm ²]	<i>n_d</i>	<i>R_t</i> [kΩcm ²]	<i>C_d</i> [μF/cm ²]	<i>R_p[*]</i> [kΩcm ²]
D₀	10.59	0.67	24.22	59.11	0.37	13.02	2.33	24.22
D₁₀	13.86	0.63	9.56	12.14	0.58	887.5	301	897.06
D₂₅	11.22	0.64	7.14	4.26	0.54	175.4	271.6	182.54
D₅₀	11.85	0.69	290	13.98	0.76	13.66	1.47	303.66

$$R_p^* = R_f + R_{ct}$$

A schematic representation of the rebar / mortar interface is shown in Figure 3a. The existence of the two zones, the intermediar zone, and the zone with charge transfer and the double layer capacitance at rebar interface are assumed. Based on these results for all samples the experimental impedance spectra were analyzed by fitting to a R((QR)(QR)) equivalent electrical circuit (Figure 3b). This circuit was used in many studies involving concrete corrosion [11-13].

The equivalent electrical circuit from Figure 3b is composed of *R_m* - the mortar resistance, *Q_f* - the constant phase element (CPE) of the film, *R_f* - the rust layer film, *Q_d* - the constant phase element (CPE) of the electric double layer and *R_t* - the charge transfer resistance at the rebar interface, *n_d*, *n_f* - coefficients representing the depressed characteristic of the capacitive

loops in the *Nyquist* diagram. Using the equation $C = (R^{1-n}Q)^{1/n}$ the values of C_d and C_f were calculated. After the fitting experimental impedance spectra the results are presented in Table 3. The quality of fitting procedure was evaluated by the chi squared (χ^2) values, which were of order 10^{-3} .

In case of a redox process, the value of the polarization resistance ($R_p = R_f + R_t$) can be correlated with the corrosion rate. Therefore analyzing the dates from Table 3 it can be seen that the polarization resistance is higher in case of 7.5 % **CSW** ($R_p = 897.06$ [$k\Omega cm^2$]) than the other samples. The results obtained from polarization curves are confirmed.

Macroscopic aspect of the studied samples

The all mortar samples were prepared and cured as a standard cement mortar. After 28 days, the samples were submitted to the corrosion investigation. The aspect of mortar samples with working electrodes after corrosion test is presented in Figure 4.

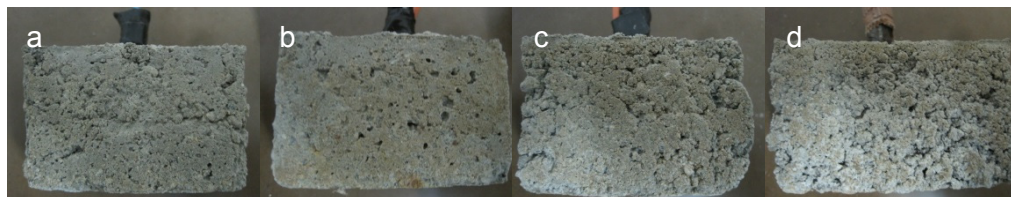


Figure 4. Aspect of samples with working electrodes (steel rebar) in mortar at different percentage of $CaSO_4$ waste: a) 0 %, b) 7.5 %, c) 18.78 %, d) 37.50 %

The pores with different sizes and shape, rounded and elongated are observed. A light yellowish red shade appears on the surface of mortar samples is attributed to the iron oxides and hydroxides present in cement mortar composition. Moreover these oxi-hydroxides can migrated from the corrosion products layer formed on the steel rebar.

Optical microscopy

The optical microscopy in polarized light performed on thin section slices obtained from studied cement mortar allowed to identify and evidence some textural aspects of samples.

From structural point of view, the samples consist of relatively small aggregates (grain sizes ranged between 0-4 mm) embedded in a fine matrix resulted by hydration reactions of cement compounds or reactions of waste components with other compounds from system.

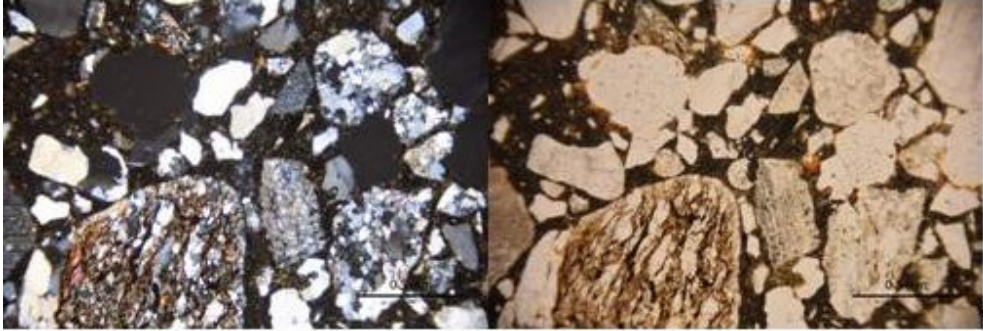


Figure 6. Textural aspects of D0 samples showing rounded aggregates consisting of quartz, muscovite, quartzite, micaschists into an isotropic matrix. (Left N+, right NII)



Figure 7. Textural aspects of D10 samples, showing a very fine crystallized matrix having rounded pores infilled with iron hydroxides. (Left N+, right NII)

The aggregates are mainly composed from sand with complex composition consisting of fragments of minerals (quartz, muscovite, etc.) and rocks, especially of metamorphic origin (quartzite, micaschists, and quartzitic schists) (Figures 6 - 9). Some fragments of rocks from aggregate (Figures 6,7) show different degree of feldspar transformation into clay minerals. As secondary minerals, iron hydroxides are also present.

Generally, the matrix is very fine grained and dominantly consists of calcium silicate hydrates, calcite, and iron hydroxides. Gypsum and anhydrite are very small in size and difficult to be identified into the thin section. In the matrix are also developed spherical pores, sometime infilled with iron hydroxides.

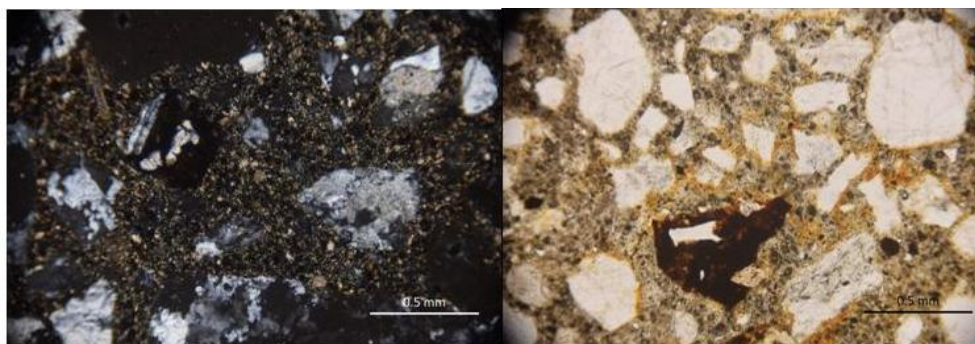


Figure 8. Textural aspects of D25 samples with fine calcite crystals in the matrix (left, N+). Iron hydroxides as irregular grain as well as developed as thin rim on the surface of the aggregate (right NII)

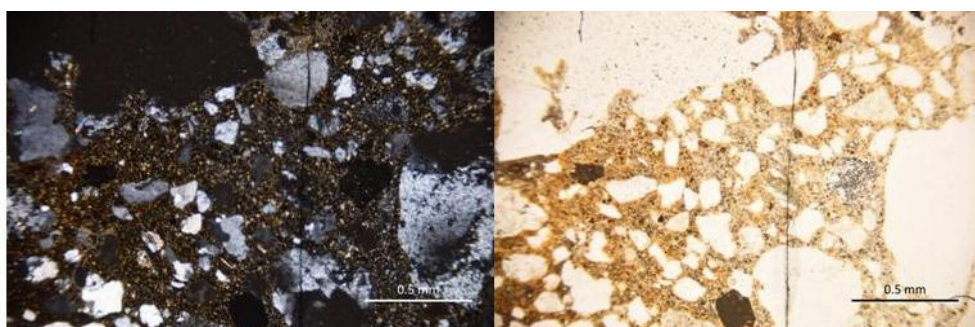


Figure 9. Textural aspect of D50 samples, with fine crystallized calcite in the matrix which is uniformly impregnated with iron hydroxides of brown color (left N+, right NII)

Mineralogical composition of studied mortars

X-ray powder diffraction patterns were realized on mixtures of cement mortar without and with calcium sulphate waste replacing the sand in various percent, conform to Table 4.

The samples tested of corrosion attack were milled till microns size of grains and the powders were investigated by X-ray powder diffraction. The XRPD patterns of the experimented samples are presented in Figure 5.

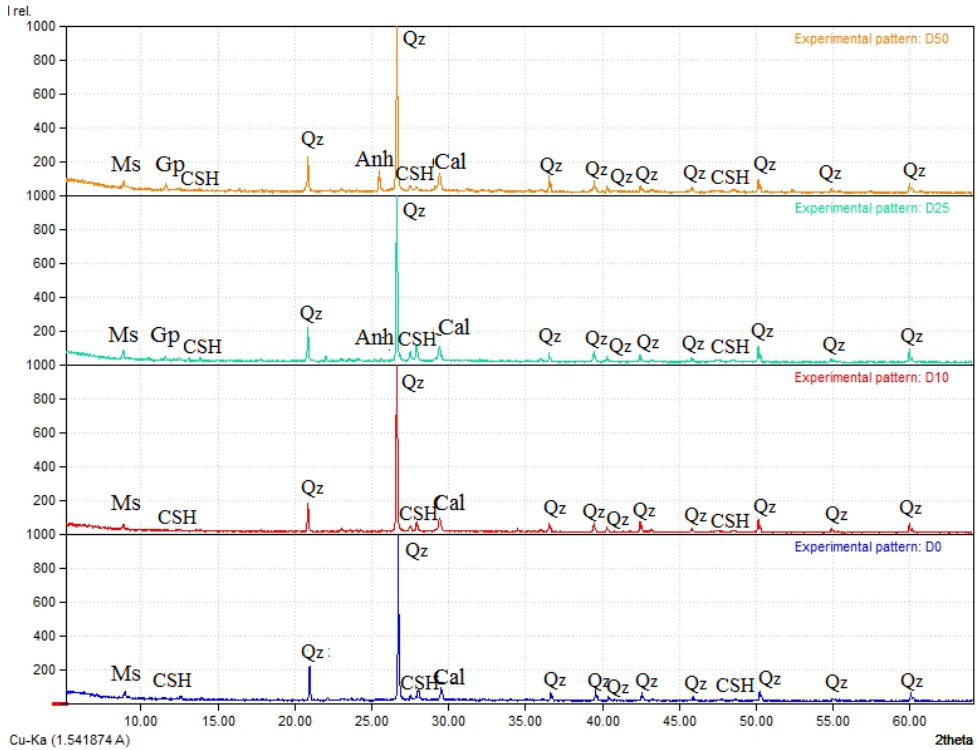


Figure 5. X-ray powder diffraction patterns of experimented samples. Qz – quartz, Anh – anhydrite, Ms – muscovite, Gp – gypsum, Cal – calcite, CSH – calcium silicate hydrate.

The X-ray powder diffraction reveals the mineral compounds in all experimented mortar samples. In the etalon sample D0 it was identified quartz and muscovite provided mainly from sand, calcite and hydration products of calcium silicates (CSH) with a low index of crystallinity and different ratio $\text{CaO}:\text{SiO}_2:\text{H}_2\text{O}$. Calcium aluminates, calcium aluminoferrites and ettringite are in small quantities and difficult to be identified. In sample D25 and D50 with a high content of calcium sulphate waste the specific peaks of anhydrite and gypsum are present. These can explain due to the present of anhydrite in waste composition. During the curing and corrosion tests, in solution, the anhydrite is partially solubilized and the gypsum is formed.

The mechanical properties of experimented samples

Compressive strength of mortars

The compressive strength of parallelepiped specimens (40x40x160 mm) with different percent of calcium sulphate waste (CSW) was tested at 14, 28 and 90 days. The results are shown in Figure 10. It can see that the compressive strength as expected decreases with the increase of CSW at all term of testing. The lowest value of strength is obtained for sample D50. The closest value of resistance compared with the etalon is for D10 sample.

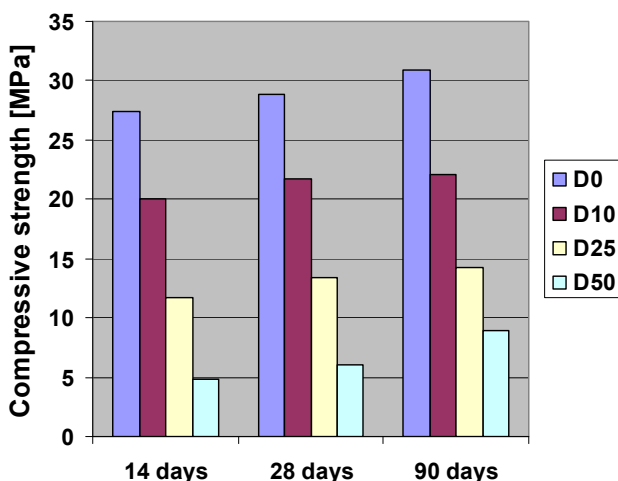


Figure 10. Compressive strength of the studied samples

Flexural strength of mortars

The flexural strength for all mortar compositions is shown in Figure 11. As expected, the values of the flexural strength have a similar behaviour as in compressive strength case. The flexural strength values decrease with increasing of calcium sulphate waste content in mortar composition. The D10 composition can be considered appropriate for use in some applications (lower mechanical resistance but higher corrosion resistance).

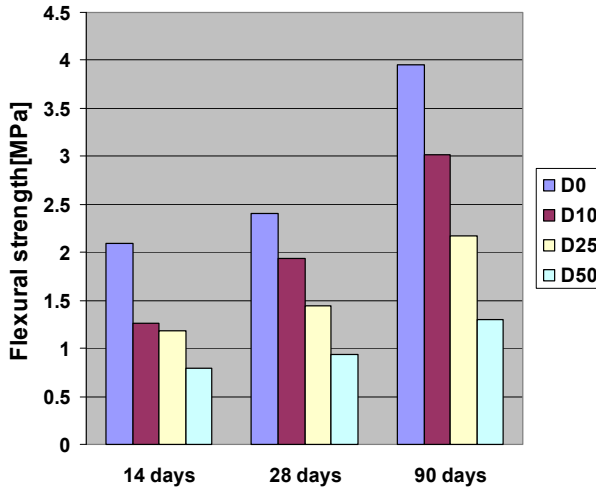


Figure 11. Flexural strength of the studied samples

CONCLUSIONS

In this study, waste materials provided from art manufacturing were used as an aggregate into cement mortar. The chemical composition of waste reveals a high content of CaO besides the SiO₂ and Al₂O₃. The main mineral compounds evidenced by X-ray powder diffraction are quartz, calcium sulphate anhydrous, and silimanite. In the cement mortar, hydration products of calcium silicates (CSH) with a low index of crystallinity and different oxide ratio CaO:SiO₂:H₂O and calcite are identified. The anhidrite and gypsum resulted from anhidrite solubilization are present in higher quantities in D25 and D50 samples than D10. Their presence drastically decreases the mechanical resistance of these samples, more compressive strength. From textural point of view, the samples consist of aggregates with grain sizes ranged between 0-4 mm (quartz, muscovite) and rocks, especially of metamorphic origin (quartzite, micaschists, and quartzitic schists) embedded in a fine matrix resulted by hydration reactions of cement compounds or reactions of waste components with other compounds from system.

Based on the electrochemical investigations (polarization and impedance measurements) it can be concluded that, in case of addition 7.5 % **CSW** in the mortar composition, the anticorrosion properties are improved.

The corrosion behavior of the rebar in mortar can be simulated with a R((QR)(QR)) electric circuit.

EXPERIMENTAL

The experimental mortar compositions contain as raw materials, cement, sand and calcium sulphate waste, table 4. The cement proportion was maintained in all the tested compositions (25 % wt). The D0 sample is the etalon mortar which does not contain waste and in the next three compositions (D10, D25 and D50) a part of sand was replaced by calcium sulphate waste (7.5, 18.78 and 37.50 %wt). As a result, the calcium sulphate in D10 composition is about 1.76 %, in D25 about 4.41 % and in D50 about 8.83 %.

Table 4. Composition of studied samples

Sample	Cement [%]	Sand [%]	Calcium sulphate waste [%]
D ₀	25	75	-
D ₁₀	25	67.5	7.50
D ₂₅	25	56.22	18.78
D ₅₀	25	37.50	37.50

The mortar samples were prepared in a laboratory cement mixer. The sand and waste in the quantity according to the recipe were added and homogenised ~30 seconds. Then the cement and water were added. The mixing continues for another 90 seconds. The mixer is stopped for 90 seconds and then it is restarted for 2 minutes. The final mixture is poured into metallic moulds (40x40x1600mm) for mechanical tests. After 24 h the mortar samples are released from the moulds and preserved in wet environment at 20 °C for 14 days, 28 days or 90 days.

The mechanical characteristics (compressive and flexural strength) are investigated after these intervals on hydraulic press CONTROLS 50-C66V2 in accordance with Romanian standard SR EN 196-1.

The electrochemical characterization was performed by a PC – controlled electrochemical analyzer PAR 2273 (Princeton Applied Research, SUA) using an electrochemical cell (Figure 12) that contains three electrodes: platinum counter electrode, a reference electrode a K / KCl and as working electrode a steel rebar, with an exposed area of 9.30 cm². For electrical contact, metal wires were attached.

The polarization curves were recorded in a potential range of ± 20 mV (for R_p determination) and of ± 200 mV vs. the value of the open circuit potential (for Tafel interpretation), with a scan rate of 10 mV / min. OCP was measured during 1 hour.

The impedance spectra were acquired in the frequency range 10 kHz to 10 mHz at 10 points / decade with an AC voltage amplitude of ± 10 mV, after the open circuit potential was carried out for 1 hour. The data were interpreted on the basis of equivalent electrical circuits, using the ZSimpWin V3.21 software for fitting the experimental data.

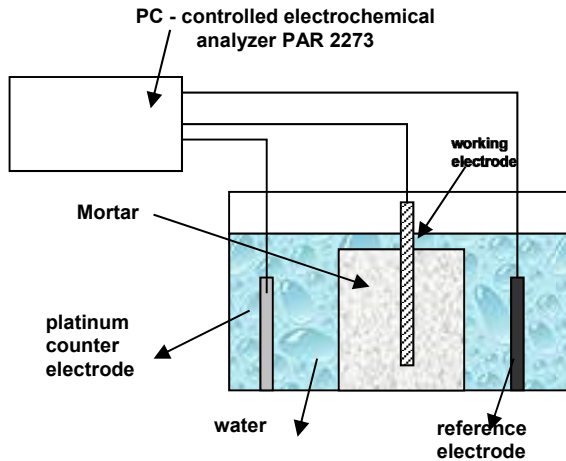


Figure 12. Electrochemical cell used for performing electrochemical measurements

Before of the electrochemical tests, the samples were maintained in water for 48 hours for the hydration of the mortar, in order to ensure conductivity between the working electrodes, reference electrode and counter electrode.

REFERENCES

1. S. Miyazawa, *Cem. Soc. Concr. Technol.*, **2011**, 64, 244 – 250.
2. E.J. Ruíz, J.R. Cortes, W.A. Aperador, *International Journal of Chemical, Molecular, Nuclear, Materials and Metallurgical Engineering*, **2015**, Vol.9, No.3.
3. S.C. Kou, F. Xing, *Advances in Materials Science and Engineering*, Volume **2012**, Article ID 263243, <http://dx.doi.org/10.1155/2012/263243>
4. D.H. Nguyen, M. Boutouil, N. Sebaibi, F. Baraud, L. Leleyter, *Construction and Building Materials*, **2017**, 135, 137 - 150.
5. S.A. Abo-El-Enein, F.S. Hashem, M.S. Amin, D.M. Sayed, *Construction and Building Materials*, **2016**, 126, 983 - 990.

6. T.S. Serniabat, M.N.N. Khan, M.F.M. Zain, *International Journal of Civil, Environmental, Structural, Construction and Architectural Engineering*, **2014**, Vol.8, No.10.
7. H. Fathi, T. Lameie, M. Maleki, R. Yazdani, *Construction and Building Materials*, **2017**, 133, 443 - 449.
8. B. Chanbane, G.A. Sholar, J.A. Musselman, G.C. Page, Ten-year performance evaluation of asphalt–rubber surface mixes. Transportation Research Record No. 1681, Transportation Research, Washington, DC, **1999**, pp. 10 - 18.
9. J., Rindl, Recycling Manager, report by Recycling manager, Dane Country, Department of Public Works, Madison, USA, **1998**.
10. M.M. Ul Islam, K.H. Mo, U.J. Alengaram, M.Z. Jumaat, *Journal of Cleaner Production*, **2016**, 137, 167 - 177.
11. F. Cao, J. Wei, J. Dong, W. Ke, *Corrosion Science*, Article in press, doi.org/10.1016/j.corsci.2015.08.020.
12. D.V. Ribeiro, J.C.C. Abrantes, *Construction and Building Materials*, **2016**, 111, 98 - 104
13. N.M. Ahmed, M.G. Mohamed, M.R. Mabrouk, A.A. ELShami, *Construction and Building Materials*, **2015**, 98, 388 - 396.

DFT STUDY OF THE TUBULAR SIZE EFFECTS ON THE PROPERTIES OF ZIGZAG BORON NITRIDE NANOTUBES

FATEMEH SHEKHOLIA LAVASANI^a, ABOLGHASEM SHAMELI^{b*},
EBRAHIM BALALI^a

ABSTRACT. Density functional theory (DFT) studies were performed on representative zigzag models of boron nitride nanotubes (BNNTs) with different structural sizes. To achieve minimized-energy structures and their properties, first, optimization calculations were performed at the B3LYP/6-311G* theoretical level for all models. Subsequently, density of states (DOS) plots, nuclear magnetic resonance (NMR) spectroscopy chemical shielding, natural bonding orbital (NBO) and nuclear quadrupole resonance (NQR) spectroscopy parameters were calculated. The results indicated that the values of energy gap, polarity and electrical charge detect the effects of structural growth in diameter and length.

Keywords: *Boron nitride; Nanotube; Density functional theory; Tubular size*

INTRODUCTION

Boron nitride nanotubes (BNNTs) are among those nanostructures which are structurally analogues to carbon nanotubes (CNTs) but they show different properties such as distinct electronic behavior [1-4]. Contrary to CNTs, BNNTs are always wide gap semiconductors with the energy gap (E_g) in the range of 4.5 to 4.9 eV, independently of tubular chirality, diameter and number of walls. In addition, BNNTs also have high degree of radial flexibility and high Young modulus, excellent mechanical properties, high thermal conductivity, and high oxidation resistance [5-8].

^a Department of Chemistry, Pharmaceutical Sciences Branch, Islamic Azad University, Tehran, Iran.

^b Department of Chemistry, Faculty of Science, Omidyeh Branch, Islamic Azad University, Omidyeh, Iran.

* Corresponding author: Shameli678@gmail.com

In this work, properties of (n,0) zigzag BNNTs (n=4-7) with various lengths were investigated based on density functional theory (DFT) calculations. To this aim, the optimized geometries, density of states (DOS), nuclear magnetic resonance (NMR) chemical shielding, natural bonding orbital (NBO) and nuclear quadrupole resonance (NQR) parameters were calculated at the B3LYP/6-311G* level of DFT using the Gaussian 03 package.

RESULTS AND DISCUSSION

First, the model structures of (4,0), (5,0), (6,0) and (7,0) BNNTs with various tubular lengths were optimized to obtain minimized-energy structures. Based on the optimizations, bond lengths, bond angles, energies, dipole moments, the highest occupied and the lowest unoccupied molecular orbitals (HOMO and LUMO) were evaluated (Tables 1-3).

Table 1. Optimized bond length of BNNTs (4,0), (5,0), (6,0), (7,0)

BNNTS (4,0)	Bond Length (Å ⁰)	BNNTS (5,0)	Bond Length (Å ⁰)	BNNTS (6,0)	Bond Length (Å ⁰)	BNNTS (7,0)	Bond Length (Å ⁰)
B1N2	1.48	B1N2	1.47	B1H43	1.19	B1H57	1.19
B1N3	1.48	B1N3	1.47	B1N63	1.46	B1N100	1.46
B1H41	1.18	B1H61	1.18	B1N75	1.46	B1N109	1.46
N2B4	1.44	N2B6	1.45	B2N51	1.46	B2N108	1.46
N2B15	1.48	N2B19	1.47	B2N69	1.45	B2N109	1.45
N3B5	1.44	N3B4	1.45	B2N70	1.46	B2N117	1.46
N3B7	1.48	N3B7	1.47	B3N70	1.46	B3N99	1.46
B4N6	1.49	B4N5	1.47	B3N75	1.45	B3N100	1.45
B4N16	1.49	B4N10	1.47	B3N76	1.46	B3N108	1.46
B5N6	1.49	N5B6	1.47	B4H44	1.19	B4H58	1.19
B5N10	1.49	N5B26	1.44	B4N75	1.46	B4N91	1.46
N6B23	1.44	B6N20	1.47	B4N81	1.46	B4N100	1.46
B7N8	1.48	B7N8	1.47	B5N76	1.46	B5N86	1.46
B7H42	1.18	B7H62	1.18	B5N81	1.45	B5N91	1.45
N8B9	1.44	N8B9	1.45	B5N82	1.46	B5N99	1.46
N8B11	1.48	N8B11	1.47	B6H45	1.19	B6H59	1.19
B9N10	1.49	B9N10	1.47	B6N81	1.46	B6N85	1.46
B9N14	1.49	B9N14	1.47	B6N87	1.46	B6N91	1.46
N10B21	1.44	N10B25	1.44	B7N82	1.46	B7N77	1.46
B11N12	1.48	B11N12	1.47	B7N87	1.45	B7N85	1.45
B11H43	1.18	B11H63	1.18	B7N89	1.46	B7N86	1.46
N40H48	1.02	N60H70	1.02	N59H60	1.01	N95H96	1.01

Bond lengths are in the ranges of 1.44-1.48 Å for B and N atoms and in the ranges of 1.01-1.02 Å for N and H atoms. Increasing the size of BNNTs, in terms of diameters and lengths, decrease the bond length of B-N and N-H. The B-H bond lengths are between 1.18-1.19 Å. Decreasing the size of BNNTs results in decreasing the B-H bond length.

Table 2 shows that the B-N-B and H-N-B bond angles are in the range of 107.5°-119.5° and 108.9°-117.6°, respectively, in which the numbers are increased to near maximum by increasing the size of nanotube. In addition, the bond angle for H-B-N is 121.1°-122.4° approaching 122.4° by decreasing the size of BNNTs ring. Dipole moments for nanotubes are recorded between 1.68-7.3 Debye. Except BNNTs (4,0), the values are increased by increasing the diameter of the nanotube ring. The energy of the BNNTs was measured in a range of -43.5eV to -121.7 eV, in which the stability of the BNNTs are reasonably increased by the size of nanotubes.

Table 2. Optimized bond angles of BNNTs (4,0), (5,0), (6,0), (7,0)

BNNTS (4,0)	Bond Angle	BNNTS (5,0)	Bond Angle	BNNTS (6,0)	Bond Angle	BNNTS (7,0)	Bond Angle
N2B1N3	112.0	N2B1N3	114.3	B1N69B2	118.7	H57B1N100	121.1
N2B1H41	122.4	N2B1H61	121.7	B1N69B12	114.1	H57B1N109	121.1
N3B1H41	122.4	N3B1H61	121.7	B2N69B12	118.6	B3N100B4	119.0
B1N2B4	116.2	B1N2B6	117.9	B2N70B3	111.5	B20N101B21	114.3
B1N2B15	107.5	B1N2B19	111.3	B2N70B18	118.7	B20N101B23	119.0
B4N2B15	116.1	B6N2B19	117.9	B3N70B18	118.7	B21N101B23	119.0
B1N3B5	116.1	B1N3B4	117.9	B19N71B20	112.4	B34N102B35	114.3
B1N3B7	107.5	B1N3B7	111.4	B19N71B30	118.5	B34N102B37	118.9
B5N3B7	116.2	B4N3B7	117.9	B20N71B30	118.5	B35N102B37	118.9
N2B4N6	119.3	N3B4N5	119.7	B31N72B32	112.3	B48N103B49	114.2
N2B4N16	119.3	N3B4N10	119.7	B31N72B42	118.7	B48N103B51	119.1
N6B4N16	113.9	N5B4N10	115.8	B32N72B42	118.7	B49N103B51	119.1
N3B5N6	119.3	B4N5B6	108.4	B29N73B30	112.3	B50N104B51	115.8
N3B5N10	119.3	B4N5B26	118.0	B29N73B32	118.4	B50N104H105	117.6
N6B5N10	113.9	B6N5B26	118.0	B30N73B32	118.4	B51N104H105	117.6
B4N6B5	103.3	N2B6N5	119.8	B17N74B18	112.4	B36N106B37	114.3
B4N6B23	116.4	N2B6N20	119.7	B17N74B20	118.5	B36N106B49	118.9
B5N6B23	116.4	N5B6N20	115.8	B18N74B20	118.5	B37N106B49	118.9
N3B7N8	112.0	N3B7N8	114.2	B1N75B3	118.6	B22N107B23	114.3
N3B7H42	122.4	N3B7H62	121.7	B1N75B4	114.1	B22N107B35	118.9
N8B7H42	122.4	N8B7H62	121.7	B3N75B4	118.6	B23N107B35	119.0
B7N8B9	116.1	B7N8B9	117.9	B3N76B5	111.6	B2N108B3	113.5
B7N8B11	107.5	B7N8B11	111.4	B3N76B17	118.8	B2N108B21	119.2

BNNTS (4,0)	Bond Angle	BNNTS (5,0)	Bond Angle	BNNTS (6,0)	Bond Angle	BNNTS (7,0)	Bond Angle
B9N8B11	116.2	B9N8B11	117.9	B5N76B17	118.8	B3N108B21	119.2
N8B9N10	119.3	N8B9N10	119.7	B20N77B21	112.4	B1N109B2	119.0
N8B9N14	119.3	N8B9N14	119.7	B20N77B29	118.5	B1N109B14	115.9
N2B1N3	112.0	N2B1N3	114.3	B1N69B2	118.7	B1N100B3	119.0
N2B1H41	122.4	N2B1H61	121.7	B1N69B12	114.1	B1N100B4	115.9
N3B1H41	122.4	N3B1H61	121.7	B2N69B12	118.6	B3N100B4	119.0
B1N2B4	116.2	B1N2B6	117.9	B2N70B3	111.5	B20N101B21	114.3
B1N2B15	107.5	B1N2B19	111.3	B2N70B18	118.7	B20N101B23	119.0
B4N2B15	116.1	B6N2B19	117.9	B3N70B18	118.7	B21N101B23	119.0
B1N3B5	116.1	B1N3B4	117.9	B19N71B20	112.4	B34N102B35	114.3
B1N3B7	107.5	B1N3B7	111.4	B19N71B30	118.5	B34N102B37	118.9
B5N3B7	116.2	B4N3B7	117.9	B20N71B30	118.5	B35N102B37	118.9
N2B4N6	119.3	B51N60H7	114.1	B31N72B32	112.3	B48N103B49	114.2
N2B4N16	119.3	B55N60H7	114.1	B37N55H56	117.2	B48N103B51	119.1
B37N39H47	108.9	N5B4N10	115.8	B32N72B42	118.7	B53N80H81	117.6
N3B5N6	119.3	B4N5B6	108.4	B29N73B30	112.3	B50N104B51	115.8

Table 3. Optimized physical properties of BNNTs (4,0), (5,0), (6,0), (7,0)

BNNTs	E (e.v)	Dipole Moment (debye)	HOMO (e.v)	LUMO (e.v)	Gap (e.v)
(7,0)	-121701.905	7.3010	-6.51836248	-1.78265812	-4.73570436
(6,0)	-91293.87084	5.4374	-6.55319384	-2.2613172	-4.29187664
(5,0)	-65224.56566	1.6823	-6.41441264	-2.9769928	-3.43741984
(4,0)	-43492.37267	6.5626	-6.63727892	-4.07200368	-2.56527524

HOMO and LUMO parameters and density of states (DOS)

Electronic density of states (DOS) of individual BNNTs are shown in Fig.1. HOMO and LUMO parts are distinguished by the orbital distribution patterns.

The electronic properties of BNNTs are often characterized in terms of their HOMO and LUMO energies and the corresponding energy gap (E_g in eV). The distribution patterns of the frontier molecular orbitals (HOMO and LUMO) [9] is shown in Fig. 1 and Table 3. Based on Fig. 1, the variance between HOMO and LUMO in (4,0) BNNT is -2.56 eV, which is less than BNNT (6,0) and (7,0). The ordering of energy gap in the four models were: $E_g(4,0) < E_g(5,0) < E_g(6,0) < E_g(7,0)$. Based on these results, we concluded that the electrical conductivity was increased by decreasing the size of nanotube.

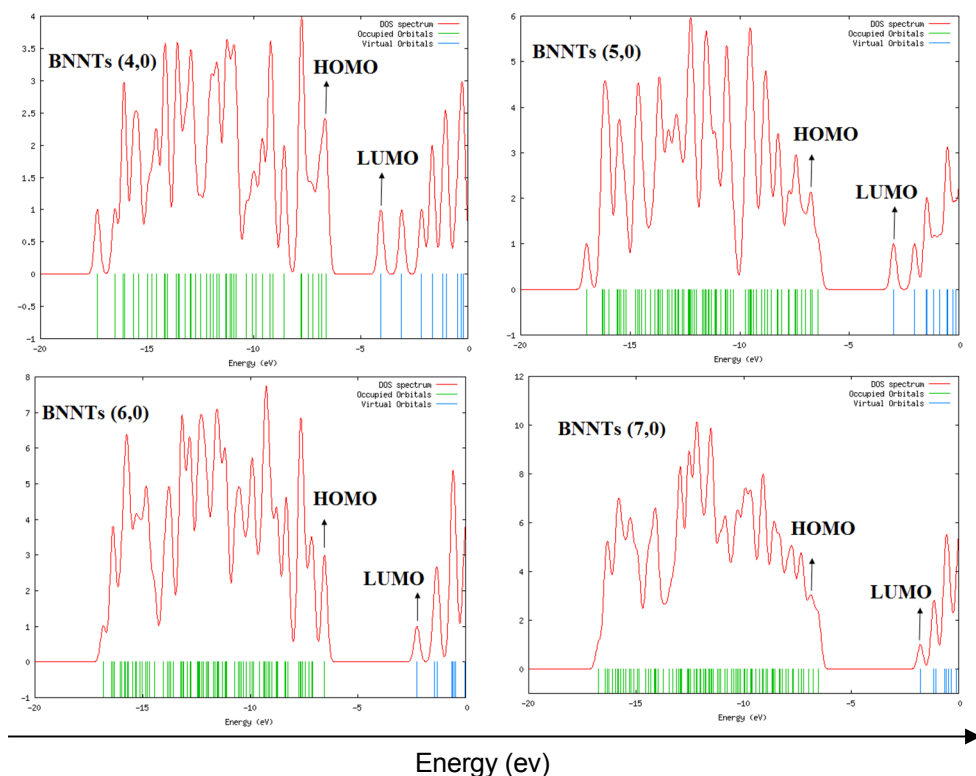


Figure 1. Diagram of the DOS per energy for BNNT; (4,0), (5,0), (6,0) and (7,0) models

Natural bonding orbital (NBO)

For a deeper understanding of the interaction between adsorbent surface and the adsorbate, the partial electronic charge densities were calculated using NBO analysis [9, 10], which opens a better view for discussing the atomic charge distributions (Table 4). In all these cases by expanding the size of the nanotube, the electronic population of the models increase and the maximum can be found in BNNTs (7,0).

Table 4. The NBO information for BNNT (4,0), (5,0), (6,0) and (7,0)

BNNTs	Charge	Core	Valence	Rydberg	Total
7,0	0.00000	223.87871	461.24112	0.88017	686.00000
6,0	0.00000	167.90644	347.36740	0.72615	516.00000
5,0	0.00000	119.92988	249.45157	0.61855	370.00000
4,0	0.00000	79.94934	167.48747	0.56319	248.00000

NUCLEAR MAGNETIC RESONANCE

Chemical shielding (CS) parameters in NMR were evaluated for the optimized BNNTs. To calculate the CS tensors, the gauge included atomic orbital (GIAO) approach was used [11]. The calculated CS tensors in principal axes system (PAS) ($\sigma_{33} > \sigma_{22} > \sigma_{11}$) were converted to measurable CS NMR parameters, isotropic and anisotropic CS (C_{SI} and C_{SA}) using Eqs. (1) and (2) [12, 13]. The evaluated NMR parameters are listed in Table 5.

$$C_{SI} = (\sigma_{11} + \sigma_{22} + \sigma_{33})/3 \quad (1)$$

$$C_{SA} = \sigma_{33} - (\sigma_{22} + \sigma_{11})/2 \quad (2)$$

The results show that the C_{SI} values of optimized (4,0), (5,0), (6,0) and (7,0) BNNTs for the B-H bonds are around 26 and 27 ppm while for the N-H bonds are around 29 and 30 ppm. The isotropic and anisotropic chemical shielding (C_{SI} and C_{SA}) parameters were calculated for the ^{11}B , ^1H and ^{15}N atoms present in the pristine structures. In addition, the tensors were converted to the isotropic C_S (C_{SI}) and the anisotropic C_S (C_{SA}) parameters. The C_{SI} is the average value of the eigenvalues of the C_S tensors, (Eq.1), and the orientation of the eigenvalues of the C_S tensors into the z-axis plays a dominant role in determining the value of the C_{SA} parameter, (Eq.2) [14]. These results show that due to the anisotropic effect, the hydrogen of B-H is de-shielding while hydrogen of N-H is shielding.

Table 5 shows that the anisotropic values of B atoms are between 42-60 ppm, which could imply de-shielding effects and tendency to the weaker magnetic fields.

Table 5. NMR parameter for BNNTs (4,0), (5,0), (6,0), (7,0)

atom	BNNTs 7,0				atom	BNNTs 6,0			
	CSA	Anisotropy	CSI	Isotropic		CSA	Anisotropy	CSI	Isotropic
B3	30.3	43.5	74.9	74.9	B2	11.5	46.2	73.1	73.1
B5	31.0	43.5	74.9	74.9	B7	11.5	46.1	73.0	73.0
B10	41.0	59.5	67.8	67.8	B19	8.4	44.7	71.8	71.8
B12	42.0	59.6	67.7	67.7	B22	8.4	44.7	71.8	71.8
B16	28.9	42.3	73.4	73.4	B31	9.4	44.9	72.4	72.4
N103	133.0	192.1	124.7	124.7	N90	165.7	196.8	113.4	113.4
N124	138.3	196.4	122.0	122.0	N91	171.3	195.5	114.4	114.4
N125	138.3	196.8	121.3	121.3	N92	163.8	194.9	115.3	115.3
N126	143.8	202.3	121.1	121.1	N93	166.1	191.7	118.2	118.2

atom	BNNTs 5,0				atom	BNNTs 4,0			
	CSA	Aniso-tropy	CSI	Isotro-pic		CSA	Aniso-tropy	CSI	Isotro-pic
B21	37.9	49.4	68.1	68.1	B30	15.5	60.5	64.0	64.0
B52	43.5	50.5	72.3	72.3	B26	15.5	60.5	64.0	64.0
B54	43.4	50.5	72.3	72.3	B13	17.3	61.4	63.6	63.6
B55	15.3	54.5	67.6	67.6	B5	17.3	61.4	63.6	63.6
N36	157.9	193.3	102.6	102.6	N32	130.9	134.9	73.3	73.3
N56	90.5	126.0	126.5	126.5	N10	183.0	193.5	77.8	77.8
N59	90.1	126.0	126.5	126.5	N3	37.1	242.5	25.1	25.1
N27	155.6	192.6	102.6	102.6	N16	183.0	193.5	77.8	77.8

However, the values of N atoms are between 126-250 ppm, which could reveal the shielding effects and tendency to higher magnetic fields.

In other words, N and B atoms show positive and negative anisotropic behaviors, respectively. That's why the B and N atoms were observed in weaker and stronger magnetic fields, respectively.

NUCLEAR QUADRUPOLE RESONANCE

Nuclear quadrupole resonance (NQR) spectroscopy is among the most important techniques to characterize the composition of chemical structures. In contrast to NMR, the NQR analysis could be found in the absence of magnetic field in nuclear conversion as a zero-filled technique. The NQR resonance is a connection between electric field gradient (EFG) and Nuclear quadrupole resonance in which the charge distribution occurred. However, the EFG shows the location of nuclei in material in which the linked valance electrons of the atoms are modified. NQR frequency shows the absolute conversion of an element. This frequency in a composite or a crystal is proportional to nuclear quadrupole resonance, nuclei properties and EFG of neighbor nuclei.

The relation between results and the calculations could be investigated using EFG tensors with the main axis of the system. The calculated EFG tensors were converted to quadrupole coupling constants (C_Q) and asymmetry parameters (η_Q), which are directly measured by nuclear quadrupole resonance (NQR) spectroscopy [15].

Using Eqs.(3) and (4), the C_Q and η_Q parameters could be found if $|q_{zz}| < |q_{yy}| < |q_{xx}|$. The standard quantity of the nuclear quadrupole momentum Q [16] are listed in Table 6.

$$C_Q = e^2 Q q_{zz} h^{-1} \quad (3)$$

$$\eta_Q = (q_{xx} - q_{yy}) / q_{zz} \quad (4)$$

Table 6. NQR parameter for BNNTs (4,0), (5,0), (6,0), (7,0)

atom	BNNTs 4,0		atom	BNNTs 5,0		atom	BNNTs 6,0		atom	BNNTs 7,0	
	η_Q	C_Q		η_Q	C_Q		η_Q	C_Q		η_Q	C_Q
B5	0.00	2.78	B1	0.00	2.78	B1	0.00	2.78	B1	0.00	2.78
B7	0.00	2.78	B4	0.00	2.78	B2	0.00	2.78	B3	0.00	2.78
B13	0.00	2.78	B13	0.00	2.78	B3	0.00	2.78	B4	0.00	2.78
B15	0.00	2.78	B15	0.00	2.78	B8	0.00	2.78	B8	0.00	2.78
B17	0.00	2.78	B26	0.00	2.78	B9	0.00	2.78	B9	0.00	2.78
B21	0.00	2.78	B34	0.00	2.78	B15	0.00	2.78	B10	0.00	2.78
B26	0.00	2.78	B42	0.00	2.78	B18	0.00	2.78	B11	0.00	2.78
B30	0.00	2.78	B51	0.00	2.78	B20	0.00	2.78	B17	0.00	2.78
B35	0.00	8.03	B52	0.00	2.78	B23	0.00	2.78	B18	0.00	2.78
B39	0.00	8.03	B54	0.00	2.78	B27	0.00	2.78	B20	0.00	2.78
average	0.00	3.19		0.00	2.78		0.00	2.78		0.00	2.78

Table 6 shows that, the values of η_Q for BNNTs are near zero while for C_Q average 2.78. In addition, the quadrupole momentum is mostly constant and aligned in z-axis.

CONCLUSIONS

In this work, the properties of different boron nitride nanotubes with zigzag chirality were investigated. The results show that by increasing the size, in terms of diameters and lengths of the BNNTs, the energy gap and polarity increased and the hybridisation form becomes sp^2 . In NMR of the BNNTs, the nitrogen atoms is shielding to the higher magnetic field and boron atoms de-shielding to the lower magnetic field. However, in NBO spectroscopy, by increasing the size of the nanotube, the electrical charge increased. In addition, based on the NQR, the effect of the gradient of the electrical field on nuclear quadrupole momentum for different size of the BNNTs were mostly equal and no obvious changes were observed.

COMPUTATIONAL DETAIL

In this study, the structure of Boron Nitride nanotube (BNNT) (4,0) (20 B, 20 N and 8 H atoms), BNNT (5, 0) (30 B, 30 N and 10 H atoms), BNNT (6, 0) (42 B, 42 N and 12 H atoms) and BNNT (7, 0) (56 B, 56 N and 14 H atoms) were investigated. All atomic geometries of the Boron Nitride nanotubes were firstly optimized at the B3LYP (exchange-correlation functional and the 6-311G* level standard basis set) to reach the minimum

energy structures with the optimized values of bond lengths and angles. Figure 2 shows the graphical representation of the optimized geometry of BNNT (7,0), drawn using Hyperchem and GaussView 5.0 software. Note that the sizes of nanotubes were increased based on the proportionality of diameter to length, in which one ring systems was added to increase either diameter or length of nanotubes.

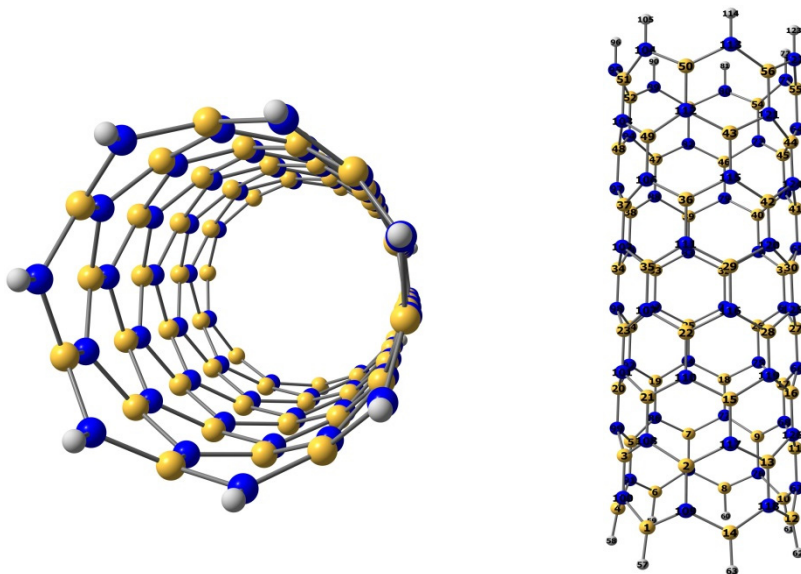


Figure 2. The optimized structure of BNNT (7,0)

Afterwards, the parameters of total energy, energy gap, dipole moment, nuclear quadrupole resonance (NQR), nuclear magnetic resonance spectroscopy (NMR) and Natural bond orbital analysis (NBO) were obtained for the optimized structures by performing single point energy calculations at the computational level of B3LYP. All calculations were performed using the Gaussian 03 package. The results were summarized in Tables 1-6.

ACKNOWLEDGMENTS

The author is grateful to Pharmaceutical Sciences Branch, Islamic Azad University of Tehran for the support of this work.

REFERENCES

1. D. Golberg, Y. Bando, K. Kurashima, T. Sato, *Chemical Physics Letters*, **2000**, 323,185.
2. D. Golberg, M. Mitome, Y. Bando, C.C. Tang and C.Y. Zhi, *Applied Physics A*, **2009**, 88, 347.
3. Y. Yap, "B-C-N Nanotubes and Related Nanostructures", Springer, New York **2009**.
4. P. Ayala, A. Rubio and T. Pichler, *Reviews in Modern Physics*, **2010**, 82, 1843.
5. R. Arenal, X. Blase, A. Loiseau, *Advanced Physics*, **2010**, 59, 101.
6. G. Chopra, A. Zettl, *Solid State Communications*, **1998**, 105, 297.
7. Y.H. Kim, K.J. Chang and S.G. Louie, *Physical Review B*, **2001**, 63, 205408.
8. A. Freitas, S. Azevedo, J.R. Kaschny, *Physica E*, **2016**, 84, 444.
9. J. Kaur, P. Singla, N. Goel, *Applied Surface Science*, **2014**, 328, 632.
10. R. Ditchfield, W.J. Hehre, J.A. Pople, *Journal Chemical Physics*. **1971**, 54, 724.
11. M. Mirzaei, *Journal of Molecular Modeling*. **2010**, 17, 89.
12. A. Shameeli, E. Balali, R. Khadivei, S. Shojaei, *Oriental Journal of Chemistry*, **2016**, 32(1), 291.
13. V.A. Ferreira, H.W. Leite Alves, *Journal Crystal Growth*, **2008**, 310, 3973.
14. M. Rezaei-Sameti, *Arabian Journal of Chemistry*, **2011**, 8, 168.
15. M. Mirzaei, M. Giahi, *Physica E*, **2010**, 42, 1667.
16. P. Pyykko, *Molecular Physics*, **2001**, 99, 1617.

ENTROPY PREDICTION OF BENZENE DERIVATIVES USING TOPOLOGICAL INDICES

HOSSEIN HOSSEINI and FATEMEH SHAFIEI^{a*}

ABSTRACT. In this study, a QSPR study relating topological indices to the entropy of 69 benzene derivatives is reported. The entropy values were calculated at HF level of theory (6-31 G basis sets) by Gaussian 98.

Multiple linear regression (MLR) provided good models with three to seven independent variables. The best model obtained is based on three descriptors: Randić, Wiener and Szeged topological indices

Keywords: *Topological indices; benzene derivatives; QSPR; MLR method.*

INTRODUCTION

One of the most important purposes in application of mathematical and statistical methods is to find a relationship between molecular structure and values of physical properties, chemical reactivity or biological activity. As a result, quantitative structure-property relationship (QSPR) and quantitative structure-activity (QSAR) studies have been promoted.

Topological indices (TIs), as molecular descriptors, are important tools in QSPR/QSAR studies [1-11]. A topological index is a graph invariant number calculated from a graph representing a molecule.

The physicochemical properties of compounds are important in many fields, including pharmaceuticals, chemistry, biochemistry and environmental sciences. Property estimations can help to minimize time and cost in producing new chemical materials with desired properties.

^a *Department of Chemistry, Science Faculty, Arak Branch, Islamic Azad University, Arak, Iran*

* *Corresponding author: f-shafiei@iau-arak.ac.ir*

Predictive methods for estimating thermodynamic properties, such as enthalpies of formation, Gibbs free energy and entropies of acyclic and aromatic compounds, on the basis of fundamental concepts on molecular structure have been reported [12].

Artificial Neural Networks were also used in developing QSPR models for prediction of physicochemical properties [13-16].

Prediction of entropies and enthalpies of organic compounds by using group contribution methods was also published [17-19]. Prediction of standard absolute entropy ($S_{298} K$) of gaseous organic and inorganic compounds was reported in [20, 21].

In thermodynamics, entropy (usual symbol S) is a measurement of the randomness or disorder of a system.

In the present work, we developed QSPR models for entropy estimation of benzene derivatives by describing the chemical structure by the aid of topological indices. Benzene derivatives are used in a wide range of technological applications.

Experimental data of benzene derivatives are often scarce, and at this point, topological descriptors provide powerful tools for modeling and extrapolating experimental data.

The main aim of this study is to illustrate the usefulness of topological indices in QSPR study of entropy (S) of benzene derivatives. As far as we are aware, this is the first QSPR study for prediction of benzene derivatives entropies using topological indices.

METHODS

The entropy(S) of 69 benzene derivatives (benzene included) was computed at the Hartree-Fock (HF) level of theory, using the ab initio 6-31G basis sets. The benzene derivatives in this set have seven different substituents, each substituent being present in at least six compounds. These substituents are amino, bromo, chloro, hydroxyl, methyl, methoxyl and nitro groups. Studied benzene derivatives and their entropy are listed in Table 1. To obtain an appropriate QSPR model we used multiple linear regression (MLR) procedure, by SPSS software, version 16, and backward stepwise regression was used to construct the QSPR models.

For drawing the graphs of our results, we used the Microsoft Office Excel – 2003 program.

Table 1. Benzene derivatives and their entropy.

Compounds		S (J/molK)	Compounds		S (J/molK)
Bromobenzene	1	317.84	4-Methylphenol	36	349.83
Phenol	2	306.46	4-Methyl-3,5-dinitroaniline	37	445.05
1,2-Dichlorobenzene	3	334.59	1,3,5-Trichlorobenzene	38	356.02
3-Chlorotoluene	4	364.05	Benzene	39	262.97
1,3-Dihydroxybenzene	5	323.62	2-Nitrotoluene	40	367.64
3-Hydroxyanisol	6	358.77	1,4-Dinitrobenzene	41	388.62
4-Methyl-3-nitroaniline	7	394.75	2-Methyl-3,6-dinitroaniline	42	441.44
2,4-Dimethylphenol	8	379.11	2-Methyl-4,6-dinitrophenol	43	441.14
2,6-Dimethylphenol	9	368.01	2,5-Dinitrotoluene	44	425.34
3-Nitrotoluene	10	380.02	1,2-Dinitrobenzene	45	353.05
2,6-Dinitrotoluene	11	418.03	1,4-Dimethoxybenzene	46	415.42
4-Methyl-2,6-dinitroaniline	12	434.81	2-Methyl-3-nitroaniline	47	393.15
5-Methyl-2,6-dinitroaniline	13	435.84	2-Methyl-4-nitroaniline	48	390.79
5-Methyl-2,4-dinitroaniline	14	452.06	4-Hydroxy-3-nitroaniline	49	384.93
2,4-Dinitrotoluene	15	424.53	4-Chloro-3-methylphenol	50	364.45
4-Nitrophenol	16	361.48	2,4,6-Tribromophenol	51	420.17
4-Chlorotoluene	17	361.72	2,4,6-Trinitrotoluene	52	374.01
2,4,6-Trichlorophenol	18	390.64	1,2,4,5-Tetrachlorobenzene	53	385.01
Toluene	19	333.15	3-Methyl-2,4-dinitroaniline	54	439.91
3-Methyl-6-nitroaniline	20	394.19	2-Methyl-3,5-dinitroaniline	55	449.66
4-Methyl-2-nitroaniline	21	394.03	3,5-Dinitrotoluene	56	449.03
1,2,4-Trichlorobenzene	22	369.29	3,4-Dinitrotoluene	57	436.01
3,4-Dichlorotoluene	23	389.83	1,2,4-Trimethylbenzene	58	390.65
2,4-Dichlorotoluene	24	371.03	2,4-Dinitrophenol	59	418.15

Compounds	S (J/molK)	Compounds	S (J/molK)		
Chlorobenzene	25	312.91	3,4-Dimethylphenol	60	366.28
1,3,5-Trinitrobenzene	26	454.21	2,4-Dichlorophenol	61	363.99
1,2,3,4-Tetrachlorobenzene	27	388.74	1,2,3-Trichlorobenzene	62	361.73
2,3,4,5,6-Pentachlorophenol	28	440.69	2-Methyl-6-nitroaniline	63	385.42
1,3-Dichlorobenzene	29	336.24	2-Methyl-5-nitroaniline	64	396.19
2-Chlorophenol	30	335.58	1,3-Dinitrobenzene	65	392.01
3-Methylphenol	31	351.15	4-Nitrotoluene	66	386.01
2,3-Dinitrotoluene	32	426.83	1,2-Dimethylbenzene	67	337.67
1,4-Dimethylbenzene	33	340.90	2-Methylphenol	68	337.29
2,3,4,5-Tetrachlorophenol	34	416.02	1,4-Dichlorobenzene	69	330.48
2,3,6-Trinitrotoluene	35	480.08			

TOPOLOGICAL INDICES

A large number of topological indices T_i s have been defined and used, majority of them being calculated from the various matrices corresponding to molecular graphs. The Adjacency matrix (A) and the Distance matrix (D) of the molecular graph have been most widely used in the definition of topological indices. The most used TIs are presented below.

Randić index (1975), ${}^1\chi(G)$, was introduced as the connectivity index [22,23] and is defined as (1):

$${}^1\chi = \sum_{\text{all edges}} (d(i)d(j))^{-0.5} \quad (1)$$

where $d(i)$ and $d(j)$ are the valencies of the vertices i and j defining the edge (i, j) .

Wiener index (1947), $W(G)$, can be defined by (2):

$$W(G) = \frac{1}{2} \sum_i \sum_j [D(i,j)] \quad (2)$$

where $D(i,j)$ is the number of edges on the shortest path joining vertex i and vertex j (i.e., the topological distance) in the graph [24].

Hyper-Wiener index, $WW(G)$, can be defined [25,26] as (3):

$$WW(G) = \frac{1}{2} \left(\sum d(u,v) + \sum (d(u,v))^2 \right) \quad (3)$$

where $d(u,v)$ denotes the distance between the vertices u and v in the graph G and the summations run over all pairs of vertices of G .

Randić's original definition (1993) [27] of the hyper-Wiener index is applicable to trees only.

Wiener polarity index (1947), $W_p(G)$, of G is the number of unordered pairs of vertices (u,v) of G lying at distance 3 to each other. The Wiener polarity index [28,29] is defined as (4):

$$WP(G) = |\{(u, v) \mid d(u, v) = 3, u, v \in V\}|. \quad (4)$$

Balaban index (1982), $J(G)$ of G was introduced in 1982 [30,31] as one of the less degenerated indices. It calculates the average distance sum connectivity index, according to eq.(5):

$$J = \frac{M}{\mu+1} \sum_{\text{all edges}} (D_i D_j)^{-0.5} \quad (5)$$

where M is the number of the edges in G ; and D_i is the distance sum from the vertex i to all the other vertices in G (i.e., the sum of all entries in the i^{th} row of the distance matrix D).

The cyclomatic number $\mu = \mu(G)$ of a polycyclic graph G is equal to the minimum number of edges that must be removed from G to transform it to the related acyclic graph. For trees, $\mu=0$; for monocycles, $\mu=1$.

Harary number, $H(G)$, was introduced in 1993 [32]. This index is defined by eq. (6)

$$H = \frac{1}{2} \sum_{i=1}^n \sum_{j=1}^n (1/D_{ij}) \quad (6)$$

Within this paper, a version of this index is calculated from the inverse of the squared elements of the distance matrix, according to eq.(7):

$$H = \frac{1}{2} \sum_i^n \sum_j^n (D_{ij})^{-2} \quad (7)$$

where D_{ij} is the entry in the distance matrix D .

Szeged index, $Sz(G)$, was introduced by Gutman [33,34] as (8):

$$Sz_v(G) = \sum_e n_u(e|G) \cdot n_v(e|G) \quad (8)$$

$n_v| = n_v(e|G)$ is the number of vertices of G whose distance to the vertex v is smaller than the distance to the vertex u . Note that vertices equidistant to u and v are not counted.

All the used topological indices were calculated in hydrogen suppressed graphs. The descriptors were calculated with Chemicalize program [35]. Seven topological indices tested in the present study are listed in Table 2.

STATISTICAL ANALYSIS

Structure-Property models (MLR models) are generated using the multi linear regression procedure of SPSS, version 16. The entropy (S , J/mol K) is used as the dependent variable and 1χ , J , H , Sz , WW , W_p and W indices are used as the independent variables. The models are assessed with r value (correlation coefficient), the r^2 (coefficient of determination), the r^2 - adjusted, the s value (root of the mean square of errors), the F value (Fischer statistic), the D value (Durbin-Watson) and the Sig (significant).

RESULTS AND DISCUSSION

Several linear QSPR models involving three to seven descriptors were established and the strongest multivariable correlations were identified by the backward method, with significant at the 0.05 level and regression analysis of the SPSS program. In the first of this study we drawn scattering plots of S versus the seven topological indices (1χ , J , H , Sz , WW , W_p , W). Some of these plots are given in Figs. 1 to 3, respectively.

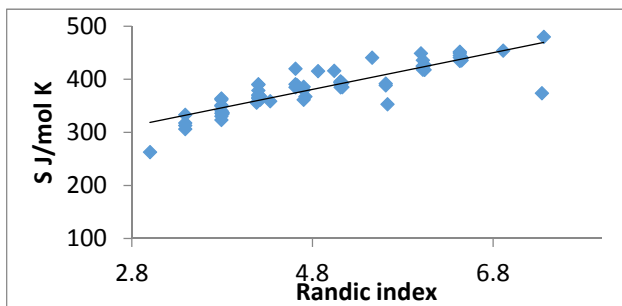


Figure 1. Plot of the Randić index (1χ) versus entropy of 69 benzene derivatives.

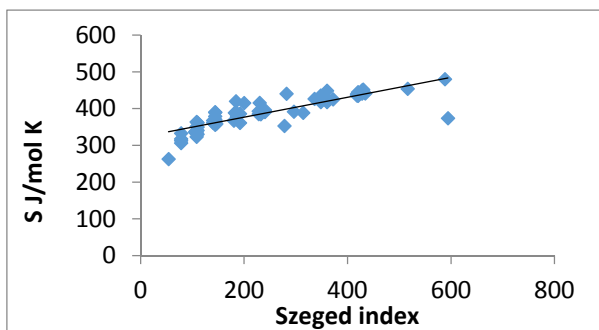


Figure 2. Plot of the Szegeid index (Sz) versus entropy of 69 benzene derivatives.

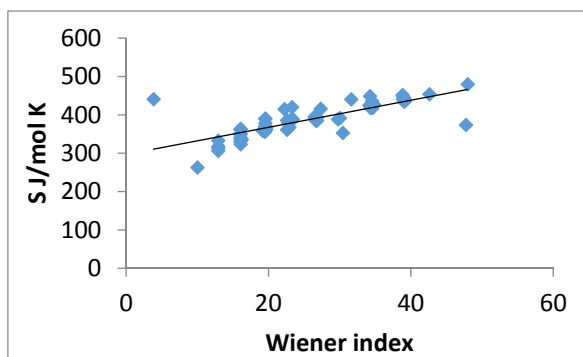


Figure 3. Plot of the Wiener (W) versus entropy of 69 benzene derivatives.

Table 2. Benzene derivatives and their topological indices, used in present study.

A	${}^1\chi$	J	H	W	WW	W_p	Sz
1	3.39	1.82	12.92	42	71	5	78
2	3.39	1.82	12.92	42	71	5	78
3	3.80	2.28	16.17	60	106	8	106
4	3.79	2.23	16.08	61	110	7	108
5	3.79	2.23	16.08	61	110	7	108
6	4.33	1.98	19.15	88	176	9	146
7	5.11	2.25	26.67	148	315	14	232
8	4.20	2.09	19.53	84	160	10	144
9	4.22	2.15	19.67	82	151	11	140
10	4.70	2.32	22.73	117	245	11	186
11	6.04	2.40	34.60	234	545	19	348
12	6.43	2.70	39.02	282	669	21	420

A	$^1\chi$	J	H	W	WW	W _p	Sz
13	6.45	2.72	39.13	281	667	22	418
14	6.43	2.65	38.83	287	698	21	430
15	6.02	2.33	34.30	240	576	18	360
16	4.70	2.26	22.60	120	262	11	192
17	3.79	2.19	16.03	62	115	7	110
18	4.61	2.49	23.28	110	215	13	184
19	3.39	1.82	12.92	42	71	5	78
20	5.11	2.22	26.60	150	327	14	236
21	5.11	2.25	26.67	148	315	14	232
22	4.20	2.09	19.53	84	160	10	144
23	4.20	2.09	19.53	84	160	10	144
24	4.20	2.09	19.53	84	160	10	144
25	3.39	1.82	12.92	42	71	5	78
26	6.91	2.46	42.60	354	906	21	516
27	4.63	2.52	23.37	109	211	14	182
28	5.46	2.76	31.60	174	357	21	282
29	3.79	2.23	16.08	61	110	7	108
30	3.80	2.28	16.17	60	106	8	106
31	3.79	2.23	16.08	61	110	7	108
32	6.04	2.47	34.83	228	511	19	336
33	3.79	2.19	16.03	62	115	7	110
34	5.04	2.39	27.32	140	281	17	230
35	7.36	2.83	47.97	405	1036	26	588
36	3.79	2.19	16.03	62	115	7	110
37	6.43	2.70	39.02	282	669	21	420
38	4.18	2.08	19.50	84	159	9	144
39	3.00	2.00	10.00	27	42	3	54
40	4.72	2.40	22.90	114	231	12	180
41	5.61	2.30	29.74	206	521	15	314
42	6.45	2.64	38.87	289	717	22	434
43	6.43	2.66	3.85	286	691	21	428
44	6.02	2.28	34.14	246	616	18	372
45	5.63	2.54	30.43	188	416	16	278
46	4.86	2.17	22.24	125	287	11	200
47	5.13	2.28	26.80	146	306	15	228
48	5.11	2.18	26.50	152	337	14	240
49	5.11	2.25	26.67	148	315	14	232
50	4.20	2.09	19.53	84	160	10	144
51	4.61	2.49	23.28	110	215	13	184
52	7.34	2.80	47.72	408	1044	25	594
53	4.61	2.46	23.23	111	220	13	186
54	6.45	2.72	39.13	281	667	22	418
55	6.43	2.66	38.85	286	691	21	428

A	1χ	J	H	W	WW	W _p	Sz
56	6.00	2.33	34.23	240	573	17	360
57	6.02	2.40	34.53	234	542	18	348
58	4.20	2.09	19.53	84	160	10	144
59	6.02	2.33	34.3	240	576	18	360
60	4.20	2.09	19.53	84	160	10	144
61	4.20	2.09	19.53	84	160	10	144
62	4.22	2.15	19.67	82	151	11	140
63	5.13	2.28	26.8	146	306	15	228
64	5.11	2.18	26.5	152	337	14	240
65	5.61	2.40	30.02	197	464	15	296
66	4.70	2.26	22.6	120	262	11	192
67	3.80	2.28	16.17	60	106	8	106
68	3.80	2.28	16.17	60	106	8	106
69	3.79	2.19	16.03	62	115	7	110

Distribution of the dependent variable against the independent variable for 69 chemicals was employed in developing quantitative structure- properties relationships. For obtaining appropriate QSPR models we used maximum R² method and followed backward regression analysis. The predictive ability of the model is discussed on the basis of predictive correlation coefficient.

QSPR MODELS FOR ENTROPY (S)

Initial regression analysis indicated that combination of seven topological indices plays a dominating role in modeling the entropy. Table 3 provides the regression parameters and quality of correlation of the proposed models for entropy of 69 benzene derivatives.

Table 3. Statistics of models calculated with SPSS software

Model	Independent variables	r	r ²	r _{adj} ²	s	F	Sig
1	Sz, J, H, W _p , 1 χ , WW, W	0.929	0.864	0.848	16.691	55.222	0.000
2	Sz, J, W _p , 1 χ , WW, W	0.929	0.864	0.850	16.559	65.454	0.000
3	Sz, W _p , 1 χ , WW, W	0.929	0.862	0.851	16.510	78.879	0.000
4	Sz, 1 χ , W _p , W	0.927	0.860	0.851	16.518	98.244	0.000
5	Sz, 1 χ , W	0.927	0.859	0.853	16.430	132.299	0.000

The best linear model contains three topological descriptors, namely, Randić (1χ), Wiener (W) and Szeged (Sz) indices.

The regression parameters of the best three descriptor correlation model are gathered in equation 9.

$$S=70.258+59.966X+2.748Sz-4.163W \quad (9)$$

$$r=0.927 ; r^2=0.859 ; r_{adj}^2 =0.859 ;$$

$$s=16.430 ; D=2.033 ;$$

$$F=132.299 ; \text{mean square} = 269.936$$

This model produced a standard error of 16.430 J mol⁻¹ K⁻¹, a correlation coefficient of 0.927, and the adjusted correlation coefficient (adjusted r-squared) was calculated as 0.859.

The result is therefore very satisfactory. Figure 4 shows the linear correlation between the observed and the predicted entropy values obtained using equation (9).

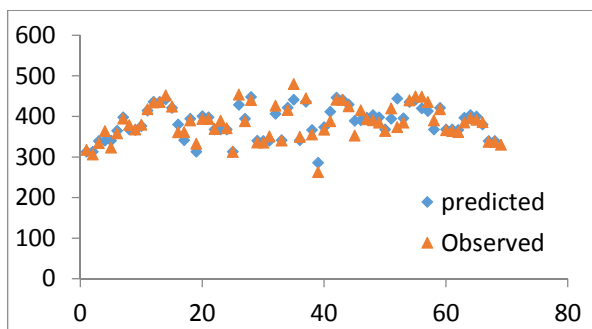


Figure 4. Comparison between the predicted and observed entropy by MLR method (cf. eq. 9)

The DURBIN-WATSON STATISTIC

To verify and validate the regression models, we will focus on the Durbin-Watson (D) statistic, unstandardized predicted and residual values.

The Durbin-Watson statistic ranges in value from 0 to 4. A value near 2 indicates non-autocorrelation; a value toward 0 indicates positive autocorrelation; a value toward 4 indicates negative autocorrelation. Therefore the value of Durbin-Watson statistic is close to 2 if the errors are uncorrelated. In our model, the value of Durbin-Watson statistic for model 5 is close to 2 (See Eq. 9) hence the errors are uncorrelated.

RESIDUAL VALUES

The residual values of entropy expressed by equation (9) are shown in Table 4. The residual values show a fairly random pattern (see Figure 5). This random pattern indicates that a linear model provides a decent fit to the data.

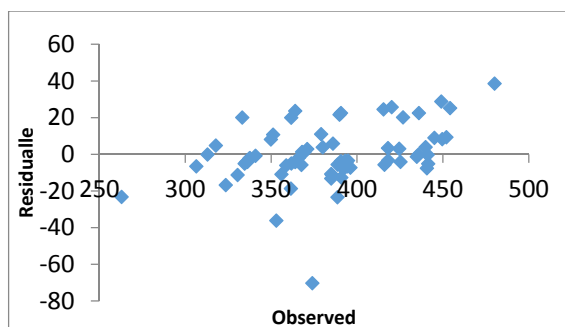


Figure 5. Plot of residuals against observed values of benzene derivatives entropy (S).

Table 4. Entropy (S) data of benzene derivatives.

No.	Observed S(J/molK)	Predicted S(J/molK)	Residual	No.	Observed S(J/molK)	Predicted S(J/molK)	Residual
1	317.835	313.051	4.784	36	349.828	341.718	8.110
2	306.457	313.051	-6.594	37	445.053	436.089	8.964
3	334.588	339.651	-5.063	38	356.019	366.955	-10.936
4	364.048	340.385	23.663	39	262.968	286.154	-23.186
5	323.616	340.385	-16.769	40	367.639	373.379	-5.740
6	358.773	364.794	-6.021	41	388.619	412.003	-23.384
7	394.751	398.127	-3.376	42	441.441	446.622	-5.181
8	379.109	368.154	10.955	43	441.136	441.422	-0.286
9	368.007	366.687	1.320	44	425.335	429.461	-4.126
10	380.017	376.180	3.837	45	353.047	389.203	-36.156
11	418.029	414.661	3.368	46	415.421	390.944	24.477
12	434.807	436.089	-1.282	47	393.149	396.660	-3.511
13	435.840	435.955	-0.115	48	390.792	403.460	-12.668
14	452.059	442.756	9.303	49	384.928	398.127	-13.199
15	424.529	421.461	3.068	50	364.454	368.154	-3.700
16	361.482	380.180	-18.698	51	420.165	394.428	25.737
17	361.720	341.718	20.002	52	374.009	444.296	-70.287
18	390.637	394.428	-3.791	53	385.007	395.761	-10.754

No.	Observed S(J/molK)	Predicted S(J/molK)	Residual	No.	Observed S(J/molK)	Predicted S(J/molK)	Residual
19	333.154	313.051	20.103	54	439.912	435.955	3.957
20	394.186	400.794	-6.608	55	449.659	441.422	8.237
21	394.032	398.127	-4.095	56	449.028	420.262	28.766
22	369.290	368.154	1.136	57	436.007	413.461	22.546
23	389.827	368.154	21.673	58	390.650	368.154	22.496
24	371.033	368.154	2.879	59	418.150	421.461	-3.311
25	312.911	313.051	-0.140	60	366.281	368.154	-1.873
26	454.207	428.958	25.249	61	363.994	368.154	-4.160
27	388.735	394.294	-5.559	62	361.725	366.687	-4.962
28	440.693	448.284	-7.591	63	385.417	396.660	-11.243
29	336.239	340.385	-4.146	64	396.188	403.460	-7.272
30	335.579	339.651	-4.072	65	392.008	400.003	-7.995
31	351.149	340.385	10.764	66	386.006	380.180	5.826
32	426.832	406.661	20.171	67	337.673	339.651	-1.978
33	340.904	341.718	-0.814	68	337.288	339.651	-2.363
34	416.018	421.738	-5.720	69	330.475	341.718	-11.243
35	480.077	441.495	38.582				

CONCLUSIONS

In this work, QSPR models for the prediction of entropy for a training set of benzene derivatives using MLR based on topological descriptors calculated from molecular structure have been developed. MLR model is proved to be a useful tool in the prediction of entropy. The aforementioned results and discussion lead us to conclude that combining the three descriptors (S_z , W , 1χ) could be used successfully for modeling and predicting entropy (S) of compounds. This model contains fewer topological descriptors, maximum of Fischer statistic value (F) and minimum root of the mean square of errors(s).

REFERENCES

1. X.J. Yao, B. Fan, J.P. Doucet, A. Panaye, M. Liu, R. Zhang, X. Zhang and Z. Hu, *QSAR & Combinatorial Science*, **2003**, 22, 29.
2. A.A. Taherpour, F. Shafiei, *Journal of Molecular Structure: THEOCHEM*, **2005**, 726, 183.
3. F. Shafiei, *Iranian Journal of Mathematical Chemistry*, **2015**, 6, 15.
4. P.R. Duchowicz, E.A. Castro, F.M. Fernández and A.N. Pankratov, *Journal of the Argentine Chemical Society*, **2006**, 94, 31.

5. Z. Lin, J. Xu, X. Zheng and Z. Li, *Acta Physico-Chimica Sinica*, **2000**, 16,153.
6. F. Gharagheizi, M.R. Samiee Gohar and M. Ghotbi Vayeghan, *Journal of Thermal Analysis and Calorimetry*, **2012**, 109, 501.
7. E. Estrada, O. Ivanciuc, I.Gutman, A.Gutierrez and L. Rodríguez, *New Journal of Chemistry*, **1998**, 22, 819.
8. H. Hosoya, M. Gotoh, M. Murakami and S. Ikeda, *Journal of Chemical Information and Computer Sciences*, **1999**, 39, 192.
9. Y.P. Du, Y.Z. Liang, B.Y. Li and C.J. Xu, *Journal of Chemical Information and Computer Sciences*, **2002**,42,1128.
10. D. Plavsic, S. Nikolic, N. Trinajstic, and Z. Mihalic, *Journal of Mathematical Chemistry*, **1993**, 12, 235.
11. A.T. Balaban, *Journal of Molecular Structure: THEOCHEM*, **1998**,165, 243.
12. P.R. Duchowicz, E.A. Castro, F.M. Fernández and A.N. Pankratov, *Journal of the Argentine Chemical Society*, **2006**, 94, 31.
13. O. Ivanciuc, *Revue Roumaine de Chimie*, **1995**,40,1093.
14. J. Taskinen and J. Yliruusi. *Advanced Drug Delivery Reviews*, **2003**, 55, 1163.
15. L.H. Hall and C.T. Story, *SAR and QSAR in Environmental Research*, **1997**, 6,139.
16. Li. Qianfeng, Chen. Xingguo and Hu. Zhide, *Chemometrics and Intelligent Laboratory Systems*, **2004**, 72, 93.
17. E.S. Domalski and E.D. Hearing, *Journal of Physical and Chemical Reference Data*, **1988**, 17, 1637.
18. J.S. Chickos, C.M. Braton, D.G. Hesse and J.F. Liebman, *The Journal of Organic Chemistry*, **1991**, 56, 927.
19. J.S. Chickos, W.E. Acree, Jr. and J.F. Liebman, *Journal of Physical and Chemical Reference Data*, **1999**, 28, 1535.
20. Mu. Lailong, Feng. Changjun, *MATCH Communications in Mathematical and in Computer Chemistry*, **2007**, 111.
21. Mu. Lailong, He. Hongmei, *Industrial & Engineering Chemistry Research*, **2011**, 50, 8764.
22. M. Randić, *Journal of Mathematical Chemistry*, **1991**, 7, 155.
23. M. Randić, *Journal of the American Chemical Society*, **1975**, 97, 6609.
24. M. Randić, *Acta Chimica Slovenica*, **2002**, 49, 483.
25. B. Zhou, I. Gutman, *Chemical Physics Letters*, **2004**, 394, 93.
26. D.J. Klein, W. Yan, Y.N. Yeh, *International Journal of Quantum Chemistry*, **2006**, 106, 1756.
27. D. J.Klein, I. Lukovits, I. Gutman, *Journal of Chemical Information and Computer Sciences*, **1995**, 35, 50.
28. M. Liu¹, B. Liu^{On}, *MATCH Communications in Mathematical and in Computer Chemistry*, **2011**, 66,293.
29. H. Deng, H. Xiao, F. Tang, *MATCH Communications in Mathematical and in Computer Chemistry*, **2010**, 63,257.
30. A.T. Balaban, *Chemical Physics Letters*, **1982**, 89, 399.
31. L. Blaha, J. Damborsky, M. Nemeč, *Chemosphere*, **1998**, 36,1345.

32. C.K. Das, B. Zhou, N. Trinajstić, *Journal of Mathematical Chemistry*, **2009**, 1369.
33. I. Gutman, S. Klavžar, *Journal of Chemical Information and Computer Sciences*, **1995**, 35, 1011.
34. P.V. Khadikar, N.V. Deshpande, P.P. Dobrynin, *Journal of Chemical Information and Computer Sciences*, **1995**, 35, 547.
35. Web search engine developed by ChemAxon; software available at <http://www.Chemicalize.Org>.

IMPACT OF THERMAL TREATMENT ON THE ANTIOXIDANT ACTIVITY OF CORNELIAN CHERRIES EXTRACT

BIANCA MOLDOVAN^a, LUMINIȚA DAVID^{a*}, SORIN CLAUDIU MAN^b

ABSTRACT. The present study aims to investigate the influence of the temperature on the radical scavenging capacity (measured by the 2, 2-azinobis (3-ethylbenzothiazolyne-6-sulphonic acid) diammonium salt radical cation assay) and ferric reducing antioxidant power (FRAP) of Cornelian cherry fruit extract. The impact of the thermal treatment was investigated by monitoring these parameters at 75°C and comparing the obtained values to those resulted by refrigerated storage of the extract. The Cornelian Cherry extract showed a great stability of the antioxidant activity after 10 days of storage at 75°C (ca. 29% loss of antioxidant capacity).

Keywords: *Cornelian cherries, antioxidant activity, thermal stability*

INTRODUCTION

The beneficial biological effects of plant-derived nutrients are well indicated by their antioxidant properties. Phytochemicals from fruits and vegetables attracted lately a great attention, especially on their ability in preventing oxidative stress caused diseases such as heart and neurodegenerative illnesses, cancer, arthritis [1, 2]. Cornelian cherries (*Cornus mas* L.) can be a valuable source of antioxidant compounds and their consumption may reduce the risk of several degenerative diseases. The main phytochemicals acting as antioxidants and free radical scavengers in these fruits are: ascorbic acid, anthocyanins, flavonoids and other polyphenols [3]. Cornelian cherries can be consumed fresh, dried or processed as marmalades or beverages.

^a Babeș-Bolyai University, Faculty of Chemistry and Chemical Engineering, 11 Arany Janos Str., 400028, Cluj-Napoca, Romania

^b Mother and Child Department, "Iuliu Hatieganu" University of Medicine and Pharmacy, 15 V. Babes Str., 400012, Cluj-Napoca, Romania

* Corresponding author: muntean@chem.ubbcluj.ro

The most extensively used method in the food processing is thermal treatment. The microbiological stability and the extent of shelf-life can be achieved by this method. Thermal processing may affect the antioxidant capacity of foods. Some studies mentioned the decrease of this parameter where others have reported an increase of the antioxidant activity after thermal treatment [4, 5]. The health promoting capacity of fruits is therefore affected by their processing history. Processing, especially thermal, is expected to affect the content and the biological activities of the bioactive components in fruits. Although the thermal degradation of Cornelian cherries' polyphenols was already investigated [6, 7] there is no study reporting the influence of the temperature on the stability of the antioxidant capacity of these fruits. There is well known that the total phenolic content is not necessarily correlated to the antioxidant activity and the thermal processing can different affect these two parameters which may vary in opposite ways. By investigating the effect of thermal treatment on cactus pears, Jaramillo-Flores et al. [8] reported a significant decrease in the total phenolic content at high temperatures but an increase of the antioxidant activity. This fact can be due to the presence of other antioxidant phytochemicals such as ascorbic acid and carotenoids. The reduction in phenolic content could not always fully predict the reduction in the antioxidant activity. Thus, the objective of this study was to investigate the effect of heating on the free radical scavenging effectiveness and reducing ability of the Cornelian cherry fruits extract.

RESULTS AND DISCUSSION

Cornelian cherry (*Cornus mas* L.) fruits are known for their elevated antioxidant activity, characteristic related to the presence of anthocyanins, flavonoids and other phenolic compounds [9]. That's why these less consumed fruits may be considered a valuable source of antioxidant compounds in the diet.

As the antioxidant capacity of fruit extracts strongly depends on the kind of individual antioxidants present in the sample, more than one assay is recommended to be used for the determination of the total antioxidant capacity of these samples. Different methods have been reported to be used for the evaluation of the in vitro antioxidant capacity of fruits of which ABTS, FRAP, DPPH, PRAP and ORAC are the most widely used [10, 11]. It is recommended that at least two of these assays to be combined in order to provide complete information on the total antioxidant activity of natural samples. FRAP (ferric reducing antioxidant power) assay and ABTS (2,2-

azinobis(3-ethylbenzothiazolyne-6-sulphonic acid diammonium salt) assays have been lately widely applied to analyse the Trolox equivalent antioxidant capacity (TEAC) of different fruits. The determined values for the antioxidant activity were 9684.62 μM Trolox and 8982.20 μM Trolox in Cornelian cherries extract as determined by ABTS and FRAP assay [12] respectively. These methods are based on different mechanisms for assessing the antioxidant capacity of samples. The ABTS assay measures the free radical scavenging capacity of antioxidant compounds, while the FRAP assay indicates the ability of these compounds to act as reducing agents. The ABTS and FRAP assays use different techniques for measuring the antioxidant capacity of a sample namely the reduction capacity (FRAP) and the diradical inhibition (ABTS). The two methods offered comparable information on the measured TEAC of Cornelian cherry fruits.

Figure 1 presents changes in the antioxidant activity of the investigated extracts during storage at 2°C and 75°C, measured by ABTS and FRAP assays.

ABTS assay indicated a *ca.* 10% reduction of the antioxidant capacity of Cornelian cherry fruits extract after 60 days of cold storage (2°C, Figure 1a). The FRAP values also declined upon refrigerated storage, but the changes were higher as compared to the ABTS assay. At the end of the storage the antioxidant activity evaluated by the FRAP assay was reduced by 17%.

Storage at 75°C (Figure 1b) resulted in a higher loss of the antioxidant capacity of the extracts. After 10 days of storage, both methods indicated a *ca.* 29% decrease of the antioxidant activity of the investigated extracts.

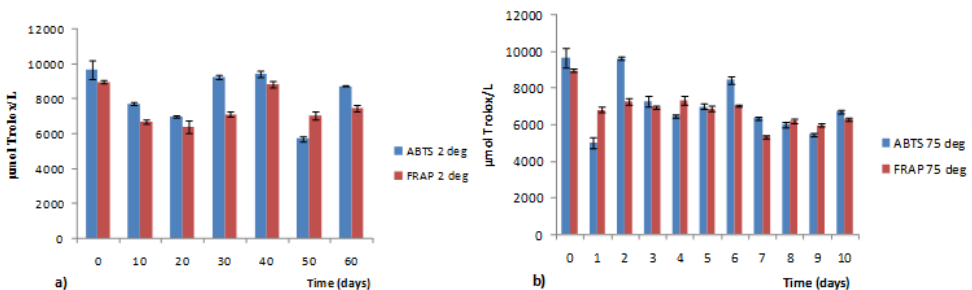


Figure 1. Changes in the antioxidant activity of the Cornelian cherries extracts during storage at: a) 2°C and b) 75°C

Regardless of storage temperature, the Cornelian cherry fruits extracts showed good storage stability in terms of the antioxidant capacity, as evaluated by both assays. These observations are in accordance with the findings of other authors who confirmed the storage stability of antioxidant capacity of other fruits such as blueberry, apricots, pomegranate plums and raspberry [13-16]. The measured values of the antioxidant capacity strongly fluctuated during the storage periods according to both applied analytical methods. This behavior can be explained by various reactions that may occur. The reduction of the antioxidant activity may be due to degradation of water soluble phenolic compounds such as anthocyanins and vitamin C [6, 17]. The increase of the antioxidant activity was not at all surprising, as also reported by other studies [18-20] and can be explained by compounds generated during Maillard reaction and also by formation of procyanidins, low molecular polymers with antioxidant activity or by generation of other degradation products of anthocyanins or phenolic acids, compounds which also present antioxidant capacity [21, 22].

Overall, the *in vitro* assays demonstrated that antioxidant capacity of Cornelian cherry fruits extract slightly decreased after the investigated storage intervals.

CONCLUSIONS

Cornelian cherry fruits are more and more investigated due to their high content of antioxidants phytochemicals which confer them numerous health benefits. The aim of the present study was to investigate the influence of temperature on the antioxidant capacity of these fruits during storage. In order to achieve this goal, the fruit extracts were stored at 75°C for 10 days. The decrease in the antioxidant activity observed during this storage period was not significant compared to refrigerated storage indicating that thermal treatments which are often applied in food processing and storage does not dramatically influence the health promoting antioxidant capacity of these fruits.

EXPERIMENTAL SECTION

Chemicals and reagents

All chemicals and reagents were purchased from Merck (Darmstadt, Germany), were of analytical grade and were used without further purification. A TYPDP1500 Water distiller (Techosklo LTD, Držkov, Czech Republic) was used to obtain the distilled water.

Plant material

Samples of Cornelian cherries were purchased in August 2016 from a local market in Cluj-Napoca, Romania. Fruits of uniform ripening stage, shape and weight were selected, washed with distilled water and used to obtain the fruit extract.

Extract preparation

The extraction procedure was conducted as described in previous studies [9]. Milled Cornelian cherry fruits were subjected to acetone extraction. The extraction was conducted at room temperature for 1 hour. The solution was filtered and the filtrate was concentrated to a solvent free extract using a rotary evaporator. The extract was divided into two portions: the first was stored at 2°C for 60 days and the second was stored in a thermostatic water bath preheated at 75°C, in order to investigate the effect of thermal treatment on the antioxidant activity of the samples. Changes in the antioxidant capacity of the samples were analyzed by measuring this parameter at different time intervals.

Determination of antioxidant activity

1. ABTS Assay

ABTS radical cation scavenging ability of the fruit extract was assessed by the method proposed by Arnao et al. [23]. Two stock solutions were prepared as follows: a 7.4 mM ABTS and a 2.45 mM potassium persulfate solution in distilled water. The ABTS^{•+} was activated by mixing equal volumes of the two stock solutions which were then allowed to react for 24 h in the dark at room temperature. The obtained solution was diluted with distilled water to obtain an absorbance of 0.8-0.9 at 734 nm. An amount of 100 µL Cornelian cherry fruit extract (128 fold diluted) was allowed to react with 6mL diluted ABTS solution for 15 minutes in the dark. Using a Perkin Elmer Lambda 25 double beam UV-Vis spectrophotometer (Perkin Elmer, Shelton, CT, USA) the absorbance of the samples and the blank was read at 734 nm. A calibration curve was used to express the antioxidant activity of the investigated samples in µmol Trolox equivalents/L extract.

2. FRAP Assay

The ferric reducing antioxidant power (FRAP) assay was performed using the method of Benzie and Strain [24]. Stock solutions of 300 mM acetate buffer (pH= 3.6), 10 mM 2,4,6-tripyridyl-s-triazine (TPTZ) solution in

40 mM HCl and 20 mM FeCl₃·6H₂O solution in distilled water were prepared. The working FRAP reagent was freshly prepared for each measurement of the antioxidant activity as follows: 2.5 mL TPTZ solution were mixed with 25 mL acetate buffer solution and 2.5 mL FeCl₃·6H₂O solution and the resulting mixture was warmed to 37°C before use. A total of 150 μL fruit extract was allowed to react to 2850 μL warm FRAP reagent for 30 minutes in the dark. Absorbance reading of the resulted colored complex was taken at 593 nm against a blank sample. The results were expressed in μmol Trolox equivalents/L extract, using a standard curve.

ACKNOWLEDGMENTS

The Ministry of Education and Scientific Research, Romania, supported this work (research Project no. 147/2011 PN-II-PT-PCCA-2011-3-1-0914).

REFERENCES

1. J. Bloomberg, *Horticultural Science*, **2003**, 38, 771.
2. B. Moldovan, L. David, M. Achim, S. Clichici, G.A. Filip, *Journal of Molecular Liquids*, **2016**, 221, 271.
3. L. David, B. Moldovan, Extraction, characterization and potential health benefits of bioactive compounds from selected *Cornus* fruits, in: *Fruits and pomace extracts: biological activity, potential applications and beneficial health effects*. Nova Science Publishers, Inc. New-York, USA, **2015**, 157-188.
4. A. Patras, N.P. Brnton, S. Da Pieve, F. Butler, G. Downey, *Inovative Food Science & Emerging Technologies*, **2009**, 10, 16.
5. E. Sikora, E. Cieslik, T. Leszczynska, A. Filipiak-Florkiewicz, M. Pisulewski-Pawel, *Food Chemistry*, **2008**, 107, 55.
6. B. Moldovan, A. Popa, L. David, *Journal of Applied Botany and Food Quality*, **2016**, 89, 208.
7. B. Moldovan, L. David, *Molecules*, **2014**, 19, 8177.
8. M.E. Jaramillo-Flores, L. Gonzalez-Cruz, M. Cornejo-Mazon, L. Dorantes-Alvarez, G.F. Gutierrez-Lopez, H. Hernandez-Sanchez, *Food Science and Technology International*, **2003**, 9, 271.
9. B. Moldovan, A. Filip, S. Clichici, R. Suharoschi, P. Bolfa, L. David, *Journal of Functional Foods*, **2016**, 26, 77.
10. B.M. Popovic, D. Stajner, K. Slavko, B. Sandra, *Food Chemistry*, **2012**, 134, 734.
11. J. Contreras-Calderon, L. Calderon-Jaines, E. Guerra-Hernandez, B. Garcia-Villanova, *Food Research International*, **2011**, 44, 2047.

12. A. Hosu, C. Cimpoiu, L. David, B. Moldovan, *Journal of Analytical Methods in Chemistry*, **2016**, Article ID 2345375, 5 pages. <http://dx.doi.org/10.1152016/2345375>.
13. J.A. Hernández-Herrero, M.J. Frutos, *International Journal of Food Science & Technology*, **2011**, *46*, 2550.
14. J. Piljac-Zegarac, D. Samec, *Food Research International*, **2011**, *44*, 345.
15. J.A., Hernández-Herrero, M.J. Frutos, *Food Chemistry*, **2014**, *154*, 199.
16. O.A. Fawole, U.L. Opara, *Industrial Crops and Products*, **2013**, *47*, 300.
17. B. Moldovan, L. David, R. Donca, C. Chisbora, *Studia UBB Chemia*, **2011**, *56*(2), 189.
18. L.F. Amaro, M.T. Soares, C. Pinho, I.F. Almeida, O. Pinho, I.M.P.L.V.O. Ferreira, *International Journal of Food Science & Technology*, **2013**, *48*, 2071.
19. B. Moldovan, O. Ghic, L. David, C. Chişbora, *Revista de Chimie*, **2012**, *63*, 463.
20. D. Fracassetti, C. Del Bo, P. Simonetti, C. Gardana, D. Klinis-Zacas, S. Ciappellano, *Journal of Agricultural and Food Chemistry*, **2013**, *61*, 2999.
21. L.L. Howard, R.L. Prior, R. Liyanage, J.O. Lay, *Journal of Agricultural and Food Chemistry*, **2012**, *60*, 6678.
22. C. Oliveira, L F. Amaro, O. Pinho, I.M. Ferreira, *Journal of Agricultural and Food Chemistry*, **2010**, *58*, 9006.
23. M.B. Arnao, A. Cano, M. Acosta, *Food Chemistry*, **2001**, *73*, 239.
24. I.F.F. Benzie, J.J. Strain, *Analytical Biochemistry*, **1996**, *239*, 70.

INCREASED CHEMICAL STABILITY OF *BACILLUS LICHENIFORMIS* α -AMYLASE UPON ACETYLATION

ADYANI AZIZAH ABD HALIM^{a,b*}, HABSAH ABDUL KADIR^b,
SAAD TAYYAB^b

ABSTRACT. Acetylated derivative (47%) of *Bacillus licheniformis* α -amylase (BLA) was prepared using acetic anhydride and its molecular properties including chemical stability were studied with the help of CD spectroscopy, analytical gel filtration and enzymatic activity measurements. Acetylated BLA preparation was found homogeneous with respect to charge and size based on electrophoretic and chromatographic results. Expansion in the molecular size of the modified BLA was evident from the decrease in its elution volume on Superdex 200 column as well as Stokes radius determination. Near-UV CD spectra suggested significant change in the tertiary structure of the acetylated BLA, whereas secondary structures remained unaltered, as judged from the far-UV CD spectra. Acetylated BLA displayed greater chemical stability against urea denaturation as revealed by the increase in the mid-point (C_m) of the denaturation curve and significant retention of biological activity at different urea concentrations. These results indicated greater conformational stability of acetylated BLA in the presence of urea.

Keywords: *Bacillus licheniformis* α -amylase, acetylation, chemical stability, urea denaturation

INTRODUCTION

The native structure of a protein is generally stabilized by different noncovalent forces, which include hydrogen bonds, ionic, van der Waals and hydrophobic interactions [1, 2]. Any minor structural change in the protein

^a Department of Oral and Craniofacial Sciences, Faculty of Dentistry, University of Malaya, 50603 Kuala Lumpur, Malaysia

^b Biomolecular Research Group, Biochemistry Programme, Institute of Biological Sciences, Faculty of Science, University of Malaya, 50603 Kuala Lumpur, Malaysia

* Corresponding author: adyanihalim82@gmail.com

molecule may affect its functions. Protein surface contributes significantly towards maintaining the native conformation of a protein through its interaction with the surrounding medium. The operational conditions of many industrial processes may lead to the exposure of proteins / enzymes to various environmental factors, such as pH, temperature, pressure and solvent composition (salts, alkali and denaturants), which are known to disrupt the native protein conformation [3]. Therefore, increasing protein stability of various industrial enzymes has become an important issue in biotechnology in order to make the industrial processes economical.

Several factors contribute toward high thermostability of enzymes, which include electrostatic interactions, metal binding sites, core hydrophobicity, high packing density etc. Protein mutants (neutral) of charged amino acid residues or charged mutants of neutral amino acids have been found to exhibit either higher or lower stability [4, 5]. For example, Miki *et al.* have reported destabilization of cytochrome c by partial charge neutralization [6]. On the other hand, replacement of two positively-charged residues (K139 and K207) in *E. coli* L-asparaginase with neutral and negative charge substitutions (K139A, K207A, K139D, K207D) has been shown to produce stable enzyme with greater resistance against heat compared to wild type [4]. A few ribonuclease Sa mutants such as Asp49→His, Asp25→Lys and Gly14→Lys have shown greater stability than the wild type [5]. Enzymatic activities of thermolysin mutants, S53D and S65D have been found 78% and 68%, respectively, higher than the wild type enzyme [7]. Chemical modification of lysine residues has also yielded negatively-charged enzymes with greater thermostability and enzymatic activity [8]. Different lysine-modified horseradish peroxidase preparations have shown greater stability in urea and dimethyl sulfoxide solutions as well as higher thermal stability [9, 10]. Lysine-modified papain has also shown increased catalytic activity and stability than native papain [11].

α -Amylases form an important group of enzymes due to their use (starch hydrolysis) in the initial stages of various industrial processes [12]. Among various α -amylases, *Bacillus licheniformis* α -amylase (BLA) has remained the enzyme of choice in many industries due to its high thermostability [13]. It consists of 483 amino acid residues [14], distributed in the form of three domains, namely, 'A', 'B' and 'C' [15]. Domain 'B' is characterized by the presence of two calcium binding sites, while the third calcium binding site is located at the interface of domains 'A' and 'C' [16]. Presence of calcium at the binding sites of this enzyme contributes significantly toward stabilization of its structure and increased enzymatic activity [17-19]. A few salt bridges present in BLA are also believed to be responsible for high thermostability of the enzyme [16]. A previous report has shown production of highly negatively-charged variants of BLA through acetylation, which were found active, thermostable and more resistant towards irreversible inactivation [8]. However, data about the influence of

acetylation on the conformational stability of BLA against urea is lacking. Here, we present our results on the production of acetylated BLA derivative with increased chemical stability.

RESULTS AND DISCUSSION

Acetylation of BLA

Modified amino groups in a protein are usually determined by TNBSA assay [20]. Any decrease in the color intensity at 335 nm of the yellow-colored trinitrophenyl derivatives formed from the reaction of TNBSA with the protein's amino groups indicates amino groups' modification. Figure 1 shows results of TNBSA color reaction obtained with native and acetylated (treated with 20-fold molar excess of acetic anhydride) BLAs. Increase in the protein concentration for both native and acetylated BLAs produced a linear increase in the absorbance at 335 nm (Abs_{335nm}). However, acetylated BLA showed reduction in the slope value compared to the native BLA, indicating lesser intensity of the trinitrophenyl derivatives. This loss in the color yield suggested modification of the amino groups of BLA. The linear plots obtained with native and acetylated BLAs (Figure 1) obeyed the following straight line equations (1) and (2), respectively.

$$Abs_{335nm} = 2.29 \times \text{Amount of protein (mg)} + 0.032 \quad (1)$$

$$Abs_{335nm} = 1.22 \times \text{Amount of protein (mg)} + 0.035 \quad (2)$$

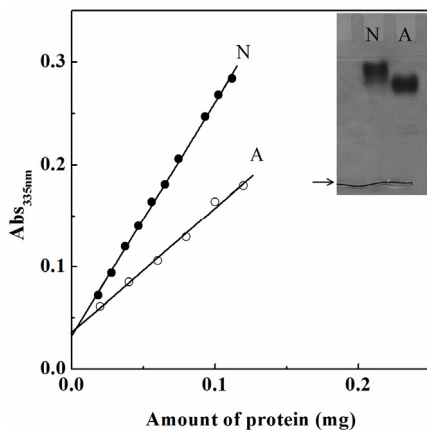


Figure 1. Determination of TNBSA color reaction of native, 'N' BLA (●) and acetylated, 'A' BLA (○). The least squares analysis was used to draw the straight lines. Insert shows electrophoretogram of native, 'N' and acetylated, 'A' BLAs on 10% polyacrylamide gel. Arrow indicates the position of the bromophenol blue as a tracking dye marker.

The percentage of modification in the acetylated BLA was found to be ~47%, as determined from the TNBSA plots of native and acetylated BLAs (Fig. 1). This yielded the number of the modified amino groups in 47% acetylated BLA as 14 based on the presence of 1 α -amino and 28 ϵ -amino groups in BLA [16].

Electrophoretic results of the native and acetylated BLAs on 10% polyacrylamide gel showed charge homogeneity due to the presence of a single major band (inset of Fig. 1). However, acetylated BLA moved with higher relative mobility (0.23) compared to 0.10 obtained with native BLA. Such increase in the relative mobility of acetylated BLA seems to be understandable as acetylation neutralized some of the positive charges in the protein [21]. These results agreed well with a previous report on carbamylation of BLA, where the modified protein showed higher mobility due to neutralization of positive charges of amino groups [22]. However, the value of relative mobility obtained with acetylated BLA was found lesser than that obtained with carbamylated BLA [22]. Since, carbamylated BLA had 81% modification, the net negative charge would have been higher than the acetylated BLA with 47% modification. The elution profiles of native and acetylated BLA preparations on a Superdex 200 column also showed a single symmetrical peak, which was suggestive of size homogeneity of these preparations (Fig. 2).

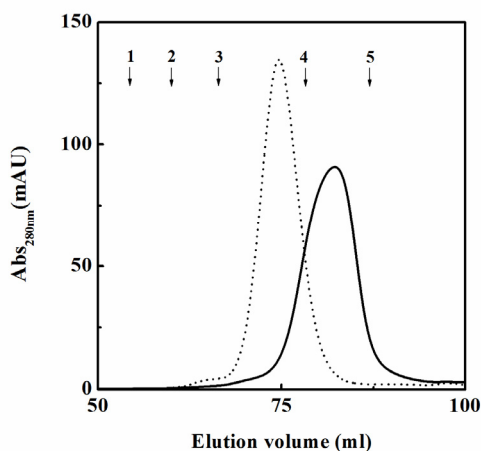


Figure 2. Elution profiles of native (—) and acetylated (.....) BLAs on Superdex 200 column (0.8 × 53.5 cm) equilibrated with 20 mM Tris-HCl buffer, pH 7.0. Protein samples (2 mg/mL) were injected through the injection valve and eluted at a flow rate of 0.5 mL/min. Arrows (1–5) indicate the position of different standard proteins: 1. β -amylase; 2. alcohol dehydrogenase; 3. BSA; 4. carbonic anhydrase and 5. myoglobin.

Conformational Changes in Acetylated BLA

Stokes radii and CD spectral measurements were made to study conformational changes in BLA upon acetylation.

Stokes Radii

Stokes radii of native and acetylated BLAs were determined on a calibrated Superdex 200 column (0.8 × 53.5 cm) in 20 mM Tris-HCl buffer, pH 7.0. The elution profiles of native (N) and acetylated (A) BLAs are shown in Figure 2. The peak positions of various standard proteins *viz.* β -amylase, alcohol dehydrogenase, BSA, carbonic anhydrase and myoglobin on the same column are indicated by arrows 1–5. The void volume and the inner volume of the column were found to be 40.66 and 110.38 mL, respectively. Table 1 shows the values of the elution volume (V_e) of different standard proteins along with native and acetylated BLAs. As shown in Figure 2 and Table 1, acetylated BLA eluted earlier ($V_e = 74.71$ mL) than the native BLA ($V_e = 82.03$ mL), suggesting increase in the hydrodynamic volume of the acetylated BLA [23, 24]. Further analysis of these elution profiles was made by transforming elution volumes of the native and acetylated BLAs as well as marker proteins into K_d and K_{av} values [25] (Table 1). These values were then treated according to the methods of Ackers [26] and Laurent and Killander [27] (columns 5 and 6 in Table 1). Linear plots obtained by these treatments (Figures 3A and B) followed equations (3) and (4), respectively.

$$\text{Stokes radius (nm)} = 7.06 \times \text{erfc}^{-1} K_d - 2.22 \quad (3)$$

$$(-\log K_{av})^{1/2} = 0.11 \times \text{Stokes radius (nm)} + 0.23 \quad (4)$$

Table 1. Analytical gel filtration data of various marker proteins, native and acetylated BLAs on Superdex 200 column (0.8 × 53.5 cm) at pH 7.0.

Proteins	V_e (mL)	K_d	K_{av}	$\text{erfc}^{-1} K_d$	$(-\log K_{av})^{1/2}$	Stokes radius (nm)
β -Amylase	54.35	0.127	0.196	1.078	0.841	5.4
Alcohol dehydrogenase	59.95	0.179	0.278	0.963	0.746	4.6
BSA	66.34	0.239	0.368	0.833	0.659	3.6
Carbonic anhydrase	78.26	0.349	0.539	0.665	0.518	2.4

Proteins	Ve (mL)	K_d	K_{av}	$\text{erfc}^{-1} K_d$	$(-\log K_{av})^{1/2}$	Stokes radius (nm)
Myoglobin	86.98	0.430	0.664	0.560	0.421	1.8
Native BLA	82.03	0.384	0.593	0.617	0.476	2.13 (Eq. 3) 2.14 (Eq. 4)
Acetylated BLA	74.71	0.316	0.488	0.709	0.558	2.78 (Eq. 3) 2.86 (Eq. 4)

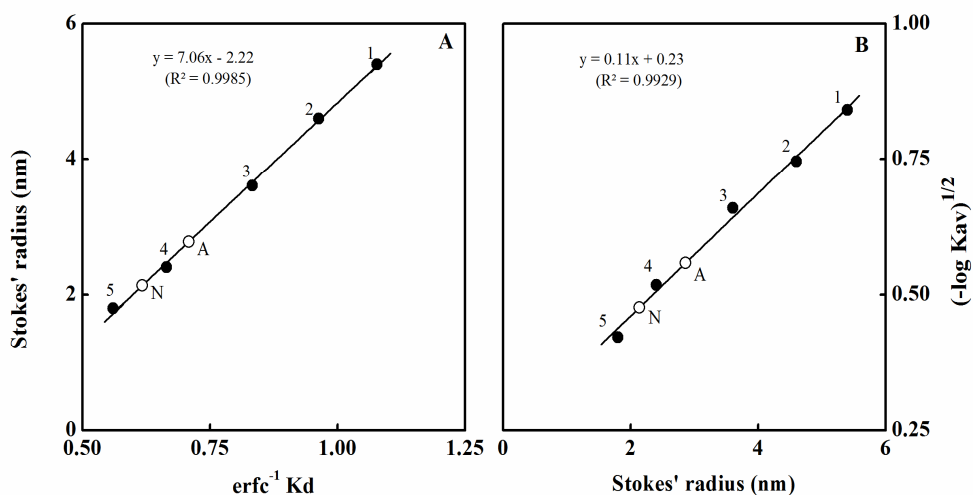


Figure 3. Stokes radii determination of native, 'N' and acetylated, 'A' BLAs according to the method of (A) Ackers [26] and (B) Laurent and Killander [27]. Numbers 1–5 refer to various standard proteins as 1. β -amylase; 2. alcohol dehydrogenase; 3. BSA; 4. carbonic anhydrase and 5. myoglobin. The least squares analysis was used to draw the straight lines.

Stokes radii of native and acetylated BLAs, obtained from equations (3) and (4) together with their mean values are listed in the last column of Table 1. The value of the Stokes radius of native BLA (2.13 nm), as determined by Superdex 200 gel filtration was found much smaller compared to the Stokes radius value (3.20 nm), obtained by dynamic light scattering [17]. Such a lower value of the Stokes radius can be ascribed to the interaction of the enzyme with various gel matrices [28]. Irrespective of this difference, acetylated BLA yielded a value of 2.82 nm for the Stokes radius (Table 1), which was higher than the Stokes radius of the native BLA, suggesting increase in the hydrodynamic volume of the enzyme. Several earlier reports have shown increase in the Stokes radius of a protein upon acetylation [29, 30]. Acetylation

of amino groups increases the net negative charge on a protein by abolishing the positive charge on amino groups, which may be responsible for such increase in the hydrodynamic volume of the protein [29, 30].

Far-UV and Near-UV CD Spectra

The far-UV and the near-UV CD spectra were used to study the effect of acetylation on the secondary and tertiary structures of BLA, respectively. Occurrence of two minima at 208 and 222 nm in the far-UV CD spectrum of native BLA (Fig. 4A) suggested the presence of the α -helical structure [31]. Acetylated BLA produced comparable CD spectrum (Fig. 4A), suggesting presence of similar secondary structures in the acetylated preparation. In a previous report, Shaw *et al.* have also shown superimposable far-UV CD spectra upon acetylation of 17 amino groups of BLA [8]. Nonetheless, significant alteration in the near-UV CD spectrum (255–285 nm) of the acetylated BLA was observed (Fig. 4B), indicating changes in the tertiary structure of BLA brought about by acetylation. This was in accordance to an earlier report on citraconylation of BLA, showing tertiary structural changes upon modification [31]. Since acetylation abolishes the positive charge on amino groups, changes in the protein's tertiary structure are expected due to alteration in the charge network of the native protein [31].

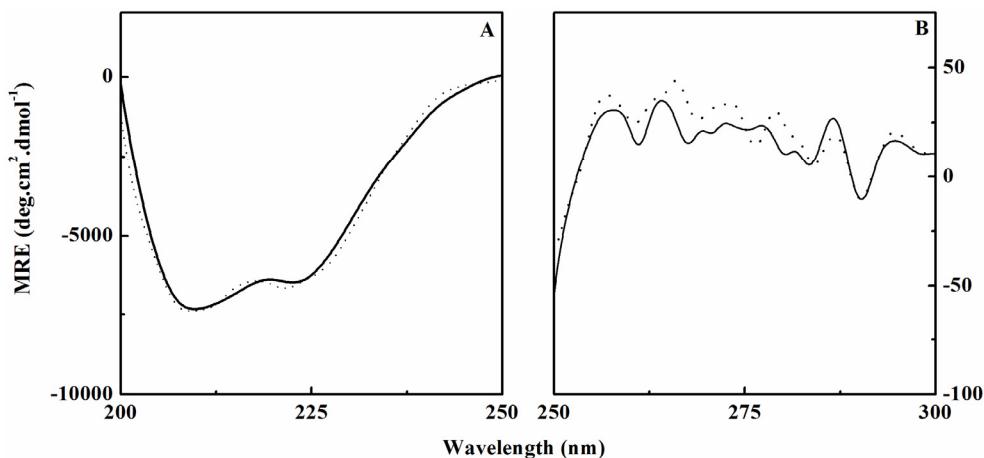


Figure 4. Far-UV CD (A) and near-UV CD (B) spectra of native (—) and acetylated (·····) BLAs, obtained in 20 mM Tris-HCl buffer, pH 7.0 at 25°C. The protein concentration and cuvette path length were 1.8 μ M; 1 mm and 9.1 μ M; 10 mm for far-UV and near-UV CD spectral measurements, respectively.

Urea Denaturation

Conformational stability of native and modified BLAs was investigated by urea denaturation studies [32]. CD spectral measurements (MRE_{222nm}) were used to monitor urea-induced structural changes in the protein. MRE_{222nm} values of the native and the modified BLAs, collected at various urea concentrations were converted into the fraction denatured, F_D and plotted against urea concentration to yield a denaturation curve (Fig. 5A). As shown in the figure, both native and modified BLAs produced a single-step, two-state transition. Urea transition for native BLA commenced at 1.75 M and sloped off at ~ 5.5 M with the mid-point (C_m) occurring at 3.55 M urea concentration (Fig. 5A). A previous study has shown the occurrence of these points at much higher urea concentrations [22] compared to those found in this study. Differential saturation of commercial BLA samples with bound calcium may account for such differences in the above values. Furthermore, use of different pH in the denaturation study may also contribute to this effect. Interestingly, the transition curve of the acetylated BLA showed a significant shift towards higher urea concentrations, suggesting higher chemical stability of the modified BLA compared to the native BLA. The values of the start-, the mid- and the end-points of the transition were obtained at 2.25, 4.0 and 6.5 M urea, respectively (Fig. 5A). These results clearly suggested stabilization of the acetylated BLA against urea denaturation.

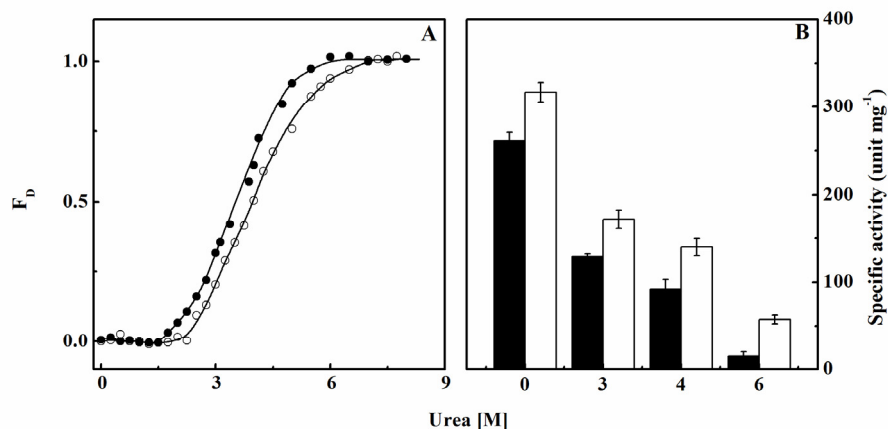


Figure 5. (A) Normalized transition curves of urea-induced structural changes in native (●) and acetylated (○) BLAs, as studied by MRE_{222nm} measurements in 20 mM Tris-HCl buffer, pH 7.0 at 25°C. (B) Effect of urea concentration on the specific activity of native (■) and acetylated (□) BLAs.

Enzymatic Activity

The enzymatic activity of native and acetylated BLAs was checked both in the absence and the presence of different urea concentrations. Figure 5B shows the effect of urea (3, 4 and 6 M) on the enzymatic activity of native and acetylated BLAs. As evident from the figure, acetylated BLA produced a significantly higher (21%) enzymatic activity compared to the native BLA in the absence of urea. In an earlier study, modified papain has been shown to exhibit significantly higher activity in buffer compared to its native counterpart [11]. About 54% and 44% enzymatic activity was retained in the acetylated BLA in the presence of 3.0 and 4.0 M urea, respectively. These values were 32% and 52%, respectively, higher than those obtained with the native BLA at these urea concentrations. Even at 6.0 M urea, acetylated BLA showed 18% retention of the enzymatic activity compared to the 6% retention observed with the native BLA.

CONCLUSIONS

Taken together, acetylated BLA (with 47% modified amino groups) was found to be more stable and resistant against urea denaturation. Since acetylation of BLA altered the tertiary structure without changing secondary structures, it seems that alteration in the overall conformation induced by abolishment of positive charges on lysine residues might have increased hydrophobic interactions in the modified protein.

EXPERIMENTAL SECTION

Materials

Bacillus licheniformis α -amylase (BLA) (lot 018K7018V), alcohol dehydrogenase, β -amylase, bovine serum albumin (BSA), carbonic anhydrase, myoglobin, Superdex® 200 (prep grade), blue dextran, 3,5-dinitrosalicylic acid, starch from potatoes and urea (SigmaUltra) were supplied by Sigma-Aldrich Co., USA. Maltose was obtained from R & M Chemicals, UK. Acetic anhydride was acquired from Riedel-de Haën, Germany. Tris base and 2,4,6-trinitrobenzene sulfonic acid (TNBSA) were the products of Amresco, USA and Pierce Chemical Company, USA, respectively. Analytical grade samples of other chemicals were used.

Analytical Methods

Protein estimations were made either by the method of Lowry *et al* [33] using BSA as the standard or spectrophotometrically on a Shimadzu double-beam spectrophotometer, model UV-2450 (Shimadzu, Kyoto, Japan), using a molar extinction coefficient of BLA as $139,690 \text{ M}^{-1} \text{ cm}^{-1}$ at 280 nm [18]. The method of Pace and Scholtz was employed to determine the concentration of the stock urea solution [34].

Polyacrylamide Gel Electrophoresis

Electrophoresis of BLA was performed under non-denaturing conditions (without sodium dodecyl sulfate) on 10% polyacrylamide gel in 25 mM Tris and 192 mM glycine buffer, pH 8.3, following the method of Laemmli [35]. About 5 μg protein in 7 μL of the sample buffer was applied into each well and the electrophoresis was performed for 45 min, using a current of 10 mA / well. Coomassie brilliant blue R-250 solution was used for gel staining as described earlier [35].

Analytical Gel Filtration

Stokes radii of native and acetylated BLAs were determined by analytical gel filtration [23]. A Superdex 200 column ($0.8 \times 53.5 \text{ cm}$), equilibrated with 20 mM Tris-HCl buffer, pH 7.0 was used in ÄKTA avant 25. Blue dextran and L-tyrosine were used to determine the void volume and inner volume of the column, respectively. Native and acetylated BLA samples as well as standard protein markers with known Stokes radii i.e. myoglobin (1.8 nm), carbonic anhydrase (2.4 nm), BSA (3.6 nm), alcohol dehydrogenase (4.6 nm) and β -amylase (5.4 nm) were also passed through the column. Each protein sample was passed at least 2–3 times to check the reproducibility of results. Normalization of the elution volume was made into distribution coefficient, K_d and available distribution coefficient, K_{av} following the standard methods [25]. The data (K_d and K_{av}) were then fitted according to the methods of Ackers [26] and Laurent and Killander [27] and the Stokes radii of native and acetylated BLAs were obtained from the linear equations of the above plots.

Circular Dichroism Spectroscopy

Any change in the secondary and tertiary structures of the acetylated BLA was studied by circular dichroism (CD) spectroscopy using Jasco spectropolarimeter, model J-815, equipped with a peltier type temperature controller (PTC-423S/15) attached to cell holder under constant nitrogen

flow. Far-UV (200–250 nm) CD spectra were used to analyze changes in the secondary structure, while tertiary structural changes were monitored by near-UV (250–300 nm) CD spectra. The CD instrument was calibrated with (+)-10-camphorsulfonic acid. The protein sample (1.8 μ M) was taken in 1 mm path length cuvette for CD spectral measurement in the far-UV range, while 9.1 μ M sample was used in 10 mm path length cuvette for near-UV CD spectra. The scan speed and response time were fixed at 100 nm / min and 1 s, respectively, throughout the experiment. Each CD spectrum was taken as an average of three scans and CD spectra were corrected by subtracting the CD spectral contribution of the blank solutions from the CD spectra of the protein. The results were transformed into mean residue ellipticity (MRE) in deg.cm².dmol.⁻¹ following the procedure described earlier [36].

Preparation of Acetylated BLA

Acetylated BLA preparation was made according to the method suggested by Riordan and Vallee [37]. Using 20-fold molar excess of acetic anhydride over protein, aliquots of acetic anhydride were added slowly to 50 mL continuously stirred BLA solution (10 mg/mL), prepared in 0.1 M sodium phosphate buffer, pH 7.4 for about 30 min at 4°C. The pH of the solution mixture was maintained at pH 7.4–7.8 with the help of 1N sodium hydroxide and stirring was continued until pH of the solution became constant. After completion of the reaction, the mixture was extensively dialyzed against 20 mM Tris-HCl buffer, pH 7.0 with several changes. TNBSA reaction method was employed to determine the extent of the lysine modification [20]. The modified protein sample was also checked for possible modification of tyrosine residues by hydroxylamine treatment [38].

Urea Denaturation

Urea denaturation studies were made in the same way as described earlier [22]. All solutions used in these experiments were prepared in 20 mM Tris-HCl buffer, pH 7.0. To 0.5 mL protein solution, taken in different tubes, different volumes of the above buffer were added, followed by the addition of increasing volumes of the stock urea solution (10.2 M) in order to achieve the desired urea concentration. The mixtures (3.0 mL) were incubated for 12 h at 25°C before CD spectral measurements. The values of MRE were converted into fraction denatured, F_D [32] and plotted against urea concentration. The mid-point, C_m values were obtained directly from the F_D curve as the urea concentration corresponding to 0.5 F_D value.

Enzymatic Activity

Native and acetylated BLAs were submitted for enzymatic activity measurements both in the absence and presence of different urea concentrations (3, 4 and 6 M) in 20 mM Tris-HCl buffer, pH 7.0 using potato starch (substrate), following the method of Bernfeld [39]. The enzymatic reaction was initiated by adding 0.4 mL of the activity buffer and 0.5 mL of the substrate solution (1% starch, w/v) to 0.1 mL of the stock enzyme solution (0.72 μ M). After 3 min incubation at 25°C, the reaction was stopped by adding 1.0 mL of 1% (w/v) 3,5-dinitrosalicylic acid and the tubes were kept in the boiling water bath for 5 min. The mixture was diluted by adding 10 mL of water into these tubes upon cooling to room temperature. The absorbance of the colored solution was measured at 540 nm against a suitable blank. The concentration of reducing sugars was determined from the maltose standard curve. The specific activity of the enzyme was calculated following the procedure described elsewhere [36]. All solutions used for enzymatic activity measurement in the presence of different urea concentrations contained the desired urea concentration. The protein samples were first incubated with different urea concentrations for 12 h at 25°C before enzymatic activity measurements.

ACKNOWLEDGEMENTS

This project was financed by University of Malaya Research Grant (RG160-11AFR) and Postgraduate Research Fund (PV018/2011B). S.T. is a member of the CRYSTAL research group. A.A.A.H. also acknowledges the UM scholarship. We thank the Dean, Faculty of Science and the Head, Institute of Biological Sciences for providing all necessary facilities and working atmosphere to carry out this work.

REFERENCES

1. C.N. Pace, B.A. Shirley, M. McNutt, K. Gajiwala, *Federation of American Societies for Experimental Biology*, **1993**, 10, 75.
2. K.A. Dill, *Biochemistry*, **1990**, 29, 7133.
3. V.I. Padma, A. Laxmi, *Process Biochemistry*, **2008**, 43, 1019.
4. J. Vidya, M.V. Ushasree, A. Pandey, *Enzyme Microbial Technology*, **2014**, 56, 15.
5. G.R. Grimsley, K.L. Shaw, L.R. Fee, R.W. Alston, B.M. Huyghues-Despointes, R. L. Thurlkill, J. M. Scholtz, C. N. Pace. *Protein Science*, **1999**, 8, 1843.

6. Y. Miki, K. Kakuyama, K. Soda, *Biosystems*, **1997**, *44*, 69.
7. T. Takita, T. Aono, H. Sakurama, T. Itoh, T. Wada, M. Minoda, K. Yasukawa, K. Inouye, *Biochimica et Biophysica Acta*, **2008**, *1784*, 481.
8. B.F. Shaw, G.F. Schneider, B. Bilgiçer, G.K. Kaufman, J.M. Neveu, W.S. Lane, J.P. Whitelegge, G.M. Whitesides, *Protein Science*, **2008**, *17*, 1446.
9. L. Hassani, R. Nourozi, *Applied Biochemistry and Biotechnology*, **2014**, *172*, 3558.
10. N.N. Ugarova, G.D. Rozhkova, I.V. Berezin, *Biochimica et Biophysica Acta*, **1979**, *570*, 31.
11. A. Szabó, M. Kotormán, I. Laczkó, L.M. Simona, *Process Biochemistry*, **2009**, *44*, 199.
12. R. Gupta, P. Gigras, H. Mohapatra, V.K. Goswami, B. Chauhan, *Process Biochemistry*, **2003**, *38*, 1599.
13. N. Declerck, M. Machius, P. Joyet, G. Wiegand, R. Huber R, C. Gaillardin, *Biologia*, **2002**, *57*, 203.
14. T. Yuuki, T. Nomura, H. Tezuka, A. Tsuboi, H. Yamagat, N. Tsukagoshi, S. Udaka, *The Journal of Biochemistry*, **1985**, *98*, 1147.
15. M. Machius, G. Wiegand, R. Huber, *Journal of Molecular Biology*, **1995**, *246*, 545.
16. N. Declerck, M. Machius, G. Wiegand, R. Huber, C. Gaillardin, *Journal of Molecular Biology*, **2000**, *301*, 1041.
17. J. Fitter, S. Haber-Pohlmeier, *Biochemistry*, **2004**, *43*, 9589.
18. A.R. Nazmi, T. Reinisch, H-J. Hinz, *Journal of Thermal Analysis and Calorimetry*, **2008**, *91*, 141.
19. A. Kumari, T. Rosenkranz, A. M. Kayastha, J. Fitter, *Biophysical Chemistry*, **2010**, *151*, 54.
20. A.F.S.A. Habeeb, *Analytical Biochemistry*, **1966**, *14*, 328.
21. M.M. Gote, M.I. Khan, J.M. Khire, *Enzyme Microbial Technology*, **2007**, *40*, 1312.
22. C.Y. Tan, R.N.Z. Raja Abdul Rahman, H.A. Kadir, S. Tayyab, *Acta Biochimica Polonica*, **2011**, *58*, 405.
23. H.N. Ong, B. Arumugam, S. Tayyab, *The Journal of Biochemistry*, **2009**, *146*, 895.
24. S.A. Datta, C.H. Mohan Rao, *The Journal of Biological Chemistry*, **2000**, *275*, 41001.
25. S. Tayyab, S. Qamar, M. Islam, *Biochemical Education*, **1991**, *19*, 149.
26. G.K. Ackers, *The Journal of Biological Chemistry*, **1967**, *242*, 3237.
27. T.C. Laurent, J. Killander, *Journal of Chromatography A*, **1964**, *14*, 317.
28. J.E. Kruger, D.R. Lineback, "Enzymes and their role in the cereal technology", AACC, Minnesota, **1987**, 117.
29. A.A. Ansari, S.A. Kidwai, A. Salahuddin, *The Journal of Biological Chemistry*, **1975**, *250*, 1625.
30. S. Tayyab, S.K. Haq, Sabeeha, M.A. Aziz, M.M. Khan, S. Muzammil, *International Journal of Biological Macromolecules*, **1999**, *26*, 173.

31. K. Khajeh, B. Ranjbar, H. Naderi-Manesh, A.E. Habibi, M. Nemat-Gorgani, *Biochimica et Biophysica Acta*, **2001**, 1548, 229.
32. Y.H. Wong, H.A. Kadir, S. Tayyab, *The Scientific World Journal*, **2013**, Article ID: 981902.
33. O.H. Lowry, N.J. Rosebrough, A.L. Farr, R.J. Randall, *The Journal of Biological Chemistry*, **1951**, 193, 265.
34. C.N. Pace, J.M. Scholtz, "Protein structure. A practical approach", Oxford University Press, New York, **1997**, 299.
35. U.K. Laemmli, *Nature*, **1970**, 227, 680.
36. C.Y. Tan, R.N.Z. Raja Abdul Rahman, H.A. Kadir, S. Tayyab, *African Journal of Biotechnology*, **2010**, 46, 7934.
37. J.F. Riordan, B.L. Vallee, *Methods in Enzymology*, **1967**, 11, 565.
38. J.F. Riordan, B.L. Vallee, *Methods in Enzymology*, **1967**, 11, 570.
39. P. Bernfeld, *Advances in Enzymology*, **1951**, 12, 379.

HETEROLOGOUS EXPRESSION AND PURIFICATION OF RECOMBINANT PROAPOPTOTIC HUMAN PROTEIN SMAC/DIABLO WITH EGFP AS FUSION PARTNER

PÁL SALAMON^{a,b}, ILDIKÓ MIKLÓSSY^a, BEÁTA ALBERT^a,
MÓNIKA KORODI^a, KATALIN NAGY^c, ILDIKÓ BAKOS^c,
SZABOLCS LÁNYI^{a,c}, CSONGOR ORBÁN^{a,*}

ABSTRACT. New proteins as molecular targets in development of therapies are discovered every day. However, study of their interactions with other proteins or binding partners in complex cellular environments has its limits. Therefore, high-yield production of these proteins in heterologous systems is a valid necessity, while obtaining these proteins linked to suitable fluorescent markers represents a step ahead in protein-protein interaction studies and cellular or subcellular localization.

In this study, we present production of human SMAC/Diablo recombinant protein with EGFP as a fusion partner. High-yield expression of the fusion protein was carried out in *E. coli* Rosetta™(DE3)pLysS strain, and an acceptable purity of the protein was obtained after affinity chromatography purification and gel filtration. The obtained protein can be further used in protein-protein interaction studies, whereas our method represents a cost-effective and efficient production method for EGFP-fused proteins, applicable for a number of therapeutically important polypeptides.

Keywords: *SMAC/Diablo, apoptosis, heterologous expression, EGFP fusion proteins*

^a SAPIENTIA Hungarian University of Transylvania, Faculty of Economics, Socio-Human Sciences and Engineering, Department of Bioengineering, 1 Libertatii Square, RO-530104, Miercurea Ciuc, Romania

^b University of Medicine and Pharmacy of Targu Mures, Faculty of Pharmacy, 38 Gheorghe Marinescu str., RO-540139, Targu Mures, Romania

^c University POLITEHNICA of Bucharest, Faculty of Applied Chemistry and Materials Science, Str. Gh. Polizu, Nr. 1-7, Sector 1, 011061 Bucuresti, Romania

* Corresponding author: orbancsongor@uni.sapientia.ro

INTRODUCTION

A complex regulatory network of protein activation and inhibition maintains optimal cellular function. In case of malfunctions of this system, various diseases can develop. Apoptosis, or programmed cell death represents a vital mechanism in maintenance of tissue homeostasis and development of the immune system. Tumor cells are responsive to both internal and external stress, while being resistant to apoptosis [1]. Changes in the rate of apoptosis may have pathological consequences: an increase in apoptosis rate can cause neurodegenerative diseases, while a decrease can cause cancer.

SMAC/Diablo (second mitochondria - derived activator of caspase direct inhibitor of apoptosis-binding protein with low pI) is a newly discovered pro-apoptotic mitochondrial caspase activator protein [1]. Changes in permeability of the mitochondrial membrane SMAC/Diablo is released in concert with cytochrome-C, and it binds to the anti-apoptosis IAPs (inhibitor of apoptosis proteins) in the cytosol. By inhibition of these proteins, apoptosis is promoted [2].

SMAC/Diablo protein was identified as a cytochrome-C/APAF-1/caspase-9 pathway caspase activation mitochondrial protein [3]. It is known that SMAC/Diablo neutralizes XIAP in the cytosol, while generating additional initiator caspase activity [1, 2]. The first 55 amino acids of the protein sequence represent a mitochondrial signal peptide, while the mature protein presents an Amino-terminal AVPI-end, which is essential for the function of SMAC/Diablo protein as a natural antagonist of anti-apoptosis proteins (IAPs) [4]. The molecular weight of the mature protein is 20.8 kDa, which occurs in the cytosol in a tetrameric structure [5]. In the BioGrid (Biological General Repository for Interaction Datasets) database there are listed a number of 45 known protein-protein interactions involving SMAC/Diablo.

The discovery of GFP protein [6, 7] and the two-photon microscope [8] allowed the development of fluorescence microscopy applications in cell biology [9]. The wide-range use of GFP is a consequence of its unique properties: reduced sensitivity to higher temperatures, detergents, alkaline pH, photobleaching, organic salts, chaotropic salts and many proteases [10]. EGFP (enhanced green fluorescent protein, a mutant version of GFP) has emerged as a powerful fluorescent label for quantitative fluorescence microscopy applications [11]. EGFP contains two amino acid substitutions (Ser65Thr and Phe64Leu), that lead to a 35-fold enhancement of fluorescence over wild-type green fluorescent protein (wtGFP) [12]. Using an EGFP-fused protein we can track and quantify the fusion protein, examine protein-protein interactions, describe biological events and signals in cells, or even apply these fusion constructs in drug discovery processes.

In the light of the above, the aim of the study was fusion of human SMAC/Diablo recombinant protein with EGFP, expression of the fusion construct in prokaryotic host cells, namely in *E. coli* Rosetta™(DE3)pLysS strain and the subsequent purification by affinity chromatography followed by gel filtration (size exclusion chromatography). The EGFP-fusion construct was intended to assure easy and specific detection of SMAC/Diablo in further experiments.

Our data supports that using a prokaryotic expression system in bioreactor cultures we can cost-effectively produce the recombinant protein in large quantities. With the affinity and gel filtration chromatography we can isolate an adequately pure protein which can be further used in oncological or cell biology research.

RESULTS AND DISCUSSION

Modelling of SMAC_EGFP fusion protein structure

In the first phase of our study, in order to assess structural stability of the created SMAC_EGFP fusion protein, and more importantly, to predict structural changes which could affect the functionally essential Amino-terminal AVPI segment of Smac/Diablo, we performed analysis of the 3D structural model of the fusion protein.

The tridimensional structure model was obtained by homology modelling, whereas homologous sequences were compiled using the Phyre2 online search engine [13].

The Amino-terminus of the recombinant fusion protein sequence starts with a methionine (Figure 1, marked in yellow), which is removed during translation by methionyl aminopeptidase. Removal of the methionine results in the mature Amino-terminus beginning with the AVPI amino acid sequence (marked in red), which is considered crucial to its interaction with the IAP proteins. EGFP is marked with green, its Carboxyl-terminus being continued with a 6xHis tag (marked in purple), required for affinity chromatography.

The tridimensional model of the fusion protein reveals presence of the significant secondary structural elements of SMAC/Diablo reported in crystallographic studies [14], as well as the free Amino-terminal AVPI sequence, whereas the EGFP presents its characteristic beta-barrel [15]. Based on the above mentioned results, we concluded that the SMAC_EGFP_His recombinant fusion protein would retain the structural elements required for SMAC/Diablo function.

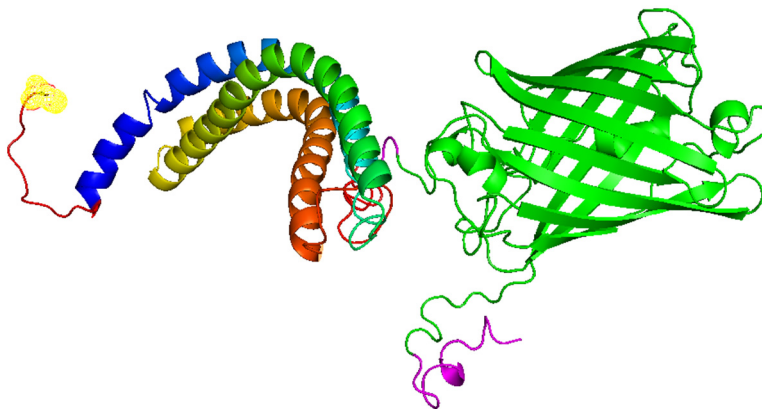


Figure 1. SMAC_EGFP 3D ribbon model.
(yellow – N terminal methionine, red – N-term AVPI, green – EGFP, purple – His tag. Structural model compiled by Phyre2 online search engine, visualized and edited in PyMol).

Design and assembly of the SMAC_EGFP_His construct

The SMAC_EGFP_His construct was designed taking into account the chosen heterologous *E. coli* pET-based expression system (pET20b vector with *E. coli* Rosetta™(DE3)pLysS as a host strain), as well as the downstream purification steps. Restriction map of the designed vector is presented in Figure 2, outlining the significant elements of the recombinant construct. Vector selection was based on our previous experience in high-yield protein production, according to which these expression plasmids proved to be extremely reliable for the production of a number of proteins.

Coding sequences for SMAC/Diablo and EGFP, respectively, were obtained by PCR, specific primers being designed (as described in the Experimental section) to assure the restriction sites selected for cloning (XbaI and BamHI for the SMAC sequence, and BamHI and NotI for EGFP).

The expression vector was obtained by directional cloning carried out with the above mentioned restriction endonucleases (details in Experimental section), whereas assembly of the two coding sequences was performed by one-step ligation. Verification of the correct plasmid assembly and conformation, respectively, and incorporation of the gene construct into the vector structure was carried out by subsequent restriction digestions. Correct integration of the SMAC_EGFP_His construct into the plasmid pET20b was verified by digestion with NotI, EcoRI and XmnI.

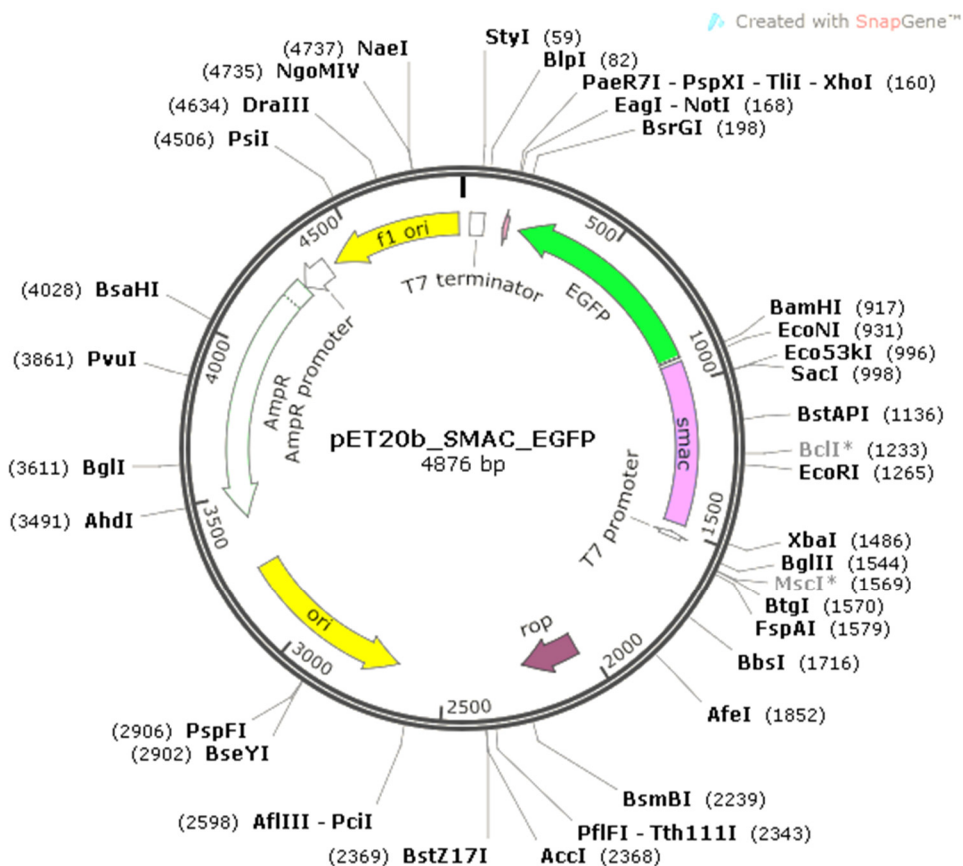


Figure 2. Restriction map of pET20b_SMAC_EGFP expression plasmid, outlining significant features of the vector (Map created in SnapGene).

The expected fragments were 3779 bp and 1097 bp for the NotI, EcoRI double digestion, respectively 2942 bp and 1934 bp for the digestion performed by the double-cutter XmnI. The results of the restriction digestions are visualized in Figure 3, where presence of restriction fragments of the expected length supports formation of the correct structure of the recombinant vector and successful ligation of the SMAC_EGFP construct.

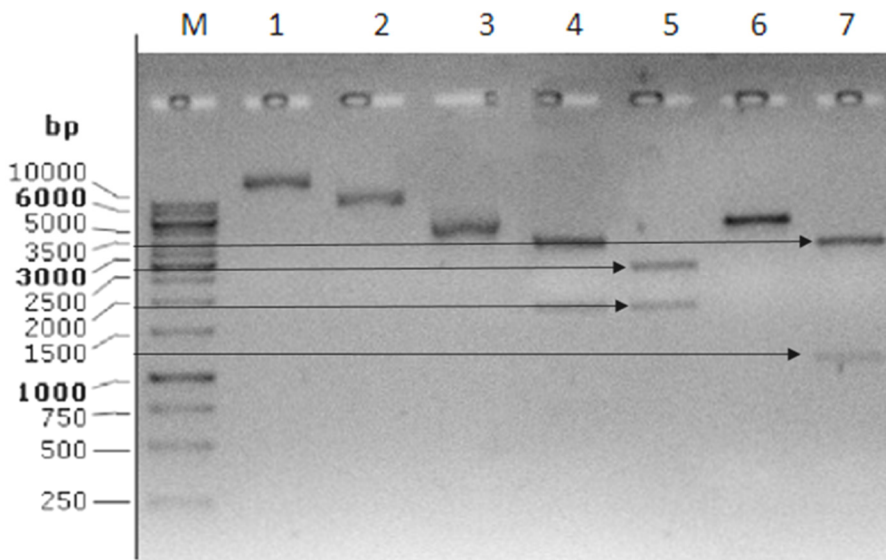


Figure 3. Result of pET20b_SMAC_EGFP plasmid digestion: (M) - 1 kb DNA ladder GeneRuler; (1) - pET20b_1; (2) - pET20b_2; (3) - pET20b; (4) - pET20b_1 XmnI; (5) - pET20b_2 XmnI; (6) - pET20b_1 Not + Eco RI; (7) - Not + Eco RI pET20b_2. (Reaction products were separated by electrophoresis on a 1% agarose gel and visualized by RedSafe staining).

High-yield expression of the SMAC_EGFP fusion protein

To ensure high-yield production of the SMAC_EGFP fusion protein, a bioreactor system was used, as cultivation of transformed expression strains under controlled process parameters offers the possibility to obtain high biomass levels, and consequently, high protein production rates.

The SMAC_EGFP recombinant protein was expressed in a Biostat A plus bioreactor, in cultures of *E. coli Rosetta*TM(DE3)pLysS strain transformed with the pET20b_SMAC_EGFP expression vector. Fermentation conditions, determined previously in small-scale expression experiments (data not shown) were 37 °C, pH 7.0, using an M9 mineral medium with 2 g/L glucose as the sole carbon source. Induction of target protein expression by the strong T7 promoter was performed by addition of 1 mM IPTG to the culture media at OD~20. During the derepression period, cells were further cultivated at 18 °C to facilitate correct folding of the protein. After 16 hours of expression, we obtained a biomass yield of 40 g WCW/1 L culture. Our procedure for high-yield protein expression obtained in high-density bacterial cultures has

resulted in similar protein production rates reported in other studies concerning expression of alcohol-dehydrogenase [16], even labeled eukaryotic proteins [17] or for expression of genes from heterologous biosynthetic pathways [18].

Two-step purification of recombinant SMAC_EGFP

As downstream experiments often require a highly purified protein solution, purification of the obtained recombinant SMAC_EGFP was carried out in two consequent steps, by Ni-affinity binding followed by size exclusion chromatography. Results of the fusion protein purification by affinity chromatography were verified by SDS-PAGE gel analysis (Figure 4, lanes 6 and 7). As our results illustrate, the Ni-NTA affinity resin non-specifically bound other proteins from the production culture, along with the target protein. However, we found our SMAC_EGFP being the predominant protein fraction with a relative molecular weight of 52 kDa in the elution fractions 6 and 7 (Figure 4). Due to non-specific binding, further purification of the protein solution was implemented by size exclusion chromatography.

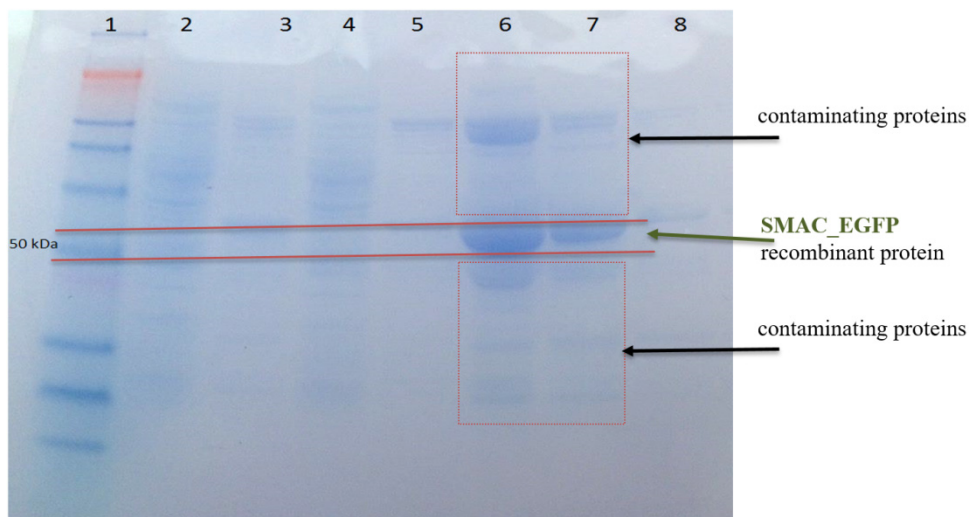


Figure 4. SDS-PAGE gel analysis of affinity chromatography purification of the obtained fusion protein. (1) - PageRuler™ Prestained NIR Protein Ladder, (molecular weight marker from Thermo Scientific™); (2) – total cell protein, (3) – total soluble protein, (4) – flow through, (5) – fraction 6, 250 mM imidazole elution, (6) – fraction 7, 250 mM imidazole elution, (7) – fraction 8, 250 mM imidazole elution, (8) – fraction 9, 250 mM imidazole elution

Based on our SDS-PAGE results (Figure 5) illustrating the downstream purification steps, the non-specifically bound proteins remaining in the eluted protein fractions after affinity purification were eliminated by size exclusion chromatography. Concentration of the recombinant protein after gel filtration was determined $2.5 (\pm 0.03)$ mg/mL, obtained in a total volume of 8 mL, with a total quantity of 20 mg pure recombinant protein SMAC_EGFP.

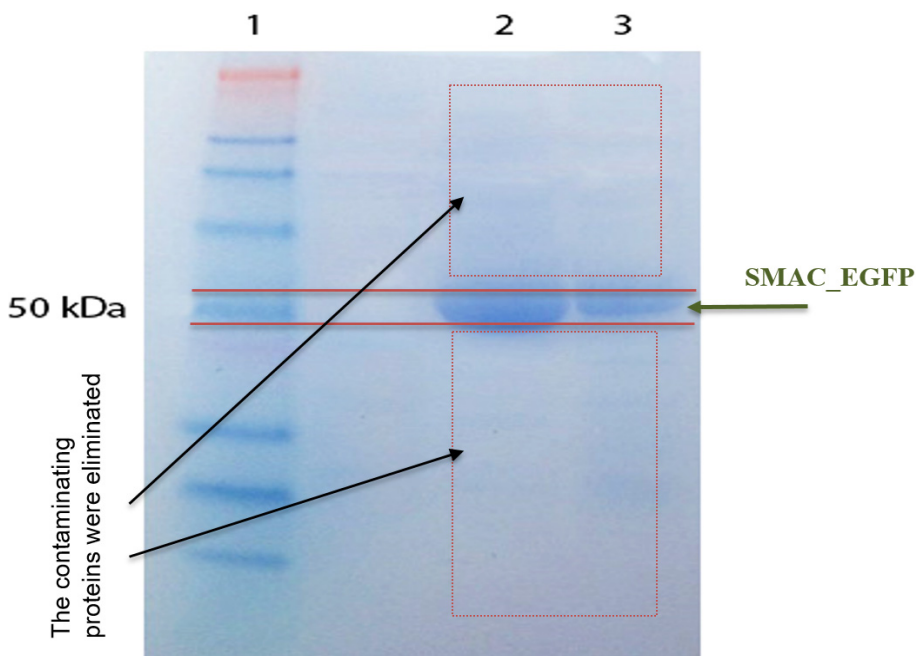


Figure 5. SDS-PAGE gel analysis of the second purification step of SMAC_EGFP by size exclusion chromatography. (1) - PageRuler™ Prestained NIR Protein Ladder (molecular weight marker from Thermo Scientific™); (2) - SMAC_EGFP eluted fraction, 20 μ L; (3) - SMAC_EGFP eluted fraction, 10 μ L

CONCLUSIONS

Based on the results of restriction endonuclease digestion confirmed by sequencing of the plasmid we have successfully assembled the SMAC_EGFP_His recombinant construct. For expression of the SMAC_EGFP recombinant protein, the *E. coli* expression strain Rosetta™(DE3) pLysS transformed with the recombinant vector was used successfully under the following conditions: 16 hours of cultivation after induction with 1 mM concentration of IPTG at 18 °C.

A significant quantity of 20 mg/L of pure recombinant SMAC_EGFP protein was obtained by applying the above conditions in a bioreactor culture. Regarding the downstream purification procedure, our two-step affinity and size exclusion chromatography protocol proved to be successful, as we obtained a protein solution in adequately pure form for further investigations, e.g. protein-protein interactions in cancer and cell and biology research.

EXPERIMENTAL SECTION

Oligonucleotide design for PCR and DNA manipulations

The properties of primers, designed for cloning are shown in table 1. During the PCR reaction the FW_BamHI_EGFP and Rev_NotI_EGFP, FW_XbaI_SMAC and Rev_BamHI_SMAC primers, respectively, were used together. In the cloning PCR reactions, the pSmac-GFP vector (nr. 40881 from ADDGENE) was used to obtain the SMAC coding sequence.

Table 1. Properties of oligonucleotides used for cloning

Name	Sequence	Nr. of nucleotides	Melting temp.	Restriction site
FW_BamHI_EGFP	5'GCGTAGGATC CCCATATGGTG AGCAAGG3'	28 bp.	60 °C	BamHI (5'...GGATCC...3')
Rev_NotI_EGFP	5'GTATTAGCGG CCGCTCTGAGT CCGGA CT TGTA CAG3'	35 bp.	60 °C	NotI (5'...GCGGCCG ...3')
FW_XbaI_SMAC	5'GGTCTAGATA AGGGAAGCTTA TGGCG3'	26 bp.	59 °C	XbaI (5'...TCTAGA...3')
Rev_BamHI_SMA C	5'GTAGTAGTAG GATCCGCATCC TCACGCAG3'	29 bp.	60 °C	BamHI (5'...GGATCC...3')

Thermal cycles and reaction components used to assemble the XbaI_SMAC_BamHI construct:

Cycles	Temp.	Time	Reaction mix	
1x	95 °C	2 min	10x PFU buffer	5 µL
35x	95 °C	0.5 min	10 mM dNTP	1 µL
	53 °C	0.5 min	100 mM FW_XbaI_SMAC primer	0.5 µL
	72 °C	1 min	100 mM Rev_BamHI_SMAC primer	0.5 µL
1x	72 °C	7 min	Template DNA	1 µL
			PFU enzyme	1 µL
			Sterile water	41 µL
			Total	50 µL

Thermal cycles and reaction components used to create the BamHI_EGFP_NotI construct:

Cycles	Temp.	Time	Reaction mix	
1x	95 °C	2 min	10x PFU buffer	5 µL
35x	95 °C	0.5 min	10 mM dNTP	1 µL
	47 °C	0.5 min	100 mM FW_BamHI_EGFP primer	0.5 µL
	72 °C	1 min	100 mM Rev_NotI_EGFP primer	0.5 µL
1x	72 °C	7 min	Template DNA	1 µL
			PFU enzyme	1 µL
			Sterile water	41 µL
			Total	50 µL

The PCR products were purified by Thermo Scientific GeneJET PCR Purification Kit, according to the manufacturer's recommendations, then in order to create cohesive ends, the samples were digested with restriction endonucleases (double digests), according to the reaction set-ups presented in Table 2. Both digests were incubated at 37 °C (Thermo-Shaker TS-100C) for 1 hour and inactivated at 80 °C for 20 minutes. The pET20b plasmid was also digested at 37 °C for 1 hour, then incubated at 80 °C for 20 minutes to inactivate the restriction enzyme.

Table 2. Restriction reaction set-up

XbaI + BamHI digestion		BamHI + NotI digestion		XbaI + NotI digestion	
XbaI_SMAC_BamHI PCR product	25 µL	BamHI_EGFP_NotI PCR product	24 µL	pET20b plasmid	10 µL
10x Tango buffer	3 µL	10x BamHI buffer	3 µL	10x Orange buffer	3 µL
XbaI enzyme (5 U/µL)	1 µL	BamHI enzyme (5 U/µL)	1 µL	XbaI enzyme (5 U/µL)	4 µL
BamHI enzyme (5 U/µL)	1 µL	NotI enzyme (5 U/µL)	2 µL	NotI enzyme (5 U/µL)	1 µL
Total	30 µL	Total	30 µL	Sterile water	12 µL
				Total	30 µL

To increase the efficiency of ligation of the digested plasmid pET20b and the digested PCR products, both were separated on a 1% agarose and the appropriate fragments were isolated with the GeneJet Gel Extraction Kit (Thermo).

The PCR products and the plasmid pET20b were ligated O.N., 16 °C using T4 DNA ligase enzyme (Thermo Scientific). Ligation mixtures were transformed into chemically competent *E. coli* Top10F and selected on ampicillin containing LB plates.

Expression of human recombinant SMAC_EGFP protein in bioreactor cultures

Recombinant protein production was carried out in a 1 L capacity Sartorius Biostat®A Plus Bioreactor, using BioPAT®MFCS/DA Supervisory Control and Data Acquisition (SCADA) Software. The reactor was firstly loaded with 1 L basic M9 broth. The system was autoclaved for 20 minutes at 120 °C, in order to ensure sterility. After sterilization, the reactor was connected to aeration, acid and base solutions, temperature control system and control unit. After the reactor has cooled down (<40 °C), thermally unstable compounds were added (Table 3. marked with *) through a sterile filter (0.25 µm). In order to homogenize the system, mixing, temperature, and pH control were launched: 400 RPM, 37 °C, pH 6.9. After the stabilization of the reactor, the reactor was inoculated under sterile conditions with 10 mL inoculum. The culture at this stage was grown at 37 °C, with a dissolved oxygen level above 40%, and pH 6.9. When the cell density reached OD₆₀₀=20, the temperature was set to 18 °C and the protein expression was induced with isopropyl-thiogalactopyranoside (IPTG) (1 mM final concentration). Protein expression was carried out at 18 °C, O.N. (16 hours).

In order to harvest the cells, 1 L culture was centrifuged (12,000xg for 10 min at 4 °C), and the cell pellets were stored at -80 °C until further processing (Thermo Scientific FORM 88000 series).

Cell lysis was performed as follows: 1 gram of cells were resuspended in 5 mL of lysis buffer (20 mM Tris-HCl (pH 8), 250 mM NaCl, 2 mM DTT, 1 mM PMSF, protease inhibitor cocktail). Cell disruption was performed with a Microfluidizer LM10, in order to increase the efficiency, the micro-flight compression was performed twice. The resulting cell extract was centrifuged at 4 °C, 60,000xg, for 60 minutes in order to separate the solubilized proteins from cellular debris.

Table 3. Composition of 1x M9 minimal broth

Component	Concentration	1000X TRACE elements	
Na ₂ HPO ₄	3.54 g/L	FeCl ₃ ×6H ₂ O	50 mM
NaCl	0.50 g/L	CaCl ₂	20 mM
KH ₂ PO ₄	3.40 g/L	MnCl ₂ ×4H ₂ O	10 mM
NH ₄ Cl*	2.00 g/L	ZnSO ₄ ×7H ₂ O	10 mM
C ₆ H ₁₂ O ₆ *	2.00 g/L	CoCl ₂	2 mM
MgSO ₄ *	2.00 mM	CuCl ₂ ×2H ₂ O	2 mM
CaCl ₂ *	0.02 mM	NiCl ₂ ×6H ₂ O	2 mM
Ampicillin*	100 µg/mL	Na ₂ MoO ₄ ×2H ₂ O	2 mM
TRACE*	1X	Na ₂ SeO ₃ ×5H ₂ O	2 mM
		H ₃ BO ₃ ×5H ₂ O	2 mM
		HCl	60 mM

*- Added after sterilization

Purification of recombinant SMAC_EGFP protein

Affinity chromatographic purification was carried out using a 2x5 ml HisTrap (GE Healthcare) column with an ÄKTA FPLC system. Data acquisition and system control were carried out with a UNICORN 5.11 software package. The column, the protein solution and the buffers were kept at 4 °C. The wash buffer contained 20 mM Tris-HCl (pH 8), 250 mM NaCl, 2 mM DTT, 1 mM PMSF, 20 mM imidazole. The elution buffer contained 20 mM Tris-HCl (pH 8), 250 mM NaCl, 2 mM DTT, 1 mM PMSF, 500 mM imidazole. Purification parameters were set at: 10 mL column volume, 1 mL/min flow rate, 2 mL fraction volume. A cell lysate of 200 mL volume was injected, while the elution step was performed in one step, at 250 mM imidazole concentration. Following affinity chromatography, the purified protein was dialyzed for 24 hours, at 4 °C, under stirring, in the following buffer: 20 mM Tris-HCl (pH 8), 250 mM NaCl, 2 mM DTT, 1 mM PMSF.

Size exclusion chromatography purification was carried out using a HiLoad16/600, Superdex 75 column with a 20 mM Tris-HCl (pH 8.0, 250 mM NaCl, 2 mM DTT, 1 mM PMSF solution as the mobile phase.

ACKNOWLEDGMENTS

Our work was carried out with the support of the Romania Ministry of Education in the framework of PN-II-PT-PCCA-2013-4 project.

REFERENCES

1. G. Martinez-Ruiz, V. Maldonado, G. Ceballos-Cancino, J. Grajeda, J. Melendez-Zajgla, *Journal of experimental & clinical cancer research*, **2008**, 27, 48.
2. A.M. Verhagen, P.G. Ekert, M. Pakusch, J. Silke, L. Connolly, G. Reid, D. Vaux, *Cell*, **2000**, 102, 43.
3. C. Du, M. Fang, Y. Li, L. Li, X. Wang, *Cell*, **2000**, 102, 33.
4. L. Ma, Y. Huang, Z. Song, S. Feng, X. Tian, W. Du, M. Wu, *Nature*, **2006**, 13, 2079.
5. E. Mastrangelo, P. Vachette, F. Cossu, F. Malvezzi, M. Bolognesi, M. Milani, *Biophysical Journal*, **2015**, 714.
6. R.Y. Tsien, *Annu. Rev. Biochem*, **1998**, 67, 509.
7. M. Chalfie, Y. Tu, G. Euskirchen, W.W. Ward, D.C. Prasher, *Science*, **1994**, 263, 802-805.
8. W. Denk, J.H. Strickler, W. W. Webb, *Science*, **1990**, 248, 73.
9. R. Yuste, *Nature*, **2005**, 902-904.
10. M.A. Ehrmann, C.H. Scheyhing, R.F. Vogel, *Letters in Applied Microbiology*, **2001**, 32, 230.
11. R.M. Hoffman, *Laboratory Investigation*, **2015**, 95, 432.
12. J. Sun, G.H. Kelemen, J.M. Fernandez-Abalos, M.J. Bibb, *Microbiology*, **1999**, 145, 2221.
13. L.A. Kelley, S. Mezulis, C.M. Yates, M.N. Wass, M.J.E. Sternberg, *Nature Protocols*, **2015**, 10, 845.
14. G. Wu, J. Chai, T.L. Suber, J.W. Wu, C. Du, X. Wang, Y. Shi, *Nature*, **2000**, 408, 1008.
15. A. Royant, M. Noirclerc-Savoie, *Journal of Structural Biology*, **2011**, 174, 385.
16. J. Glazyrina, E. Materne, T. Dreger, D. Storm, S. Junne, T. Adams, G. Greller, P. Neubauer, *Microbial Cell Factories*, **2010**, 9, 42.
17. A. Sivashanmugam, V. Murray, C. Cui, Y. Zhang, J. Wang, Q. Li, *Protein Science*, **2009**, 18(5), 936.
18. Z. Lai, R. Rahim, A. Ariff, R. Mohamad, *Journal of Microbiology, Biotechnology and Food Sciences*, **2016**, 6(3), 905-910.

FINAL RADIOCARBON INVESTIGATION OF PLATLAND TREE, THE BIGGEST AFRICAN BAOBAB

ADRIAN PATRUT^{a,*}, STEPHAN WOODBORNE^b,
ROXANA T. PATRUT^c, LASZLO RAKOSY^c, GRANT HALL^d,
ILEANA-ANDREEA RATIU^a, KARL F. VON REDEN^e

ABSTRACT. The article discloses the main results of our new investigation of Platland tree, a.k.a. Sunland baobab, the largest known African baobab. Our recent research was motivated by the three successive splits of 2016 and 2017, which determined the collapse and demise of the stems that have built the main unit of the tree. According to our new findings concerning the architecture of large and old baobabs, we established that Platland tree has a double closed-ring shaped structure and consists of two units/rings that close two separate false cavities. The larger unit was composed of five fused stems, out of which four toppled and died, while the fifth stem is already broken. The smaller unit, which is still standing, consists of three fused stems. We also determined that the larger unit had an age of 800 yr, while the smaller unit is 1100 yr old.

Keywords: AMS radiocarbon dating, *Adansonia digitata*, tropical trees, ring-shaped structure, age determination, false cavity.

INTRODUCTION

The African baobab (*Adansonia digitata* L.), which has a natural distribution in mainland Africa, is the largest and best-known of the nine *Adansonia* species [1-3]. In 2005, we initiated a long-term research for

^a Babeş-Bolyai University, Faculty of Chemistry and Chemical Engineering, 11 Arany Janos, RO-400028, Cluj-Napoca, Romania.

^b iThemba Laboratories, Box 722 Somerset West, 7129, South Africa.

^c Babeş-Bolyai University, Faculty of Biology and Geology, 44 Gheorghe Bilascu, RO-400015, Cluj-Napoca, Romania.

^d Mammal Research Institute, University of Pretoria, 0001, South Africa.

^e NOSAMS Facility, Dept. of Geology & Geophysics, Woods Hole Oceanographic Institution, Woods Hole, MA 02543, U.S.A.

* Corresponding author: apatrut@gmail.com

clarifying several controversial aspects concerning the architecture, growth and age of the African baobab. The research is mainly based on our methodology which consists of AMS radiocarbon dating of small wood samples collected from inner cavities, but also from deep incisions in the stems, fractured stems and from the exterior of large baobabs [4-8].

According to dating results, all large baobabs are multi-stemmed. Due to the special ability of baobabs to produce stems periodically during their life cycle, they develop architectures of increasing complexity. Therefore, we focused on the investigation of superlative individuals, i.e., very large and potentially old baobabs. We documented the open and closed ring-shaped structures, which are the most important architectures that enable African baobabs to reach old ages and large sizes. We also identified the presence of false cavities, which are large natural empty spaces between several fused stems disposed in a closed ring-shaped structure, which have never been filled with wood [9-13]. The oldest dated *A. digitata* specimens were found to have ages greater than 2000 yr [14,15]. Dated growth rings of several African baobab specimens act as a proxy climate archive and have been used for past climate reconstruction in southern Africa [16,17].

The Platland tree, a.k.a. Sunland baobab, is or was the biggest African baobab and also angiosperm, with a total wood volume of 501 m³ [8]. The Platland tree is probably the most promoted and visited African baobab. It is widely known especially due to the pub which was established inside its largest false cavity. Over the past years, we visited and investigated several times this superlative baobab. In our first radiocarbon investigation of a live African baobab, we determined the fire history of the Platland tree, by dating several new growths layers which covered the original old wood from its cavities. These new growth layers were triggered by successive fires inside the cavities [7]. In the second investigation, we determined the ages of the two units which build the Platland tree [8].

Here we present new results of the investigation of the Platland tree, mainly carried out after the successive splits of 2016 and 2017, which determined the collapse and death of its larger unit.

RESULTS AND DISCUSSION

The Platland tree and its area. The Platland tree is located on the private Sunland Mango Nursery of the former Platland farm, at 10 km from Modjadjiskloof and 25 km from Tzaanen, in the Limpopo Province, South Africa. Its GPS coordinates are 23°37.259' S, 030°11.888' E and the altitude is 717 m. Mean annual rainfall in the area is 802 mm (Modjadjiskloof station).

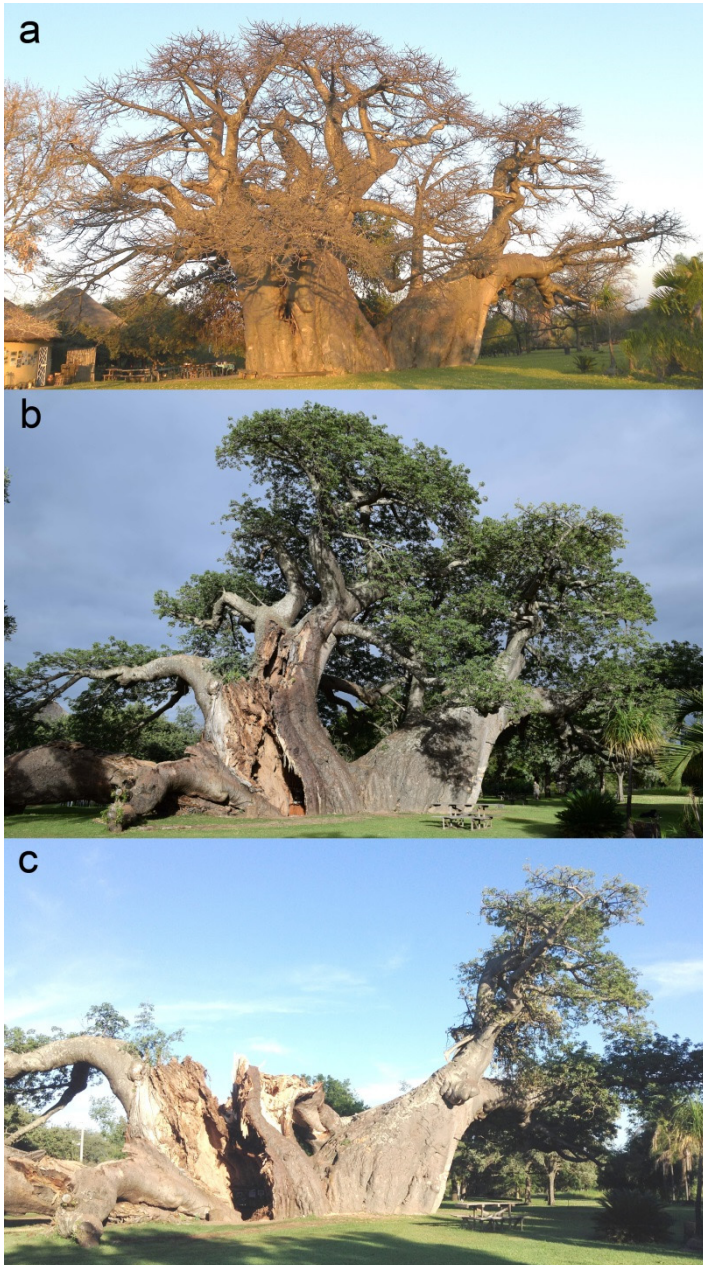


Figure 1. General view of the Platland tree taken from the east: **(a)** when it was still the largest African baobab; **(b)** after the second split of August 2016; **(c)** after the third split of April 2017.

The Platland tree consists of two units I and II, which are both multi-stemmed (**Figure 1a**). Its maximum height was 18.9 m, the circumference at breast height (cbh; at 1.30 m above ground level) was 34.11 m and the basal surface of 67.9 m² corresponded to a formal diameter of 9.30 m. The overall wood volume was 501 m³, out of which 364 m³ for unit I and 137 m³ for unit II. The horizontal canopy dimensions are 37.7 x 32.4 m [8].

The Platland tree has a double closed ring-shaped structure with two false cavities. The two units that build the tree correspond each to a closed ring. The two rings/units are connected by a fused section, which covers a shared cbh of 4.10 m and has a maximum height of 2.20 m. The two false cavities are connected by a small opening.

The cavity inside the larger unit I has a maximum length of 4.60 m, a width of 4.81 m, a height of 4.88 m and a basal surface of 15.9 m². The false cavity inside the smaller unit II has the linear dimensions of 1.67 x 2.50 x 2.47 m and a basal surface of 2.8 m².

Unfortunately, the larger unit I of Platland tree split three times, in May 2016, August 2016 and April 2017. Four of its five stems toppled and died. The fifth stem which is broken will also collapse soon (**Figure 1b** and **1c**). The stems of the larger unit I were partially rotten. It is still uncertain whether the smaller unit II, composed of three stems, which was hit during the third split, will survive or not.

Wood samples. Five wood samples (labelled 11-15) were collected from two fallen stems of unit I. Other two samples (labelled 21 and 22) were collected from the walls of the false cavity inside unit II.

A number of seven small pieces/segments, of the length of 0.001 m each, were extracted from the samples 11-15 and from the deepest ends of samples 21 and 22.

AMS results and calibrated ages. Radiocarbon dates of the seven segments are listed in Table 1. Radiocarbon dates and errors were rounded to the nearest year. The radiocarbon dates are expressed in ¹⁴C yr BP (radiocarbon years before present, i.e., before the reference year AD 1950).

Calibrated (cal) ages, expressed in calendar years, are also displayed in Table 1. The 1- σ probability distribution was selected to derive calibrated age ranges. For four sample segments the 1- σ distribution is consistent with only one range of calendar years. For the other three sample segments, the 1- σ distribution is consistent with two or three ranges of calendar years. For these three segments, the confidence interval of one range is considerably greater than that of the other(s); therefore, it was selected as the cal AD range of the segment for the purpose of this discussion. For obtaining single calendar age values of sample segments, we derived a mean age of each

segment from the selected range (marked in bold). Calendar ages of segments represent the difference between AD 2017 and the mean value of the selected range, with the corresponding error. Calendar ages and errors were rounded to the nearest 5 yr.

Table 1. AMS Radiocarbon dating results and calibrated calendar ages of samples/segments collected from the Platland tree.

Sample (Segment)	Depth ¹ [height ²] (10 ⁻² m)	Radiocarbon date [error] (¹⁴ C yr BP)	Cal AD range 1-σ [confidence interval]	Sample age [error] (cal yr)
11	-	665 [± 23]	1314-1358 [54.4%] 1380-1391 [13.8%]	680 [± 20]
12	-	765 [± 18]	1276-1294 [68.2%]	730 [± 10]
13	-	546 [± 19]	1413-1434 [68.2%]	595 [± 10]
14	-	728 [± 16]	1282-1302 [52.3%] 1365-1375 [15.9%]	725 [± 10]
15	-	785 [± 18]	1266-1288 [68.2%]	740 [± 10]
21	35 [135]	914 [± 25]	1160-1208 [68.2%]	835 [± 25]
22	42 [160]	978 [± 14]	1046-1089 [41.0%] 1109-1120 [7.9%] 1130-1151 [19.3%]	950 [± 20]

¹ Depth in the wood from the sampling point.

² Height above ground level.

Dating results of samples (segments). The five sample segments 11-15 originate from relatively central positions of two fallen and broken stems of unit I, namely from different heights (4.3–10.5 m), i.e., distances from their original base. Their radiocarbon dates between 546 ± 19 and 785 ± 18 BP correspond to calibrated ages of 595 ± 10 and 740 ± 10 calendar yr. Other samples collected from areas around the circumference of the two fallen stems, in direction of the cavity and in the opposite direction toward the outer part/exterior were also dated and found to be greater than Modern (> Modern). In such cases, the dated wood is very young, being formed after AD 1950. The two sample segments 21 and 22, which represent the deepest end of the two samples collected from the walls of the false cavity inside unit II, had radiocarbon dates of 914 ± 25 and 978 ± 14 BP. These values correspond to calibrated ages of 835 ± 25 and 950 ± 20 calendar yr.

Architecture of the Platland tree. The Platland tree was composed of two interconnected units, which were both multi-stemmed. Each unit, which has a false cavity inside, exhibits a closed ring-shaped structure. Thus, the

Platland tree has a double closed ring-shaped structure with two distinct false cavities that communicate via a small opening. The largest unit I was composed of five perfectly fused stems, that collapsed one after another during the three successive splits. The still standing smaller unit II consists of three fused stems.

Ages of the two units of Platland tree. The ages of the five samples 11-15 extracted from two toppled and broken stems of unit I, that were partially rotten, were between 595 and 740 yr. The oldest samples originate from areas close to the presumptive pith (at the respective height) for stems which belong to a closed-ring shaped structure. We consider that the age of the oldest part of unit I must have been close to 800 yr.

The oldest dated sample segment corresponds to the deepest end of sample 22, which was collected from the inner cavity walls inside unit II. This segment that correspond to a depth of 0.42 m in the wood from the sampling point, was 950 yr old. By considering that the width of the cavity walls in this area is 1.20 m and also the age sequences of stems which belong to a ring-shaped structure, we estimate that the age of unit II is around 1100 yr.

These ages of the two units of Platland tree are very close to the age values proposed by us in a previous research, in which we also discussed a possible scenario for explaining why the smaller unit II is considerably older than the larger unit I [8].

CONCLUSIONS

The research presents the results of the final investigation of the largest known African baobab, namely the Platland tree, a.k.a. Sunland baobab, located in the Limpopo province, South Africa. This new research, which was mainly based on AMS (accelerator mass spectrometry) radiocarbon dating, aimed to establish the true architecture and age of the baobab. We determined that the Platland tree has a double closed ring-shaped structure and consists of two units/rings with two distinct false cavities inside.

The larger unit/ring was composed of five fused stems, while the smaller unit/ring consists of three fused stems. In 2016 and 2017, the larger unit split three times, so that four stems toppled and died. According to the new dating results, the larger unit was 800 yr old, while the still standing smaller unit has an age of 1100 yr.

The death of the majority of the oldest and largest African baobabs, which were all located in southern Africa, over the past years, is an event of an unprecedented gravity. The fact that these demises were not caused by an epidemic suggests that they were engendered by significant modifications of the climate conditions, which affect especially southern Africa. The devastating drought over the past years in southern Africa was determined mainly by the

intensification of El Niño, which warms the waters in the equatorial Pacific and can lead to unusually heavy rains in some parts of the world and drought elsewhere. The Platland tree might be the latest victim of these climate modifications.

EXPERIMENTAL SECTION

Sample collection. The five wood samples 11-15, which originate from unit I, were extracted with a sharp instrument from central areas of two fallen and broken stems, which were partially decayed. The other two samples 21 and 22 were collected by using a Haglöf CH 800 increment borer (0.80 m long, 0.0054 m inner diameter) from the walls of the cavity inside unit II. A number of seven tiny pieces/segments of the length of 0.001 m were extracted from each wood sample. The segments were processed and investigated by AMS radiocarbon dating.

Sample preparation. The standard acid-base-acid pretreatment method was used for removing soluble and mobile organic components. The pretreated samples were combusted to CO₂ by using the closed tube combustion method [18]. Then, CO₂ was reduced to graphite on iron catalyst, under hydrogen atmosphere [19]. Finally, the resulting graphite samples were analysed by AMS.

AMS measurements. AMS radiocarbon measurements were performed at the NOSAMS Facility of the Woods Hole Oceanographic Institution (Woods Hole, MA, U.S.A.) by using the Pelletron® Tandem 500 kV AMS system. The obtained fraction modern values, corrected for isotope fractionation with the normalized $\delta^{13}\text{C}$ value of -25‰ , were ultimately converted to a radiocarbon date.

Calibration. Radiocarbon dates were converted into calendar ages with OxCal v4.2 for Windows [20], using the SHCal13 atmospheric set [21].

ACKNOWLEDGMENTS

Authors thank Heather and Doug van Heerden, the owners of Sunland Nursery, for granting permission and providing support for the investigation and sampling of the Platland baobab. The research was funded by the Romanian Ministry of Scientific Research CNCS-UEFISCDI under grant PN-II-ID-PCE-2013-76.

REFERENCES

1. G.E. Wickens, P. Lowe, "The Baobabs: Pachycauls of Africa, Madagascar and Australia", Springer, Dordrecht, **2008**.
2. D.A. Baum, *Annals of the Missouri Botanical Garden*, **1995**, *82*, 440-471.
3. J.D. Pettigrew, L.K. Bell, A. Bhagwandin, E. Grinan, N. Jillani, J. Meyer, E. Wabuyele, C.E. Vickers, *Taxon*, **2013**, *61*, 1240-1250.
4. A. Patrut, K.F. von Reden, D.A. Lowy, A.H. Alberts, J.W. Pohlman, R. Wittmann, D. Gerlach, L. Xu, C. S. Mitchell, *Tree Physiology*, **2007**, *27*, 1569-1574.
5. A. Patrut, K.F. von Reden, D.A. Lowy, D.H. Mayne, K. E. Elder, M.L. Roberts, A.P. McNichol, *Nuclear Instruments and Methods in Physics Research Section B*, **2010**, *268*, 910-913, doi: 10.1016/j.nimb.2009.10.062.
6. A. Patrut, D.H. Mayne, K.F. von Reden, D.A. Lowy, S. Venter, A.P. McNichol, M.L. Roberts, D. Margineanu, *Radiocarbon*, **2010**, *52*, 727-734.
7. A. Patrut, D.H. Mayne, K.F. von Reden, D.A. Lowy, R. Van Pelt, A.P. McNichol, M.L. Roberts, D. Margineanu, *Radiocarbon*, **2010**, *52*, 717-726.
8. A. Patrut, K.F. von Reden, R. Van Pelt, D.H. Mayne, D.A. Lowy, D. Margineanu, *Annals of Forest Science*, **2011**, *68*, 993-1003.
9. A. Patrut, S. Woodborne, K.F. von Reden, G. Hall, M. Hofmeyr, D. Lowy, R.T. Patrut, *PLoS ONE*, **2015**, *10(1)*, e0117193, doi: 10.1371/journal.pone.0117193.
10. A. Patrut, S. Woodborne, R.T. Patrut, G. Hall, L. Rakosy, K.F. von Reden, D. Lowy, D. Margineanu, *Studia UBB Chemia*, **2015**, *LX*, 4, 7-20.
11. A. Patrut, L. Rakosy, R.T. Patrut, I.A. Ratiu, E. Forizs, D.A. Lowy, D. Margineanu, K.F. von Reden, *Studia UBB Chemia*, **2016**, *LXI*, 4, 7-20.
12. A. Patrut, R.T. Patrut, L. Rakosy, J. Bodis, D.A. Lowy, E. Forizs, K.F. von Reden, *Studia UBB Chemia*, **2016**, *LXI*, 4, 21-30.
13. A. Patrut, S. Garnaoud, O. Ka, R.T. Patrut, T. Diagne, D.A. Lowy, E. Foris, J. Bodis, K.F. von Reden, *Studia UBB Chemia*, **2017**, *LXII*, 1, 111-120, doi:10.24193/subbchem.2017.1.09.
14. A. Patrut, K.F. von Reden, D.H. Mayne, D.A. Lowy, R.T. Patrut, *Nuclear Instruments and Methods in Physics Research Section B*, **2013**, *294*, 622-626, doi: 10.1016/j.nimb.2012.04.025.
15. A. Patrut, S. Woodborne, K.F. von Reden, G. Hall, R.T. Patrut, L. Rakosy, P. Danthu, J.-M. Leong Pock-Tsy, D.A. Lowy, D. Margineanu, *Radiocarbon*, **2017**, *59(2)*, 435-448, doi: 10.1017/RDC.2016.92.
16. S. Woodborne, G. Hall, I. Robertson, A. Patrut, M. Rouault, N.J. Loader, M. Hofmeyr, *PLoS ONE*, **2015**, *10(5)*, e0124202, doi: 10.1371/journal.pone.0124202.
17. S. Woodborne, P. Gandiwa, G. Hall, A. Patrut, J. Finch, *PLoS ONE*, **2016**, *11(7)*, e015936, doi: 10.1371/journal.pone.0159361.
18. Z. Sofer, *Analytical Chemistry*, **1980**, *52*, 1389-1391.
19. J.S. Vogel, J.R. Southon, D.E. Nelson, T. A. Brown, *Nuclear Instruments and Methods in Physics Research Section B*, **1984**, *5*, 289-293.
20. C. Bronk Ramsey, *Radiocarbon*, **2009**, *51*, 337-360.
21. A.G. Hogg, Q. Hua, P.G. Blackwell, M. Niu, C.E. Buck, T.P. Guilderson, T.J. Heaton, J.G. Palmer, P.J. Reimer, R.W. Reimer, C.S.M. Turney, R.H. Zimmerman, *Radiocarbon*, **2013**, *55*, 1889-1903.

RADIOCARBON DATING OF A VERY LARGE AFRICAN BAOBAB FROM LIMPOPO, SOUTH AFRICA: INVESTIGATION OF THE SAGOLE BIG TREE

ADRIAN PATRUT^{a,*}, ROXANA T. PATRUT^b,
ROBERT VAN PELT^c, DANIEL A. LOWY^d, EDIT FORIZS^a,
JENÖ BODIS^a, DRAGOS MARGINEANU^a,
KARL F. VON REDEN^e

ABSTRACT. The article reports the AMS (accelerator mass spectrometry) radiocarbon dating results of Sagole Big tree, a giant African baobab from Limpopo, South Africa. Several wood samples were collected from the walls of its inner cavity and dated by radiocarbon. The age values along the cavity samples increase with the distance into the wood. This anomaly shows that the cavity is a false one. The oldest sample segment had a radiocarbon date of 781 ± 29 BP, which corresponds to a calibrated age of 740 ± 15 yr. We estimate that the oldest part of the Sagole baobab has an age of 800-900 yr. We determined that the tree has a closed ring-shaped structure, which consists of a large unit with six fused stems and of two additional leaning stems.

Keywords: AMS radiocarbon dating, *Adansonia digitata*, tropical trees, ring-shaped structure, age determination, false cavity.

^a Babeş-Bolyai University, Faculty of Chemistry and Chemical Engineering, 11 Arany Janos, RO-400028, Cluj-Napoca, Romania.

^b Babeş-Bolyai University, Faculty of Biology and Geology, 44 Gheorghe Bilascu, RO-400015, Cluj-Napoca, Romania.

^c Institute for Redwood Ecology, Humboldt State University, Arcata, CA 95521, U.S.A.

^d Nova University, 5000 Dawes Ave., Alexandria, VA 22311, U.S.A.

^e NOSAMS Facility, Dept. of Geology & Geophysics, Woods Hole Oceanographic Institution, Woods Hole, MA 02543, U.S.A.

* Corresponding author: apatrut@gmail.com

INTRODUCTION

In 2005, we started a long-term research in order to elucidate several aspects related to the architecture, growth and age of the African baobab (*Adansonia digitata* L.). The research is mainly based on our approach which also allows to investigate and date standing and live baobab specimens. The methodology consists of AMS radiocarbon dating of small wood samples collected from inner cavities and/or deep incisions/entrances in the stems, fractured stems and from the outer part of large baobabs [1-5].

Owing to the special ability of baobabs to produce stems periodically during their life cycle, over time they develop architectures of increasing complexity. That is why our research focused on superlative baobabs, i.e., very large and/or old specimens. According to radiocarbon dating results, all large baobabs are multi-stemmed. We identified the open and closed ring-shaped structures, which are the most important architectures that enable African baobabs to reach old ages and large sizes [6, 7]. Old baobabs have often large cavities, especially in the central area of their trunk/stems. In normal cavities generated by wood removal, the pith/centre of the stem is located inside the cavity. For wood samples extracted from normal cavities, age values decrease continuously from the cavity walls toward the outer part of the stem. Our research of large and old baobabs has identified a major anomaly in the age sequence of cavity samples dated by radiocarbon. In these cases, ages of samples collected from their inner cavities increase from the cavity walls up to a certain distance into the wood, after which they decrease toward the outer part. The only possible explanation for this finding is that such cavities are only natural empty spaces between several fused stems disposed in a closed ring-shaped structure, which were never filled with wood. We named them false cavities. The first significant difference between false and normal cavities is the presence or absence of the bark inside the cavity. Unlike normal cavities, which become larger over time due to continuous decay, false cavities tend to become smaller as a result of stem growth [7-10]. The oldest dated *A. digitata* individuals were found to have ages up to 2500 years [11, 12].

Dated growth rings of several investigated African baobab specimens, which may act as a proxy climate archive, were used for past climate reconstruction in southern Africa [13, 14].

Here we present the investigation results of a giant baobab, i.e., the Sagole Big tree from Limpopo Province, South Africa. The Sagole baobab is included in the Big Tree Register. According to a very controversial formula proposed by the Dendrological Society for calculating the tree size, it has a size index of 426 and it has been officially declared the largest Champion Tree of South Africa [15].

RESULTS AND DISCUSSION

The Sagole Big tree and its area. The Sagole Big tree is located in Zwigodini village at 54 km NNW of Tshipise, in Mutale Municipality, Vhembe District, Limpopo Province, South Africa. The GPS coordinates are 22°30.002' S, 030°37.995' E and the altitude is 359 m. Mean annual rainfall in the area is 354 mm.

Mapping results. The Sagole Big tree consists of a very large unit, which is multi-stemmed and heavily buttressed; it also has two additional leaning stems (**Figure 1**). It has a maximum height of 19.8 m, the circumference at breast height (cbh; at 1.30 m above ground level) is 34.35 m and the basal footprint of 60.6 m², which corresponds to a formal diametre of 9.64 m.



Figure 1. General view of the Sagole Big tree taken from the west.

The overall wood volume is 414 m³, out of which 252 m³ below 5 m and 162 m³ above 5 m. After the recent splits of Platland tree, which had a total wood volume of 501 m³ [16], the Sagole Big tree becomes the largest African baobab (**Figure 2**). The canopy has a total volume of 16,032 m³ and a total surface of 134 m³, which corresponds to a mean crown diametre of 42.7 m.

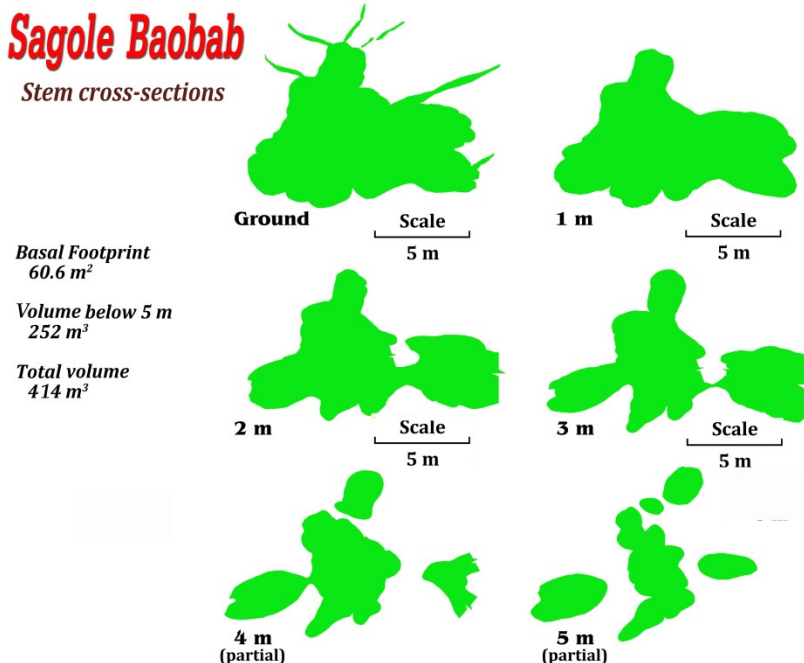


Figure 2. Cross sectional areas of the trunk/stems of Sagole tree at different heights (ground level, 1 m, 2 m, 3 m, 4 m and 5 m).

The Sagole Big tree has a closed ring-shaped structure with a false cavity inside the large unit. The large unit consists of six fused main stems, out of which four build the ring and two are outside the ring. By also considering the two leaning stems, the Sagole baobab consists of eight stems.

The main part of the false cavity, which is covered by bark, has a length of 2.20 m (NS) and a width of 2.70 m (WE); the maximum height is 7.41 m and the basal surface 4.8 m^2 . The cavity also has an appendix toward the north, which is 1.10 m long, has a maximum width of 0.70 m and is not accessible. The entrance into the cavity is possible from the south via a small corridor with a length of 1.30 m, a width between 0.70 and 1.00 m and a height of 3.90 m (**Figure 3**). Similarly to other false cavities, the cavity of Sagole tree is only an empty space between the stems that build the ring. This space which was never filled with wood becomes smaller over time, due to stem growth. There is also a kind of extension toward the south between the two leaning stems, like an uncovered aisle, with a length of 4.36 m and a width of 1.07 m at its end.

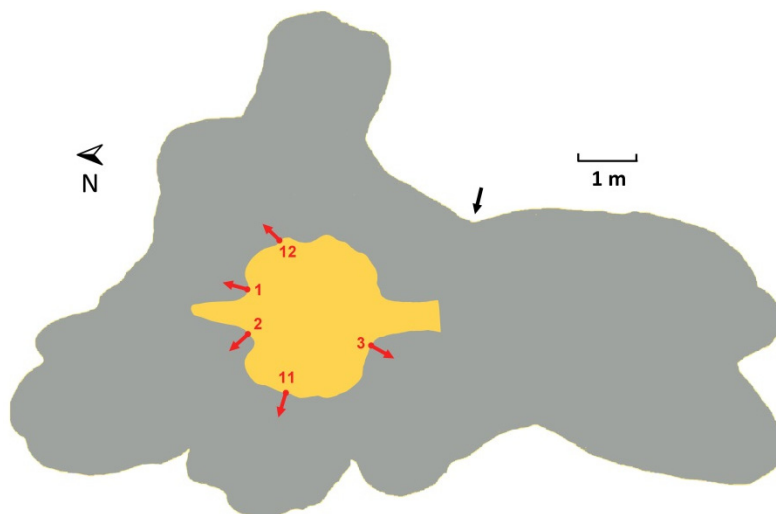


Figure 3. Cross-section of the Sagole tree (at 1 m above ground), showing the position of the false cavity, the positions of the five sampling points and the sampling directions.

Wood samples. Three wood samples (labelled 1-3) were collected from the northern and western walls of the false cavity, at low heights between 0.33 and 0.40 m. The sample lengths were 0.56, 0.33 and 0.30 m. Other two samples (labelled 11 and 12) were collected from the western and eastern walls of the cavity, at greater heights of 1.36 and 1.30 m. These samples were 0.64 and 0.43 m long. A number of 13 small pieces/segments, each of the length of 0.001 m (marked as a, b, c), were extracted from determined positions of the five samples.

AMS results and calibrated ages. Radiocarbon dates of the 13 segments are listed in Table 1. Radiocarbon dates and errors were rounded to the nearest year. The radiocarbon dates are expressed in ^{14}C yr BP (radiocarbon years before present, i.e., before the reference year ad 1950). Calibrated (cal) ages, expressed in calendar years, are also displayed in Table 1. The 1- σ probability distribution was selected to derive calibrated age ranges. For five sample segments, the 1- σ distribution is consistent with only one range of calendar years. For the other eight sample segments, the 1- σ distribution is consistent with two or three ranges of calendar years. For these eight segments, the confidence interval of one range is considerably greater than that of the other(s); therefore, it was selected as the cal AD range of the segment for the purpose of this discussion. For obtaining single calendar age values of sample segments, we

derived a mean calendar age of each segment from the selected range (marked in bold). Calendar ages of segments represent the difference between AD 2017 and the mean value of the selected range, with the corresponding error. Calendar ages and errors were rounded to the nearest 5 yr.

Table 1. AMS Radiocarbon dating results and calibrated calendar ages of samples/segments collected from the Sagole baobab.

Sample (Segment)	Depth ¹ [height ²] (10 ⁻² m)	Radiocarbon date [error] (¹⁴ C yr BP)	Cal AD range 1-σ [confidence interval]	Sample age [error] (cal yr)
1a	20 [33]	195 [± 23]	1670-1696 [20.6%] 1725-1784 [38.2%] 1794-1808 [9.4%]	260 [± 30]
1b	46 [33]	390 [± 18]	1478-1509 [28.0%] 1580-1621 [40.2%]	415 [± 20]
1c	56 [33]	480 [± 25]	1436-1458 [68.2%]	570 [± 10]
2a	21 [33]	197 [± 26]	1668-1696 [19.2%] 1725-1786 [39.7%] 1793-1808 [9.4%]	260 [± 30]
2b	33 [33]	275 [± 21]	1640-1668 [68.2%]	365 [± 15]
3a	10 [40]	227 [± 18]	1667-1672 [6.2%] 1741-1796 [42.0%]	250 [± 25]
3b	20 [40]	335 [± 27]	1510-1576 [52.0%] 1622-1640 [16.2%]	475 [± 35]
3c	30 [40]	436 [± 21]	1452-1490 [68.2%]	545 [± 20]
11a	20 [136]	270 [± 19]	1644-1668 [68.2%]	360 [± 10]
11b	40 [136]	530 [± 25]	1419-1442 [68.2%]	590 [± 10]
11c	64 [136]	781 [± 29]	1234-1244 [12.2%] 1264-1291 [56.0%]	740 [± 15]
12a	25 [130]	212 [± 20]	1670-1688 [8.8%] 1734-1784 [53.8%] 1794-1800 [5.6%]	260 [± 25]
12b	43 [130]	333 [± 24]	1510-1551 [37.0%] 1558-1574 [12.4%] 1622-1642 [18.8%]	485 [± 20]

¹ Depth in the wood from the sampling point.

² Height above ground level.

Dating results of samples (segments). We extracted and dated two or three segments from each sample. For all five samples, the ages of segments increase with the distance into the wood. Consequently, the oldest segments were extracted from the sample ends. For the first three samples collected at lower heights, labelled 1-3, the oldest dated segments, i.e., 1c and 3c, correspond to distances of 0.56 m and 0.30 m into the wood. Their radiocarbon dates of 480 ± 20 and 436 ± 21 BP correspond to calibrated ages of 570 ± 10 and 545 ± 20 calendar yr. For samples 11 and 12 collected at greater heights, the oldest segment 11c, which is also the deepest, was positioned at 0.64 m from the sampling point. Its radiocarbon date of 781 ± 29 BP corresponds to a calibrated age of 740 ± 15 calendar yr.

Architecture and age of the Sagole tree. For the five samples collected from the cavity, the age values increase with the depth into the wood. This anomaly is characteristic only to false cavities. We already mentioned that the Sagole baobab has a closed ring-shaped structure with a false cavity inside the ring.

The tree is composed of a large unit, which consists of six fused main stems, and two leaning stems.

For baobabs that exhibit a closed ring-shaped structure, the oldest stems are always around the false cavity. The oldest dated sample segment 11c has an age of 740 ± 15 yr. The segment originates from a distance of 0.64 m from the inner cavity walls. In this area, the depth of the cavity walls was of 1.60 m. Taking into account our previous research on age sequences along samples collected from stems that build the ring, we consider that the position of segment 11c was close to the point of maximum age in the corresponding direction. Therefore, we estimate that in the point of maximum age, this stem has an age of 800-900 yr, i.e., 850 ± 50 yr. The age of the two stems of the large unit which grow outside the ring, as well as the age of the two leaning stems, that have not been dated, must be considerably lower than the ring, probably up to 500-600 yr.

The age of 800-900 yr for the oldest part of Sagole tree determined via radiocarbon dating, is considerably younger than the age values proposed by other tree researchers. Such high values were suggested by considering the girth of the baobab, which is exaggerated by the buttresses and especially by the leaning stems, but also by the overall size which is due to the large number of stems that build the tree. On the other hand, the age we determined for the Sagole tree is comparable to the age of the large unit of the Platland tree, which toppled and died recently [16]. Finally, we mention that the largest trees are usually not the oldest. The largest specimens are those which had grown very fast when they were young and continued their rapid growth [5].

CONCLUSIONS

The research discloses the main results of the radiocarbon investigation of a giant African baobab, the Sagole Big tree, located in the Limpopo Province, South Africa. The main aim of the research was to determine the architecture and age of the baobab, as well as its accurate size. With a total wood volume of 414 m³, the Sagole Big tree has just become the largest known African baobab. Five wood samples were collected from the walls of its inner cavity. The age values of segments extracted from these samples increase with the distance into the wood. This anomaly is specific to false cavities. The oldest sample segment had a radiocarbon date of 781 ± 29 BP, which corresponds to a calibrated age of 740 ± 15 calendar yr. Based on dating results and accurate measurements, we consider that the oldest part of the Sagole baobab has an age of 800-900 yr. The tree exhibits a closed ring-shaped structure with a false cavity inside. It consists of a large six-stemmed unit and of two additional leaning stems.

EXPERIMENTAL SECTION

Measurements. The external measurements of the Sagole Big tree and the measurements inside the inner cavity was performed by using a Bosch DLE 70 Professional laser rangefinder (Robert Bosch GmbH, Stuttgart, Germany) and graduated tapes. Cross-sections of the baobab at ground level, 1, 2, 3, 4 and 5 m were mapped by setting up a frame around the tree with a graduated tape. A compass and an Impulse 200 laser rangefinder (Laser Technology, Inc., Centennial, CO, U.S.A.) were used to map the cross-sections. Additional cross-sections on the largest section were mapped at 6.5 and 8 m. All of the mostly round branch and stem sections above or around this had their basal diameters estimated by using a Criterion 400 survey laser (Laser Technology, Inc., Centennial, CO, U.S.A.). System lengths were either measured directly or interpreted from detailed photos of the tree structure without leaves. Parabolic or conic equations were used for these smaller systems based on how robust and foliated each system was.

Sample collection. The wood samples were collected from the false cavity walls in the time frame 2008-2011, by using Haglöf CH 600 (0.60 m long, 0.0054 m inner diameter) and Haglöf CH 800 (0.80 m, 0.0108 m) increment borers. A number of tiny pieces/segments of the length of 0.001 m were extracted from each wood sample. The segments were processed and investigated by AMS radiocarbon dating.

Sample preparation. AMS measurements. See our first article in this issue [16].

Calibration. Radiocarbon dates were converted into calendar ages with OxCal v4.2 for Windows [17], using the SHCal13 atmospheric set [18].

ACKNOWLEDGMENTS

Authors thank Diana H. Mayne and Sarah Venter for collecting samples, for participating in field investigations of the baobab and for helpful discussions. The research was funded by the Romanian Ministry of Scientific Research CNCS-UEFISCDI under grant PN-II-ID-PCE-2013-76.

REFERENCES

1. G.E. Wickens, P. Lowe, "The Baobabs: Pachycauls of Africa, Madagascar and Australia", Springer, Dordrecht, **2008**.
2. A. Patrut, K.F. von Reden, D.A. Lowy, A.H. Alberts, J.W. Pohlman, R. Wittmann, D. Gerlach, L. Xu, C. Mitchell, *Tree Physiology*, **2007**, *27*, 1569-1574.
3. A. Patrut, D.H. Mayne, K.F. von Reden, D.A. Lowy, S. Venter, A.P. McNichol, M.L. Roberts, D. Margineanu, *Radiocarbon*, **2010**, *52*, 727-734.
4. A. Patrut, D.H. Mayne, K.F. von Reden, D.A. Lowy, R. Van Pelt, A.P. McNichol, M. L. Roberts, D. Margineanu, *Radiocarbon*, **2010**, *52*, 717-726.
5. A. Patrut, K.F. von Reden, R. Van Pelt, D.H. Mayne, D.A. Lowy, D. Margineanu, *Annals of Forest Science*, **2011**, *68*, 993-1003.
6. A. Patrut, S. Woodborne, K.F. von Reden, G. Hall, M. Hofmeyr, D. Lowy, R.T. Patrut, *PLoS ONE*, **2015**, *10(1)*, e0117193, doi: 10.1371/journal.pone.0117193.
7. A. Patrut, S. Woodborne, R.T. Patrut, G. Hall, L. Rakosy, K.F. von Reden, D.A. Lowy, D. Margineanu, *Studia UBB Chemia*, **2015**, *LX*, 4, 7-20.
8. A. Patrut, L. Rakosy, R.T. Patrut, I.A. Ratiu, E. Forizs, D.A. Lowy, D. Margineanu, K.F. von Reden, *Studia UBB Chemia*, **2016**, *LXI*, 4, 7-20.
9. A. Patrut, R.T. Patrut, L. Rakosy, J. Bodis, D.A. Lowy, E. Forizs, K.F. von Reden, *Studia UBB Chemia*, **2016**, *LXI*, 4, 21-30.
10. A. Patrut, S. Garnaud, O. Ka, R.T. Patrut, T. Diagne, D.A. Lowy, E. Foris, J. Bodis, K.F. von Reden, *Studia UBB Chemia*, **2017**, *LXII*, 1, 111-120, doi:10.24193/subbchem.2017.1.09.
11. A. Patrut, K.F. von Reden, D.H. Mayne, D.A. Lowy, R.T. Patrut, *Nuclear Instruments and Methods in Physics Research Section B*, **2013**, *294*, 622-626, doi: 10.1016/j.nimb.2012.04.025.

12. A. Patrut, S. Woodborne, K.F. von Reden, G. Hall, R.T. Patrut, L. Rakosy, P. Danthu, J-M. Leong Pock-Tsy, D.A. Lowy, D. Margineanu, *Radiocarbon*, **2017**, 59(2), 435-448, doi:10.1017/RDC.2016.92.
13. S. Woodborne, G. Hall, I. Robertson, A. Patrut, M. Rouault, N.J. Loader, M. Hofmeyr, *PLoS ONE*, **2015**, 10(5), e0124202, doi:10.1371/journal.pone.0124202.
14. S. Woodborne, P. Gandiwa, G. Hall, A. Patrut, J. Finch, *PLoS ONE* **2016**, 11(7), e015936. doi:10.1371/journal.pone.0159361.
15. N. Esterhuysen, J. von Breitenbach, H. Söhnge, I. van der Merwe, "Remarkable Trees of South Africa" second edition, Briza, Pretoria, **2016**.
16. A. Patrut, S. Woodborne, R.T. Patrut, L. Rakosy, G. Hall, I.A. Ratiu, K.F. von Reden, *Studia UBB Chemia*, **2017**, 62(2), 347-354, doi: 10.24193/subbchem.2017.2.27.
17. C. Bronk Ramsey, *Radiocarbon*, **2009**, 51, 337-360.
18. A.G. Hogg, Q. Hua, P.G. Blackwell, M. Niu, C.E. Buck, T.P. Guilderson, T.J. Heaton, J.G. Palmer, P.J. Reimer, R.W. Reimer, C.S.M. Turney, R.H. Zimmerman, *Radiocarbon*, **2013**, 55, 1889-1903.

N'-BENZYLIDENE-N-(THIAZOLYL)ACETOHYDRAZIDE DERIVATIVES: SYNTHESIS AND ANTIMICROBIAL ACTIVITY EVALUATION

**ADRIANA GROZAV^a, BOGDAN STANCU^{b*}, COSMINA BOARI^c,
FLORE CHIRILA^c, NICODIM FIT^{c*}, CASTELIA CRISTEA^d**

ABSTRACT. A series of new *N'*-benzylidene-*N*-(thiazolyl)acetohydrazide derivatives was obtained by the acetylation of 2-(2-benzylidenehydrazinyl)thiazole derivatives using acetic anhydride. The antimicrobial activity of the new and parent compounds was screened against Gram-positive and Gram-negative bacteria using agar well diffusion method. 4-Methyl-2-[2-(4-hidroxi-benzylidene)-hidrazinil]-thiazole was identified as the most efficient, with a broad activity spectrum against both Gram positive and Gram negative bacteria.

Key words: *acetohydrazide, thiazole, antimicrobial*

INTRODUCTION

The screening of antibacterial activity of novel synthetic compounds keep on as an evolving research enquiry for the development of effective and safe antimicrobial agents. Antibiotics resistance developed by bacteria became a significant concern in health, medical and environmental area, due to the fact that it may turn out to be a major threat for individuals with poor immune systems. For instance, the diabetic foot ulcer complicated by bacterial infections is in 50% of the cases responsible for reducing the life quality of the patients, amputations and morbidity [1].

^a Faculty of Pharmacy, "Iuliu Hațieganu" University of Medicine and Pharmacy, RO-400012, Victor Babes 41, Cluj-Napoca, Romania.

^b Faculty of Medicine, "Iuliu Hațieganu" University of Medicine and Pharmacy, RO-400349, Louis Pasteur 4, Romania.

^c Faculty of Veterinary Medicine, University of Agricultural Sciences and Veterinary Medicine Cluj-Napoca, Calea Mănăștur 3-5, 400372, Cluj-Napoca, Romania.

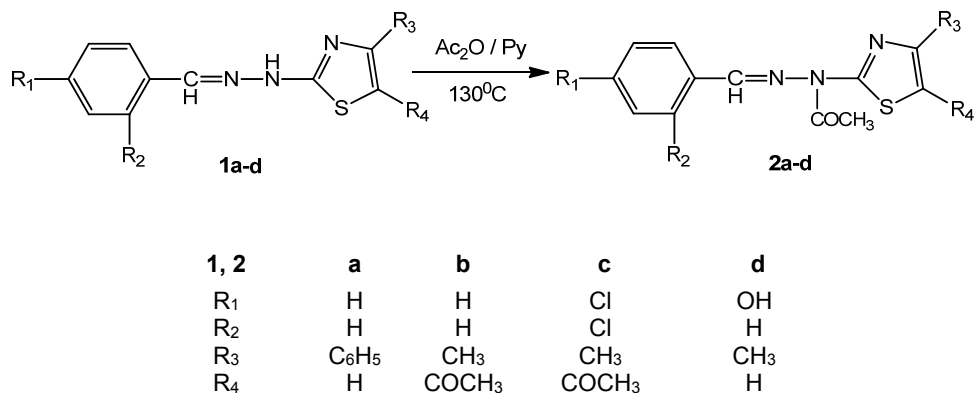
^d "Babes-Bolyai" University, Faculty of Chemistry and Chemical Engineering, RO-400028, Cluj-Napoca, Romania.

* Corresponding authors: bstancu7@yahoo.com, nfit@usamvcluj.ro

1,3-Thiazole heterocyclic unit appeared in the structure of several synthetic hydrazine derivatives with diverse biological activity, e.g. anti-inflammatory [2], antimicrobial [3-7], anticonvulsant [8], anti-tumor [9], antifungal [10,11], or antioxidant representatives [12,13]. Continuing our studies devoted to the chemical synthesis of new thiazole derivatives [14-19], in this work we report four new *N'*-benzylidene-*N*-(thiazolyl)acetohydrazide derivatives. The antimicrobial activity screening against several Gram positive and Gram negative bacteria strains reported in this study included both the newly synthesized (thiazolyl)acetohydrazide derivatives and the parent 2-(2-benzylidenehydrazinyl)thiazole derivatives which were previously synthesized by Hantzsch condensation of arylidene-thiosemicarbazones with α -halogenocarbonyl derivatives [14]

RESULTS AND DISCUSSIONS

The acylation of 2-(2-benzylidenehydrazinyl)thiazole derivatives **1a-d** with acetic anhydride in the presence of catalytic amounts of pyridine afforded the new *N'*-benzylidene-*N*-(thiazolyl)acetohydrazide derivatives **2a-d** in high yields (scheme 1). The structure of the new compounds was unambiguously assigned based on spectroscopic data and elemental analysis.



Scheme 1. Synthesis of *N'*-benzylidene-*N*-(thiazolyl)acetohydrazide derivatives

The antimicrobial activity of **1a-d** and **2a-d** was tested *in vitro* against 20 bacterial strains isolated from human venous leg ulcers secretions samples, from patients admitted to Emergency Clinical Hospital Cluj County. In Table 1 are summarized the values of the inhibition zones determined by agar well diffusion

method. A structure-activity correlation between the *in vitro* antimicrobial activity and the structural modifications associated to the substitution pattern of the phenyl ring (unsubstituted, *o,p*-dihalogenated, *p*-hydroxylated), or the thiazole ring (4-phenyl, 4-methyl, 5-acetyl) can be observed.

Table 1. Antimicrobial activity of **1a-d** and **2a-d** determined by diffusion method – inhibition zones (in mm)

Micro org. strain	Mean of the inhibition zone diameter [mm]								
	1a	2a	1b	2b	1c	2c	1d	2d	Positive control ^h
1 ^a	6.10	6.21	6.13	0	0	0	17.18	0	0
2 ^a	6.12	8.23	12.51	10.14	0	0	11.48	0	27.16
3 ^a	0	0	0	0	0	0	13.52	0	25.02
4 ^a	8.12	6.21	7.63	7.31	0	0	19.72	0	14.77
5 ^a	6.14	0	0	6.32	0	0	14.93	11.69	0
6 ^a	0	0	6.45	6.12	0	0	12.34	0	9.66
7 ^a	6.85	7.01	6.04	6.95	0	0	15.35	14.12	0
8 ^a	6.10	6.13	6.15	6.21	0	0	18.01	0	9.81
9 ^a	6.01	6.02	6.05	6.46	0	0	18.13	0	7.35
10 ^a	6.89	6.21	7.03	6.75	0	0	15.64	0	11.97
11 ^b	6.45	6.09	6.08	6.01	0	0	19.24	0	16.63
12 ^b	6.12	6.78	8.34	8.02	0	0	16.35	0	15.57
13 ^c	8.25	8.86	9.34	9.21	0	0	11.44	0	0
14 ^c	6.04	7.64	8.05	8.56	0	0	20.91	0	18.12
15 ^d	7.86	7.03	11.56	14.31	0	7.44	15.54	8.32	16.52
16 ^d	7.86	6.28	8.12	9.43	0	0	14.97	0	14.33
17 ^d	7.24	7.01	6.98	7.21	0	0	15.88	0	21.24
18 ^e	7.08	6.03	6.87	7.21	0	0	20.48	0	27.10
19 ^f	6.74	7.15	6.98	7.12	0	0	8.24	0	0
20 ^g	7.21	8.31	7.28	7.25	0	0	8.34	0	0

^aMicroorganisms strains: ^a*Staphylococcus aureus*; ^b*Staphylococcus epidermidis*; ^c*Trueperella pyogenes*; ^d*Bacillus licheniformis*; ^e*Pediococcus pentosaceus*, ^f*Enterococcus faecium*; ^g*Pseudomonas aeruginosa*. ^h Amoxicilin 30 µg

DMSO did not produced any inhibition zone.

Inhibition zone diameter larger than 7mm indicates susceptibility of the microorganism to the tested compounds.

Moderate susceptibilities of the microorganisms to compounds containing a 2-substituted thiazole ring (**1a**, **2a**) as well as 2,3-disubstituted thiazole ring **1b**, **2b** can be observed in table 1, with the exception of a noticeable activity of **1b**, **2b** against *S. aureus* strain 2 and *B. licheniformis* strain 15. In

these cases, the structural modification introduced by acetylation of the hydrazide unit did not cause a major modification of the antimicrobial activity in comparison to the parent compounds.

According to our experimental results, all the tested microorganisms proved to be resistant to the *o,p*-chlorinated derivative **1c** (which did not produce any inhibition zone) as well as to its acetyl derivative **2c**, with one exception for *B. licheniformis* strain 15 which displayed *in vitro* susceptibility.

As it may be seen from Table 1, all the tested microorganism strains appeared highly susceptible to the hydroxy derivative **1d**, which produced the largest growth-inhibition zones (8.24-19.72 mm); in many cases **1d** proved to be more efficient than the standard antibiotic Amoxicillin which was used in our experiments as a positive control. Microorganism strains 5, 13, 19, 20 proved to be resistant to amoxicillin, appeared largely susceptible to **1d**.

The acetylation of the hydrazide unit of **1d** caused the suppression of antimicrobial activity in relation to the majority of the tested microorganisms (only *S aureus* stains 5, 7 and *B. licheniformis* strain 15 appeared susceptible to **2d**).

The structural modifications brought by different substitution patterns of the tested compounds also contributed to the variation of their polarity and distribution on the Mueller Hinton agar, thus affecting the *in vitro* experimental results. The formation of hydrogen bonds between *p*-hydroxyphenyl derivative and agar may have favored the increase of the susceptibility results recorded in the case of **1d**.

CONCLUSIONS

The acylation of 2-(2-benzylidenehydrazinyl)thiazole derivatives can be conveniently performed using acetic anhydride in the presence of catalytic amounts of pyridine.

The antimicrobial activity of the new *N*'-benzylidene-*N*-(thiazolyl)acetohydrazide derivatives and their parent 2-(2-benzylidenehydrazinyl)thiazole derivatives tested *in vitro* by agar well diffusion method against 20 bacterial strains isolated from human samples indicated 4-methyl-2-[2-(4-hydroxybenzylidene)hydrazinyl]-thiazole **1d** as the most efficient, with a broad activity spectrum against both Gram positive and Gram negative bacteria. All the microorganisms tested proved to be resistant to 5-acetyl-4-methyl-2-[2-(2,4-dichlorobenzylidene)hydrazinyl]-thiazole **1c**. The acetylation of the hydrazide unit mainly suppressed or reduced the antimicrobial activity of the 2-(2-benzylidenehydrazinyl)thiazole derivatives.

EXPERIMENTAL

Melting points were determined on open glass capillaries using an Electrothermal IA 9000 digital melting point apparatus. The mass spectra were recorded using a Varian MAT-311A. The $^1\text{H-NMR}$ spectra were recorded with Bruker WM-400 spectrometer in the CDCl_3 . The quantitative elemental analyses were recorded using an Vario EL analyser.

Chemical Synthesis

2-(2-Benzylidenehydrazinyl)thiazole derivatives **1a-d** were prepared according to our previously reported procedure [14].

General procedure of acetylation of 2-(2-Benzylidenehydrazinyl)thiazole derivatives

Hydrazinothiazole (**1a-d**) (2 mmol) was treated with acetic anhydride (2 ml) and catalytic amounts of pyridine. The resulting mixture was heated at reflux for 5 minutes and further concentrated under reduced pressure. The product was precipitated by adding ethanol. The obtained solid was recrystallized from ethanol.

N'-benzylidene-*N*-(4-phenylthiazol-2-yl)acetohydrazide **2a**

Brown crystals, yield 2.4 g, 75%; m.p. 152-153 °C; MS (EI) m/z : 321 (M^+); 279; 176; 134; 77; 43 (100%);

Calcd. for: $\text{C}_{18}\text{H}_{15}\text{N}_3\text{OS}$, C, 67.27; H, 4.70; N 13.07; Found: C, 67.32; H, 4.75; N, 13.05; $^1\text{H-NMR}$ (400MHz, CDCl_3) δ ppm: 2.67 (s, 3H, CH_3), 6.85 (s, 1H, Th-CH), 7.41-7.49 (m, 6H, ArH), 7.74 -7.9 (m, 4H, ArH), 8.95 (s, 1H, $\text{CH}=\text{N}$).

N-(5-acetyl-4-methylthiazol-2-yl)-*N'*-benzylideneacetohydrazide **2b** Yellow crystals; yield 2.26 g, 76%; m.p. 134-135 °C; MS (EI) m/z : 301 (M^+); 258; 224; 197; 104; 77; 43 (100%); $^1\text{H-NMR}$ (400MHz, CDCl_3) δ ppm: 2.26 (s, 3H, CH_3), 2.56 (s, 3H, CH_3), 2.68 (s, 3H, CH_3), 7.48-7.54 (m, 3H, ArH), 7.82 (d, $^3J=8.2$ Hz, 2H), 9.19 (s, 1H, $\text{CH}=\text{N}$). Calcd. for: $\text{C}_{15}\text{H}_{15}\text{N}_3\text{O}_2\text{S}$, C, 59.78; H, 5.02; N 13.94; Found: C, 60.32; H, 5.10; N, 13.96;

N-(5-acetyl-4-methylthiazol-2-yl)-*N'*-(2,4-dichlorobenzylidene)acetohydrazide **2c**

White-yellow crystals; yield 2.69 g, 73%, m.p. 207 °C, MS (EI) m/z : 369/371 (M^+M^{+2}); 327; 292; 198; 183; 156; 141; 71; 43 (100%); $^1\text{H-NMR}$ (400MHz, CDCl_3) δ ppm: 2.44 (s, 3H, CH_3), 2.61(s, 3H, CH_3), 2.75 (s, 3H,

CH₃), 7.52 (d, ³J=8.1 Hz, 1H, ArH), 7.71 (s, 1H, ArH), 7.98 (d, ³J=8.1 Hz, 1H, ArH), 9.24 (s, 1H, CH=N). Calcd. for: C₁₅H₁₃Cl₂N₃O₂S, C, 48.66; H, 3.54; N 11.35; Found: C, 48.72; H, 3.61; N, 11.56;

***N'*-(4-hydroxybenzylidene)-*N*-(4-methylthiazol-2-yl)acetohydrazide 2d:**

White crystals; yield 1.96 g, 72%, m.p. 105-106 °C, MS (EI) *m/z*: 275 (M⁺); 233; 156; 114; 106; 43 (100%); ¹H-NMR (400MHz, CDCl₃) δ ppm: 2.24 (s, 3H, CH₃), 2.68 (s, 3H, CH₃), 4.96 (bb, 1H, OH), 6.33 (s, 1H, Th-CH), 6.92 (d, 2H, ³J = 8.1 Hz), 7.58 (d, 2H, ³J = 8.1 Hz), 7.97 (s, 1H, CH=N); Calcd. for: C₁₃H₁₃N₃O₂S, C, 56.71; H, 4.76; N 15.26; Found: C, 56.82; H, 4.83; N, 15.28;

Antimicrobial test

Agar well diffusion method

The in vitro antimicrobial activity of **1a-d** and **2a-d** was conducted by the routine agar well-diffusion method, similarly to the procedure used in disk-diffusion method according to the Clinical and Laboratory Standards Institute (CLSI) CLSI-M02-A10 (2009) as described by Markey et co.,[20] with some modification depending on the tested products.

In this study, a total of 20 bacterial strains collected from patients admitted to Emergency Clinical Hospital Cluj County were isolated from human venous leg ulcers secretions samples as follows: ten strains of *Staphylococcus aureus*, two strains of *Staphylococcus epidermidis*, two strains of *Trueperella pyogenes*, three strains of *Bacillus licheniformis*, one strain of *Pediococcus pentosaceus*, one strain of *Enterococcus faecium* and one strain of *Pseudomonas aeruginosa* strains. Characterization of the pathogens was based on the classical phenotype: morphological, cultural and biochemical methods and for identification an automated microbiology system VITEK 2 compact, bioMérieux was used.

The bacterial strains were inoculated separately on nutrient agar plate (Merck, Germany) and incubated at 37±2°C for 24 hours.

Than a standardized inoculum of the tested microorganism with an optical density adjusted to a 0.5 McFarland turbidity standard (approximately 10⁶UFC/ml) in a sterile saline solution were prepared. The Mueller Hinton agar plates (Merck, Germany) were than inoculated by spreading a volume of 500 µl the microbial suspension over the entire agar surface. After the plates dried at 35°C for 15-20 minutes seven radially hole with a diameter of 5 mm were punched aseptically and a volume of 25 µL of the synthetic compounds solution in DMSO at 100 mM concentration were disposed into each well. As a negative and positive control DMSO (Dimethyl Sulfoxide) and Amoxicillin 30 µg/ml

were used. The Petri dishes were incubated in an aerobic atmosphere at $37\pm 2^{\circ}\text{C}$ for 48 hours. All the procedures were carried out in duplicates, then the diameter of the inhibition zones (in mm) was measured with electronic caliper with digital screen.

The rights of the patients regarding the confidentiality of personal information were respected in agreement to Helsinki declaration of Ethical Principles for Medical Research Involving Human Subjects.

ACKNOWLEDGMENTS

This work was supported by the Swiss Enlargement Contribution in the framework of the Romanian-Swiss Research Program, project number IZERZO-142198/1 (A. Grozav). This paper was published under the frame of European Social Found, Human Resources Development Operational Programme 2007-2013, project no. POSDRU/159/1.5/S/136893" (A. Grozav).

REFERENCES

1. M. C. Zanella, B. Kressmann, L. Wuarin, B. Coulin, S. Maître, D. Suva, B. A. Lipsky, I. Uçkay, *Revue Medecale Suisse*, **2016**, *12*, 514.
2. R. D. Kamble, R. J. Meshram, S. V. Hese, R. A. More, S. S. Kamble, R. N. Gacche, B. S. Dawane, *Computational Biology and Chemistry*, **2016**, *61*, 86.
3. N. Seelam, S. P. Shrivastava, *Journal of Saudi Chemical Society*, **2016**, *20*, 33.
4. S. Bondock, T. Naser, Y. A. Ammar, *European Journal of Medicinal Chemistry*, **2013**, *62*, 270.
5. E. B. Silva, D. A. O. Silva, A. R. Oliveira, C. H. S. Mendesa, T. A. R. Santosc, A. C. Silva, M. C. A. Castro, R. S. Ferreira, D. R. M. Moreira, M. V. O. Cardoso, C. A. Simone, V. R. A. Pereirac, A. C. L. Leite, *European Journal of Medicinal Chemistry*, **2017**, *130*, 39.
6. T. A. R. Santos, A. C. Silva, E. B. Silva, P. A.T. Moraes Gomes, J. W. P. Espindola, M. V. O. Cardoso, D. R. M. Moreira, A. C. L. Leite, V. R. A. Pereira, *Biomedicine & Pharmacotherapy*, **2016**, *82*, 555.
7. G. M. Reddy, J. R. Garcia, V. H. Reddy, A. M. Andrade, A. Camilo, R. A. P. Ribeiro, S. R. de Lazaro, *European Journal of Medicinal Chemistry*, **2016**, *123*, 508.
8. N. Siddiqui, W. Ahsan, *European Journal of Medicinal Chemistry*, **2010**, *45*, 1536.
9. A. Andreani, M. Rambaldi, F. Andreani, R. Bossa, I. Galatulas, *European Journal of Medicinal Chemistry*, **1988**, *23*, 385.
10. Z. Gao-Feng, J. Leng, N. Darshini, T. Shubhavathi, H. K. Vivek, A. M. Asiri, H. M. Marwani, K. P. Rakesh, N. Mallesha, N. Bionda, R. Fleeman, H. Wang, A. Ozawa, R. A. Houghten, L. Shaw, *Bioorganic & Medicinal Chemistry Letters*, **2017**, *27(14)*, 3148.

11. Y. Li, N. Bionda, R. Fleeman, H. Wang, A. Ozawa, R. A. Houghten, L. Shaw, *Bioorganic & Medicinal Chemistry*, **2016**, *24*, 5633.
12. A. Andreani, A. Leoni, A. Locatelli, R. Morigi, M. Rambaldi, R. Cervellati, E. Greco, T. P. Kondratyuk, E. J. Park, K. Huang, R. B. Breemen, J. M. Pezzuto, *European Journal of Medicinal Chemistry*, **2013**, *68*, 412.
13. A. Grozav, I. D. Porumb, L. I. Găină, L. Filip, D. Hanganu, *Molecules*, **2017**, *22*, 260.
14. A. Grozav, L. I. Găină, V. Pileczki, O. Crisan, L. Silaghi-Dumitrescu, B. Therrien, V. Zaharia, I. Berindan-Neagoe, *International Journal of Molecular Science*, **2014**, *15*, 22059.
15. M. Sabou, A. Grozav, L. M. Junie, M. Flota, V. Zaharia, C. Cristea, *Studia UBB Chemia*, **2016**, *61*, 117.
16. A. Ignat, T. Lovasz, M. Vasilescu, E. Fischer-Fodor, C. B. Tatomir, C. Cristea, L. Silaghi-Dumitrescu, V. Zaharia, *Archiv der Pharmacie Chemistry in Life Sciences* **2012**, *345*, 574.
17. V. Zaharia, A. Ignat, N. Palibroda, B. Ngameni, V. Kuete, C. N. Fokunang, M. L. Mougang, B. T. Ngadjui, *European Journal of Medicinal Chemistry*, **2010**, *45*, 5080.
18. A. Ignat, V. Zaharia, C. Mogosan, N. Palibroda, C. Cristea, L. Silaghi-Dumitrescu, *Farmacia*, **2010**, *58*, 290.
19. B. Brem, E. Gal, C. Cristea, L. Găină, A. Grozav, V. Zaharia, L. Silaghi-Dumitrescu, *Studia UBB Chemia*, **2015**, *60* (2), 320.
20. B. Markey, F. Leonard, M. Archambault, A. Cullinane, D. Maguire, *Clinical Veterinary Microbiology*, Second edition, Elsevier, **2013**.

COMPARATIVE CHARACTERIZATION OF BASIL, MINT AND SAGE EXTRACTS

RAMONA BLEIZIFFER^a, CORNELIA MESAROS^b,
SONIA SUVAR^a, PAULA PODEA^{c*}, ANDREEA IORDACHE^d,
FLORENTINA-DIANA YUDIN^a, MONICA CULEA^a

ABSTRACT. Aromatic plants are widely used in food preparation for aroma and fragrance, but they are also a good source of amino acids and fatty acids. Three indigenous species, Basil (*Ocimum basilicum*), mint (*Mentha piperita*) and sage (*Salvia officinalis*) which are traditionally used in medicine and food, were characterized and compared in terms of volatile extracts, amino acids, fatty acids contents and antioxidant activities. The gas chromatographic–mass spectrometry (GC–MS) method is a suitable technique for the characterization of the compounds of the herbs extracts. Antioxidant activity was measured using extracts ability to scavenge DPPH radicals. Linalool was found the major compound in basil, menthol in mint and α -thujone in sage. The dominant amino acids identified in the plants extracts were glutamic acid and aspartic acid in basil and mint, while proline was found in high concentration in sage and mint. The total free fatty acids (TFA) were highest in mint, followed by sage and basil. The essential omega 3 alpha-linolenic acid (ALA) was identified in all three extracts. All samples exhibited antioxidant activity, sage extract having the highest antioxidant activity.

Keywords: *Ocimum basilicum*, *Mentha piperita*, *Salvia officinalis*, volatile compounds, amino acids, fatty acids.

INTRODUCTION

Basil (*Ocimum basilicum*), mint (*Mentha piperita*) and sage (*Salvia officinalis*), belonging to the Lamiaceae family, are medicinal plants and culinary herbs due to their delicate aroma and fragrance. Basil, one of the most important

^a Babeş-Bolyai University, Faculty of Physics, 1 Kogălniceanu str., 400084 Cluj-Napoca, Romania.

^b University of Medicine and Pharmacy, 38 Gh. Marinescu St., Târgu Mureş, Romania.

^c Babeş-Bolyai University, Faculty of Chemistry and Chemical Engineering, 1 Kogălniceanu str., 400084 Cluj-Napoca, Romania.

^d National R&D Institute for Cryogenics and Isotopic Technologies, 4 Uzinei str., 240050 Râmnicu Vâlcea, Romania.

* Corresponding author: mpaula@chem.ubbcluj.ro

and widely used spices, has been shown to have antioxidant, antibacterial, and anti-diarrheal activities [1]. Mint (*Mentha piperita*) has anti-inflammatory, cytotoxic and antioxidant activities [2]. Sage (*Salvia officinalis*) has a savory, peppery flavor and is used as condiment. Sage's studies in healthy humans have demonstrated improved memory, attention/executive function, alertness and mood, improved cognitive functioning and behavioral function [3-5]. It can be used also in treating digestive disorders such as poor digestion and bloating.

Herbs are often used in our food as condiments, tea or in pharmaceutical extracts. Most of these herbs are investigated for their nutritional and pharmaceutical properties. The optimization of micronutrients in our food is very important. Amino acids play an important role in human nutrition. The level of essential amino acids dictates food nutritive value. The free amino acids have an important effect in food flavor, influence its palatability, and contribute to the formation of amines and volatile compounds. Omega-3 fatty acids supplementations in humans have beneficial effects on subjective global assessment score and metabolic profiles. Amino acids, fatty acids and qualitative chemical composition of herbs may be influenced by environmental and geographical conditions.

The aim of investigations was to determine the differences between three herbs purchased from Romania with respect of the essential amino acids and fatty acids present in this herbs often used as tea or condiments. Also their volatile compounds and antioxidant activity were compared.

For the characterization of the compounds in herbs extracts, gas chromatography-mass spectrometry (GC-MS) analysis is a suitable technique. Amino acids and fatty acids were first derivatized to obtain trifluoroacetyl ester derivatives in the case of amino acids [6-11] and fatty acids methyl esters (FAMES) for free fatty acids [12-17]. Antioxidant activities of extracts were also compared.

RESULTS AND DISCUSSION

In the present work we have evaluated and compared the chemical composition of volatiles, amino acids and fatty acids contents in three herbs species: basil, mint and sage. For compounds characterization of herbs extracts, different approaches involving extraction methods, purification by ion exchange technique in the case of amino acids, derivatization steps and gas chromatography-mass spectrometry (GC-MS) analysis were applied.

For the amino acids and fatty acids analysis, the methods were validated injecting standard solutions of amino acids and fatty acids respectively. Samples are following the same derivatization procedure as standards. Good values for linearity, precision, accuracy and limit of detection were obtained [6].

The quantitative method gave a good linearity regression curve, obtained with standards with known concentration of each amino acid, in the range 0-100 $\mu\text{g}\times\text{mL}^{-1}$ and by adding the same quantity of internal standard (50 $\mu\text{g}\times\text{mL}^{-1}$). The internal standard, ^{15}N -glycine, (99 atom % ^{15}N) and glycine required correction by deconvolution and matrix calculation. Fractional isotopic abundances for natural glycine and isotopomer were obtained experimentally [8,9] (Table 1).

Table 1. The matrix design (left) and the pseudoinverse matrix (right) used for glycine calculation [6]

Glycine	[M]	[M+1]	Glycine	[M]	[M+1]
n.a.	0.95	0.05	n.a.	1.05	-0.05
^{15}N	0.01	0.99	^{15}N	-0.01	1.01

Glycine was calculated by matrix and regression curve calculation. Precision and accuracy for glycine, measured for standards of 20 and 30 $\mu\text{g}\times\text{mL}^{-1}$ (n=7), showed very good results, lower than 6% and respectively 11%.

Method validation, using amino acid standards following the extraction and derivatization procedure (n=3), gave good results. The regression curves for each amino acid standard were studied between of 0 and 150 $\text{mg}\times\text{mL}^{-1}$, and the same quantity of internal standard was added. Good linearity results for amino acids were found, the regression coefficient over 0.99 for Ala, Gly, Thr, Ser, Leu, Ile, Pro, Orn and higher than 0.97 for the other standards. The precision and accuracy were lower than 20%, for standards of 60 and 80 $\text{mg}\times\text{mL}^{-1}$, respectively. The limits of detection (LODs) ranged from 10^{-3} for alanine, glycine, ornithine, and leucine to 10^{-2} mg mL^{-1} .

The volatile extracts of basil gave as major compounds: linalool (26.13%), estragole (21.16%), caryophyllene (10.13%) and limonene (8.18%). Sage gave as major compounds: α -thujone (25.08%), camphor (20.46%), eucalyptol (13.85%) and β -thujone (13.37%) (Fig.1). In mint, the major compounds were menthol (37.7%), isomenthone (15.97%), eucalyptol (5.44%) and menthofuran (4.8%) (Fig. 2).

COMPARATIVE CHARACTERIZATION OF BASIL, MINT AND SAGE EXTRACTS

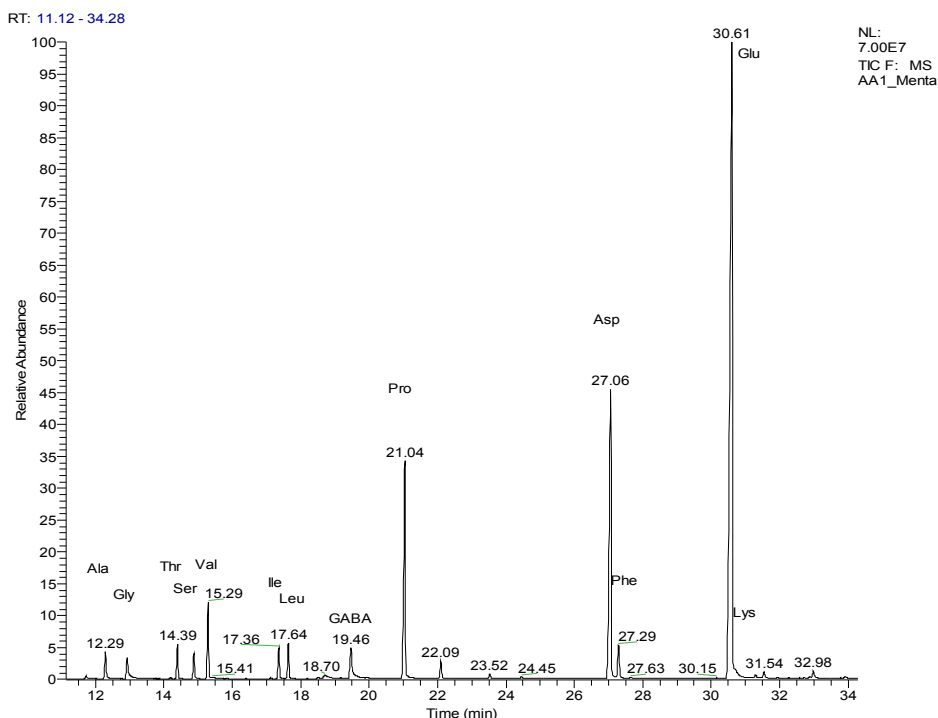


Figure 3. GC-MS separation and identification of amino acids present in mint extract

Fig. 3 presents the total ion chromatogram (TIC) of amino acids separated and identified in mint extract. NIST library was used for compounds identification. The elution order was: alanine (Ala), glycine (Gly), threonine (Thr), serine (Ser), valine (Val), leucine (Leu), isoleucine (Ile), γ -aminobutyric acid (GABA), proline (Pro), methionine (Met), aspartic acid (Asp), phenylalanine (Phe), ornithine (Orn), glutamic acid (Glu), lysine (Lys), tyrosine (Tyr).

The dominant amino acids identified were glutamic acid and aspartic acid in basil and mint and proline content was higher in sage and mint. We found that in sage, proline, glutamic acid, gamma-aminobutyric acid, alanine, valine and glycine were important quantitatively. The highest free total amino acids were observed in mint and sage, over $1 \text{ mg} \cdot \text{g}^{-1}$ (Fig.4). Fig. 5 presents the ratio EAA/TAA (essential amino acids/total amino acids) which is higher in basil, followed by mint and sage. The highest concentration of essential amino acids were found in mint ($1.07 \text{ mg} \cdot \text{g}^{-1}$), followed by sage ($0.33 \text{ mg} \cdot \text{g}^{-1}$) and basil ($0.1 \text{ mg} \cdot \text{g}^{-1}$) (Table 2, Fig. 6).

Analyzing the fatty acids content in these three herbs, essential omega 3 alpha-linolenic acid (ALA) were identified and the highest content was found in basil, followed by sage and mint. Also, the total free fatty acids

(TFA) content was determined in basil (72.8 mg.g⁻¹), mint (13.3 mg.g⁻¹) and sage (98.8 mg.g⁻¹). The unsaturated fatty acids (UFA) and polyunsaturated fatty acids (PUFA) were analyzed, the content been higher in sage and basil in comparison with mint. The ratio UFA/SFA was higher in basil and mint, followed by sage (Table 3, Fig. 8).

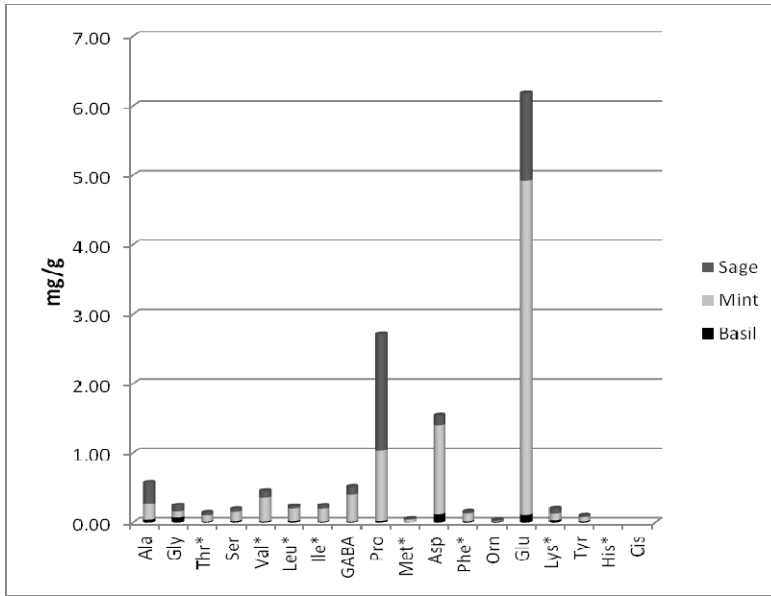


Figure 4. Free amino acids comparison in basil, sage and mint extracts (mg.g⁻¹)

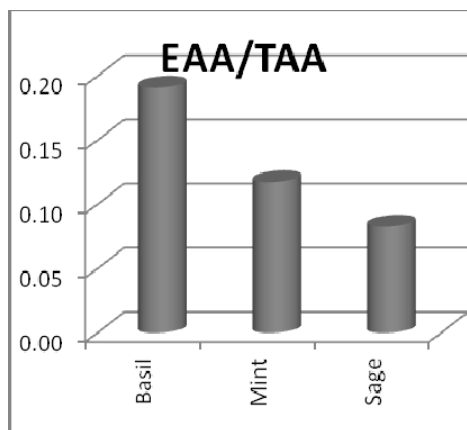


Figure 5. Free amino acids comparison in basil, sage and mint extracts (mg.g⁻¹)

COMPARATIVE CHARACTERIZATION OF BASIL, MINT AND SAGE EXTRACTS

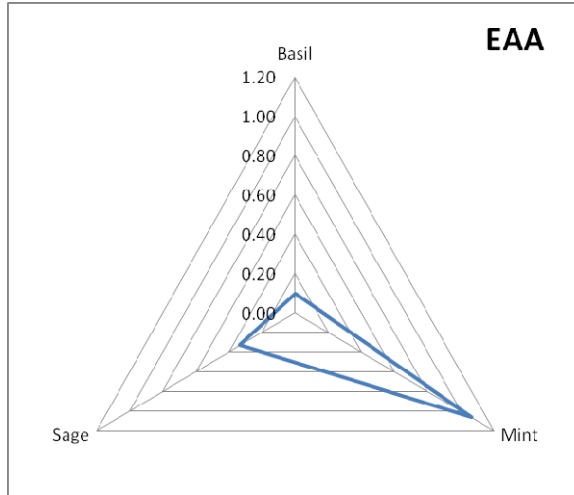


Figure 6. Comparison of essential amino acids in the three herbs extracts ($\text{mg} \cdot \text{g}^{-1}$)

Table 2. Amino acids values, in $\text{mg} \cdot \text{g}^{-1}$, in the analyzed herbs

AA/Herbs	Basil	Mint	Sage
Ala	0.04	0.22	0.32
Gly	0.07	0.09	0.09
Thr*	0.01	0.09	0.04
Ser	0.02	0.14	0.04
Val*	0.01	0.34	0.10
Leu*	0.02	0.18	0.04
Ile*	0.01	0.19	0.05
GABA	0.01	0.38	0.12
Pro	0.02	1.01	1.68
Met*	0.00	0.04	0.01
Asp	0.12	1.28	0.15
Phe*	0.01	0.12	0.03
Orn	0.01	0.01	0.01
Glu	0.11	4.81	1.26
Lys*	0.03	0.10	0.07
Tyr	0.02	0.06	0.04
TAA	0.51	9.07	4.03
EAA	0.10	1.07	0.33
EAA/TAA	0.19	0.12	0.08

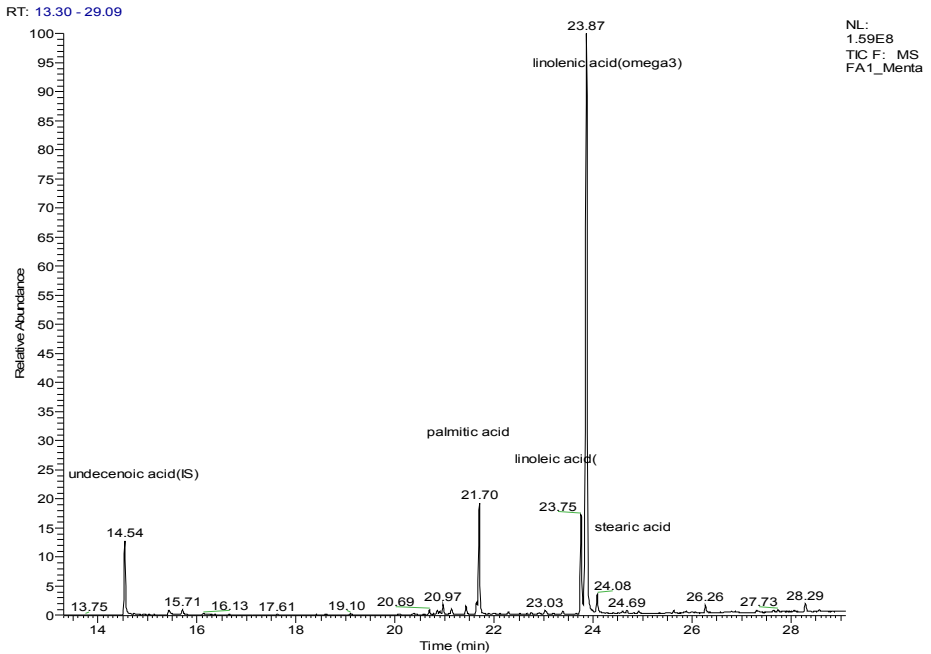


Figure 7. GC-MS separation and identification of fatty acids in mint extract

The identified fatty acids separated as FAMES in the mint extract is presented in Fig.7. The omega-3 linolenic acid was the highest concentrated fatty acid determined in each herb extract.

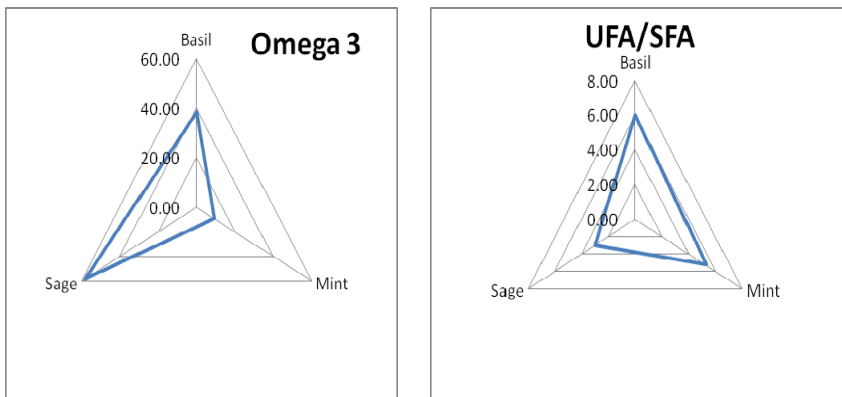


Figure 8. Linolenic acid and UFA/SFA ratio comparison in the herbs studied

Table 3. Free fatty acids(FA) values, in mg·g⁻¹, in the analyzed herbs

FA	Basil	Mint	Sage
C16:1	0.12	0.18	0.60
C16:0	7.12	1.44	13.65
C18:2	23.89	1.44	15.36
C18:3	38.39	9.55	58.11
C18:0	2.66	0.37	3.54
C20:0	0.26	0.13	4.33
C22:0	0.13	0.13	1.81
C24:0	0.18	0.04	1.38
omega6/omega3	0.62	0.15	0.26
MUFA	0.12	0.18	0.60
UFA	62.41	11.18	74.06
SFA	10.35	2.11	24.70
PUFA	62.28	11.00	73.46
UFA/SFA	6,03	5,30	3,00
TFA	72,76	13,29	98,76

Antioxidant activity was determined using DPPH scavenging activity. All three herbs ethanolic extracts showed an antioxidant activity. Sage and mint extracts proved to have a very high antioxidant potential, while basil showed a moderate antioxidant potential. The half maximal effective concentration (EC₅₀) for each type of extract was determined. The most antioxidant extract was sage extract (EC₅₀= 8.22 µg*mL⁻¹), followed by mint extract EC₅₀=13.65 µg*mL⁻¹, and basil extract EC₅₀=112.58 µg*mL⁻¹. The percentage of DPPH scavenging activity at 50 µg*mL⁻¹ of each plant extract, after 30 minutes was determined and the highest value was obtained in sage extract (92.26%) followed by mint extract (88.66%) and basil extract (24.28%).

Comparing the DPPH scavenging activity of these three plants extracts with plants extracts from other geographical sources, showed that we have obtained similar results. Our sage extract (92.26%), from Târgu Mures area, proved to have comparable DPPH scavenging activity with other sage extracts from different Romanian sources (85.12%) [18], but higher than methanolic extract from Tunisia. (EC₅₀=29.33 µg*mL⁻¹) [19]. *Mentha piperita*, from Târgu Mures (EC₅₀=13.65 µg*mL⁻¹) area, exhibits a lightly higher activity than *Mentha piperita* from Northeastern Algeria (EC₅₀=17.00µg*mL⁻¹) [20], while DPPH scavenging activity of our mint ethanolic extracts (88.66%) showed higher activity than diethylether mint extract from Saudi Arabia (34.21%) [21].

The EC 50% of our *Ocimum basilicum* ethanolic extract ($EC_{50}=112.58 \mu\text{g}\cdot\text{mL}^{-1}$) showed comparable activity with other ethanolic basil extract from different Romanian sources ($EC_{50}=124.95 \mu\text{g}\cdot\text{mL}^{-1}$) [22], while aqueous basil extract from Serbia ($EC_{50}=17.93 \mu\text{g}\cdot\text{mL}^{-1}$) showed a powerful scavenging activity [23].

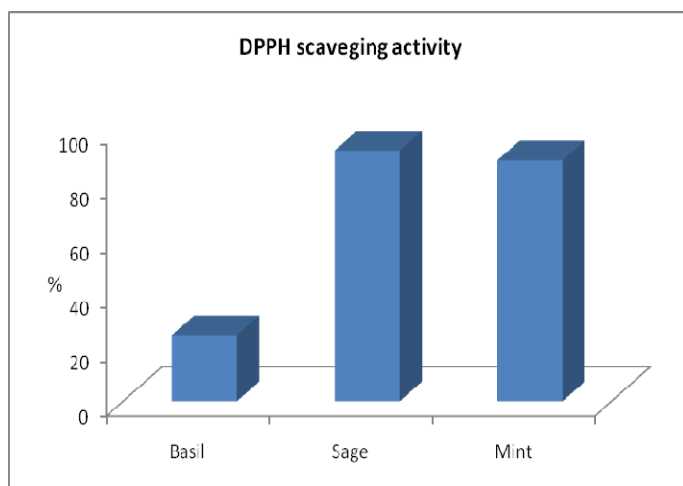


Figure 9. DPPH scavenging activity of ethanolic herbs extracts ($50 \mu\text{g}\cdot\text{mL}^{-1}$)

CONCLUSIONS

The GC-MS is a suitable technique for the characterization of the compounds of the herbs extracts. The validation parameters: linearity, correlation coefficients, precision, accuracy, in the range of interest, were good. Isotopic dilution by using a labeled internal standard increased precision and avoids the overlapping of analyzed compounds. The methods are useful for nutrient and diet control. The compounds identified in the herbs studied are characteristic for the odour or aroma of these plants.

The highest free total amino acids were observed in mint and sage ($>4 \text{ mg}\cdot\text{g}^{-1}$). Proline was higher in sage and mint. The presence of omega 3 fatty acid is very important for healthy and the highest quantity was found in sage, followed by basil and mint. Sage and mint extract proved to have a high and comparable antioxidant activity, while basil extract have a moderate antioxidant activity.

EXPERIMENTAL SECTION

Materials and methods

Plants, basil (*Ocimum basilicum*), mint (*Mentha piperita*) and sage (*Salvia officinalis*), were purchased from Botanical Garden of Târgu Mures, Transylvania, Romania. All reactive and standards were purchased from Merck (Darmstadt, Germany).

GC-MS apparatus

A DSQ Thermo Finnigan Proanalysis, Bucharest, Romania quadrupole mass spectrometer coupled with a Trace GC was used. Gas chromatography was performed on a 5% phenyl methylpolysiloxane Rtx-5MS capillary column, 30 m × 0.25 mm, 0.25 µm film thickness in a suitable temperature program. In the case of amino acids separation the program was: from 70 °C, 2 min, 5 °C/min to 110 °C, 10 °C/min to 290 °C, 16 °C/min to 300 °C. [1]. The temperature program for FAMES and volatiles separation was: 50 °C for 2 min rising with a rate of 8 °C/min at 310 °C (8 minutes). Helium was used as carrier gas at a flow rate of 1 mL/min. 1 µL of each sample was injected into the GC-MS using the split mode (10:1) using a TriPlus autosampler (Proanalysis, Bucharest, Romania). The mass spectrometer was operated in EI mode at 70 eV, emission current was 100 µA and mass spectra mass range 50-500 a.m.u. Transfer line temperature was set at 250 °C, injector at 250 °C and ion source at 250 °C. Antioxidant activity was determined using a Varian Cary 50 Spectrophotometer.

Extraction procedures

For extraction and derivatization of amino acids, 100 mg of crushed leaves were extracted with 1 ml of 6% trichloroacetic acid in a ultrasound bath for 5 min. The mixture was centrifuged for 5 min at 6000 rpm and supernatant was collected for purification. 0.5 ml of the supernatant and 50 µg [¹⁵N]-glycine (internal standard) was passed through a Dowex 50W-W8 exchange resin, 4 x 40 mm column (activated). The collected solution was dried in a nitrogen flow at 60 °C or by using a vacuum centrifuge at 60 °C. The derivatization method included an esterification of the carboxylic function using 200 µl butanol : acetyl chloride (4:1 v/v), for 1 h at 110 °C, followed by an acetylation of the amine function using 100 µl trifluoroacetic anhydride, for 20 min at 80 °C.

For extraction and derivatization of fatty acids, 100mg of crushed leaves was sonicated with 0.6 ml water/NaCl and 0.8 ml methanol for 1 min, then mixed with 0.8 ml chloroform and 3 min centrifuged (5800 rot/min); the lower layer was collected and extraction was repeated with 0.4 ml chloroform. The lower chloroform phase containing the extracted fatty acids was then dried in a nitrogen flow, at 60°C.

The lipids were converted to corresponding FAMES by esterification of the carboxylic functions with 200 µL methanol: acetyl chloride 4:1 (v:v), 20 min, 80°C. The derivatives were evaporated to dryness by a nitrogen stream, at 60°C, and then dissolved in 500 µL dichloromethane. 10 µg of C11:1 was added to each sample for GC-MS quantitation.

For extraction of volatiles, 100 mg of crushed leaves were ultrasounded and extracted with 1mL ethanol at 60°C for 15 minutes. The mixture was centrifuged at 5800 rpm and the supernatant collected filtered and injected in the GC/MS and tested for antioxidant activity.

For determination of antioxidant activity, DPPH antioxidant assay was used. A solution of 40µM 2,2-diphenyl-1-picrylhydrazil (DPPH•) in ethanol was decolorize using different concentration of each plant extract. The monitoring of DPPH reduction was followed at 517nm. The percentage of DPPH scavenging activity is expressed using following formula: $DPPH_{inhibition\%} = [(A_i - A_t) / A_i] \times 100$. For determination of effective concentration (EC₅₀), different concentration of each plant extract 5 µg/mL, 10 µg/mL, 20 µg/mL, 50 µg/mL, 100µg/mL were used. The EC₅₀ was determined by plotting the DPPH_{inhibition%} against used extract concentration.

REFERENCES

1. Y. Lu, B. Gao, P. Chen, D. Charles, L. Yu, *Food Chemistry*, **2014**, *154*, 262.
2. Z. Sun, H. Wang, J. Wang, L. Zhou, P. Yang, *PLOS ONE*, **2014**, *9(12)*: e114767.
3. D.O. Kennedy, E. L. Wightman, *Advances in Nutrition: An International Review Journal*, **2011**, *2*, 32.
4. S. Akhondzadeh, M. Noroozian, M. Mohammadi, S. Ohadinia, A.H. Jamshidi, M. Khani, *Journal of Clinical Pharmacy and Therapeutics*, **2003**, *28*, 53.
5. S. Vogl, P. Picker, J.Mihaly-Bison et al., *Journal of Ethnopharmacology*, **2013**, *149*, 750.
6. M. Culea, E. Horj, A. Iordache, O. Cozar, *Asian Journal of Chemistry*, **2011**, *23*, 4279.
7. C. Mesaros, M. Culea, A. Iordache, O. Cozar, *Bulletin UASVM Agriculture*, **2009**, *66*, 111.
8. J. I. Brauman, "Spectral Analysis: Methods and Techniques", Ed. by J. A. Blackburn, Marcel Dekker, New York, **1970**.

9. M. Culea and D.L. Hachey, *Rapid Communication in Mass Spectrometry*, **1995**, *9*, 655.
10. T. Hodisan, M. Culea, C. Cimpoiu, A. Cot, *Journal of Pharmaceutical and Biomedical Analysis*, **1998**, *18*, 319.
11. M. Culea, S. Scrob, S. Suvar, P. Podea, I. Has, S. Muste, *Analytical Letters*, **2015**, *48*, 37.
12. D. Cocan, E. Horj, M. Culea, V. Miresan, A. Pinte, *Bulletin of USAMV, Cluj-Napoca, Agriculture*, **2010**, *67*, 132.
13. A. Iordache, M. Culea, E. Horj, O. Cozar, *Romanian Journal of Physics*, **2011**, *56*, 7-8, 963.
14. A. Pinte, A. Varga, P. Stepnowski, C. Socaciu, M. Culea, H.A. Diehl, *Phytochemical Analysis*, **2005**, *16*, 188.
15. M. D. Huynh, D. D. Kitts, *Food Chemistry*, **2009**, *114*, 912.
16. U. Chukwuemeka, G. I. Ndukwe, T. O. Audu, *Internet Journal of Food Safety*, **2008**, *10*, 9.
17. N. M. Arat, I. H. Haliloğlu, Ö. Ayik, *Turkish Journal of Veterinary and Animal Sciences*, **2003**, *27*, 311.
18. A. V. Pop, M. Tofană, S. A. Socaci, D. Vârban, M. Nagy, Maria-D.Borş, S. Sfechiş, *Bulletin UASVM Food Science and Technology*, **2015**, *72*, 210.
19. I. Hamrouni-Sellami, F.Z. Rahali, I.B. Rebey et al., *Food Bioprocess Technology*, **2013**, *6*, 806.
20. A. Benabdallah, C. Rahmoune, M. Boumendjel, O. Aissi, C. Messaoud, *Asian Pacific Journal of Tropical Biomedicine*, **2016**, *6(9)*, 760–766.
21. F. Al-Juhaimi, K. Ghafoor, *Pakistan Journal of Botany*, **2011**, *43(4)*, 2235.
22. L. Vlase, D. Benedec, D. Hanganu, G. Damian, I. Csillag, B. Sevastre, A. Mot, R. Silaghi-Dumitrescu, I. Tilea, *Molecules*, **2014**, *19*, 5490-5507.
23. B. Kaurinovic, M. Popovic, S. Vlajsajjevic, S. Trivic, *Molecules*, **2011**, *16*, 7401-7414.

CHANGES IN TOTAL PHENOL CONTENT AND ANTIOXIDANT ACTIVITY OF GREEK TABLE OLIVE CULTIVAR *AMFISSIS* DURING MATURATION

NIKOLAOS GOUGOULIAS^a, LIVIU GIURGIULESCU^{b*},
IOANNIS VAGELAS^a, ELENI WOGIATZI^a,
MARIA-NEKTARIA NTALLA^c

ABSTRACT. The *Amfissis* cultivar olive fruits grown in the region of Larissa, central Greece, were studied for the changes in total polyphenol content, phenolic fractions and antioxidant capacity during maturation period (four months). It has been established that the total phenol content and antioxidant capacity, change in broad ranges depending on the ripening stage of fruits. The content of total phenols in the *Amfissis* cultivar during maturation varied from 3.9 to 11.9 mg (GAE) g⁻¹ FW. The highest content of total phenols has been found in the harvest stage (December). The content of flavonoid phenols ranges from 3.12 to 9.47 mg (GAE) g⁻¹ FW. The highest content of flavonoid phenols was determined the time period of the harvesting. The content of non-flavonoid phenols during ripening of olive fruit ranges from 0.78 to 2.43 mg (GAE) g⁻¹ FW. The highest content of NFP was determined the time period of the harvesting (black color). The inhibition concentration (IC₅₀) of extract during maturation of the olive fruit in all stages ranges from (735 to 130) mg/l. The lowest inhibition concentration (highest antioxidant capacity) was observed in the collection stage of the olive fruits. The obtained results have a direct impact on the harvesting date of the table cultivar *Amfissis*, influencing the sensory properties and the quality of the olive fruit.

Keywords: Antioxidant activity FRAP; Olives, *Amfissis*; Total phenols

^a Department of Agronomy Technology, Technological Educational Institute of Thessaly, 41110 Larissa, Greece.

^b Department of Chemistry and Biology, Technical University of Cluj Napoca, North University Center of Baia Mare, 430122 Baia-Mare, Romania.

^c Department of Computer Science and Engineering, Data Analysis, Technological Educational Institute of Thessaly, 41110 Larissa, Greece.

* Correspondence author: giurgiulescu@gmail.com

INTRODUCTION

The fruits are natural reservoir of phenolic compounds and natural antioxidants [1-3]. *Olea europaea L.* is a tree widely cultivated in the Mediterranean area for oil production and for table olives production. Table olives are a traditional Greek product, important component of the Mediterranean diet. Olive fruits are rich in flavonoids, secoiridoids, phenolic acids and phenolic alcohols [4-7] which exercise high antioxidant activity. Olives cultivar *Amfissis* are used usually as table olives and to a lesser degree for oil production.

Phenolic compounds influence the sensory properties of the olive fruits. Oleuropein is a phenolic compound from olives responsible for their bitterness [8-10]. The inclusion of table olive in a diet reduces the risk of cardiovascular and some cancer diseases [11-12].

Important changes in phenolic content and antioxidant activity during fruits development was reported [3]. The concentration of oleuropein in the olive fruit decreases with development and maturation of fruit [9,13]. The changes in phenolic composition during the maturation of olive fruits are due to hydrolysis of glycosides, oxidation and polymerization of phenolic compounds [14-15].

The aim of this study was the determination of phenolic content and antioxidant activity, in different stages of maturation of *Amfissis* cultivar fruits grown on the region Sykourio, Larissa, Greece.

RESULTS AND DISCUSSIONS

Soil samples collected from olive orchard were analyzed for inorganic nutrient element (N, P, K, Mn, Zn and Cu) and organic matter content. The soil was a Sandy Loam (SL), with high content in organic matter and nutrients (Table 1).

Figure 1 shows that the concentration of total phenols increased continuously (from 3.9 to 10.1 mg (GAE) g⁻¹ FW) between the first sampling in August (green color fruits) until the time of the fourth sampling in October (reddish-purple color fruits). Then, during ripening between fourth (reddish-purple color) and fifth sampling (purple-black color), the concentration of total phenols showed a stagnation. However, in the last phase of maturity, corresponding to the period between of the purple-black color and of the black color (harvest season), the concentration of total phenols increased again and reached the maximum value (11.9 mg (GAE) g⁻¹ FW).

To the same conclusions arrived some researchers which studied the change in the total phenolic content during ripening for some olive fruits from Tunisia [16]. Contrary, decrease of the content total phenolic during ripening

of olive fruits for some cultivars of Italy observed by [14, 17-19]. In addition, decrease total phenols during ripening for some cultivars of Australian observed by [20]. These differences in the variability of total phenols likely due to the different cultivars, in soil and climatic conditions of each region.

Table 1. Chemical properties of soils from olive orchard

Soil properties	Soil depth	
	(0-30) cm	(30-60) cm
Texture	Sandy Loam	Sandy Loam
pH (1:5)	7.72 ± 0.31	7.68 ± 0.31
EC (1:5), dS m ⁻¹	0.48 ± 0.03	0.41 ± 0.03
CaCO ₃ (%)	6.67 ± 0.34	11.52 ± 0.58
Organic matter (%)	2.42 ± 0.12	1.63 ± 0.08
N-inorganic (mg kg ⁻¹)	174.3 ± 9.68	110.8 ± 6.16
K-exchangeable (mg kg ⁻¹)	328.4 ± 14.29	214.2 ± 9.87
P -Olsen (mg kg ⁻¹)	20.8 ± 1.39	12.4 ± 0.95
Cu-DTPA (mg kg ⁻¹)	2.43 ± 0.22	1.84 ± 0.15
Zn-DTPA (mg kg ⁻¹)	4.67 ± 0.31	2.34 ± 0.18
Mn-DTPA(mg kg ⁻¹)	7.43 ± 0.68	3.78 ± 0.32

Data represent average and SE deviation, (n) = 4.

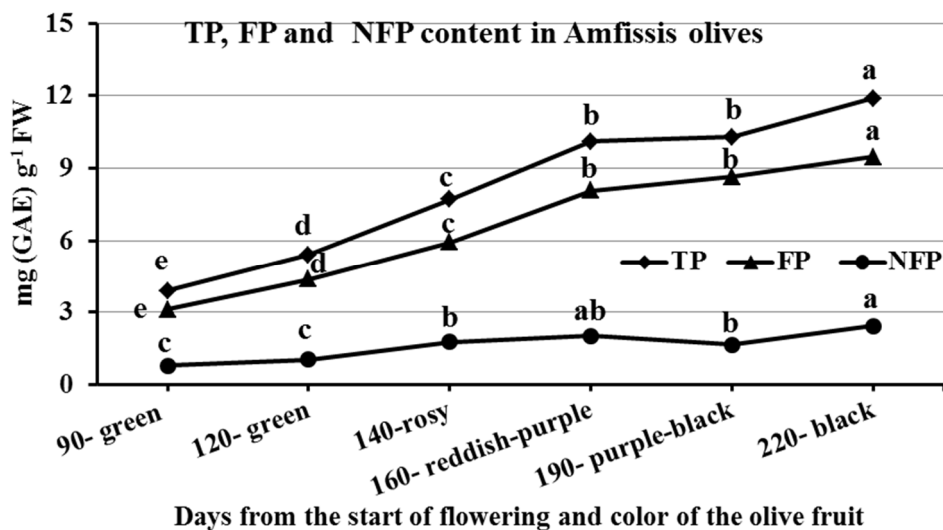


Figure 1. Changes of total phenol (TP) content, flavonoid phenols (FP) and non-flavonoid phenols (NFP) during maturation of the olive cultivar *Amfissis* at 90; 120; 140; 160; 190 and 220 days from start of flowering, respectively. Characteristics labeled with the same letter do not differ significantly according to the Tukey's test (P=0.05).

The variation of the content of flavonoid phenols during ripening of olive fruit was similar to that of total phenols. The content of flavonoid phenols ranges from 3.12 to 9.47 mg (GAE) g⁻¹ FW (Figure 1). The lowest content of FP was determined the time period of the first sampling (green color), and the highest the time period of the harvesting (black color). The FP content in the olive fruit during the second sampling (green color) constitutes 80.90% of TP amount, whereas during the third sampling (rosy color) it is lower and reached 77.01 %.

The flavonoid phenols (FP) cover a great number of phenolic compounds in the olive fruits, from which prevail the fractions of flavones and flavonols, and exhibit different functions. The content flavones (luteolin, luteolin 7-O-glucoside, apigenin) and flavonols (rutin and quercetin) showing different changes during ripening of olive fruit [13].

The content of non-flavonoid phenols during ripening of olive fruit ranges from 0.78 to 2.43 mg (GAE) g⁻¹ FW. The lowest content of FP was determined the time period of the first and second sampling (green color fruits), and the highest the time period of the harvesting (black color fruits) (Figure 1).

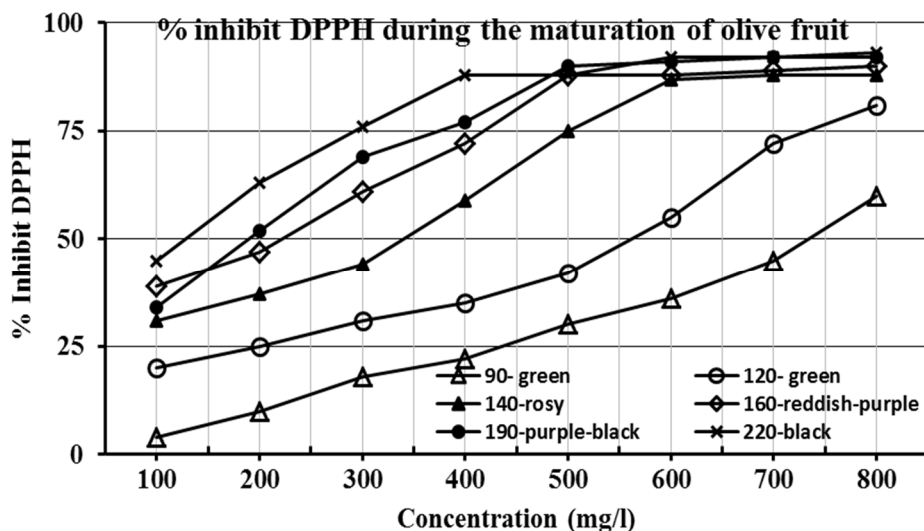


Figure 2. Inhibition percentage DPPH in different concentrations of the extract of samples, during maturation of the olive cultivar *Amfissis*. 90; 120; 140; 160; 190 and 220 days from start of flowering, respectively. Data represent average, (n) = 4.

The scavenging effect of *Amfissis* olives was also examined using different concentrations of extracts in 80% methanol (Figure 2). The results are expressed as percentage of the absorbance decrease of DPPH• solution in the presence of different concentrations of extracts to the absorbance of DPPH• solution.

From the Figure 2 we can observe that the increase of inhibition percentage DPPH• is function of increasing concentration of the extract, for all phases of maturation.

The concentration of the extract required to reduce the absorbance of solution DPPH• 50%, constitutes the inhibition concentration (IC_{50}). The lowest inhibition concentration (IC_{50}) corresponds in the highest antioxidant capacity.

Figure 3 shows that the inhibition concentration (IC_{50}) of extract during maturation of the olive fruit in all stages ranges from (735 to 130) mg/l. The lowest inhibition concentration (highest antioxidant capacity) was observed in the collection stage of the olive fruits (black color). The correlation between the inhibition concentration (IC_{50}) of the extracts during maturation of the olive fruit and the contents of TP was high, with correlation coefficient (r^2) equal to: 0.972.

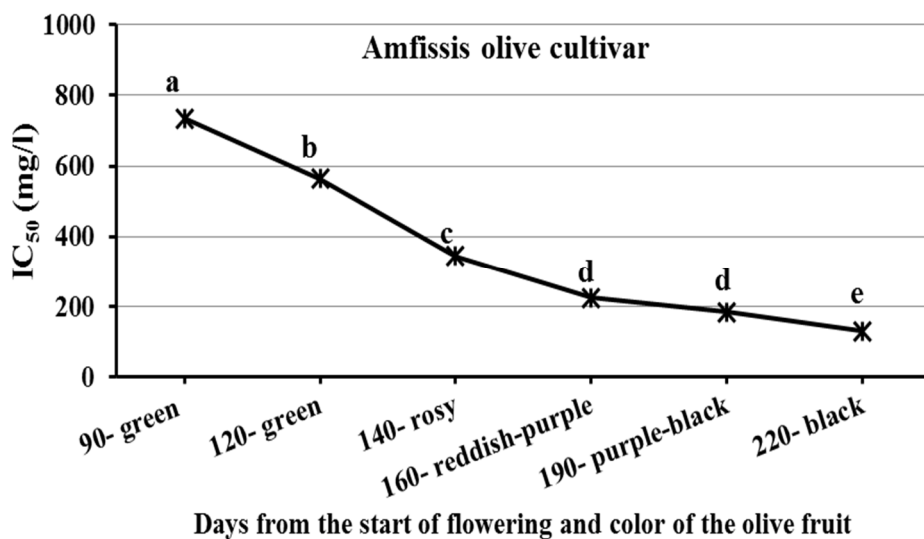


Figure 3. Antioxidant capacity expressed by median inhibition concentration (IC_{50}) during maturation of the olive cultivar *Amfissis*. At 90, 120, 140, 160, 190 and 220 days from start of flowering, respectively. Each characteristic of the graph labeled with the same letter do not differ significantly according to the Tukey's test ($P=0.05$).

Our results are in agreement with the data obtained by other authors which reported decrease of value (IC_{50}) during maturation of the olive fruit [21]. These values show that the *Amfissis* olives have highest antioxidant capacity during maturation from some olives cultivars of Tunisia [21]. Contrary, increase of the value (IC_{50}) during maturation of the olive fruit observed by other authors [19]. These differences in the antioxidant capacity of the olive fruit during maturation, due in the quantitative composition of polyphenols and in structure of individual compounds, as a result of the cultivar and climatic factors [13, 22].

Each characteristic of the graph with the same letter do not differ significantly according to the Tukey's test ($P=0.05$).

CONCLUSIONS

Flavonoids, non-flavonoids, total phenols content and antioxidant capacity of the table olive *Amfissis* vary with stages maturation, demonstrating the importance of behavior of the *Amfissis* cultivar. Contrary with most olive varieties, the *Amfissis* cultivar in the region Larissa, presents the highest total phenolic compounds content and antioxidant activity at the harvest stage (10 December).

The obtained results have a direct impact on the harvesting date of the table cultivar *Amfissis*, influencing the sensory properties and the quality of the olive fruit.

EXPERIMENTAL SECTION

Experimental

The study was carried out in the olive orchard Papadoulis in an area located in region Sykourio, Larissa, Greece, (latitude $39^{\circ}43'30''N$, longitude $22^{\circ}44'30''E$, 270 m altitude), during the 2015-2016 season. The climate in the area is Mediterranean, with cold rainy winters, average $(5-7)^{\circ}C$, dry hot summers, average $(25-28)^{\circ}C$ and average annual precipitation 432 mm. In the olive orchard, the *Amfissis* cultivar grown, 1970 the planting took place with 7m distance tree from tree and 7.5 m distance line from line. 50 kg manure corresponding to 1.10 kg Nitrogen, 0.95 kg Potassium, 0.35 kg Phosphorus and 11.5 kg Organic matter per tree added, and 2000 m³ irrigation water per hectare added.

Olives samples were collected from the beginning of development and at different stages of maturation of olive *Amfissis*, where are observed changes in fruit color with the appearance of the green color (1 August, 90 days from start of flowering), green color (120 days from start of flowering), of the rosy color (140 days from start of flowering), of the reddish purple color (160 days from start of flowering), of the purple-black color (190 days from start of flowering), and black color (220 days from start of flowering). Two trees were chosen, and were sampled of olive fruits half kilogram with four replicates from each tree, from all the orientations and without type of disease.

Preparation of the methanol extracts

The flesh was separated from the kernel and 100 g of flesh for each treatment were subjected to freeze drying for further extraction and determination of humidity. The dry mass was crushed and stored in clean bottles in refrigeration [23]. Two g of dry sample was extracted two times with 50 mL of 80% aqueous methanol for 24 h at 150 rpm, the methanolic extracts were combined and washed two times with 25 mL n-hexane in order to eliminate the oil of the methanolic extract [24]. The separation of the phases was performed with separating funnels. Subsequently the methanolic extract was evaporated under nitrogen, and the residue was dissolved in 50 mL of 80% aqueous methanol, stored in clean bottles in refrigeration in the dark until its use.

Methods of analyses

Soil was analyzed using the following methods which are referred by Page (1982) [25].

Organic matter was analyzed by chemical oxidation with 1 mol L⁻¹ K₂Cr₂O₇ and titration of the remaining reagent with 0.5 mol L⁻¹ FeSO₄.

Inorganic nitrogen was extracted with 0.5 mol L⁻¹ CaCl₂ and estimated by distillation in the presence of MgO and Devarda's alloy, respectively. Available P forms (Olsen P) was extracted with 0.5 mol L⁻¹ NaHCO₃ and measured by spectroscopy. Exchangeable form of potassium was extracted with 1 mol L⁻¹ CH₃COONH₄ and measured by flame Photometer (Essex, UK).

Available forms of Mn, Zn, and Cu were extracted with DTPA (diethylene triamine pentaacetic acid 0.005 mol L⁻¹ + CaCl₂ 0.01 mol L⁻¹ + triethanolamine 0.1 mol L⁻¹) and measured by atomic absorption. The samples were analyzed by Atomic Absorption (Spectroscopy Varian Spectra AA 10 plus, Victoria, Australia), with the use of flame and air-acetylene mixture [26].

Electrical conductivity (EC) and pH measured in the extract (1 part soil : 5 parts H₂O).

Determination of total polyphenolics (TP). Total polyphenolic content was determined with the Folin-Ciocalteu (F.-C.) reagent according to the method by [27] using the microvariant proposed by [28] and the results were expressed as gallic acid equivalent (GAE) in mg g⁻¹ fresh weight.

Nonflavonoid phenols (NFP). The content of NFP was determined with the F.-C. reagent after removing the flavonoid phenols (FP) with formaldehyde according to the method by [29] and was expressed as gallic acid equivalent (GAE) in mg g⁻¹ fresh weight.

Flavonoid phenols (FP). Flavonoid phenols were determined as a difference between the content of total phenols (TP) and nonflavonoid phenols (NFP). Their amount was evaluated as gallic acid equivalent in mg g⁻¹ fresh weight.

Determination of antiradical activity (DPPH•). The antiradical activity of the methanol extracts was determined according to the method by [30] using the stable free radical 2,2'-diphenyl-1-picrylhydrazyl (DPPH•). The antiradical activity was expressed through IC₅₀ (Inhibition concentration, mg/l), which expresses the concentration of the extract required to reduce the absorbance of solution DPPH 50%. The absorbance reduction calculated according to the formula (1):

$$\% \text{ Inhibit DPPH} = (\text{Absorbance}_{\text{DPPH}} - \text{Absorbance}_{\text{Simple}}) / \text{Absorbance}_{\text{DPPH}} \times 100. \quad (1)$$

The concentration was found from the graph of inhibition percentage DPPH with different concentrations of samples.

Statistical analysis

Data were analyzed using the MINITAB [31] statistical package. The experiment had four replications. Analysis of variance was used to assess treatment effects. Mean separation was made using Tukey's test when significant differences (P=0.05) between treatments were found.

REFERENCES

1. N. Gougoulias, *Oxidation Communications*, **2014**, 37 (3), 713-721.
2. N. Gougoulias, P. Vyrlas, L. Giurgiulescu, D. Kalfountzos, F. Eugenia, *Carpathian Journal of Food Science and Technology*, **2015**, 7(4), 119-125.

3. N. Gougoulis, A. Papachatzis, I. Vagelas, L. Giurgiulescu, A. Karaboula, D. Kalfountzos, *Studia UBB Chemia*, **2016**, *LXI*, 4, 295 – 303.
4. D. Boskou, F. Visioli, *Metabolic and technological aspects*, **2003**, 161-169.
5. M. Bouaziz, R.J. Grayer, M.S. Simmonds, M. Damak, S. Sayadi, *Journal of agricultural and food chemistry*, **2005**, *53*(2), 236-241.
6. A. Dağdelen, G. Tümen, M.M. Özcan, E. Dündar, *Food chemistry*, **2013**, *136*(1), 41-45.
7. S. Silva, L. Gomes, F. Leitao, A.V. Coelho, L.V. Boas, *Food Science and Technology International*, **2006**, *12*(5), 385-395.
8. M. Brenes, L. Rejano, P. Garcia, A.H. Sanchez, A. Garrido, *Journal of Agricultural and Food Chemistry*, **1995**, *43*(10), 2702-2706.
9. M. Esti, L. Cinquanta, E. La Notte, *Journal of Agricultural and Food Chemistry*, **1998**, *46*(1), 32-35.
10. F. Visioli, S. Bellosta, C. Galli, *Life sciences*, **1998**, *62*(6), 541-546.
11. R.W. Owen, R. Haubner, G. Würtele, W.E. Hull, B. Spiegelhalder, H. Bartsch, *European Journal of Cancer Prevention*, **2004**, *13*(4), 319-326.
12. E. Tripoli, M. Giammanco, G. Tabacchi, D. Di Majo, S. Giammanco, M. La Guardia, *Nutrition research reviews*, **2005**, *18*(01), 98-112.
13. M. Bouaziz, M. Chamkha, S. Sayadi, *Journal of agricultural and food chemistry*, **2004**, *52*(17), 5476-5481.
14. R. Briante, M. Patumi, S. Limongelli, F. Febbraio, C. Vaccaro, A. Di Salle, F. La Cara, R. Nucci, *Plant Science*, **2002**, *162*(5), 791-798.
15. D. Ryan, M. Antolovich, P. Prenzler, K. Robards, S. Lavee, *Scientia Horticulturae*, **2002**, *92*(2), 147-176.
16. M. Bouaziz, H. Jemai, W. Khabou, S. Sayadi, *Journal of the Science of Food and Agriculture*, **2010**, *90*(10), 1750-1758.
17. R. Fernandez-Orozco, M. Roca, B. Gandul-Rojas, L. Gallardo-Guerrero, *Journal of Food Composition and Analysis*, **2011**, *24*(6), 858-864.
18. G. Menz, F. Vriesekoop, Physical and chemical changes during the maturation of Gordal Sevillana olives (*Olea europaea* L., cv. Gordal Sevillana). *Journal of agricultural and food chemistry*, **2010**, *58*(8), 4934-4938.
19. J. R. Morelló, M. P. Romero, M. J. Motilva, *Journal of agricultural and food chemistry*, **2004**, *52*(19), 6002-6009.
20. D. Ryan, K. Robards, S. Lavee, Changes in phenolic content of olive during maturation. *International journal of food science & technology*, **1999**, *34*(3), 265-274.
21. N. Damak, M. Bouaziz, M. Ayadi, S. Sayadi, M. Damak, *Journal of agricultural and food chemistry*, **2008**, *56*(5), 1560-1566.
22. A. Petridis, I. Therios, G. Samouris, *HortScience*, **2012**, *47*(3), 339-342.
23. G. Boskou, F.N. Salta, S. Chrysostomou, A. Mylona, A. Chiou, N.K. Andrikopoulos, *Food Chemistry*, **2006**, *94*(4), 558-564.
24. G. Rigane, R.B. Salem, S. Sayadi, M. Bouaziz, *Journal of food science*, **2011**, *76*(7), C965-C973.
25. M. Varian, Flama Atomic Absorption Spectroscopy. Analytical Methods. Varian Australia. Publ. N0: 85-100009-00, **1989**.

26. A. L. Page, *Methods of soil analysis. Part 2. Chemical and microbiological properties.* American Society of Agronomy, Soil Science Society of America, **1982**.
27. V.L. Singleton, J.A. Rossi, *American journal of Enology and Viticulture*, **1965**, *16(3)*, 144-158.
28. B. Baderschneider, D. Luthria, A.L. Waterhouse, P. Winterhalter, *VITIS-Journal of Grapevine Research*, **2015**, *38(3)*, 127-131.
29. T. E. Kramling, V. L. Singleton, *American Journal of Enology and Viticulture*, **1969**, *20(2)*, 86-92.
30. W. Brand-Williams, M.E. Cuvelier, C.L.W.T. Berset, Use of a Free Radical Method to Evaluate Antioxidant Activity. *LWT- Food Science and Technology*, **1995**, *28(1)*, 25-30.
31. B.F. Ryan, B.L. Joiner, J.D. Cryer *MINITAB Handbook: Updated for release 14*, 5th edition, **2005**.